


**Cornell NanoScale
Facility (CNF)**

**RESEARCH
ACCOMPLISHMENTS**

2023-2024

1 μm

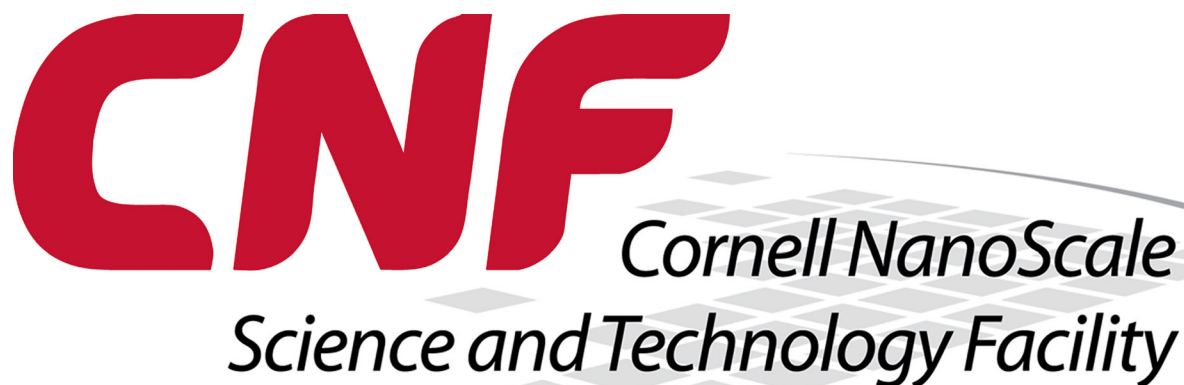


*Scanning electron microscope image
of a super-conducting quantum
interference device, or SQUID loop.*



**Empire State
Development**

**Cornell
Research
& Innovation**



250 Duffield Hall • 343 Campus Road • Ithaca NY 14853-2700
Phone: 607.255.2329 • Fax: 607.255.8601
Email: information@cnf.cornell.edu • Website: www.cnf.cornell.edu

Cornell NanoScale Facility 2023-2024 Research Accomplishments

CNF Lester B. Knight Director:
Jeeyoung Judy Cha

CNF Director of Operations:
Ronald Olson

Cornell NanoScale Facility (CNF) is a member of the
National Nanotechnology Coordinated Infrastructure (www.nnci.net)
and is supported by the National Science Foundation under Grant No. NNCI-2025233,
New York State Empire State Development, Cornell University, Industry, and our Users.

The 2023-2024 CNF Research Accomplishments are also available on the web in full color:
http://cnf.cornell.edu/publications/research_accomplishments

© 2024



2023-2024 CNF Research Accomplishments

TABLE of CONTENTS

Technical Reports by Section pages ii-v
 Photography Credits page v
 Directors’ Introduction page vi
 A Selection of 2023 CNF Research-Related
 Patents, Presentations, and Publications pages vii-xix
 2023-2024 CNF Research Accomplishments pages 2-175
 Index pages 176-179

BIOLOGICAL APPLICATIONS, 2-27

Development of a Biomembrane Platform for
 the Study of Virus Infection 2
 Metamaterial Elliptical Cylinder for High
 Sensitive
 Single-Molecule Torque Detection 4
 Building Microfluidics Devices
 to Study Zinc Metal Homeostasis in *E. Coli*
 Communities 6
 Design and Application of Microfluidic Devices
 to Study
 the Effect of the Physical Microenvironment
 on Cellular Function 8
 Metasurface-Enhanced Mid-Infrared
 Microscopy for Imaging Living Cells 10
 Time-Lapse Mid-Infrared Spectroscopy of Live
 Cells
 Using High-Aspect-Ratio Metal-on-
 Dielectric Nanostructures 12
 Biomimetic Loading Promotes Maturation and
 Suppresses Pathological Progression
 of Chick Embryonic Cardiomyocytes in
 Engineered Heart Tissues 14
 Micro-Scale Optoelectronic Transduced

Electrodes
 (MOTEs) for Chronic *in vivo* Neural
 Recording 16
 On-Chip Cell Transportation and Rotation
 Using Vibration-Induced Flow 18
 Fabrication of Microchip Devices for
 Organ-on-a-Chip and Lab-on-a-Chip
 Applications 20
 Investigating the Effect of the Tumor
 Microenvironment
 on Metastatic Progression Using Micro and
 Nano-Scale Tools 22
 Increasing Microfabrication Yield of
 Template-Based Carbon Nanotube Arrays
 for Gene Transfer 24
 High-Density, Integrated,
 Multi-Functional Neural Probe for Small
 Animals 26
CHEMISTRY, 28-33
 Sequence-Defined Peptoids as Next-Generation
 EUV Photoresists 28
 Direct Functionalization of Polyethylene
 Surfaces
 with High Density Polymer Brushes 30

New High-Resolution Resists for EUV Lithography32

ELECTRONICS, 34-53

Fabrication of 2D-Material-Based Ionic Transistors34

Optimizing Annealing Temperature for Ohmic Contacts to AlGaIn/GaN36

Fabrication of Interdigitated Electrodes for use in a Homebuilt Electron Force Microscope38

Ferroelectric Hafnium Zirconium Oxide Under the Gate of AlN/GaN High Electron Mobility Transistors40

Improving Interface Quality and Repeatability in Contacts to β -Ga₂O₃ by Metal-First Processing42

Transparent Dual Polarized Antenna44

Superconducting Microwave Devices at the CNF.46

System-on-Foil48

ASIC Design for a Fast X-Ray Pixel Array Detector50

Preferential Electro spray Deposition onto Interdigitated Electrodes52

MATERIALS, 54-79

Micro-Scale Ceramic Additive Manufacturing for Aerospace Applications54

Synthesis of Temperature-Responsive Hydrogel Particles for Hydraulic Control of Cooled Short Circuits56

Low Loss Superconducting LC Resonator for Strong Coupling with Magnons58

Investigation of Dry Chemical Actuators Using Palladium Thin Films60

Metal-Organic Framework-Inspired Metal-Containing Clusters for High-Resolution Patterning62

Thiol-Norbornene Photopolymer for Two-Photon Photopolymerization64

Influence of Ligand for Metallo-Elastomer Design66

Fabrication of Polymer Grafted Core-Shell Nanoparticles68

Quasi-2D Materials for Ultra-Low Resistance Electrical Interconnects70

Lithiation Induced Phases in 1T-MoTe₂ Nanoflakes72

Measuring Microplastic Migration Through Human Intestinal Mucus74

Fabrication of Non-Volatile Memory Transistors Using Hybrid Two-Dimensional Materials 76

FuSe Internship78

MECHANICAL DEVICES, 80-87

Harnessing Magnetic-Field Driven Actuation for Microscale Motion in MEMS-Inspired Device80

Fabrication of Micro Scale Triboelectric Microphone82

Magnetically Programmed Diffractive Robotics 84

Microwave Frequency Acoustic Resonators for Quantum Applications86

OPTICS & OPTO-ELECTRONICS, 88-101

High Efficiency Fiber-Chip Coupling88

Programmable Poling for Electric Field Induced Second Harmonic Generation . . .90

HfO₂-Based Platform for High Index Contrast Visible and UV Integrated Photonics92

Metamaterial Spectrometer: A Low SWaP, Robust, High Performance Hyperspectral Sensor for Land and Atmospheric Remote Sensing94

optiXphere Sensor Development	96	Magnetometry	124
Dual-Band Metalenses for Imaging and Absolute Temperature Detection	98	Fabrication of Fluxonium-Like Qubits.. . . .	126
Diffractive Optical Element Manufacturing Feasibility	100	Characterization of Fluxonium Qubits.. . . .	128
PHYSICS & NANO-STRUCTURE PHYSICS, 102-135		Probing Two-Dimensional Van der Waal Heterostructure and Height Characterization.	130
Nanomolding of Topological Materials for Interconnects	102	Observation of Exciton Polariton Band Structure	132
Micro-Additive Manufacturing Processes for Electrochemical CO ₂ Reduction	104	Using Photolithography to Mass-Produce Rings of Controlled Size	134
Study Unconventional Spin-Orbit Torque Generation on Micron-Sized Devices Fabricated with Photolithography	106	PROCESS & CHARACTERIZATION, 136-177	
Van der Waals Magnetic Tunnel Junctions with Metallic Transition Metal Dichalcogenide Electrodes	108	Fabrication of Superconducting Resonators on hBN Thin Films	136
Nanofabricated Superconducting Devices for Vortex Dynamics and Qubits	110	Fabrication and Characterization of High- Resistivity Silicon Interposers	138
Fabrication of Nanoscale Josephson Junctions for Quantum Coherent Superconducting Circuits	112	Atomic Layer Deposition of High-K Dielectrics 140	
Realization of the Haldane Chern Insulator in a Moiré Lattice	114	Investigating the Lateral Spreading of Vanadium-Based Ohmic Contacts.. . . .	142
Giant Spin Hall Effect in AB-Stacked MoTe ₂ / WSe ₂ Bilayers	116	Effect of Temperature on Particle Morphology Polymerized via Initiated Chemical Vapor Deposition in Liquid Crystal.. . . .	144
Thin-Film Deposition for Surface Characterization Studies for Superconducting Radio Frequency Cavity Application.	118	Stoichiometric Dependence of Physical & Electrical Properties of Silicon Nitride	146
Imaging Pulse-Induced Charge Density Wave Switching in 1T-TaS ₂	120	Atomic Layer Etching of III-Nitride Semiconductors	148
Manufacturing SiN Bullseye Cavities and SOI Photonic Crystal Nanobeam Cavities.	122	Fabricating Oxygen Managed and Thermally Robust Nb-Based Josephson Junction	150
Weak Link Superconducting Quantum Interference Devices for High-Resolution Scanning		Measuring Thickness of Extracellular Vesicle Mucin Coatings Using Nanoparticle Tracking Analysis . . .	152
		Polymer Film Microstructures via Surface-Directed Condensed Droplet Polymerization.	154

Tuning the Surface Wettability of Alumina Membrane for Carbonate Crystallization 156

Lithography for Topological Nanowires . . . 158

Through-Silicon Vias for Substrate-Integrated Waveguides 160

**CNF NORDTECH Internship:
Characterization of Oxynitride Films . . . 162**

Nanotechnology Workforce and Curriculum Development 164

Cornell NanoScale Facility High School Summer Internship 166

The Effects of Nitrogen Annealing on Etch Rates of HDPECVD and PECVD Silicon Dioxide Films 168

The Effects of Nitrogen Annealing on Stress of HDPECVD and PECVD Silicon Dioxide Films 170

The Viability of 1,3,3,3-Tetrafluoropropene as a Low Global Warming Potential Silicon Dioxide Etch Gas at the Cornell NanoScale Facility 172

An Evaluation of 1,3,3,3-Tetrafluoropropene as a Low Global Warming Potential Silicon Dioxide Etch Gas at the Cornell NanoScale Facility 174

PHOTOGRAPHY CREDITS

This year’s front cover image is from the report “Weak Link Superconducting Quantum Interference Devices for High-Resolution Scanning Magnetometry”; CNF Project Number: 3017-22, Principal Investigator: Katja Nowack; User: Alex Striff; Affiliation: Laboratory of Atomic and Solid State Physics, Cornell University – and was used with their permission. The full report starts on page 124.

The back cover image is from the report “Micro-Additive Manufacturing Processes for Electrochemical CO2 Reduction”; Summer Program: 2024 Cornell NanoScale Science & Technology Facility Research Experience for Undergraduates Program with Morgan State University, Principal Investigator: Sadaf Sobhani; CNF Summer Student: Hunter Saylor; Student Affiliation: Electrical and Computer Engineering, Morgan State University. The full report starts on page 104.

**COMMENTS, FEEDBACK,
AND SUGGESTIONS ARE
ALWAYS WELCOME.**

**FEEL FREE TO USE OUR
ONLINE USER COMMENT
FORM AT
[HTTPS://WWW.
CNFUSERS.CORNELL.
EDU/USER_FEEDBACK](https://www.cnfusers.cornell.edu/user_feedback)**

2023-2024 CNF Research Accomplishments

DIRECTORS' INTRODUCTION

The Cornell NanoScale Science and Technology Facility (CNF) takes pride in presenting this annual compilation of technical reports from our research groups who make good use of the extensive array of resources provided by the CNF. See the latest issue of our newsletter, the NanoMeter, to learn more about our new and existing programs and opportunities, latest tool acquisitions, updated capabilities and EWD (Education Workforce Development) initiatives (<https://www.cnf.cornell.edu/publications/nanometer>).

The 2023-2024 CNF Research Accomplishments showcases excellence in research while underscoring the diverse array of cutting-edge advancements spanning various fields of science and technology.

This book includes 75 technical reports from our active users and principal investigators and twelve final reports from our 2024 summer program undergraduate students. Almost every section begins with one of our CNF Research Experiences for Undergraduates (CNF REU) Program reports.

To wrap up, the 2023 CNF-related patents, presentations, and publications referred to as “the PPPs”- are listed. These 200 + items highlight the remarkable advancements achieved at the CNF.

We appreciate all the contributors who provided input to this publication, which can also be found online at https://www.cnf.cornell.edu/publications/research_accomplishments .

As always, we welcome your comments, concerns, and questions. Simply email us at information@cnf.cornell.edu

Judy Cha, Lester B. Knight Director

Allison Godwin, Associate Director

Ron Olson, Director of Operations

Lynn Rathbun, Laboratory Manager

2023-2024 CNF Research Accomplishments

A SELECTION OF 2023 CNF-RESEARCH-RELATED PATENTS, PRESENTATIONS, AND PUBLICATIONS

“15-GHz Epitaxial AlN FBARs on SiC Substrates”; Zhao, W.; Asadi, M.J.; Li, L.; Chaudhuri, R.; Nomoto, K.; Xing, H.G.; Hwang, J.C.M.; Jena, D., *IEEE Electron Device Letters*, IEEE (2023).

“2.2 W/mm at 94 GHz in AlN/GaN/AlN High-Electron-Mobility Transistors on SiC”; Hickman, A.; Chaudhuri, R.; Li, L.; Nomoto, K.; Moser, N.; Elliott, M.; Guidry, M.; Shinohara, K.; Hwang, J.C.M.; Xing, H.G.; Jena, D., *physica status solidi (a)*, Vol. 220, Issue 16, pgs 2200774, DOI 10.1002/pssa.202200774 (2023).

“A 3D biomimetic model of lymphatics reveals cell-cell junction tightening and lymphedema via a cytokine-induced ROCK2/JAM-A complex”; Lee, E.; Chan, S.-L.; Lee, Y.; Polacheck, W.J.; Kwak, S.; Wen, A.; Nguyen, D.-H.T.; Kutys, M.L.; Alimperti, S.; Kolarzyk, A.M.; Kwak, T. J.; Eyckmans, J.; Bielenberg, D.R.; Chen, H.; Chen, C.S., *Proceedings of the National Academy of Sciences*, Vol. 120, Issue 41, pgs e2308941120, DOI 10.1073/pnas.2308941120 (2023).

“A 3D Human Lymphatic Vessel-on-Chip Reveals the Roles of Interstitial Flow and VEGF-A/C for Lymphatic Sprouting and Discontinuous Junction Formation”; Ilan, I.S.; Yslas, A.R.; Peng, Y.; Lu, R.; Lee, E., *Cellular and Molecular Bioengineering*, Vol. 16, Issue 4, pgs 325-339, DOI 10.1007/s12195-023-00780-0 (2023).

“A human initial lymphatic chip reveals distinct mechanisms of primary lymphatic valve dysfunction in acute and chronic inflammation”; Kraus, S.; Lee, E., *Lab on a Chip*, Royal Society of Chemistry (2023).

“A model heterostructure with engineered Berry curvature”; Schreiber, N.J.; Miao, L.; Goodge, B.H.; Kourkoutis, L.F.; Shen, K. M.; Schlom, D.G., *APL Materials*, AIP Publishing, Vol. 11, Issue 6 (2023).

“A multiplexed microfluidic continuous-flow electroporation system for efficient cell transfection”; VanderBurgh, Jacob A.; Corso, Grant T.; Levy, Stephen L.; Craighead, Harold G., *Research Square*, posted 01 Nov 2023, <https://doi.org/10.21203/rs.3.rs-3538613/v1> (2023).

“A Non-Perturbative, Low-Noise Surface Coating for Sensitive Force-Gradient Detection of Electron Spin Resonance in Thin Films”; Boucher, Michael C.; Isaac, Corinne E.; Sun, Peter; Borbat, Peter P.; Marohn, John A., *ACS Nano*, Vol. 17, Issue 2, pgs 1153-1165, DOI 10.1021/acsnano.2c08635 (2023).

“A Photopolymer Composition Comprising Norbornene-derived Oligomers”; Yifan (Warrick) Ma, Yadong Wang, 10780, Invention Status; Unfiled, Invention, Disclosure Date 6/5/23 (2023).

“A puzzling insensitivity of magnon spin diffusion to the presence of 180-degree domain walls”; Li, Ruofan; Riddiford, Lauren J.; Chai, Yahong; Dai, Minyi; Zhong, Hai; Li, Bo; Li, Peng; Yi, Di; Zhang, Yuejie; Broadway, David A., *Nature Communications*, Nature Publishing Group UK London, Vol. 14, Issue 1, pgs 2393 (2023).

“A Wireless Sensor Array System Coupled with Data Analysis Methodologies towards Remote Monitoring of Human Breaths”; Dinh, Dong; Shang, Guojun; Yan, Shan; Luo, Jin; Huang, Aimin; Yang, Lefu; Lu, Susan; Zhong, Chuan-Jian, *IEEE Sensors Journal*, IEEE (2023).

“Absence of 3a0 Charge Density Wave Order in the Infinite Layer Nickelates”; Parzyck, C.; Gupta, N.; Wu, Y.; Anil, V.; Bhatt, L.; Bouliane, M.; Gong, R.; Gregory, B.; Luo, A.; Sutarto, R.; He, F.; Chuang, Y.; Zhou, T.; Herranz, G.; Kourkoutis, L.; Singer, A.; Schlom, D.; Hawthorn, D.; Shen, K., *arXiv 2307.06486 [cond-mat]* (2023).

“Absorption and scattering limits of integrated photonics in the visible spectrum”; Zanarella, Mateus Corato; Ji, Xingchen; Mohanty, Aseema; Lipson, Michal, *Optica Open*, preprint posted on 2023-05-10, <https://doi.org/10.1364/opticaopen.22783628.v1> (2023).

“Accurate doping profile extraction for predictive SPAD design”; Bonzi, Andrea; Laita, Gabriele; Rech, Ivan; Gulinatti, Angelo, *Emerging Imaging and Sensing Technologies for Security and Defence VIII*, SPIE, Vol. 12740, pgs 80-84 (2023).

“Active Tuning of the Microresonator Coupling Condition with Coupled Rings”; Zhao, Y., McNulty, K.J., et al., *CLEO 2023* (2023), paper SW4L.8. *CLEO: Science and Innovations*, Optica Publishing Group, p. SW4L.8. Available at: https://doi.org/10.1364/CLEO_SI.2023.SW4L.8 (2023).

“Additive Manufacturing and Characterization of Porous Ceramic Electro Spray Emitters”; Chamieh, Suhail; Petro, Elaine; Sobhani, Sadaf, *AIAA SCITECH 2023 Forum*, American Institute of Aeronautics and Astronautics, DOI 10.2514/6.2023-0261 (2023).

“Agarose-based 3D Cell Confinement Assay to Study Nuclear Mechanobiology”; Elpers, M.A.; Varlet, A.-A.; Agrawal, R.; Lammerding, J., *Current Protocols*, Vol. 3, Issue 7, pgs e847, DOI 10.1002/cpz1.847 (2023).

“AI-Based Image Processing for Photoresist Latent Image Enhancement: AM: Advanced Metrology”; Chen, Jiaxian; Davaji, Benyamin; Doerschuk, Peter C.; Lal, Amit; McCold, Cliff; Paranjpe, Ajit, 2023 34th Annual SEMI Advanced Semiconductor Manufacturing Conference (ASMC), IEEE, DOI: 10.1109/ASMC57536.2023.10121143 (2023).

“All-dielectric, visible wavelength focusing metalens with planar surface for mechanical robustness”; Park, J.-S., K. Vaillancourt, S. W. D. Lim, C. M. Spaegele, and F. Capasso, *CLEO 2023 Technical Digest Series* (Optica Publishing Group, 2023), paper SF3K.3, https://doi.org/10.1364/CLEO_SI.2023.SF3K.3 (2023).

“All-glass 100 mm Diameter Visible Metalens for Imaging the Cosmos”; Park, J.-S.; Lim, S.W.D.; Amirzhan, A.; Kang, H.; Karrfalt, K.; Kim, D.; Leger, J.; Urbas, A.M.; Ossiander, M.; Li, Z.; Capasso, F., arXiv 2307.08186 [astro-ph, physics:physics] (2023).

“All-optical frequency division on-chip using a single laser”; Zhao, Y., J.K. Jang, K.J. McNulty, X. Ji, Y. Okawachi, M. Lipson, A.L. Gaeta, arXiv:2303.02805 [physics.optics] [Submitted on 6 Mar 2023] (2023).

“AlN/AlGaIn/AlN quantum well channel HEMTs”; Singhal, Jashan; Kim, Eungkyun; Hickman, Austin; Chaudhuri, Reet; Cho, Yongjin; Xing, Huili G.; Jena, D., *Applied Physics Letters*, AIP Publishing, Vol. 122, Issue 22 (2023).

“An Integrative Approach Towards Understanding Drivers of Tumor Cell Heterogeneity”; Shimpi, Adrian, Cornell University 2023 Ph.D. Thesis (2023).

“Anisotropic gigahertz frequency antiferromagnetic resonance in easy-axis van der Waals semiconductor”; Cham, T.M.J., APS March Meeting 2023, Las Vegas, Contributed Talk (2023).

“Anomalous Vortex Microwave Response in Disordered Granular AI Resonators”; Plourde, B.L.T., Workshop on disordered superconductors and quantum circuits, Invited talk, Les Houches, France, June 7, 2023 (2023).

“Atomically smooth films of CsSb: a chemically robust visible light photocathode”; Parzyck, C.; Pennington, C.; DeBenedetti, W.; Balajka, J.; Echeverria, E.; Paik, H.; Moreschini, L.; Faeth, B.; Hu, C.; Nangoi, J.; Anil, V.; Arias, T.; Hines, M.; Schlom, D.; Galdi, A.; Shen, K.; Maxson, J., *APL Materials*, arXiv:2305.19553 [cond-mat, physics:physics], Vol. 11, Issue 10, pgs 101125, DOI 10.1063/5.0166334 (2023).

“BinDev: a Metric of Geometric Accuracy for Plasma-etch 3D Modeling Using Computer Vision: YM: Yield Methodologies”; Xie, Y.; Davaji, B.; Doerschuk, P.C.; Lal, A.; Chakarov, I.; Wen, S.; Hargrove, M.; Fried, D., 2023 34th Annual SEMI Advanced Semiconductor Manufacturing Conference (ASMC), IEEE, DOI: 10.1109/ASMC57536.2023.10121089 (2023).

“Biphasic Chemokinesis of Mammalian Sperm”; Zaferani, Meisam; Abbaspourrad, Alireza, *Physical Review Letters*, Vol. 130, Issue 24, pgs 248401, DOI 10.1103/PhysRevLett.130.248401 (2023).

“Bistability and Irregular Oscillations in Pairs of Opto-Thermal Micro-Oscillators”; Bhaskar, Aditya; Walth, Mark; Rand, Richard H.; Zehnder, Alan T., *Proceedings of the 2022 Annual Conference on Experimental and Applied Mechanics*, Vol. 4, pgs 19-23; *Advancements in Optical Methods, Digital Image Correlation & Micro-and Nanomechanics* (2023).

“BLAST: A Wafer-scale Transfer Process for Heterogeneous Integration of Optics and Electronics”; Ji, Yanxin; Cortese, Alejandro J.; Smart, Conrad L.; Molnar, Alyosha C.; McEuen, Paul L., arXiv 2302.05801 [physics] (2023).

“Bone-matrix mineralization dampens integrin-mediated mechanosignalling and metastatic progression in breast cancer”; Choi, S.; Whitman, M.; Shimpi, A.A.; Sempertegui, N.D.; Chiou, A.E.; Druso, J.E.; Verma, A.; Lux, S.C.; Cheng, Z.; Paszek, M., *Nature Biomedical Engineering*, Nature Publishing Group UK London, pgs 1-18 (2023).

“Bone-matrix mineralization dampens integrin-mediated mechanosignalling and metastatic progression in breast cancer”; Choi, S.; Whitman, M.A.; Shimpi, A.A.; Sempertegui, N.D.; Chiou, A.E.; Druso, J.E.; Verma, A.; Lux, S.C.; Cheng, Z.; Paszek, M., *Nature Biomedical Engineering*, Vol 7(11), 1455-1472 (2023). <https://doi.org/10.1038/s41551-023-01077-3> (2023).

“Bottom Tunnel Junction Light-emitting Field-effect Transistors”; Shyam Bharadwaj, Austin Hickman, Debdeep Jena, Kevin Lee, Kazuki Nomoto, Vladimir Protasenko, Len van Deurzen, H. Grace Xing, 9544-03-US, United States, US from PCT, Allowed, 1/14/23, 18/016,334 (2023).

“Changes in magnetic properties of a 2D magnet in proximity to a 3D topological insulator”; Jain, Rakshit; Gupta, Vishakha; Alnaser, Husain; Vashist, Amit; Deshpande, Vikram; Sparks, Taylor; Ralph, Daniel, *Bulletin of the APS March Meeting 2023, Las Vegas, Nevada* (March 5-10), Abstract: Y56.00006 (2023).

“Characterization of cells and tissues using a compact GHz ultrasonic imager”; Baskota, Anuj; Kuo, Justin; Ardanuç, Serhan; Lal, Amit, 2023 IEEE International Ultrasonics Symposium (IUS), IEEE, pgs 1-4 (2023).

“Characterization of the on-chip cavity coupled emission of 2D materials at room temperature”; Granados-Baez, M.; Mukherjee, A.; Qiu, L.; Chakraborty, C.; Vamivakas, A. N.; Cardenas, J., *Optical Materials Express*, Optica Publishing Group, Vol. 13, Issue 4, pgs 843-849 (2023).

“Characterizing the Capacitance of Josephson Junctions for Topologically Protected Qubits”; Cole, Bradley, et al., American Physical Society March Meeting, Contributed talk, Las Vegas, NV, March 8, 2023 (2023).

“Chemiresistive Sensor Array with Nanostructured Interfaces for Detection of Human Breaths with Simulated Lung Cancer Breath VOCs”; Shang, G.; Dinh, D.; Mercer, T.; Yan, S.; Wang, S.; Malaei, B.; Luo, J.; Lu, S.; Zhong, C.-J., *ACS Sensors*, Vol. 8, Issue 3, pgs 1328-1338, DOI 10.1021/acssensors.2c02839 (2023).

“Chip for dielectrophoretic microbial capture, separation and detection I: theoretical basis of electrode design”; Weber, Monika U.; Janusz J Petkowski, Robert E Weber, Bartosz Krajnik, Slawomir Stemplewski, Marta Panek, Tomasz Dziubak, Paulina Mrozinska, Anna Piela, Siu Lung Lo, *Nanotechnology*, Published 20 January 2023, Volume 34, Number 13 135502, DOI 10.1088/1361-6528/aca5c (2023).

“Chip for dielectrophoretic microbial capture, separation and detection II: experimental study”; Weber, Monika U.; Janusz J Petkowski, Robert E Weber, Bartosz Krajnik, Slawomir Stemplewski, Marta Panek, Tomasz Dziubak, Paulina Mrozinska, Anna Piela, Emil Paluch, *Nanotechnology*, Published 13 February 2023, Volume 34, Number 17 175502, DOI 10.1088/1361-6528/acb321 (2023).

“Chip-Based All-Optical Frequency Division”; Zhao, Y., Jang, J.K., McNulty, K.J., Ji, X., et al., *Optica Nonlinear Optics Topical Meeting 2023* (2023), paper W3A.2. *Nonlinear Optics*, Optica Publishing Group, p. W3A.2. <https://doi.org/10.1364/NLO.2023.W3A.2> (2023).

“Chip-scale simulations in a quantum-correlated synthetic space”; Javid, U.A.; Lopez-Rios, R.; Ling, J.; Graf, A.; Staffa, J.; Lin, Q.; *Nature Photonics*, Nature Publishing Group UK London, pgs 1-8 (2023).

“Coacervate Formulations of CXCR-Activating Peptides for Controlled Release in Ophthalmic and Topical Treatments”; S. Swamynathan, Y. Wang, A. Wells, 9787-04-PC, (PCT App), PCT - Patent Cooperation Treaty, Filed, 11/29/23, PCT/U2023/081556 (2023).

“Coacervate-Filled Lipid Vesicles for Protein Delivery”; Yeh, Chia-Wei; Wang, Yadong, *Macromolecular Bioscience*, Vol. 23, Issue 6, pgs 2200538, DOI 10.1002/mabi.202200538 (2023).

“Coherent Combining for High-Power Kerr Combs”; Bok Young Kim, Yoshitomo Okawachi, Jae K. Jang, Xingchen Ji, Michal Lipson, Alexander L. Gaeta, *Laser & Photonics Reviews*, Vol 17, Issue 8, August, 2023, 2200607, <https://doi.org/10.1002/lpor.202200607> (2023).

“Coherent Resonant Tunneling Transport through Non-centrosymmetric GaN/AlN Multi-barrier Heterostructures”; Encomendero, Jimmy; Protasenko, Vladimir; Jena, D.; Xing, G., *Bulletin of the APS March Meeting 2023*, Las Vegas, Nevada (March 5-10), Abstract: Y40.00002 (2023).

“Colimitation of light and nitrogen on algal growth revealed by an array microhabitat platform”; Liu, Fangchen; Gaul, Larissa; Giometto, Andrea; Wu, Mingming, arXiv 2307.02646v1 [Submitted on 5 Jul 2023] (2023).

“Compositions And Methods For Promoting Wound Healing And Minimizing Scarring”; Y. Wang, A.Wells, 9787-03-PC, (PCT App), PCT - Patent Cooperation Treaty, Filed, 3/21/23, PCT/US23/64780 (2023).

“Controlled Molten Metal Deposition”; Atieh Moridi, Kaushalendra Singh, 9707-03-US, United States, US from PCT, Prosecution, 6/22/23, 18/269,051 (2023).

“Controlled Molten Metal Deposition”; A. Moridi, K. Singh, 9707-04-EP, Europe, EPC - European Patent Convention, Prosecution, 7/20/23, 21912244.7 (2023).

“Convergent Approaches to Delineate the Metabolic Regulation of Tumor Invasion by Hyaluronic Acid Biosynthesis”; Shimpi, A.A.; Tan, M.L.; Vilkhovoy, M.; Dai, D.; Roberts, L.M.; Kuo, J.C.-H.; Huang, L.; Varner, J.D.; Paszek, M.; Fischbach, C., *Advanced Healthcare Materials*, Vol. 12, Issue 14, pgs 2202224, DOI 10.1002/adhm.202202224 (2023).

“Craft Knowledge and the Advancement of Science: The Role of Scientific Support Occupations in Shared Research Facilities”; Bovenberg, Danielle Elaine, University of California, Santa Barbara 2023 Ph.D. Thesis (2023).

“Cross-plane thermal conductivity of h-BN thin films grown by pulsed laser deposition”; Alvarez, G.A.; Christiansen-Salameh, J.; Biswas, A.; Puthirath, A.B.; Jeong, E.; Kwon, J.; Lee, J.; Gray, T.; Vajtai, R.; Ajayan, P.M., *Applied Physics Letters*, AIP Publishing, Vol. 122, Issue 23 (2023).

“Defeating broken symmetry with doping: Symmetric resonant tunneling in noncentrosymmetric heterostructures”; Encomendero, Jimmy; Protasenko, Vladimir; Jena, D.; Xing, Huili G., *Physical Review B*, Vol. 107, Issue 12, pgs 125301, DOI 10.1103/PhysRevB.107.125301 (2023).

“Design and Implementation of an AlScN-Based FeMEMS Multiplier for In-Memory Computing Applications”; Jadhav, Shubham; Gund, Ved; Ramesh, Madhav; Jena, D.; Lal, Amit, 2023 IEEE International Symposium on Applications of Ferroelectrics (ISAF), IEEE, pgs 1-4 (2023).

“Deterministic Access of High-Power, Normal-GVD Kerr-Comb States”; Sanyal, S., et al., *CLEO 2023* (2023), paper FW4B.3. *CLEO: Fundamental Science*, Optica Publishing Group, p. FW4B.3. Available at: https://doi.org/10.1364/CLEO_FS.2023.FW4B.3 (2023).

- “Development of High-Performance Niobium-3 Tin Cavities at Cornell University”; Shpani, L.; Arnold, S.; Gaitan, G.; Liepe, M.; Oseroff, T.; Porter, R.; Sitaraman, N.; Stilin, N.; Sun, Z.; Verboncoeur, N., Proc. 21th Int. Conf. RF Supercond. (SRF’23), Grand Rapids, MI, USA, pp. 600-606. doi:10.18429/JACoW-SRF2023-WEIAA04 (2023).
- “Device-Scale Nanochannel Evaporator for High Heat Flux Dissipation”; Ranjan, Durgesh; Maroo, Shalabh C., *Advanced Materials Interfaces*, Vol. 10, Issue 23, pgs 2300129, DOI 10.1002/admi.202300129 (2023).
- “Devices Including (III_x, Aly)Oz Superlattices”; D. Jena, G. Khalsa, H. Nair, V. Protasenko, Y.F. Zhang, 10253-02-PC, (PCT App), PCT - Patent Cooperation Treaty, Filed, 4/26/23, PCT/US23/19910 (2023).
- “Devices with Compositionally graded alloy layers”; S. Agrawal, J. Dill, J. Encomendero, D. Jena, L. van Deurzen, H. G. Xing, 10998-01-US, United States, MPP - Manuscript Plus Provisional, Filed, 12/9/23, 63/608,246 (2023).
- “Discovery of superconductivity in β -Nb 2 N and its electronic properties”; Ithepalli, A.; Jena, D.; Wright, J.; Pieczulewski, N.; Muller, D.; Xing, H.; Tang, H.; Wang, D.; Bulletin of the APS March Meeting 2023, Las Vegas, Nevada (March 5-10), Abstract: Q27.00002 (2023).
- “Distributed polarization doping of AlGaN heterostructures for laser diodes, light-emitting diodes, and power diode applications”; S. Agrawal, J. Dill, J. Encomendero, D. Jena, L. van Deurzen, H. G. Xing, 10998, Invention Status; Filed - Attorney Instructed to File, Disclosure Date 11/30/23 (2023).
- “Double U-Net based Virtual Metrology on Plasma-Etch CD-SEM Images: AM: Advanced Metrology”; Ding, S.; Peng, Y.; Davaji, B.; Doerschuk, P.C.; Lal, A.; Clark, J.; Bordonaro, G.; Genova, V.; Ober, C.K.; Ayres, S., 2023 34th Annual SEMI Advanced Semiconductor Manufacturing Conference (ASMC), IEEE, DOI: 10.1109/ASMC57536.2023.10121128 (2023).
- “Downconversion of Phonons to Suppress Correlated Errors in Superconducting Qubit Arrays”; Iaia, Vito, Syracuse University Ph.D. Thesis, June 2023 (2023).
- “Dropwise Condensation in Ambient on a Depleted Lubricant-Infused Surface”; Ranjan, Durgesh; Maheswar Chaudhary, An Zou, and Shalabh C. Maroo, *ACS Appl. Mater. Interfaces* 2023, 15, 17, 21679-21689, April 20, 2023, <https://doi.org/10.1021/acsmi.3c02450> (2023).
- “Dualtronics: Expanding the functionality of polar substrates”; Debdeep Jena, Henryk Turski, Len van Deurzen, H. Grace Xing, 10966, Invention Status; Filed - Attorney Instructed to File, Invention, Disclosure Date 11/5/23 (2023).
- “Duplex Microstructures in Additive Manufacturing Through Thermo-Mechanical Treatment of Defective Parts”; J. Bustillos, A. Moridi, 9700-03-US, United States, US from PCT, Filed, 7/6/23, 18,260,582 (2023).
- “Durable and regenerative superhydrophobic surface using porous nanochannels”; Ranjan, Durgesh; Zou, An; Maroo, Shalabh C., *Chemical Engineering Journal*, Elsevier, Vol. 455, pgs 140527 (2023).
- “Electric field induced migration of native point defects in Ga₂O₃ devices”; Haseman, Micah S.; Ramdin, Daram N.; Li, Wenshen; Nomoto, Kazuki; Jena, D.; Xing, Huili G.; Brillson, Leonard J., *Journal of Applied Physics*, Vol 133, Issue 3, Pages 3570 (2023).
- “Electrically empowered microcomb laser”; Ling, Jingwei; Zhengdong Gao, Shixin Xue, Qili Hu, Mingxiao Li, Kaibo Zhang, Usman A. Javid, Raymond Lopez-Rios, Jeremy Staffa, Qiang Lin, arXiv:2310.20157 [physics.optics] [Submitted on 31 Oct 2023] (2023).
- “Electrically-controlled Varifocal and Bifocal-Bicolor Metalenses Embedded in a Liquid Crystal”; Bosch, M., Shcherbakov, M., Won, K., Lee, H-S., Shvets, G., 2023 Conference on Lasers and Electro-Optics (CLEO), 07-12 May 2023, <https://ieeexplore.ieee.org/abstract/document/10259976> (2023).
- “Electronic nematic order in the normal state of strontium ruthenate”; Russell, Ryan S.; Nair, Hari P.; Shen, Kyle M.; Schlom, Darrell G.; Harter, John W., *Physical Review B*, Vol. 108, Issue 8, pgs L081105, DOI 10.1103/PhysRevB.108.L081105 (2023).
- “Elucidating Molecular-Scale Principles Governing the Anchoring of Liquid Crystal Mixtures on Solid Surfaces”; Gold, J.I.; Sheavly, J.K.; Bao, N.; Yu, H.; Rajbangshi, J.; Schauer, J.J.; Zavala, V.M.; Abbott, N.L.; Van Lehn, R.C.; Mavrikakis, M., *ACS Nano*, acsnano.3c06735, DOI 10.1021/acsnano.3c06735 (2023).
- “Emergence of ferromagnetism at the onset of moiré Kondo breakdown”; Zhao, W.; Shen, B.; Tao, Z.; Kim, S.; Knüppel, P.; Han, Z.; Zhang, Y.; Watanabe, K.; Taniguchi, T.; Chowdhury, D.; Shan, J.; Mak, K.F., arXiv 2310.06044 [Submitted on 9 Oct 2023] [cond-mat] (2023).
- “Emergent layer stacking arrangements in c-axis confined MoTe₂”; Hart, J.L.; Bhatt, L.; Zhu, Y.; Han, M.-G.; Bianco, E.; Li, S.; Hynek, D.J.; Schneeloch, J.A.; Tao, Y.; Louca, D., *Nature Communications*, Nature Publishing Group UK London, Vol. 14, Issue 1, pgs 4803 (2023).
- “Emerging technologies for musculoskeletal disease modeling and regenerative medicine”; Gawri, R.; Travascio, F.; Varghese, V.; Cheng, C.-K.; Shi, Z.-C.; Mao, N.-F.; Huang, Z.B.; Nie, M.D.; Zhang, N.Z.; Liu, S., *Frontiers Media SA*, pgs 251 (2023).
- “Energy and Thermal Management Using Micro/Nano Scale Geometries”; Poudel, Sajag, 16th ASNEng Annual Conference, July 2023, ResearchGate, DOI: 10.13140/RG.2.2.18402.30404 (2023).

“Engineered Biomaterials for Developing the Next Generation of In Vitro Tumor Models”; Kilian, K.; Fischbach, C.; Fong, E.L.S.; *Advanced Healthcare Materials*, Volume: 12, Issue: 14 Pages: 2300411 (2023).

“Engineered second-order nonlinearity in silicon nitride”; Zhang, Yi; Nauriyal, Juniyali; Song, Meiting; Baez, Marissa Granados; He, Xiaotong; Macdonald, Timothy; Cardenas, Jaime, *Optical Materials Express*, Optica Publishing Group, Vol. 13, Issue 1, pgs 237-246 (2023).

“Engineering large perpendicular magnetic anisotropy in amorphous ferrimagnetic gadolinium cobalt alloys”; Srinivasan, Karthik; Chen, Yulan; Cestarollo, Ludovico; Dare, Darrah K.; Wright, John G.; El-Ghazaly, Amal, *Journal of Materials Chemistry C*, Royal Society of Chemistry, Vol. 11, Issue 14, pgs 4820-4829 (2023).

“Engineering metabolic time-sharing in a clonal *Escherichia coli* population”; Papazotos, Fotini, Concordia University 2023 Ph.D. Thesis (2023).

“Enhanced Magnetic Anisotropy for Reprogrammable High-Force-Density Microactuators”; Chen, Yulan; Srinivasan, Karthik; Choates, Marcus; Cestarollo, Ludovico; El-Ghazaly, Amal, *Advanced Functional Materials*, pgs 2305502, DOI 10.1002/adfm.202305502 (2023).

“Enhanced Surface Superconductivity of Niobium by Zirconium Doping”; Sitaraman, N.; Sun, Z.; Francis, B.; Hire, A.; Oseroff, T.; Baraissov, Z.; Arias, T.; Hennig, R.; Liepe, M.; Muller, D.; Transtrum, M.; Center for Bright Beams, *Physical Review Applied*, Vol. 20, Issue 1, pgs 14064, DOI 10.1103/PhysRevApplied.20.014064 (2023).

“Enhanced TC in SrRuO₃/DyScO₃ (110) thin films with high residual resistivity ratio”; Schreiber, N.J.; Miao, L.; Nair, H.P.; Ruf, J.P.; Bhatt, L.; Birkholzer, Y.A.; Kotsonis, G.N.; Kourkoutis, L.F.; Shen, K.M.; Schlom, D.G., *APL Materials*, AIP Publishing, Vol. 11, Issue 11 (2023).

“Entangling interactions between artificial atoms mediated by a multimode left-handed superconducting ring resonator”; T. McBroom-Carroll, A. Schlaves, X. Xu, J. Ku, B. Cole, S. Indrajeet, M. D. LaHaye, M. H. Ansari, B. L. T. Plourde, arXiv:2307.15695 [Submitted on 28 Jul 2023] (2023).

“Epitaxial Na_xCoO₂ Thin Films via Molecular-Beam Epitaxy and Topotactic Transformation: A Model System for Sodium Intercalation”; Matson, Stephanie D.; Sun, Jiaxin; Huang, Jason J.; Werder, Don J.; Schlom, Darrell G.; Singer, Andrej, *The Journal of Physical Chemistry C*, Vol. 127, Issue 14, pgs 6638-6644, DOI 10.1021/acs.jpcc.3c00298 (2023).

“Epitaxial Sc_xAl_{1-x}N Semiconductor Devices”; Joseph Casamento, Benyamin Davaji, Ved Gund, Debdeep Jena, Amit Lal, Hyunjea Lee, Takuya Maeda, H. Grace Xing, 9924-02-US, United States, US from PRV, Filed, 5/17/23, 18/198,515 (2023).

“Event-driven MEMS vibration sensor: Integration of triboelectric nanogenerator and low-frequency switch”; Mousavi, M.; Alzgoool, M.; Davaji, B.; Towfighian, S., *Mechanical Systems and Signal Processing*, Elsevier, Vol. 187, pgs 109921 (2023).

“Evidence of frustrated magnetic interactions in a Wigner-Mott insulator”; Tang, Y.; Su, K.; Li, L.; Xu, Y.; Liu, S.; Watanabe, K.; Taniguchi, T.; Hone, J.; Jian, C.-M.; Xu, C., *Nature Nanotechnology*, Nature Publishing Group UK London, Vol. 18, Issue 3, pgs 233-237 (2023).

“Exchange bias between van der Waals materials: tilted magnetic states and field-free spin-orbit-torque switching”; Cham, T.M.J., *Spin Dynamics in Nanostructures Gordon Research Conference 2023*, Poster Presentation, Les Diablerets, Switzerland (2023).

“Exchange bias between van der Waals materials: tilted magnetic states and field-free spin-orbit-torque switching”; Cham, T.M.J., R.J. Dorrian, X.S. Zhang, A.H. Dismukes, D.G. Chica, A.F. May, X. Roy, D.A. Muller, D.C. Ralph, Y.K. Luo, *Advanced Materials*, 06 October 2023 <https://doi.org/10.1002/adma.202305739> (2023).

“Exciton density waves in Coulomb-coupled dual moiré lattices”; Zeng, Y.; Xia, Z.; Dery, R.; Watanabe, K.; Taniguchi, T.; Shan, J.; Mak, K.; *Nature Materials*, Nature Publishing Group UK London, V.22, I.2, pgs 175-9 (2023).

“Excitonic and deep-level emission from N- and Al-polar homoepitaxial AlN grown by molecular beam epitaxy”; van Deurzen, L.; Singhal, J.; Encomendero, J.; Pieczulewski, N.; Chang, C.; Cho, Y.; Muller, D.A.; Xing, H.G.; Jena, D.; Brandt, O.; Lähnemann, J., *APL Materials*, arXiv:2305.10542 [cond-mat], Vol. 11, Issue 8, pgs 81109, DOI 10.1063/5.0158390 (2023).

“Exploring the Evolution of Organofluorine-Containing Compounds during Simulated Photolithography Experiments”; Jacob, Paige; Helbling, Damian E., *Environmental Science & Technology*, Vol. 57, Issue 34, pgs 12819-12828, DOI 10.1021/acs.est.3c03410 (2023).

“Extracting Mural and Volumetric Growth Patterns of Platelet Aggregates on Engineered Surfaces by Use of an Entity Tracking Algorithm”; Kang, Junhyuk; Jayaraman, Anjana; Antaki, James F.; Kirby, Brian J., *ASAIO Journal (American Society for Artificial Internal Organs)*, NIH Public Access, Vol. 69, Issue 4, pgs 382 (2023).

“Extraordinary permittivity characterization of 4H SiC at millimeter-wave frequencies”; Li, Lei; Reyes, Steve; Asadi, Mohammad Javad; Fay, Patrick; Hwang, James, *Applied Physics Letters*, AIP Publishing, Vol. 123, Issue 1 (2023).

“Faster sperm selected by rheotaxis leads to superior early embryonic development in vitro”; Yaghoobi, M.; Abdelhady, A.; Favakeh, A.; Xie, P.; Cheung, S.; Mokhtare, A.; Lee, Y.; Nguyen, A.; Palermo, G.; Rosenwaks, Z.; *Lab on a Chip*, Royal Society of Chemistry (2023).

“Fiber array to chip attach using laser fusion splicing for low loss”; Nauriyal, J.; Song, M.; Zhang, Y.; Granados-Baez, M.; Cardenas, J.; Optics Express, Optica Publishing Group, Vol. 31, Issue 13, pgs 21863-21869 (2023).

“Fiber to Chip Fusion Splicing for Low Loss Optical Coupling”; Nauriyal, Juniyali, University of Rochester 2023 Ph.D. Thesis (2023).

“Gas-phase microactuation using kinetically controlled surface states of ultrathin catalytic sheets”; Bao, N.; Liu, Q.; Reynolds, M.F.; Figueras, M.; Smith, E.; Wang, W.; Cao, M.C.; Muller, D.A.; Mavrikakis, M.; Cohen, I.; McEuen, P.L.; Abbott, N.L., Proceedings of the National Academy of Sciences, Vol. 120, Issue 19, pgs e2221740120, DOI 10.1073/pnas.2221740120 (2023).

“Gate-tunable heavy fermions in a moiré Kondo lattice”; Zhao, Wenjin; Shen, Bowen; Tao, Zui; Han, Zhongdong; Kang, Kaifei; Watanabe, Kenji; Taniguchi, Takashi; Mak, Kin Fai; Shan, Jie, Nature, Nature Publishing Group UK London, Vol. 616, Issue 7955, pgs 61-65 (2023).

“Generation of Low-Frequency Kerr Combs in Highly Compact Photonic Structures”; Beals, G., et al., CLEO 2023 (2023), paper STh4F.2. CLEO: Science and Innovations, Optica Publishing Group, p. STh4F.2. Available at: https://doi.org/10.1364/CLEO_SI.2023.STh4F.2 (2023).

“Group III Oxide Devices with Select Iron Doped Areas”; B. Cromer, D. Dryden, D. Jena, H. G. Xing, 10396-02-PC, (PCT App), PCT - Patent Cooperation Treaty, Filed, 8/4/23, PCT/US23/29539 (2023).

“Growth windows of epitaxial NbN x films on c -plane sapphire and their structural and superconducting properties”; Wright, John G.; Xing, Huili G.; Jena, D., Physical Review Materials, Vol. 7, Issue 7, pgs 74803, DOI 10.1103/PhysRevMaterials.7.074803 (2023).

“Hardware implementation of quantum stabilizers in superconducting circuits”; Dodge, K.; Liu, Y.; Klots, A. R.; Cole, B.; Shearrow, A.; Senatore, M.; Zhu, S.; Ioffe, L. B.; McDermott, R.; Plourde, B. L. T., Physical Review Letters, Vol. 131, Issue 15, pgs 150602, DOI 10.1103/PhysRevLett.131.150602 (2023).

“Heat transfer characteristics of turbulent flow of supercritical carbon dioxide (sCO₂) in a short-heated microchannel”; Manda, Uday; Anatoly Parahovnik, Sagnik Mazumdar, Yoav Peles, International Journal of Thermal Sciences, Volume 192, Part A, October 2023, 108389 (2023).

“Heat Transfer of Supercritical CO₂ Near the Critical Condition Inside a Microchannel”; Ahmed, Pranzal; Parahovnik, Anatoly; Peles, Yoav, Heat Transfer Summer Conference, American Society of Mechanical Engineers, Vol. 87165, pgs V001T10A001 (2023).

“HfO₂-based Platform for High Index Contrast Visible and UV Integrated Photonics”; Jaramillo, Oscar; Massai, Leonardo; Mehta, Karan, 2023 Conference on Lasers and Electro-Optics (CLEO), IEEE, Date of Conference: 07-12 May 2023 (2023).

“High Signal-to-Noise Ratio Event-Driven MEMS Motion Sensing”; Mousavi, Mohammad; Alzgoool, Mohammad; Davaji, Benyamin; Towfighian, Shahrzad, Small, pgs 2304591, DOI 10.1002/sml.202304591 (2023).

“High-Concentration Self-Assembly of Zirconium- and Hafnium-Based Metal-Organic Materials”; Jerozal, Ronald T., Tristan A. Pitt, Samantha N. MacMillan, Phillip J. Milner, Nanoporous Materials and Their Applications Gordon Research Conference, Poster Presentation, Andover, NH. August, 2023 (2023).

“High-Concentration Self-Assembly of Zirconium- and Hafnium-Based Metal-Organic Materials”; Jerozal, Ronald T., Tristan A. Pitt, Samantha N. MacMillan, Phillip J. Milner, UB Chemistry Graduate Student Symposium, Poster Presentation, University at Buffalo, Buffalo, NY. May, 2023. (2023).

“High-Concentration Self-Assembly of Zirconium- and Hafnium-Based Metal-Organic Materials”; Jerozal, Ronald T., Tristan A. Pitt, Samantha N. MacMillan, Phillip J. Milner, Western New York Inorganic Symposium, Poster Presentation, University at Rochester, Rochester, NY. August, 2023 (2023).

“High-Concentration Self-Assembly of Zirconium- and Hafnium-Based Metal-Organic Materials”; Jerozal, Ronald T.; Pitt, Tristan A.; MacMillan, Samantha N.; Milner, Phillip J., Journal of the American Chemical Society, Vol. 145, Issue 24, pgs 13273-13283, DOI 10.1021/jacs.3c02787 (2023).

“High-Efficiency, 80 mm Aperture Metalens Telescope”; Zhang, L., S. Chang, X. Chen, Y. Ding, M. Rahman, Y. Duan, M. Stephen, and X. Ni, Nano Lett. 2023, 23, 1, 51-57, December 16, 2022, <https://doi.org/10.1021/acs.nanolett.2c03561> (2023).

“High-Gain Parametric Amplification On-Chip at Low Pump Powers”; Zhao, Y., Jang, J.K., Ji, X., Okawachi, Y., et al., CLEO 2023 (2023), paper SF2P.1. CLEO: Science and Innovations, Optica Publishing Group, p. SF2P.1. Available at: https://doi.org/10.1364/CLEO_SI.2023.SF2P.1 (2023).

“High-speed tunable microwave-rate soliton microcomb”; He, Yang; Lopez-Rios, Raymond; Javid, Usman A.; Ling, Jingwei; Li, Mingxiao; Xue, Shixin; Vahala, Kerry; Lin, Qiang, Nature Communications, Nature Publishing Group UK London, Vol. 14, Issue 1, pgs 3467 (2023).

“Hybrid electrical and magnetic resonance device based on Vanadium Tetracyanoethylene”; Michael Flatte, Gregory Fuchs, Ezekiel Johnston-Halperin, 10624, Invention Status; Unfiled, Invention, Disclosure Date 2/3/23 (2023).

“In Vitro Modeling and Analysis to Investigate the Metabolic Regulation of Breast Cancer Invasion Towards the Vasculature”; Tan, M.L., Cornell 2023 Ph.D. Thesis (2023).

“Increasing Density of Semiconductor Devices on a substrate”; D. Jena, H. Turski, L. van Deurzen, H. G. Xing, 10966-01-US, United States, MPP - Manuscript Plus Provisional, Filed, 11/14/23, 63/548,460 (2023).

“Infection-on-a-chip for viral entry modeling”; Daniel, Susan; Chao, Zhongmou; Selivanovitch, Ekaterina; Kallitsis, Konstantinos; Lu, Zixuan; Owens, Roisin, Research Square, posted 14 Nov 2023, <https://doi.org/10.21203/rs.3.rs-3353086/v1> (2023).

“Integrated Quantum Computing with Epitaxial Materials”; Phillip Dang, Debdeep Jena, Guru Khalsa, John Wright, H. Grace Xing, 9762-03-US, United States, US from PCT, Filed, 8/16/23, 18/277,519 (2023).

“Integrated, Compact, and Tunable Band-Interleaving of a Kerr Comb Source”; Wang, S., et al., CLEO 2023 (2023), paper STh3J.6. CLEO: Science and Innovations, Optica Publishing Group, p. STh3J.6. Available at: https://doi.org/10.1364/CLEO_SI.2023.STh3J.6 (2023).

“Interfacing Superconducting Qubits with Cryogenic Digital Circuits”; Plourde, B.L.T., Moonshot Goal 6 International Symposium 2023, Invited talk, Tokyo, Japan, July 19 (2023).

“Inverse doping profile extraction for predictive SPAD modeling”; Bonzi, A.; Laita, G.; Rech, I.; Gulinatti, A.; 2023 International Conference on Numerical Simulation of Optoelectronic Devices (NUSOD), IEEE, pgs 15-16 (2023).

“Inverse doping profile extraction for predictive SPAD modeling”; Bonzi, Andrea; Laita, Gabriele; Rech, Ivan; Gulinatti, Angelo, Proceedings of the 2023 SPIE 12512, Advanced Photon Counting Techniques XVII, 1251207 (15 June 2023); doi: 10.1117/12.2665696 (2023).

“Inverted transfection spectroscopy of live cells using metallic grating on elevated nanopillars”; Mahalanabish, Aditya; Huang, Steven H.; Shvets, Gennady, bioRxiv, Cold Spring Harbor Laboratory, pgs 2023-09 (2023).

“Kinetic Insights into Bridge Cleavage Pathways in Periodic Mesoporous Organosilicas”; Sun, Zeming; Connolly, Aine; Thompson, Michael O., arXiv 2301.06222 [cond-mat, physics:physics] (2023).

“Ladder-shaped microfluidic system for rapid antibiotic susceptibility testing”; Nguyen, A.V.; Yaghoobi, M.; Azizi, M.; Davaritouchaee, M.; Simpson, K.W.; Abbaspourrad, A., Communications Engineering, Nature Publishing Group UK London, Vol. 2, Issue 1, pgs 15 (2023).

“Large regenerative parametric amplification on chip at ultra-low pump powers”; Zhao, Y., Jang, J.K., Ji, X., Okawachi, Y., et al., Optica, 10(7), pp. 819-825. <https://doi.org/10.1364/OPTICA.483466> (2023).

“Lattice-matched AlScN/GaN for optoelectronic devices”; J. Casamento, D. Jena, T. Nguyen, C. Savant, L. van Deurzen, H. G. Xing; 10886-01-US, United States, Manuscript Plus Provisional, Filed, 9/27/23, 63/540,746 (2023).

“Lattice-matched AlScN/GaN for optoelectronic devices”; Joseph Casamento, Debdeep Jena, Thai-Son Nguyen, Chandrashekhar Savant, Len van Deurzen, H. Grace Xing, 10886, Invention Status; Filed - by Cornell, Invention, Disclosure Date 9/11/23 (2023).

“Layered Microneedles ”; Yadong Wang, Nathaniel Wright, 10684-01-US, United States, MPR - Manuscript Provisional, Filed, 4/20/23, 63/497,394 (2023).

“Layered Microneedles for Controlled Release”; Yadong Wang, Nathaniel Wright, 10684, Invention Status; Filed - by Cornell, Invention, Disclosure Date 3/29/23 (2023).

“Lewis acidity and substituent effects influence aldehyde enolization and C-C coupling in beta zeolites”; He, W.; Potts, D.S.; Zhang, Z.; Liu, B.; Schuarca, R.L.; Hwang, S.-J.; Bond, J.Q.; Flaherty, D.W.; Cybulskis, V.J., Journal of Catalysis, Elsevier, Vol. 427, pgs 115105 (2023).

“Lipocoacervate application in inducing immunotolerance for islet transplant”; Haval Shirwan, Yadong Wang, Nathaniel Wright, 10736, Invention Status; Unfiled, Invention, Disclosure Date 3/16/23 (2023).

“Lipocoacervates and Methods of Making and Using Same”; Y. Wang, C.-W. Yeh, 10527-01-US, United States, EPR - Enhanced Provisional, Filed, 5/24/23, 63/468,678 (2023).

“Liquid Crystalline Emulsions and Uses Thereof”; Nicholas Abbott, Sangchul Roh, 9736-03-US, United States, US from PCT, Filed, 12/7/23, 18/568,233 (2023).

“Localized measurements of water potential reveal large loss of conductance in living tissues of maize leaves”; Jain, P.; Huber, A.E.; Rockwell, F.E.; Sen, S.; Holbrook, N. M.; Stroock, A.; bioRxiv, Cold Spring Harbor Laboratory, pgs 2023-06 (2023).

“Long-Lived Dynamics Enables Exciton-Polariton Upconversion in CdSe Nanoplatelets”; Amin, M., E. Koessler, O. Morshed, F. Awan, N. Cogan, R. Collison, W. Girten, C. Leiter, A.N. Vamivakas, P. Huo, T. Krauss, ChemRxiv Nanoscience, Oct 12, 2023 Version 1 (2023).

“Low Stress Bilayer LPCVD-PECVD SiN Waveguides for Kerr Frequency Comb Generation”; McNulty, K.J., et al., CLEO 2023 (2023), paper STh1J.2. CLEO: Science and Innovations, Optica Publishing Group, p. STh1J.2. Available at: https://doi.org/10.1364/CLEO_SI.2023.STh1J.2 (2023).

“Low-Loss, High Extinction Ratio Fiber to Chip Connection via Laser Fusion for Polarization Maintaining Fibers”; Kumar, Sushant; Nauriyal, Juniyali; Cardenas, Jaime, 2023 Optical Fiber Communications Conference and Exhibition (OFC), IEEE, pgs 1-3 (2023).

“Macrocyclic Chelators and Methods of Use for the Separation of Rare Earth Elements”; Yangyang Gao, Justin Wilson, 10702-01-US, United States, MPP - Manuscript Plus Provisional, Filed, 5/26/23, 63/469,088 (2023).

“Magnetic skyrmion resonance with density control”; Olszewski, Maciej; Lai, Audre; Zhang, Xiyue; Muller, David; Fuchs, Gregory; Ralph, Daniel, Bulletin of the APS March Meeting 2023, Las Vegas, Nevada (March 5-10), Abstract: M44.00007 (2023).

“Massively scalable Kerr comb-driven silicon photonic link”; Rizzo, A.; Novick, A.; Gopal, V.; Kim, B.Y.; Ji, X.; Daudlin, S.; Okawachi, Y.; Cheng, Q.; Lipson, M.; Gaeta, A.L., Nature Photonics, Nature Publishing Group UK London, Vol. 17, Issue 9, pgs 781-790 (2023).

“Materials Characterizations and Process Optimizations Enabling the Additive Fabrication of Electronics for RF, High-Power, and Device Packaging Applications”; Richmond, Dylan J, State University of New York at Binghamton 2023 Ph.D. Thesis (2023).

“Materials design for superconducting RF cavities: electroplating Sn, Zr and Au onto Nb and chemical vapor deposition”; Sun, Z.; Liepe, M. U.; Oseroff, T.; Baraissov, Z.; Muller, D. A.; Thompson, M. O.; Proc. 21th Int. Conf. RF Supercond. (SRF’23), Grand Rapids, MI, USA, Jun. 2023, pp. 401-404. doi:10.18429/JACoW-SRF2023-TUPTB006 (2023).

“Measurements of the amplitude-dependent microwave surface resistance of an Au/Nb bilayer”; Oseroff, T.; Sun, Z.; Liepe, M.; Proc. 21th Int. Conf. RF Supercond. (SRF’23), Grand Rapids, MI, USA, Jun. 2023, pp. 369-373. doi:10.18429/JACoW-SRF2023-TUCBA01 (2023).

“Measurements of the amplitude-dependent microwave surface resistance of an Au/Nb bilayer”; Oseroff, Thomas; Sun, Zeming; Liepe, Matthias, Superconductor Science and Technology, Vol. 36, Issue 11, pgs 115009, DOI 10.1088/1361-6668/acf88d (2023).

“Measurements of variable capacitance using single port radio frequency reflectometry”; Celis-Cordova, R.; Gose, J.; Brown, A.; Behn, A.; Huebner, M.; Williams, E.; Xiang, Y.; Chisum, J.; Orlov, A.; Snider, G.; Review of Scientific Instruments, AIP Publishing, Vol. 94, Issue 8 (2023).

“Mechanical compression regulates tumor spheroid invasion into a 3D collagen matrix”; Pandey, Mrinal; Suh, Young Joon; Kim, Minha; Davis, Hannah Jane; Segall, Jeffrey E.; Wu, Mingming, arXiv 2307.01289v1 [2023 Jul 3] (2023).

“Mechanical stimuli activate gene expression via a cell envelope stress sensing pathway”; Harper, C., W. Zhang, J. Lee, J.-H. Shin, M. Keller, E. van Wijngaarden, E. Chou, Z. Wang, T. Dörr, P. Chen, C. J. Hernandez, Scientific Reports, Nature Publishing Group UK London, Vol. 13, Issue 1, pgs 13979 (2023).

“Membrane Pore Size Distribution by Design via Kinetic Engineering Using Initiated Chemical Vapor Deposition”; Khlyustova, Alexandra; Cheng, Yifan; Yang, Rong, Macromolecules, Vol. 56, Issue 16, pgs 6492-6500, DOI 10.1021/acs.macromol.3c01078 (2023).

“Metamaterial spectrometer on a chip for hyperspectral imaging and atmospheric sounding”; Crouse, D.; Bendoyim, I.; Lepak, L.A.; Leitch, J.; Applegate, J.; High Contrast Metastructures XII, SPIE, Vol. 12432, pgs 44-49 (2023).

“Metastable Phase Formation and Materials Discovery in Complex Oxide Thin Films via Laser Spike Annealing”; Connolly, A, Cornell University 2023 Ph.D. Thesis (2023).

“Metasurface enhanced infrared spectroscopy using vertical nanostructures”; Mahalanabish, Aditya; Huang, Steven H.; Shvets, Gennady, Label-free Biomedical Imaging and Sensing (LBIS) 2023, SPIE, Vol. 12391, pgs 105-110 (2023).

“Metasurface-enhanced infrared reflection chemical imaging on live and fixed cells with a QCL microscope”; Shen, P.-T.; Huang, S.H.; Sartorello, G.; Shvets, G.; Advanced Chemical Microscopy for Life Science and Translational Medicine 2023, SPIE, Vol. 12392, pgs 50-56 (2023).

“Metasurface-enhanced infrared spectroscopy in multiwell format for real-time assaying of live cells”; Huang, S.H.; Sartorello, G.; Shen, P.-T.; Xu, C.; Elemento, O.; Shvets, G.; Lab on a Chip, Royal Society of Chemistry, Vol. 23, Issue 9, pgs 2228-2240 (2023).

“Method for Protecting Reactive Materials with Atomically Thin Film”; W. DeBenedetti, M. Hines, 9602-03-US, United States, US from PCT, Filed, 11/7/23, 18/559,491 (2023).

“Methods of making Ceramic Electro Spray Emitters, Ceramic Electro Spray Emitters and Uses Thereof”; Suhail Chamieh, Elaine Petro, Sadaf Sobhani, 10526-01-US, United States, MPP - Manuscript Plus Provisional, Converted, 1/6/23, 63/437,537 (2023).

“Microscopic, continuum, compliant, and electronically configurable metamaterial robots”; Itai Cohen, Jacob Pelster, 10868-01-US, United States, MPP - Manuscript Plus Provisional, Filed, 10/27/23, 63/546,116 (2023).

“Microscopic, continuum, compliant, and electronically configurable metamaterial robots”; I. Cohen, X. Jia, Q. Liu, J. Pelster, Y. Zhang; 10868, Invention Status; Filed - by Cornell, Invention, Disclosure Date 8/29/23 (2023).

“Microwave Annealer for Semiconductor Wafers”; M. Asadi, G. Fabi, J. Hwang, J. Joo, C. Savant, 10318-03-PC, (PCT App), PCT - Patent Cooperation Treaty, Filed, 4/28/23, PCT/US2023/20415 (2023).

“Microwave vortex dynamics in superconducting granular aluminum resonators”; Larson, Clay, et al., American Physical Society March Meeting, Contributed talk, Las Vegas, NV, March 10, 2023. (2023).

“Mimicking Kidney Flow Shear Efficiently Induces Aggregation of LECT2, a Protein Involved in Renal Amyloidosis”; Ha, J.-H.; Xu, Y.; Sekhon, H.; Wilkens, S.; Ren, D.; Loh, S.N.; bioRxiv, Cold Spring Harbor Laboratory Preprints (2023).

“Modeling Algal Growth Under Controlled Microenvironment Using a Microfluidic Platform”; Liu, Fangchen, Cornell University 2023 Ph.D. Thesis (2023).

“Multimode entangling interactions between transmons coupled through a metamaterial ring-resonator: experiment”; McBroom, T., et al., American Physical Society March Meeting, Contributed talk, Las Vegas, NV, March 6 (2023).

“N-polar GaN/AlGaIn/AlN high electron mobility transistors on single-crystal bulk AlN substrates”; Kim, E.; Zhang, Z.; Encomendero, J.; Singhal, J.; Nomoto, K.; Hickman, A.; Wang, C.; Fay, P.; Toita, M.; Jena, D., Applied Physics Letters, AIP Publishing, Vol. 122, Issue 9 (2023).

“Nanoliter Electronics for Wireless Chemistry”; Norris, Samantha, Cornell University 2023 Ph.D. Thesis (2023).

“Nanomolding of metastable Mo4P3”; Kiani, Mehrdad T.; Sam, Quynh P.; Jin, Gangtae; Pamuk, Betül; Han, Hyeuk Jin; Hart, James L.; Stauff, J. R.; Cha, Judy J., Matter, Elsevier, Vol. 6, Issue 6, pgs 1894-1902 (2023).

“Nanoscale magnetic field sensing with spin-Hall nanoo oscillator devices”; Xie, Yanyou; Cheung, Hil Fung Harry; Fuchs, Gregory D., arXiv 2303.02478 [cond-mat] (2023).

“Nanoscale reshaping of resonant dielectric microstructures by light-driven explosions”; Shcherbakov, M.R.; Sartorello, G.; Zhang, S.; Bocanegra, J.; Bosch, M.; Tripepi, M.; Talisa, N.; AlShafey, A.; Smith, J.; Londo, S., Nature Communications, Nature Publishing Group UK London, Vol. 14, Issue 1, pgs 6688 (2023).

“Nanoscale Surface Structure of Nanometer-Thick Ferroelectric BaTiO₃ Films Revealed by Synchrotron X-ray Scanning Tunneling Microscopy: Implications for Catalytic Adsorption Reactions”; Abbasi, P.; Shirato, N.; Kumar, R.E.; Albelo, I.V.; Barone, M.R.; Cakan, D.N.; Cruz-Jáuregui, M.; Wieghold, S.; Schlom, D.G.; Rose, V., ACS Appl. Nano Mater. 2023, 6, 3, 2162-2170, January 18, 2023, <https://doi.org/10.1021/acsnm.2c05257> (2023).

“Nitrogen and phosphorus removal from urine using modified biochars”; Gaunt, John; Johannes Lehmann, Rebecca Nelson, MPP - Manuscript Plus Provisional, 63/480,403, United States (2023).

“Noise Properties of Microresonator-Based Optical-Parametric Oscillators”; Zhao, Y., Jang, J.K., Ji, X., McNulty, K.J., et al., CLEO 2023, Conference on Lasers and Electro-Optics (CLEO), pp. 1-2. Available at: <https://ieeexplore.ieee.org/abstract/document/10260160> (2023).

“Non-equilibrium ordering of liquid crystalline (LC) films driven by external gradients in surfactant concentration”; Maiti, Soumita; Roh, Sangchul; Cohen, Itai; Abbott, Nicholas L., Journal of Colloid and Interface Science, Vol 637, Pages 134-146 (2023).

“Non-Oxide Ceramic Additive Manufacturing Processes for Aerospace Applications”; D’Orazio, Giancarlo, Grace E. Falanga, Zachariah Chazen, Jason Jones and Sadaf Sobhani, AIAA SCITECH 2023 Forum, Session: Materials for Additive Manufacturing, Published Online:19 Jan 2023, <https://doi.org/10.2514/6.2023-0315> (2023).

“Numerical Modeling of Phonon-Mediated Quasiparticle Generation in Superconducting Qubits”; Yelton, Eric, et al., American Physical Society March Meeting, Contributed talk, Las Vegas, NV, March 8, 2023. (2023).

“Occurrence and Transformation of Per-and Polyfluoroalkyl Substances in Semiconductor Fabrication Wastewater”; Jacob, P.V., Cornell University 2023 Ph.D. Thesis (2023).

“On Applications of Qualitative Dynamics to Microfluidic Systems”; Gonzalez, Arnaldo Rodriguez, Cornell University 2023 Ph.D. Thesis (2023).

“On the Effect of Sudden Contraction of CO₂ in Microchannels for Enhancing the Cooling Performance”; Niazi, S.; Parahovnik, A.; Peles, Y.; Heat Transfer Summer Conference, American Society of Mechanical Engineers, September 26, Paper No: HT2023-105745, V001T07A001, <https://doi.org/10.1115/HT2023-105745> (2023).

“On-Chip 2D Material Microring Laser Operating at Room Temperature”; Baez, Marissa Granados, University of Rochester 2023 Ph.D. Thesis (2023).

“Optical implant for in-vivo measurements in plants”; Vesna Bacheva, Margaret Frank, Alice Gevorgyan, Abraham Stroock, I-Feng Wu, 10803, Invention Status; Unfiled, Invention, Disclosure Date 7/6/23 (2023).

“Optical Probe for Measuring Photon Density”; Dunbar, Tom, Provisional Patent application filed, number 63463624, May 3rd 2023 (2023).

“Peptide-macrocyclic conjugates for the separation of rare earth elements”; Yangyang Gao, Justin Wilson, 10702, Invention Status; Filed - Attorney Instructed to File, Invention, Disclosure Date 4/12/23 (2023).

“Phase Transition of MoTe₂ Controlled in van der Waals Heterostructure Nanoelectromechanical Systems”; Ye, Fan; Islam, Arnob; Wang, Yanan; Guo, Jing; Feng, Philip X.-L., Small, Vol. 19, Issue 5, pgs 2205327, DOI 10.1002/smll.202205327 (2023).

“Phenylalanine-Assisted Conductivity Enhancement in PEDOT:PSS Films”; Chamria, Div; Alpha, Christopher; Adhikari, Ramesh Y., ACS Omega, Vol. 8, Issue 8, pgs 7791-7799, DOI 10.1021/acsomega.2c07501 (2023).

“Polymer Nanostructures, Methods of Making Same, and Uses Thereof”; Y. Huang, C. Ober, Inventors: Information: US from PCT, 18/103,274, United States (2023).

“Polypeptoids, Exploring the Power of Sequence Control in a Photoresist for Extreme-Ultraviolet Lithography”; Käfer, Florian; Wang, Chaoqiuyu; Huang, Yuming; Bard, Francesca; Segalman, Rachel; Ober, Christopher K., *Advanced Materials Technologies*, pgs 2301104, DOI 10.1002/admt.202301104 (2023).

“PP2A methylesterase PME-1 suppresses anoikis and is associated with therapy relapse of PTEN-deficient prostate cancers”; Aakula, A., A. Isomursu, C. Rupp, A. Erickson, N. Gupta, O. Kauko, P. Shah, A. Padzik, Y. Pokharel, A. Kaur, S. Li, L. Trotman, P. Taimen, A. Rannikko, J. Lammerding, I. Paatero, T. Mirtti, J. Ivaska, J. Westermarck, *Molecular Oncology*, Vol 17, Issue 6, Pages 1007-1023 June (2023).

“Probabilistic Phase Labeling and Lattice Refinement for Autonomous Material Research”; Chang, M.; Ament, S.; Amsler, M.; Sutherland, D.R.; Zhou, L.; Gregoire, J.M.; Gomes, C.P.; van Dover, R.B.; Thompson, M.O., arXiv 2308.07897 [cond-mat] (2023).

“Probing the Melting Transitions in Phase-Change Superlattices via Thin Film Nanocalorimetry”; Zhao, J.; Khan, A.; Efremov, M.; Ye, Z.; Wu, X.; Kim, K.; Lee, Z.; Wong, H.; Pop, E.; Allen, L.; *Nano Letters*, Vol. 23, Issue 10, pgs 4587-4594, DOI 10.1021/acs.nanolett.3c01049 (2023).

“Programmable Ferroelectric HZO NEMS Mechanical Multiplier for in-Memory Computing”; Jadhav, S.; Gund, V.; Lal, A.; 2023 IEEE 36th International Conference on MEMS, IEEE, pgs 519-521 (2023).

“Progress on Zirconium-Doped Niobium Surfaces”; Sitaraman, N. S.; Gaitan, G.; Oseroff, T.; Baraissov, Z.; Sun, Z.; Muller, D.; Arias, T. A.; Liepe, M. U., Proc. 21th Int. Conf. RF Supercond. (SRF’23), Grand Rapids, MI, USA, Jun. 2023, pp. 398-400. doi:10.18429/JACoW-SRF2023-TUPTB004 (2023).

“Proteomics and cytokine analyses distinguish myalgic encephalomyelitis/chronic fatigue syndrome cases from controls”; Giloteaux, Ludovic; Li, Jiayin; Hornig, Mady; Lipkin, W. Ian; Ruppert, David; Hanson, Maureen R., *Journal of Translational Medicine*, Vol. 21, Issue 1, pgs 322, DOI 10.1186/s12967-023-04179-3 (2023).

“Pulse-Induced CDW Transitions in 1T-TaS₂ Studied with in situ Cryo-TEM and Electric Biasing”; Hart, James L.; Siddique, Saif; Schnitzer, Noah; Kourkoutis, Lena F.; Cha, Judy J., *Microscopy and Microanalysis*, Volume 29, Issue Supplement_1, 1 August 2023, Pages 1714-1715, <https://doi.org/10.1093/micmic/ozad067.886> (2023).

“Pushing the Limits of Photonics in the Visible Spectrum”; Corato-Zanarella, M. et al.; CLEO 2023, paper SF3K.1. CLEO: Science and Innovations, Optica Publishing Group, https://doi.org/10.1364/CLEO_SI.2023.SF3K.1 (2023).

“Quantum devices with left-handed ring resonators”; Plourde, B.L.T., M. Ansari, T. McBroom, X. Xu, A. Schlaves, US Patent Application, 18/225,837, 2023 (2023).

“Quantum stabilizers implemented with superconducting hardware”; Dodge, Kenneth, et al., American Physical Society March Meeting, Contributed talk, Las Vegas, NV, March 8, 2023. (2023).

“Rapid headspace solid-phase microextraction sheets with direct analysis in real time mass spectrometry (SPMESH-DART-MS) of derivatized volatile phenols in grape juices and wines”; Bates, Terry L.; Sacks, Gavin L., *Analytica Chimica Acta*, Elsevier, Vol. 1275, pgs 341577 (2023).

“Rapid, Repeatable, and Robust Analysis of Trace Level Volatile Organic Compounds Using Planar Headspace Extraction Geometries Coupled to Chromatography-Free Ambient Ionization-Mass Spectrometry: Solid Phase Microextraction Sheets and Beyond”; Bates, Terry Lee, Cornell University 2023 Ph.D. Thesis (2023).

“Reactive Extrusion of Nonmigratory Active and Intelligent Packaging”; Redfearn, Halle N.; Warren, Matthew K.; Goddard, Julie M., *ACS Applied Materials & Interfaces*, Vol. 15, Issue 24, pgs 29511-29524, DOI 10.1021/acsami.3c06589 (2023).

“Real-space imaging of periodic nanotextures in thin films via phasing of diffraction data”; Shao, Z.; Schnitzer, N.; Ruf, J.; Gorobtsov, O.; Dai, C.; Goodge, B.; Yang, T.; Nair, H.; Stoica, V.; Freeland, J.; Ruff, J.; Chen, L.; Schlom, D.; Shen, K.; Kourkoutis, L.; Singer, A., *Proceedings of the National Academy of Sciences*, Vol. 120, Issue 28, pgs e2303312120, DOI 10.1073/pnas.2303312120 (2023).

“Recreating the Biological Steps of Viral Infection on a Bioelectronic Platform to Profile Viral Variants of Concern”; Chao, Z., E. Selivanovitch, K. Kallitsis, Z. Lu, A. Pachaury, R. Owens, S. Daniel, bioRxiv, November 12, 2023, doi: <https://doi.org/10.1101/2023.11.11.566634> (2023).

“Redox-Enabled Microscale Opto-Electronically Transduced Electrodes (ReMOTES)”; Ghajari, Shahaboddin; Lee, Sunwoo; Norris, Samantha L.; McEuen, Paul L.; Molnar, Alyosha C., 2023 IEEE International Symposium on Circuits and Systems (ISCAS), IEEE, pgs 1-5 (2023).

“Reduction of correlated errors in superconducting qubits using normal metal back-side metallization”; Iaia, Vito, et al., American Physical Society March Meeting, Contributed talk, Las Vegas, NV, March 8, 2023. (2023).

“Reusing End-of-life Plastics within Alternate Cementitious Binders”; Sriramya Nair, 10690, *Invention Status; Closed - In Process*, Invention, Disclosure Date 3/24/23 (2023).

“Reversible Computing: Adiabatic Capacitive Logic”; Cordova, Rene Celis, University of Notre Dame 2023 Ph.D. Thesis (2023).

“RF High-Electron-Mobility Transistors Including Group III-N Stress Neutral Barrier Layers with High Breakdown Voltages”; Samuel Bader, Reet Chaudhuri, Austin Hickman, Debdeep Jena, H. Grace Xing, 8773-02-US, United States, Patent Issued, Issued, 6/4/20, 16/893,074, 7/25/23, 11,710,785 (2023).

“RF operation of AlN/Al_{0.25}Ga_{0.75}N/AlN HEMTs with f T/f max of 67/166 GHz”; Kim, E.; Singhal, J.; Hickman, A.; Li, L.; Chaudhuri, R.; Cho, Y.; Hwang, J.; Jena, D.; Xing, H.G., Applied Physics Express, IOP Publishing, Vol. 16, Issue 11, pgs 111003 (2023).

“Rigidified Macrocyclus, Complexes With Radionuclides, And Use In Targeted Radiotherapy Of Cancer”; Karthika Kadassery, Justin Wilson, 9893-03-US, United States, US from PCT, Filed, 11/20/23, 18/562,744 (2023).

“Room temperature optically detected magnetic resonance of single spins in GaN”; Luo, Jialun; Geng, Yifei; Rana, Farhan; Fuchs, Gregory D., arXiv 2306.12337 [cond-mat, physics:quant-ph] (2023).

“Room-Temperature Strong Coupling between CdSe Nanoplatelets and a Metal-DBR Fabry-Pérot Cavity”; Morshed, O.; Amin, M.; Collison, R.; Cogan, N.; Koessler, E.; Tumié, T.; Girtén, W.; Awan, F.; Mathis, L.; Huo, P., ChemRxiv Physical Chemistry, Oct 11, Version 1 (2023).

“Sagnac interferometry for high-sensitivity optical measurements of spin-orbit torque”; Karimeddiny, Saba; Cham, Thow Min Jerald; Smedley, Orion; Ralph, Daniel C.; Luo, Yunqiu Kelly, Science Advances, Vol. 9, Issue 36, pgs eadi9039, DOI 10.1126/sciadv.adi9039 (2023).

“Sagnac interferometry for high-sensitivity spin-orbit torque measurements with the ferromagnetic insulator bismuth-substituted yttrium iron garnet (Bi: YIG)”; Luo, Yunqiu Kelly; Jain, Rakshit; Khurana, Bharat; Ross, Caroline; Ralph, Daniel, Bulletin of the APS March Meeting 2023, Las Vegas, Nevada (March 5-10), Abstract: Q57.00005 (2023).

“Scalable continuous-flow electroporation platform enabling T cell transfection for cellular therapy manufacturing”; VanderBurgh, J.A.; Corso, T.N.; Levy, S.L.; Craighead, H.G.; Scientific Reports, Nature Publishing Group UK London, Vol. 13, Issue 1, pgs 6857 (2023).

“Scaled-Up Synthesis of Freestanding Molybdenum Disulfide Membranes for Nanopore Sensing”; Alibakhshi, Mohammad Amin; Kang, Xinqi; Clymer, David; Zhang, Zhuoyu; Vargas, Anthony; Meunier, Vincent; Wanunu, Meni, Advanced Materials, Vol. 35, Issue 12, pgs 2207089, DOI 10.1002/adma.202207089 (2023).

“Scanning SQUID microscopy (SSM) on van der Waals heterostructure with in situ uniaxial strain”; Bai, Ruiheng; Schaefer, Brian; Jarjour, Alexander; Nowack, Katja, Bulletin of the APS March Meeting 2023, Las Vegas, Nevada (March 5-10), Abstract: S30.00004 (2023).

“Self-Heating Based Locking of a Laser to a High-QSi₃N₄ Microcavity”; Dacha, S.K., et al., CLEO 2023, p. SW4L.4. CLEO: Science and Innovations, Optica Publishing Group, https://doi.org/10.1364/CLEO_SI.2023.SW4L.4 (2023).

“Self-powered triboelectric MEMS accelerometer”; Alzgoool, M.; Tian, Y.; Davaji, B.; Towfighian, S.; Nano Energy, Elsevier, Vol. 109, pgs 108282 (2023).

“Self-Injection Locked Frequency Conversion Laser”; Ling, J.; Staffa, J.; Wang, H.; Shen, B.; Chang, L.; Javid, U.A.; Wu, L.; Yuan, Z.; Lopez-Rios, R.; Li, M.; He, Y.; Li, B.; Bowers, J.E.; Vahala, K.J.; Lin, Q., Laser & Photonics Reviews, Vol. 17, Issue 5, pgs 2200663, DOI 10.1002/lpor.202200663 (2023).

“Sequence-defined polypeptoid CARs for electron-beam and EUV lithography”; Kaefer, Florian; Ober, Christopher K.; Meng, Zoey; Segalman, Rachel; de Alaniz, Javier Read, Advances in Patterning Materials and Processes XL, SPIE, Vol. 12498, pgs 222-226 (2023).

“Silicon Implantation and Annealing in β -Ga₂O₃: Role of Ambient, Temperature, and Time”; Gann, K.; Pieczulewski, N.; Gorsak, C.; Heinselman, K.; Asel, T.; Noesges, B.; Smith, K.; Dryden, D.; Xing, H.; Nair, H.; Muller, D.; Thompson, M., arXiv 2311.00821 [cond-mat, physics:physics] (2023).

“Silicon-doped β -Ga₂O₃ films grown at 1 μ m/h by suboxide molecular-beam epitaxy”; Azizie, K.; Hensling, F.; Gorsak, C.; Kim, Y.; Pieczulewski, N.A.; Dryden, D.M.; Senevirathna, M.K.; Coye, S.; Shang, S.; Steele, J., APL materials, AIP Publishing, Vol. 11, Issue 4 (2023).

“Single cell dynamics of the Lac operon induction”; Cortes, Louis; Lambert, Guillaume, Bulletin of the APS March Meeting 2023, Las Vegas, Nevada (March 5-10), Abstract: N10.00006 (2023).

“Single Particle Analysis of H3N2 Influenza Entry Differentiates the Impact of the Sialic Acids (Neu5Ac and Neu5Gc) on Virus Binding and Membrane Fusion”; Chien, Y.-A. A.; Alford, B.K.; Wasik, B.R.; Weichert, W.S.; Parrish, C.R.; Daniel, S.; Journal of Virology, Vol. 97, pgs e01463-22, DOI 10.1128/jvi.01463-22 (2023).

“Smooth, homogeneous, high-purity Nb₃Sn superconducting RF resonant cavity by seed-free electrochemical synthesis”; Sun, Z.; Baraissov, Z.; Porter, R.; Shpani, L.; Shao, Y.; Oseroff, T.; Thompson, M.; Muller, D.; Liepe, M., Superconductor Science and Technology, IOP Publishing, Vol. 36, Issue 11, pgs 115003 (2023).

“Solderable Multisided Metal Patterns Enables 3D Integrable Direct Laser Written Polymer MEMS”; Ivy, Landon; Lal, Amit, 2023 Conference on Lasers and Electro-Optics (CLEO), San Jose, CA, USA, 2023, pp. 1-2., DOI: 10.1109/ICMTS55420.2023.10094101 (2023).

- “Solute Transport in Engineered Living Materials Using Bone-Inspired Microscale Channel Networks”; Van Wijngaarden, Ellen W.; Bratcher, Samantha; Lewis, Karl J.; Hernandez, Christopher J., *Advanced Engineering Materials*, pgs 2301032, DOI 10.1002/adem.202301032 (2023).
- “Spin manipulation in van der Waals ferromagnets and antiferromagnets”; Cham, T.M.J., *Symposium on Magnetic Manipulation and Excitations in 2D Magnets*, APS March Meeting 2023, Invited Symposium Talk, Las Vegas (on behalf of Professor Dan Ralph) (2023).
- “Spontaneous supercrystal formation during a strain-engineered metal-insulator transition”; Gorobtsov, O.; Miao, L.; Shao, Z.; Tan, Y.; Schnitzer, N.; Goodge, B.; Ruf, J.; Weinstock, D.; Cherukara, M.; Holt, M.; Nair, H.; Chen, L.; Kourkoutis, L.; Schlom, D.; Shen, K.; Singer, A., *arXiv* 2311.11842 [cond-mat] (2023).
- “Strong variation of spin-orbit torques with relative spin relaxation rates in ferrimagnets”; Zhu, Lijun; Ralph, Daniel C., *Nature Communications*, Nature Publishing Group UK London, Vol. 14, Issue 1, pgs 1778 (2023).
- “Structural, optical, and thermal properties of BN thin films grown on diamond via pulsed laser deposition”; Biswas, A.; Alvarez, G.; Li, T.; Christiansen-Salameh, J.; Jeong, E.; Puthirath, A.; Iyengar, S.; Li, C.; Gray, T.; Zhang, X.; Pieshkov, T.; Kannan, H.; Elkins, J.; Vajtai, R.; Birdwell, A.; Neupane, M.; Garratt, E.; Pate, B.; Ivanov, T.; Zhao, Y.; Tian, Z.; Ajayan, P., *Phys Review Mats*, Vol. 7, Issue 9, pgs 94602, DOI 10.1103/PhysRevMaterials.7.094602 (2023).
- “Supercooling of the A phase of 3He”; Tian, Y.; Lotnyk, D.; Eyal, A.; Zhang, K.; Zhelev, N.; Abhilash, T.; Chavez, A.; Smith, E.; Hindmarsh, M.; Saunders, J., *Nature Communications*, Nature Publishing Group UK London, Vol. 14, Issue 1, pgs 148 (2023).
- “Superfluid response of an atomically thin gate-tuned van der Waals superconductor”; Jarjour, Alexander; Ferguson, G. M.; Schaefer, Brian T.; Lee, Menyoun; Loh, Yen Lee; Trivedi, Nandini; Nowack, Katja C., *Nature Communications*, Nature Publishing Group UK London, Vol. 14, Issue 1, pgs 2055 (2023).
- “Surface Characterization Studies of Gold-Plated Niobium”; Seddon-Stettler, S.G.; M. Liepe, T.E. Oseroff, N. Sitaraman, and Z. Sun, *Proc. 21th Int. Conf. RF Supercond. (SRF’23)*, Grand Rapids, MI, USA, Jun. 2023, pp. 290-292. doi:10.18429/JACoW-SRF2023-MOPMB076 (2023).
- “Surface oxides, carbides, and impurities on RF superconducting Nb and Nb₃Sn: A comprehensive analysis”; Sun, Z.; Baraissov, Z.; Dukes, C.; Dare, D.; Oseroff, T.; Thompson, M.; Muller, D.; Liepe, M., *Superconductor Science and Technology*, Vol. 36, Issue 11, pgs 115030, DOI 10.1088/1361-6668/acff23 (2023).
- “Switchable moiré potentials in ferroelectric WTe₂/WSe₂ superlattices”; Kang, K.; Zhao, W.; Zeng, Y.; Watanabe, K.; Taniguchi, T.; Shan, J.; Mak, K., *Nature Nanotechnology*, Nature Publishing Group UK London, pgs 1-6 (2023).
- “Synthesis of N-Substituted Maleimides and Poly (styrene-co-N-maleimide) Copolymers and Their Potential Application as Photoresists”; Eken, Gozde Aktas; Käfer, Florian; Yuan, Chenyun; Andrade, Ivan; Ober, Christopher K., *Macromolecular Chemistry and Physics*, Vol. 224, Issue 1, pgs 2200256, DOI 10.1002/macp.202200256 (2023).
- “Synthesis of Shape-Controlled Polymer Nano-Microstructures using Initiated Chemical Vapor Deposition (ICVD) Polymerization in Structured Liquids”; Nicholas Abbott, Apporva Jain, Soumyamouli Pal, Rong Yang, 10334-02-PC, (PCT App), PCT - Patent Cooperation Treaty, Filed, 5/8/23, PCT/US23/66722 (2023).
- “Synthesis, Hole Doping, and Electrical Properties of a Semiconducting Azatriangulene-Based Covalent Organic Framework”; Burke, D.; Dasari, R.; Sangwan, V.; Oanta, A.; Hirani, Z.; Pelkowski, C.; Tang, Y.; Li, R.; Ralph, D.; Hersam, M.; Barlow, S.; Marder, S.; Dichtel, W., *Journal of the American Chemical Society*, Vol. 145, Issue 22, pgs 11969-11977, DOI 10.1021/jacs.2c12371 (2023).
- “Targeted Discovery of Low-Coordinated Crystal Structures via Tunable Particle Interactions”; Pan, Hillary; Dshemuchadse, Julia, *ACS Nano*, Vol. 17, Issue 8, pgs 7157-7169, DOI 10.1021/acsnano.2c09131 (2023).
- “The lamin A/C Ig-fold undergoes cell density-dependent changes that alter epitope binding”; Wallace, M.; Fedorchak, G.; Agrawal, R.; Gilbert, R.; Patel, J.; Park, S.; Paszek, M.; Lammerding, J., *Nucleus*, Vol. 14, Issue 1, pgs 2180206, DOI 10.1080/19491034.2023.2180206 (2023).
- “The roles of sub-micron and microscale roughness on shear-driven thrombosis on titanium alloy surfaces”; Jayaraman, Anjana; Kang, Junhyuk; Antaki, James F.; Kirby, Brian J., *Artificial Organs*, Vol. 47, Issue 3, pgs 490-501, DOI 10.1111/aor.14467 (2023).
- “Thermal conductivity enhancement of aluminum scandium nitride grown by molecular beam epitaxy”; Alvarez, G.; Casamento, J.; Van Deurzen, L.; Khan, M.; Khan, K.; Jeong, E.; Ahmadi, E.; Xing, H.; Jena, D.; Tian, Z., *Materials Research Letters*, Vol. 11, Issue 12, pgs 1048-1054, DOI 10.1080/21663831.2023.2279667 (2023).
- “Thermodynamic evidence of fractional Chern insulator in moiré MoTe₂”; Zeng, Y.; Xia, Z.; Kang, K.; Zhu, J.; Knüppel, P.; Vaswani, C.; Watanabe, K.; Taniguchi, T.; Mak, K.; Shan, J., *Nature*, Nature Publishing Group UK London, Vol. 622, Issue 7981, pgs 69-73 (2023).
- “Thin Film Iridium Electrodes for Hexagonal Ferroelectrics”; Megan Holtz, Darrell Schlom, Rachel Steinhardt, 9189-02-US, United States, Patent Issued, Issued, 10/21/20, 17/076,131, 6/13/23, 11,678,587 (2023).

“Tissue Scaffold Materials for Tissue Regeneration and Methods of Making”; John Morgan, Jason Spector, Abraham Stroock, 6458-13-JP, Japan, Patent Issued, Issued, 7/29/19, 2019-133223, 8/30/23, 73430374 (2023).

“Tissue Scaffold Materials for Tissue Regeneration and Methods of Making”; John Morgan, Jason Spector, Abraham Stroock, 6458-14-IL, Israel, Patent Issued, Issued, 2/8/20, 273135, 10/2/23, 273135 (2023).

“Transport Properties of Polarization-Induced 2D Electron Gases in Epitaxial AlScN/GaN Heterojunctions”; Nguyen, Thai-Son; Casamento, Joseph; Savant, Chandrashekhar; Cho, Yongjin; Xing, Huili G.; Jena, D., Bulletin of the APS March Meeting 2023, Las Vegas, Nevada (March 5-10), Abstract: Y40.00008 (2023).

“Tunable Non-Reciprocal Phase Shifter and Spin-Coated Ferrites for Adaptive Microwave Circuits”; Srinivasan, Karthik; El-Ghazaly, Amal, 2023 International Microwave and Antenna Symposium (IMAS), IEEE, pgs 62-65 (2023).

“Tuning ferromagnetism in 2D magnet/topological insulator heterostructures across room temperature by epitaxial growth”; Zhou, W.; Bishop, A.; Zhang, X.; Robinson, K.; Lyalin, I.; Cham, T.; Li, Z.; Cheng, S.; Bailey-Crandell, R.; Luo, Y., Bulletin of the APS March Meeting 2023, Las Vegas, Nevada (March 5-10), Abstract: D42.00006 (2023).

“Tuning the Curie temperature of a two-dimensional magnet/topological insulator heterostructure to above room temperature by epitaxial growth”; Zhou, W.; Bishop, A.; Zhang, X.; Robinson, K.; Lyalin, I.; Li, Z.; Bailey-Crandell, R.; Cham, T.; Cheng, S.; Luo, Y.; Ralph, D.; Muller, D.; Kawakami, R., Phys Review Mats, Vol. 7, Issue 10, pgs 104004, DOI 10.1103/PhysRevMaterials.7.104004 (2023).

“Two-Dimensional Violet Phosphorus P11: A Large Band Gap Phosphorus Allotrope”; Cicirello, Gary; Wang, Mengjing; Sam, Quynh P.; Hart, James L.; Williams, Natalie L.; Yin, Huabing; Cha, Judy J.; Wang, Jian, Journal of the American Chemical Society, Vol. 145, Issue 14, pgs 8218-8230, DOI 10.1021/jacs.3c01766 (2023).

“Ultra-Low-Loss Silicon Nitride Photonics Based on Deposited Films Compatible with Foundries”; Ji, X.; Okawachi, Y.; Gil-Molina, A.; Corato-Zanarella, M.; Roberts, S.; Gaeta, A.; Lipson, M., Laser & Photonics Reviews, Vol. 17, Issue 3, pgs 2200544, DOI 10.1002/lpor.202200544 (2023).

“Ultrabroadband, high color purity multispectral color filter arrays”; Xiang, J.; Song, M.; Zhang, Y.; Kruschwitz, J.; Cardenas, J.; arXiv 2310.15437 [physics] (2023).

“Understanding Gold Mesopyramid Formation on Silicon and Strategies for Creating Patterns of Them”; Dice, Nathan P., Aaron J. Austin, Phadindra Wagle, Emrah Turgut, D.N. McIlroy, Materials Science and Engineering: B, Volume 297, November 2023, 116759 (2023).

“Understanding Gold Mesopyramid Formation on Silicon and Strategies for Creating Patterns of Them”; McIlroy, David N.; Dice, Nathan P.; Austin, Aaron J.; Wagle, Phadindra; Turgut, Emrah, SSRN, Posted: 4 Apr 2023, <https://ssrn.com/abstract=4409881> or <http://dx.doi.org/10.2139/ssrn.4409881> (2023).

“Understanding How Metal-Ligand Coordination Enables Solvent Free Ionic Conductivity in PDMS”; Zhang, X.; Dai, J.; Tepermeister, M.; Deng, Y.; Yeo, J.; Silberstein, M., Macromolecules, Vol. 56, Issue 8, pgs 3119-3131, DOI 10.1021/acs.macromol.2c02519 (2023).

“Uric acid detecting and degrading bacteria”; Gozde Gencer, Christopher Mancuso, John March, 8813-02-PC, (PCT App), PCT - Patent Cooperation Treaty, Filed, 10/3/23, PCT/US23/75818 (2023).

“Virtual High-Throughput Screening of Vapor-Deposited Amphiphilic Polymers for Inhibiting Biofilm Formation”; Feng, Z.; Cheng, Y.; Khlyustova, A.; Wani, A.; Franklin, T.; Varner, J.; Hook, A.; Yang, R., Advanced Materials Technologies, Vol. 8, Issue 13, pgs 2201533, DOI 10.1002/admt.202201533 (2023).

“Widely tunable and narrow-linewidth chip-scale lasers from near-ultraviolet to near-infrared wavelengths”; Corato-Zanarella, Mateus; Gil-Molina, Andres; Ji, Xingchen; Shin, Min Chul; Mohanty, Aseema; Lipson, Michal, Nature Photonics, Nature Publishing Group UK London, Vol. 17, Issue 2, pgs 157-164 (2023).

“ZrNb (Cx) RF superconducting thin film with high critical temperature in the theoretical limit”; Sun, Ze.; Oseroff, T.; Baraissov, Z.; Dare, D.; Howard, K.; Thompson, M.; Muller, D.; Liepe, M., arXiv 2302.14410 [Submitted on 28 Feb 2023 (v1), last revised 12 Jun 2023 (this version, v2)] (2023).

2023-2024

**Cornell NanoScale
Facility (CNF)**

**RESEARCH
ACCOMPLISHMENTS**

Development of a Biomembrane Platform for the Study of Virus Infection

CNF Project Number: 1686-08

Principal Investigator(s): Susan Daniel

User(s): Zhongmou Chao, Alexis Ostwalt, Jordan Fitzgerald, Eleanor Best

Affiliation(s): Smith School of Chemical and Biomolecular Engineering, Cornell University

Primary Source(s) of Research Funding: Defense Threat Reduction Agency

Contact: sd386@cornell.edu, zc83@cornell.edu

Research Group Website: <https://daniel.cbe.cornell.edu/>

Primary CNF Tools Used: Heidelberg DWL2000 Mask Writer, ABM Contact Aligner,

Odd Hour E-beam Evaporator, Oxford PECVD, PT-740 etcher, Disco Dicing Saw, Bruker AFM

Abstract:

As a “label-free” alternative to optical sensing, electrical sensing represents a more feasible, reproducible, and scalable detection method [1,2]. Among various electrical sensing techniques, the non-invasive electrochemical impedance spectroscopy (EIS) technique is especially suitable for accurately quantifying the bio-recognition events occurring at a variety of biointerfaces, such as bacterial, viral, cellular and synthetic lipid membranes [3,4]. Our group aims to design a microelectrode system that will support the self-assembly of lipid vesicles (SLBs) on the electrode surfaces, and their electrical properties (resistance, capacitance) can be extracted by applying an alternating voltage and recording the current response [4-7]. We have recently demonstrated such platform can be used to recreate viral infection of host cell and can differentiate different virus mutations [8]. Future work plan to incorporate microfluidic system with the microelectrode system.

Summary of Research:

To fabricate the microelectrode devices, photomasks were created using the Heidelberg DWL2000 Mask writer and used with the ABM Contact Aligner to pattern photoresist that was spun onto a fused silica wafer. A first layer of gold contact pad was patterned following the developing of S1813 photoresist and the deposition of Au thin film. A thin layer of SiO₂ insulating layer is then deposited directly on top of the Au contact pad using Oxford PECVD. Electrode area was then patterned on SiO₂ following the spin-coating and developing of the second layer of photoresist. PT-740 etched was then used to etch the exposed SiO₂ until Au contact pad has been exposed. A conductive polymer, PEDOT:PSS was then spun over the fused silica wafer followed by the deposition of a Germanium hard mask (odd hour e-beam evaporator). A third layer of photolithography

was performed on a layer of negative photoresist (nLOF 2020) spun on top of Ge, where all resists above Ge at areas except active electrode surface were developed. Unprotected Ge and PEDOT:PSS underneath were then etched using PT-740. Ge on top of active electrode area was then etched in water bath overnight.

Once the microelectrode device was fabricated, a PDMS well was stamped directly on top to create a reservoir for SLB self-assembly and allow following EIS measurement.

References:

- [1] Berggren, Magnus, and Agneta Richter. Dahlfors. “Organic bioelectronics.” *Advanced Materials* 19.20 (2007): 3201-3213.
- [2] Chalklen, Thomas, Qingshen Jing, and Sohini Kar-Narayan. “Biosensors based on mechanical and electrical detection techniques.” *Sensors* 20.19 (2020): 5605.
- [3] Magar, Hend S., Rabeay YA Hassan, and Ashok Mulchandani. “Electrochemical Impedance Spectroscopy (EIS): Principles, Construction, and Biosensing Applications.” *Sensors* 21.19 (2021): 6578.
- [4] Lisdat, F., and D. Schäfer. “The use of electrochemical impedance spectroscopy for biosensing.” *Analytical and Bioanalytical Chemistry* 391.5 (2008): 1555-1567.
- [5] Tang, Tiffany, et al. “Functional infectious nanoparticle detector: Finding viruses by detecting their host entry functions using organic bioelectronic devices.” *ACS Nano* 15.11 (2021): 18142-18152.
- [6] Bint E Naser, Samavi Farnush, et al. “Detection of Ganglioside-Specific Toxin Binding with Biomembrane-Based Bioelectronic Sensors.” *ACS Applied Bio Materials* 4.11 (2021): 7942-7950.
- [7] Pappa, Anna-Maria, et al. “Optical and electronic ion channel monitoring from native human membranes.” *ACS Nano* 14.10 (2020): 12538-12545.
- [8] Chao, Zhongmou, et al. “Recreating the biological steps of viral infection on a cell-free bioelectronic platform to profile viral variants of concern.” *Nature Communications* 15.1 (2024): 5606.

Metamaterial Elliptical Cylinder for High Sensitive Single-Molecule Torque Detection

CNF Project Number: 1738-08

Principal Investigator(s): Michelle D. Wang

User(s): Yifeng Hong

*Affiliation(s): Department of Electrical and Computer Engineering, Cornell University;
Department of Physics, Cornell University; Howard Hughes Medical Institute*

Primary Source(s) of Research Funding: Howard Hughes Medical Institute

Contact: mdw17@cornell.edu, yh874@cornell.edu

Research Group Website: <http://wanglab.lasp.cornell.edu/>

Primary CNF Tools Used: ASML Deep Ultraviolet Stepper, Oxford 81 Etcher, Oxford 82 Etcher, Oxford PECVD, SC4500 Odd-Hour Evaporator, SC4500 Even-Hour Evaporator, Zeiss Supra SEM, Zeiss Ultra SEM

Abstract:

To facilitate the single-molecule torque measurement with the angular optical trap (AOT), we designed and fabricated novel metamaterial elliptical cylinders for higher torque resolution. By designing the cylinders to a smaller size, the torque resolution was improved over standard existing technique (quartz cylinders). The linear and angular trapping stiffness of the metamaterial elliptical cylinder can be controlled by tuning the mixing ratio of SiO_2 and Si_3N_4 to effectively modify the refractive index of the cylinder. These metamaterial elliptical cylinders can improve the utility of the AOT in investigating DNA-protein interactions.

Summary of Research:

Torsional stress results in one of the main topological challenges in cells and plays an important role in fundamental biological processes, for example transcription and replication. In replication, torsion can accumulate both upstream and downstream of the replication fork. We are specifically interested in how DNA responds to torsion and what kinds of DNA structures form in response to topological changes. To quantitatively study these questions, our lab developed the angular optical trap (AOT) to measure torque at the single-molecule level [1-3]. As a standard configuration of the AOT, linearly polarized light is used to trap and rotate a birefringent particle anchored with a torsionally constrained DNA molecule for manipulation and measurement [2,3].

Historically, functionalized nanofabricated quartz cylinders ($n_c = 1.54$ and $n_o = 1.53$ at 1064 nm) with typical dimensions of diameter $D \sim 500$ nm and height H

~ 1000 nm were utilized to simultaneously apply force and rotation to an attached DNA molecule for extension and torque measurements [2].

To facilitate the torque detection and allow better resolution, a smaller sample is required. However, a smaller quartz cylinder has a lower linear/angular trapping stiffness, resulting in the necessity of using high laser power, which may cause photodamage to a biological substrate [4].

To bypass this issue, we designed and fabricated multilayered elliptical cylinders with an effectively higher refractive index and a ~ 3 -fold volume reduction in comparison to the previous quartz cylinders. These changes increased the torque resolution while maintaining strong linear/angular trapping stiffness. These cylinders were composed of silicon dioxide SiO_2 ($n_1 = 1.45$ at 1064 nm) and silicon nitride Si_3N_4 ($n_2 = 2.01$ at 1064 nm) (Figure 1), effectively resulting in a metamaterial [5].

As one can tell from the tensor (Figure 1), this metamaterial did not have birefringent effect at the xy-plane, thus we introduced shape anisotropy (i.e. utilizing elliptical shape) to generate torque for AOT manipulation (Figure 2).

Conclusions and Future Steps:

These metamaterial elliptical cylinders have a decreased γ_θ over our existing quartz cylinders, which facilitates an increased torque resolution for single-molecule AOT experiments. We believe these cylinders can have a significant impact on DNA torsional studies.

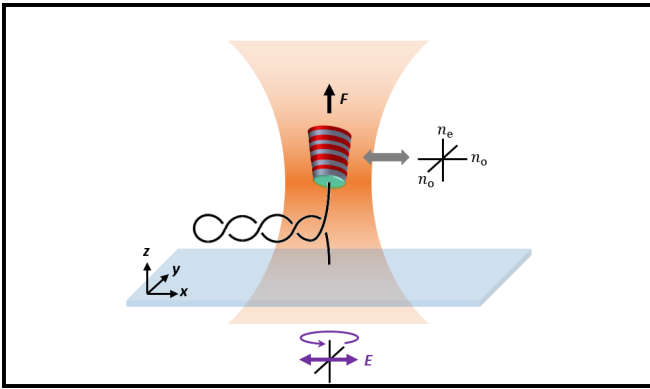


Figure 1: Experimental configuration of winding a DNA molecule with a metamaterial elliptical nanocylinder on the AOT. The long axis tends to align to the beam polarization when the beam is rotated.

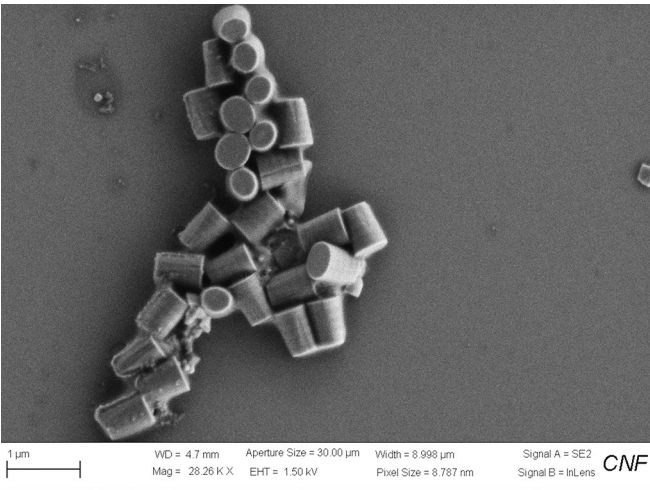


Figure 2: A scanning electron microscope image of metamaterial elliptical cylinders.

References:

- [1] La Porta, A. and M.D. Wang, Optical Torque Wrench: Angular Trapping, Rotation, and Torque Detection of Quartz Microparticles. *Physical Review Letters*, 2004. 92(19): p. 190801.
- [2] Deufel, C., et al., Nanofabricated quartz cylinders for angular trapping: DNA supercoiling torque detection. *Nature Methods*, 2007. 4(3): p. 223-225.
- [3] Gao, X., et al., Torsional Stiffness of Extended and Plectonemic DNA. *Physical Review Letters*, 2021. 127(2): p. 028101.
- [4] Neuman, K.C., et al., Characterization of Photodamage to Escherichia coli in Optical Traps. *Biophysical Journal*, 1999. 77(5): p. 2856-2863.
- [5] Cai, W. and V.M. Shalaev, *Optical metamaterials: fundamentals and applications*. 2010, New York: Springer. xii, 200 p.

Building Microfluidics Devices to Study Zinc Metal Homeostasis in *E. Coli* Communities

CNF Project Number: 1844-09

Principal Investigator(s): Peng Chen

User(s): Felix Alfonso

Affiliation(s): Department of Chemistry and Chemical Biology, Cornell University

Primary Source(s) of Research Funding: National Institute of Health, the National Institute of General Medical Sciences

Contact: pc252@cornell.edu, fsa33@cornell.edu

Research Group Website: <http://chen.chem.cornell.edu/>

Primary CNF Tools Used: Heidelberg Mask Writer DWL2000, SUSS MA6-BA6 Contact Aligner, Oxford Cobra ICP Etcher, Plasma-Therm Deep Silicon Etcher, P7 Profilometer

Abstract:

Microbial life has a set of molecular tools to import essential nutrients from the surrounding environment and when necessary, efflux the excess to prevent harmful toxicity. The aim of this study is to elucidate the role individual bacterial cells play in achieving metal homeostasis at the community level. With this in mind, we engineered a custom microfluidic device that facilitates the controlled growth of *Escherichia coli* (*E. coli*) colonies within well-defined microchambers. These chambers' dimensions are carefully matched to the diameter of *E. coli* cells, thereby allowing for strategic cellular confinement — a critical aspect of our investigative method. The microfluidic devices we employed exhibit dynamic environmental control features, enabling us to switch solutions rapidly for stable, pulse, or step-function nutrient exposure as well as the creation of nutrient gradients. We employed advanced molecular biology techniques to engineer *E. coli* strains equipped with fluorescent protein reporters. This unique genetic modification allowed us to visualize and quantify gene expressions linked to the intricate influx and efflux ion channels, with particular emphasis on those specific to zinc. The insights derived from this study could have profound implications for our understanding of microbial ecosystems and their interactions with the environment.

Summary of Research:

Zinc, a fundamental micronutrient, is indispensable for all living organisms [1]. It serves vital functions in protein folding, catalysis, and gene regulation [2,3]. An imbalance in zinc levels, either a deficiency or an excess, can trigger substantial alterations in the gut microbiome, thereby resulting in adverse health conditions [4,5]. Microbes have developed molecular mechanisms to

efficiently import nutrients from the environment and efflux under excess. To regulate these efflux pumps, bacteria modulate the transcription of protein pumps using metal-responsive transcription regulators. These regulators monitor the cellular concentration of metal ions, guiding cells towards achieving an optimal state of metal homeostasis.

Our project is designed to explore and quantify the management of Zn^{2+} within a microbiome, shedding light on the role individual cells assume in establishing community-wide metal homeostasis. We have chosen *Escherichia coli* (*E. coli*) as our model organism to investigate the complexities of community-derived zinc metal regulation. *E. coli*'s natural motility and poor adherence to substrates present challenges for long-duration imaging studies. However, microfluidics technology offers an effective solution, providing a controlled environment conducive to studying bacterial communities [6]. A microfluidic platform permits tight control of the nutrients influx and has been successfully used for long-timescale imaging studies [7]. The microfluidic device employed in our study is engineered

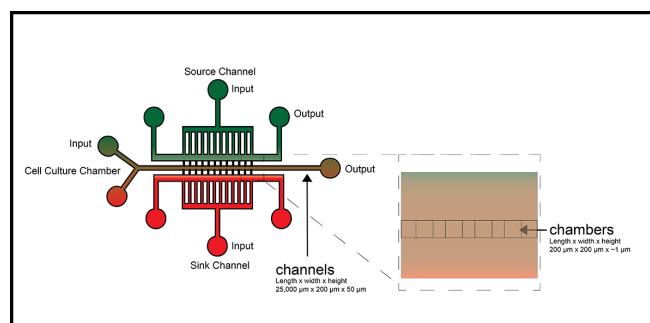


Figure 1: Schematic of gradient generating microfluidic device showing the source and sink channels and the chamber.

with three key components: a gradient generator, channels, and microchambers. The microchambers' depth is tailored to match the diameter of an *E. coli* cell ($\sim 1 \mu\text{m}$), thereby facilitating the efficient confinement of colonies. The gradient generator was designed with the goals of creating a stable concentration gradient and minimization of convection inside the chambers. The design presented by E. Bernson, and A. Shamloo provided an optimal method to create a stable gradient inside the chamber (Figure 1, 8-9). This is accomplished by having a source chamber and a sink chamber. The molecule of interest diffuses through the micro capillaries that connect the source and sink to the main culture chamber.

The construction of these microfluidic devices relies on established silicon nanofabrication technology. The fabrication scheme is summarized in Figure 2. The fabrication process begins with silicon wafers being cleaned with piranha solution. They are then coated with photoresists, which are removed 2 mm from the wafer's edge using an edge bead removal system. The substrate is patterned using a pre-designed photomask created with the Heidelberg Mask Writer DWL2000. The Karl SUSS MA6-BA6 contact aligner provides UV light exposure for the wafer, which is developed and cleaned with a brief oxygen plasma treatment. Chambers are created by etching approximately $\sim 1 \mu\text{m}$ of silicon using the Oxford Cobra ICP Etcher, and then the photoresist is removed with a stripper bath. The chamber's height is measured using a profilometer. Channel construction involves the use of SU-8 lithography, where SU-8 is spin-coated onto the substrate and patterned with the Karl SUSS MA6-BA6 contact aligner. After a curing

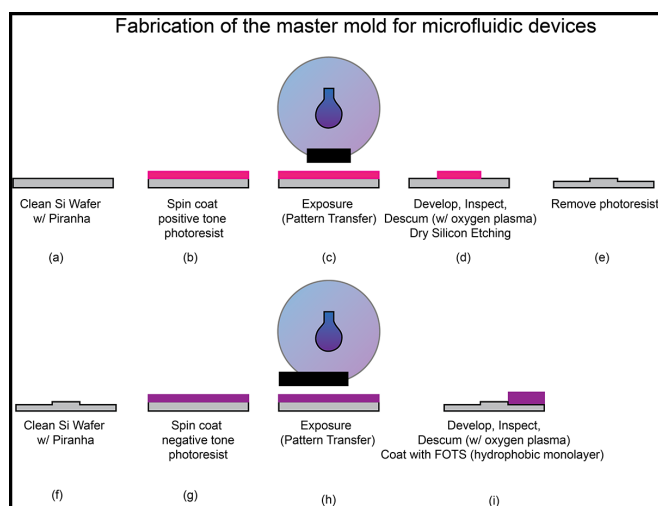


Figure 2: Fabrication of microfluidic devices combining dry etching to construct the chambers and SU-8 lithography to construct the channels.

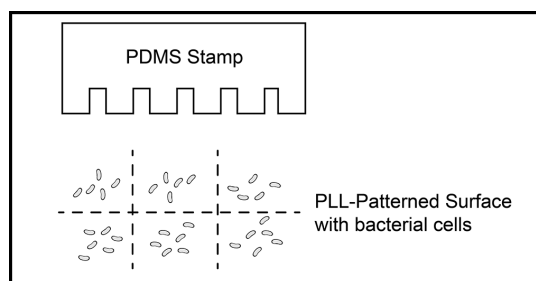


Figure 3: Patterning of the coverslip surface using PDMS stamps coated with PLL.

phase on a hot plate at 95°C , the unpolymerized SU-8 is removed with the developer. The resulting structure is then hard baked for 10 minutes at 200°C . The final step entails coating the silicon mold with a hydrophobic molecular monolayer such as tridecafluoro-1,1,2,2-tetrahydrooctyl trichlorosilane (FOTS) to facilitate PDMS removal. After casting PDMS on the silicon mold, the microfluidic devices are bonded to coverslips and inspected under a microscope. Cells are loaded into the chambers and imaged with a microscope equipped with the appropriate laser line and filters. Currently, we are exploring new methods to load the bacterial cells into the microchambers such as patterning the surface of the coverslip using PDMS stamps coated with PLL (Figure 3). The overall goal is to pattern the surface with cells to match the geometry of microfluidic devices to achieve better spatially distributed cells.

References:

- [1] R. R. Robert B. Saper, Zinc: An Essential Micronutrient. *Am. Fam. Physician.* 79, 768 (2009).
- [2] S. Tan, D. Guschin, A. Davalos, Y.-L. Lee, A. W. Snowden, Y. Jouvenot, H. S. Zhang, K. Howes, A. R. McNamara, A. Lai, C. Ullman, L. Reynolds, M. Moore, M. Isalan, L.-P. Berg, B. Campos, H. Qi, S. K. Spratt, C. C. Case, C. O. Pabo, J. Campisi, P. D. Gregory. *Proc. Natl. Acad. Sci. U. S. A.* 100, 11997-12002 (2003).
- [3] C. Andreini, I. Bertini, in *Encyclopedia of Metalloproteins* (Springer, New York, NY, 2013), pp. 2549-2554.
- [4] S. R. Gordon, S. Vaishnav. *The Journal of Immunology.* 204, 83.18-83.18 (2020).
- [5] O. Koren, E. Tako. *Proc. AMIA Annu. Fall Symp.* 61, 16 (2020).
- [6] F. Wu, C. Dekker. *Chem. Soc. Rev.* 45, 268-280 (2016).
- [7] D. Binder, C. Probst, A. Grünberger, F. Hilgers, A. Loeschcke, K.-E. Jaeger, D. Kohlheyer, T. Drepper. *PLoS One.* 11, e0160711 (2016).
- [8] E. Bernson, Development of a Microfluidic Platform for Cell migration Studies along Gradients (2012) (available at <https://odr.chalmers.se/items/8199a5e9-f3f0-4824-9056-51f603dcfd7d>).
- [9] A. Shamloo, N. Ma, M.-M. Poo, L. L. Sohn, S. C. Heilshorn. *Lab Chip.* 8, 1292-1299 (2008).

Design and Application of Microfluidic Devices to Study the Effect of the Physical Microenvironment on Cellular Function

CNF Project Number: 2065-11

Principal Investigator(s): Jan Lammerding

User(s): Richa Agrawal, Maggie Elpers, Eitan Jentis, Sarah Henretta

*Affiliation(s): Meinig School of Biomedical Engineering,
Weill Institute for Cell and Molecular Biology; Cornell University*

*Primary Source(s) of Research Funding: NIH award R01 GM137605; NIH award R01 HL082792;
NIH award R35 GM153257; NIH award 1U54 CA261694*

*Contact: jan.lammerding@cornell.edu, ra664@cornell.edu,
mae228@cornell.edu, ej225@cornell.edu, sjh333@cornell.edu*

Research Group Website: <http://lammerding.wicmb.cornell.edu/>

*Primary CNF Tools Used: PT 770, Oxford Cobra, Heidelberg DWL 2000 Mask Writer, Karl Suss MA6,
Anatech SCE-110-RF Resist Stripper, P-7 Profilometer, MVD 100, Oxford 81, Unaxis 700, EcoClean tool*

Abstract:

The physical environment of cells directly modulates their function and fate. Using microfabricated devices that mimic the confined spaces within tissues, we previously demonstrated that cell migration through tight spaces is limited by the deformability of the large cell nucleus, and that the physical stress associated with such ‘confined migration’ can result in nuclear envelope rupture, DNA damage, and changes in chromatin organization [1-5]. As part of this project, we applied our microfluidic devices to study confined migration, identifying a novel mechanism by which cells squeeze their nucleus through small spaces [6], while also developing novel devices to enable the collection of large numbers of cells that have completed confined migration for genomic and transcriptomic analysis. Additionally, we developed a novel device to precisely confine cells to specific heights with micron resolution [7]. Expanding our mechanobiology research into another direction, we have begun developing microstructured surfaces that promote differentiation of cardiac and skeletal muscle stem cells into more mature muscle cells, thus enabling us to study the effect of disease-causing mutations on muscle function.

Research Summary:

During *in vivo* migration, immune cells, fibroblasts, or metastatic tumor cells traverse interstitial spaces as small as 1-2 μm in diameter. This ‘confined migration’ requires the deformation not only of the soft cell body but also the rate-limiting step of deforming the relatively rigid nucleus [1]. To study these processes in more detail, we have previously designed and fabricated polydimethyl siloxane (PDMS) microfluidic devices to

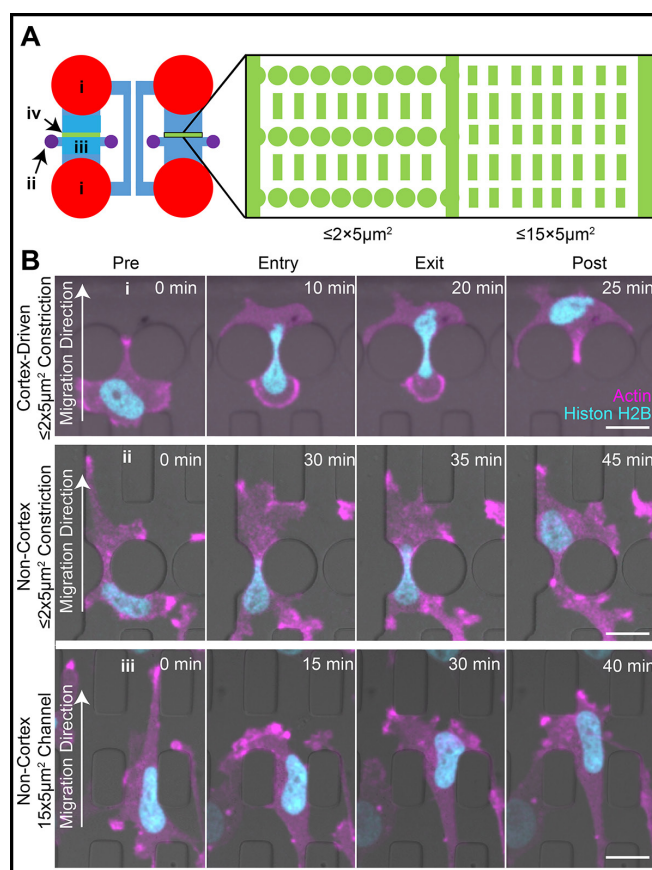


Figure 1: Microfluidic migration device to study confined migration mechanisms. (A) Overview of microfluidic migration device. (B) Time-lapse microscopy sequence of cells migrating through confined spaces using rear cortex contraction (top) or nuclear pulling (center and bottom) mechanism. Figure panels reproduced from Keys, et al. [7].

model the confined spaces that cancer cells may encounter during the metastatic process (Figure 1A) [8]. Using time-lapse imaging of cells expressing fluorescently labeled cytoskeletal components, we identified that cells can either use a ‘nuclear pulling’ mechanism, in which contraction of actomyosin fibers pull the nucleus through the tight space, or a ‘rear cortex contraction’ mechanism, in which contraction of the back of the cell generates a hydrostatic pressure gradient within the cell that drives the nucleus through the constriction (Figure 1B). We confirmed the biophysical mechanisms using laser ablation and fluorescent reporters. This work was recently published in the *Journal of Cell Science* [6].

Since the previous generation of microfluidic devices could not collect sufficient numbers of cells that have migrated through the confined spaces to perform biochemical or sequencing-based analyses, we designed novel migration devices that enable collection of 1000’s of cells post confined migration. We optimized several fabrication steps for these devices, including etching with hydrogen bromide in the Oxford Cobra etcher to achieve vertical device features in the mold for the PDMS microfluidic devices. We are currently in the process of applying these devices to analyze the effect of confined migration on gene expression and changes in chromatin organization in cancer cells.

In addition to the migration devices, we also developed a cell confinement device (Figure 2), in which we can precisely confine cells using an agarose pad containing micro-pillars fabricated to the height of interest (i.e., 3-15 μm). To make the device, agarose is cast onto a mold consisting of a silicon wafer fabricated to contain the negatives of the desired pillar features, and the agarose device is cut out and placed onto cells seeded on a glass-bottomed dish. The silicon wafer is fabricated using photolithography with SU-8 photoresist. We have fabricated devices with various heights to induce different degrees of confinement. The devices are suitable for short- and long-term confinement studies and compatible with imaging of both live and fixed samples. This work was recently published in *Current Protocols in Cell Biology* [5]. We are currently applying these devices to assess the effect of confinement on polarization and gene expression in primary bone marrow-derived macrophages.

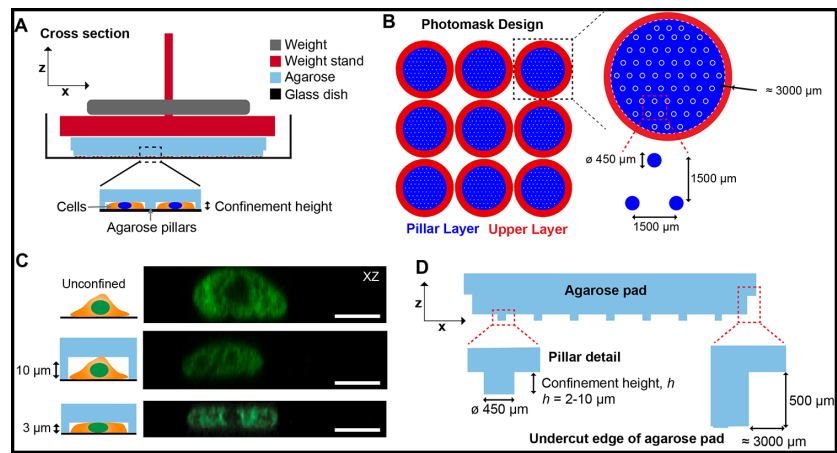


Figure 2: Agarose-based cell confinement device. (A) Cross section (left) schematic of the confinement device assembly. Assembly includes a glass bottomed dish (black), agarose device (blue), weight holder (red), and weight (gray). (B) Overlay of the lower- and upper-layer photomask designs showing the array of micropillars for one confinement device. (C) Representative images of breast cancer cells with nuclei fluorescently labeled with histone 2B-mNeonGreen under either unconfined, confined to 10 μm , or confined to 3 μm conditions. Scale bars: 10 μm . (D) Schematic depiction of a single agarose device. Figure adapted from Elpers, et al. [5].

Lastly, we recently designed microstructured substrates consisting of approximate 800 nm x 800 nm (W x H) ridges that promote alignment and maturation of muscle cells grown on them. To fabricate the structures, OiR620-7i photoresist was spun onto silicon wafers and exposed using the i-line stepper. Next, the Oxford 81 etcher was used to perform a descum process to prepare the wafer for deep silicon etching. The Unaxis 700 Deep Silicon Etcher was used to etch ca. 800 nm into the silicon. Excess photoresist is stripped using the EcoClean tool, and a FOTS coating is applied using the MVD 100 so that a PDMS cast can be made of the wafer, which then serves as the actual microstructured substrate for the cells. The transparent and flexible PDMS allows for imaging cells through the substrate, and also for applying uniaxial strain to the substrate, mimicking muscle contraction.

Taken together, these examples illustrate new uses of the available nanofabrication technologies to create improved in vitro models to study confined cell migration and mechanobiology.

References:

- [1] Davidson, P., et al. *Cell Mol Bioeng*, 2014. 7(3): p. 293-306.
- [2] Bell, E.S., et al. *Oncogene*, 2022. 41(36): p. 4211-4230.
- [3] Denais, C.M., et al. *Science*, 2016. 352(6283): p. 353-8.
- [4] Shah, P., et al. *Curr Biol*, 2021. 31(4): p. 753-765 e6.
- [5] Hsia, C.R., et al. *iScience*, 2022. 25(9): p. 104978.
- [6] Keys, J., et al. *J Cell Sci*, 2024. 137(12).
- [7] Elpers, M.A., et al. *Curr Protoc*, 2023. 3(7): p. e847.
- [8] Davidson, P.M., et al. *Integr Biol*, 2015. 7(12): p. 1534-46.

Metasurface-Enhanced Mid-Infrared Microscopy for Imaging Living Cells

CNF Project Number: 2472-16

Principal Investigator(s): Gennady Shvets

User(s): Steven He Huang, Po-Ting Shen

Affiliation(s): Applied and Engineering Physics, Cornell University

Primary Source(s) of Research Funding: National Cancer Institute of the National Institutes of Health award number R21 CA251052. National Institute of General Medical Sciences of NIH award number R21 GM138947

Contact: gs656@cornell.edu, hh623@cornell.edu, ps944@cornell.edu

Research Group Website: <http://shvets.aep.cornell.edu>

Primary CNF Tools Used: JEOL 9500, SC4500 Evaporator, Zeiss Supra SEM, PDMS Casting Station, Anatech Resist Strip, Glen 1000 Resist Strip, DISCO Dicing Saw

Abstract:

We have developed Metasurface-Enhanced Mid-Infrared Microscopy (MEMIM) as a novel tool for chemical imaging of living cells. In MEMIM, cells are cultured on an array of plasmonic nanoantennas (metasurface), and their near-field interaction alters the scattering cross-section of the nanoantennas, making the cells visible in the far field. The imaging contrast arises from the mid-infrared vibrational absorption of the cells, primarily originating from the major classes of biomolecules including DNA, proteins, and lipids. Our technology is a label-free, non-destructive imaging technique with chemical contrast, holding wide potential applications in biomedical research.

Summary of Research:

Infrared (IR) spectroscopy and chemical imaging are widely used to identify chemical compounds through their molecular vibration fingerprints and has found many applications in biological analysis. Yet, the use of IR microscopy for imaging living cells is challenging due to the attenuation of IR light in water, necessitating the use of thin flow cells or attenuated total reflection (ATR) configurations that are difficult to scale to high-throughput measurements. In the past, we have used plasmonic metasurfaces to overcome this challenge, demonstrating the spectroscopic measurement of changes related to cell adhesion and dissociation, cholesterol depletion, and activation of intracellular signaling pathways [1,2]. Recently, we have expanded this technique to a novel chemical imaging technique, called MEMIM, to image living cells in physiological conditions. In MEMIM, cells are grown on an array of resonant plasmonic nanoantennas called metasurfaces. These resonant nanoantennas interact with the cells in the near-field through their plasmonic hotspots, in

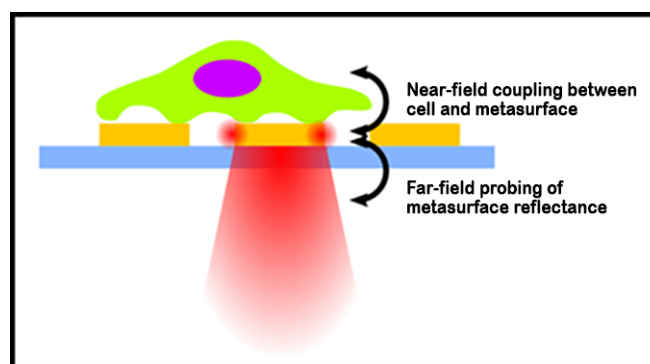


Figure 1: Metasurface-enhanced infrared spectroscopy and chemical microscopy. The near-field interaction of cells with metasurface results in SEIRA, which changes the scattering cross section of the individual nanoantennas. This interaction is probed in the far-field via metasurface reflectance, allowing for non-perturbative infrared spectroscopy of living cells.

an effect called surface-enhanced infrared adsorption (SEIRA), leading to a modulation in the far-field scattering cross-section of the nanoantennas. Images of analytes on the metasurface are formed by a mid-infrared laser scanning microscope, focused to the plane of the metasurface (Figure 1).

Our mid-IR metasurface is fabricated as an array of gold nanoantennas on IR transparent CaF₂ substrates (0.5 mm thick). The substrate is first cleaned using oxygen plasma etcher (Anatech or Glen 1000 Resist Strip). Metasurface patterns are defined using electron beam lithography with the JEOL 9500 system and poly(methyl methacrylate) (PMMA) as the resist. 5 nm Cr adhesion layer and 70 nm Au are deposited using SC4500 evaporator. As the final step, oxygen plasma etcher (Anatech or Glen 1000 Resist Strip) is used to clean the metasurface sample. The metasurface is then attached to superstructures for cell culture chambers and cells are grown on top of the metasurface.

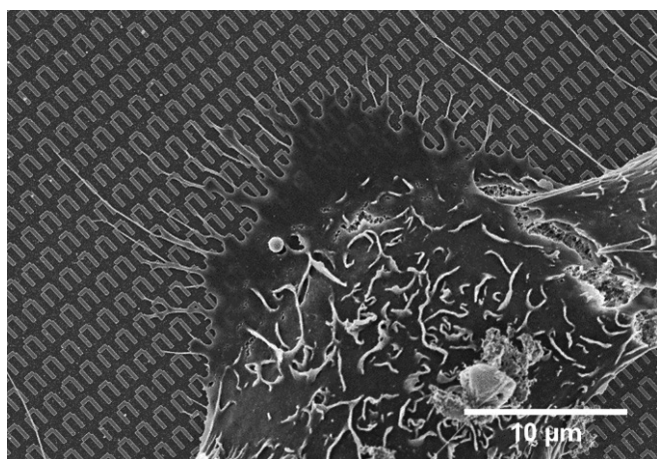


Figure 2: Scanning electron microscope image of a A431 human skin cancer cell on the metasurface. Scale bar: 10 μm .

Figure 2 shows a scanning electron microscope image of a cell on the metasurface.

Our group recently designed and built an inverted point-scanning confocal microscope using a mid-IR quantum cascade laser (QCL) light source. The emission from a QCL is focused on a diffraction-limited spot on the metasurface and scanned across it by moving the sample with a motorized microscope stage. The reflection, modulated by the metasurface's near-field interaction with the analyte, is collected by a liquid-nitrogen-cooled mercury-cadmium-telluride (MCT) mid-IR detector. The lateral resolution of our imaging system is diffraction-limited to about 5 μm .

Using this setup, we have demonstrated the efficacy of MEMIM for label-free imaging of both fixed and living cells on the metasurface. Images of fixed 3T3-L1 fibroblasts (pre-adipocytes), shown in Figure 3, reveal clear chemical contrast from proteins (amide I/II bands, 1500-1700 cm^{-1}) and DNA (PO₂-phosphate bands, 1085 cm^{-1}). Comparison with fluorescent images shows good correlation, with phosphate band IR images aligning well with nucleus-stained fluorescence images. The protein IR image also matches the actin-

stained fluorescence image, capturing the cell's outer morphology, although differences arise because the protein IR image includes all proteins, not just actin. Lipid droplets in differentiated 3T3-L1 adipocytes can also be imaged through the C=O ester carbonyl vibration of the lipids at 1740 cm^{-1} (image not shown). We also performed time-lapse imaging of living cells (data not shown) to monitor cell adhesion and motility on the metasurface. These live cell imaging results confirm that living cells can be imaged using our technique without affecting cell viability and behavior under mid-IR light.

Conclusions and Future Steps:

We have developed a plasmonic metasurface-based mid-infrared chemical imaging technology for the label-free, non-destructive imaging of living cells with chemical contrast. Imaging cells with contrast arising from proteins, DNAs, and lipids have been demonstrated. This technique could allow for the non-perturbative metabolic imaging of living cells over several days, which is currently not possible using other similar techniques. We plan to expand this technology to the metabolic imaging of cells using small IR-active metabolic labels, such as azides, deuterium, and ¹³C. This could help in characterizing heterogeneity in metabolic rates within the cell population and how they are changed through drug treatment or other environmental cues, with implications in metabolic diseases such as diabetes and fatty liver diseases.

References:

- [1] Huang, S. H., et al. Monitoring the effects of chemical stimuli on live cells with metasurface-enhanced infrared reflection spectroscopy. *Lab Chip* 21, 3991-4004 (2021).
- [2] Huang, S. H., et al. Metasurface-enhanced infrared spectroscopy in multiwell format for real-time assaying of live cells. *Lab Chip* 23, 2228-2240 (2023).

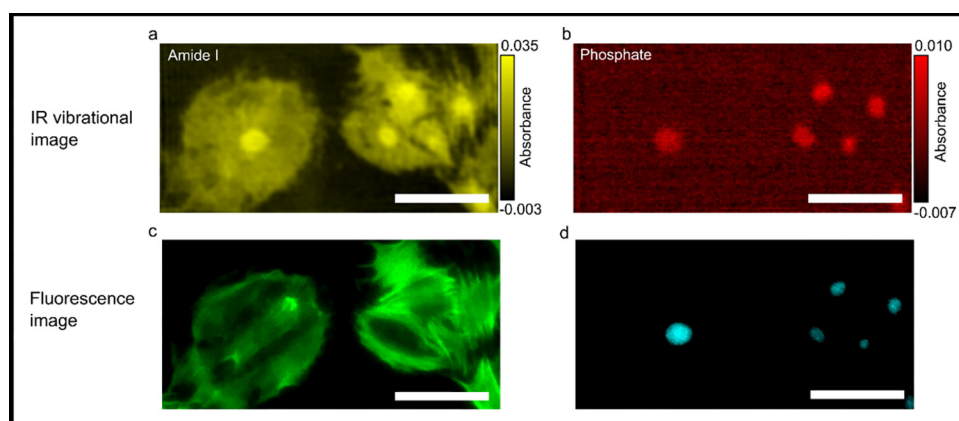


Figure 3: Metasurface-enhanced IR chemical microscopy of fibroblasts. (a): IR vibrational image at amide I band (1655 cm^{-1} , contrast from total proteins). (b): IR vibrational image at phosphate band (1085 cm^{-1} , contrast from DNA). (c): Actin-stained fluorescent image. (d): Nucleus-stained fluorescent image. Scale bar: 100 μm .

Time-Lapse Mid-Infrared Spectroscopy of Live Cells Using High-Aspect-Ratio Metal-on-Dielectric Nanostructures

CNF Project Number: 2472-16

Principal Investigator(s): Gennady Shvets

User(s): Aditya Mahalanabish, Dias Tulegenov

Affiliation(s): Applied and Engineering Physics, Cornell University

Primary Source(s) of Research Funding: National Cancer Institute of the National Institutes of Health award number R21 CA251052; National Institute of General Medical Sciences of the NIH award number R21 GM138947

Contact: gshvets@cornell.edu, am2952@cornell.edu, dt483@cornell.edu

Research Group Website: <http://shvets.aep.cornell.edu>

Primary CNF Tools Used: JEOL 9500, SC4500 Evaporator, Zeiss Ultra Scanning Electron Microscope, Oxford Plasma Enhanced Chemical Vapor Deposition, Plasma-Therm 740, Anatech Resist Strip, DISCO Dicing Saw

Abstract:

Our group previously introduced Metasurface-Enhanced Infrared Spectroscopy (MEIRS) for spectral analysis and chemical imaging of live cells. MEIRS uses plasmonic nanoantenna arrays (metasurfaces) to enhance infrared signals by coupling molecular vibrations to plasmonic resonances. However, flat plasmonic metasurfaces (2D nanoantennas) have a limited probing volume near the plasma membrane. Inspired by high-aspect-ratio nanostructures, we demonstrate that integrating plasmonic metasurfaces with tall dielectric nanostructures significantly improves FTIR spectroscopy sensing capabilities.

Summary of Research:

Infrared (IR) spectroscopy is widely employed to identify chemical compounds and has numerous biological applications. We developed Metasurface-Enhanced Infrared Spectroscopy (MEIRS) to measure live cell activity under physiological conditions. In MEIRS, cells are cultured on plasmonic nanoantenna arrays (metasurfaces) that enhance IR absorption. We have utilized MEIRS to detect changes in cell adhesion, cholesterol levels, and intracellular signaling [1,2]. This work improves on MEIRS by combining plasmonic metasurfaces with nano-topography to enhance FTIR sensitivity and pave the way for an optical platform to study cell-nanostructure interactions.

Figures 1(a) and 1(b) illustrate schematics of different device designs we fabricated. Figure 1(a) shows a nanoantenna array atop dielectric pillars (referred to as 3D nanoantennas), while Figure 1(b) displays an array of gratings atop dielectric pillars (referred to as 3D nanogratings). These high-aspect-ratio metasurfaces consist of gold nanoantennas on silica nanopillars deposited on IR-transparent CaF₂ substrates. The CaF₂ substrate is first cleaned using an oxygen plasma etcher (Anatech Resist Strip) and then coated with a 1 μ m layer of SiO₂ using plasma-enhanced chemical vapor deposition (Oxford PECVD) to form the dielectric thin film. Metasurface patterns are defined using electron beam lithography with the JEOL 9500 system and poly(methyl methacrylate) (PMMA) as the resist. Layers of 5 nm Cr, 70 nm Au, and 20 nm Cr (as a hard mask for the subsequent etch step) are deposited using the SC4500 evaporator. If necessary, metasurfaces fabricated on large substrates (up to 4" diameter) are diced into smaller pieces using a DISCO dicing saw. The final step involves cleaning the metasurface sample with an oxygen plasma etcher (Anatech Resist Strip).

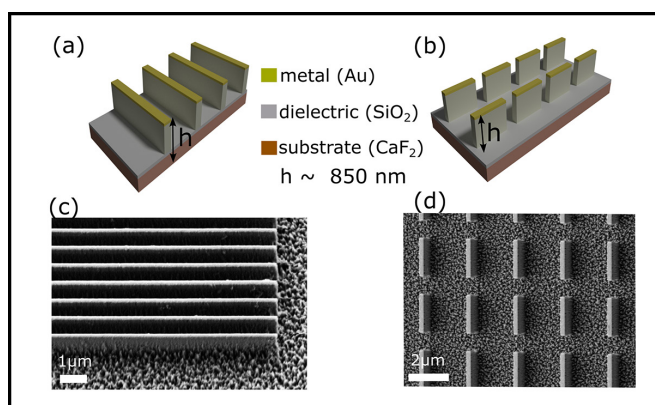


Figure 1: High-aspect-ratio metal-on-dielectric metasurfaces. (a) and (b) show schematic of 3D nanograting device and 3D nanoantenna metasurface respectively. (c) and (d) are SEM images of the fabricated 3D nanograting device and 3D nanoantenna metasurface respectively (Scale bar: 1 μ m and 2 μ m, respectively).

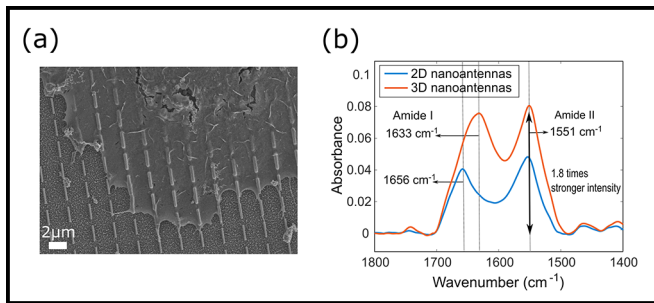


Figure 2: (a) SEM image of a human skin cancer cell on the 3D nanoantenna metasurface. (Scale bar: 2 μm) (b) Comparison of Fourier Transform Infrared Absorbance spectra of human skin cancer cells grown on 2D and 3D nanoantenna metasurfaces.

The metasurface is then attached to superstructures for cell culture chambers, and cells are grown on top of the metasurface for analysis. Figure 1(c) shows the fabricated 3D nanoantennas device, and Figure 1(d) depicts the fabricated 3D nanograting device.

When cells attach to high-aspect-ratio metasurfaces, they exhibit cellular responses not observed with flat 2D nanoantennas. One notable response is the induction of plasma membrane curvature, leading to cell deformation and wrapping around the vertical structures in accordance with the surface nanotopography. This phenomenon of cell wrapping addresses the issue of shallow field penetration seen with 2D metasurfaces, utilizing an optical process called transfection.

Figure 2(a) shows an SEM image of fixed and dried cells grown on these 3D nanoantennas. The nanoantennas, which are 1.8 μm long, reflect light in the spectral region of 1500 cm^{-1} to 1700 cm^{-1} , suitable for analyzing proteins (amides) in cells. Figure 2(b) compares the infrared absorbance spectra obtained from cells grown on 2D and 3D nanoantenna metasurfaces. Spectra from the 3D nanoantenna metasurfaces (about 850 nm tall) exhibit a 1.8-fold improvement in spectral intensity in the Amide II region. A signature of unique cellular responses induced by the vertical nanostructures is also evident from the peak shift in the Amide I region observed in Figure 2(b).

While the 3D nanoantennas are resonant structures that reflect light only in specific spectral ranges based on antenna design, the 3D nanograting device shown in Figures 1(b) and 1(d) is a broadband optical device utilizing non-resonant plasmonic structures [3]. This device functions similarly to a wire grid polarizer under normal incidence, reflecting light with an electric field polarized parallel to the gratings when the

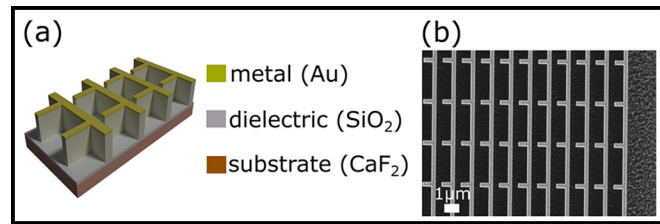


Figure 3: Grantenna — a device which can function as both 3D nanoantenna and 3D nanograting depending on the incident light polarization. (a) Schematic of device. (b) SEM image of fabricated device. (Scale bar: 1 μm).

grating periodicity is much smaller than the incident wavelength. This broadband reflectance device can be used for biological sensing of cells or other analytes in the region between the dielectric pillars. For the 3D nanoantennas, the plasmonic near fields are strongest near the gold nanoantenna, while for the 3D nanograting, the fields are strongest near the substrate (away from the gold layer) due to the standing wave effect. This makes the two devices complementary for studying live cells. The 3D nanoantennas are particularly sensitive to the cellular region around the metallic nanoantenna (the plasma membrane), whereas the 3D nanograting is more sensitive to the cell body in the trenches separating the tall dielectric gratings.

The device shown in Figure 3 combines the functionality of 3D nanoantennas and 3D nanograting into one, which we refer to as Grantennas. Depending on the polarization of the incident light, this device functions as either a 3D nanoantenna metasurface or a 3D nanograting. In the future, in addition to microwell-based cellular spectroscopy, we plan to employ these devices for rapid chemical imaging of live cells with sub-cellular resolution.

References:

- [1] Huang, S. H., et al. Monitoring the effects of chemical stimuli on live cells with metasurface-enhanced infrared reflection spectroscopy. *Lab Chip* 21, 3991-4004 (2021).
- [2] Huang, S. H., et al. Metasurface-enhanced infrared spectroscopy in multiwell format for real-time assaying of live cells. *Lab Chip* 23, 2228-2240 (2023).
- [3] Mahalanabish, A.; Huang, S.; Shvets, G. Inverted Transfection Spectroscopy of Live Cells Using Metallic Grating on Elevated Nanopillars. *ACS Sens* 9 (3), 1218-1226 (2024).

Biomimetic Loading Promotes Maturation and Suppresses Pathological Progression of Chick Embryonic Cardiomyocytes in Engineered Heart Tissues

CNF Project Number: 2619-17

Principal Investigator(s): Jonathan T. Butcher

User(s): Mong Lung Steve Poon

Affiliation(s): Department of Biomedical Engineering, Cornell University

Primary Source(s) of Research Funding: Additional Ventures Single Ventricle Research Fund; National Institutes of Health R01 HL160028

Contact: jtb47@cornell.edu, mp773@cornell.edu

Research Group Website: <https://www.butcherlab.com/>

Primary CNF Tools Used: Objet30 pro 3D printer

Abstract:

Mechanical stimulation of engineered cardiac tissue was shown to improve cardiomyocyte maturation by emulating the mechanical loadings cardiomyocyte experienced during cardiac cycle, namely resistance to contraction (Afterload) and cyclic stretching (Preload). Nevertheless, many existing platforms for cyclic stretching pose the risk of inducing human cardiac pathology. In this study, we developed a novel bioreactor system to more accurately recapitulate the *in vivo* loading condition, allowing cyclic stretching with active contractile work production and duty cycling incorporated in between each stretch. Our focus was to investigate the functionalities, maturation, and pathological progression of embryonic chicken engineered heart tissues (EHTs) subjected to three distinct mechanical stimulation regimens, including (i) static control, (ii) afterload no duty cycle (Afterload NoDC), and (iii) afterload duty cycle (Afterload DC). We showed that Afterload DC improved tissue functionalities, maintaining higher contractile force and frequency. This was achieved by prohibiting early tissue compaction during stimulation. Tissues exposed to Afterload DC demonstrated enhanced cardiomyocyte maturation evidenced by improved sarcomeric organization.

Moreover, Afterload DC suppressed the transcriptional expressions of pathological hypertrophy and fibrosis markers, including TGF.2, COL5A2, and POSTN. Collectively, Afterload DC significantly promoted the functionality of EHTs by enhancing cardiomyocyte maturation and suppressing cardiac pathology. This study highlighted the remarkable potential of biomimetic loadings in facilitating tissue maturation.

Summary of Research:

To determine if utilizing a mechanical stimulation regimen that can provide cyclic stretching while allowing contractile work production improves the tissue functionalities, contractile forces and frequencies of EHTs during auxotonic contraction were measured over seven days of stimulation (Figure 1). A

decline in contractile force was observed from D5 to D11 in all conditions (Figure 1A). However, both Afterload DC and Afterload NoDC groups had a general maintenance of the contractile force across culture time with a less degree of a decline. When comparing each condition, the afterload DC conditioned tissues showed a significantly greater force compared to the other conditions observed as early as the fifth day of stimulation. In terms of contractile frequency, Afterload NoDC and Afterload DC led to an increase in contractile frequency to a level significantly higher than that of the static control starting from D7 (Figure 1B). This incline in contractile frequency was shown to be followed by a mild decrease until D11 while most of the tissues in static control gradually lost their contraction.

To examine the effect of different mechanical stimulation regimens on tissue compaction, brightfield images of EHTs were taken over the culture period (Figure 2A). EHTs from all regimens exhibited spontaneous compaction in volume from D4 to D5 prior to the application of mechanical stimulation (Figure 2B). From D5, both Afterload NoDC and Afterload DC interrupted the compaction process, leading to significantly higher tissue volume of EHTs on D8 relative to those from the static control. This prohibiting effect was sustained until D11 only in Afterload NoDC, whereas EHTs subjected to Afterload DC showed a tissue volume similar to that of the static control. Our results showed that the percentage change of tissue volume from D5 to D8 was significantly and positively correlated with the percentage change of contractile force, in which afterload NoDC and afterload DC promote higher tissue volume and therefore higher contractile force (Figure 2C).

We investigated whether the improved tissue functionalities of EHTs following Afterload NoDC and Afterload DC conditioning is associated with enhanced cardiomyocyte maturation [1]. To do so, EHTs were stained with α -Actinin to visualize the sarcomeric organization of cardiomyocytes (Figure 3A). As expected, tissues exposed to Afterload

NoDC and Afterload DC conditioning demonstrated more aligned sarcomere structure compared to those in the static control group. More importantly, both mechanical stimulation regimens led to sarcomere and z-band lengths resembling that of the mature chick cardiomyocytes.

Increasing afterload was shown to promote pathological hypertrophy and fibrosis despite improved tissue functionalities of EHTs. Here, EHTs subjected to Afterload NoDC condition were stretched while being prohibited from contractile work production by providing a consistently high afterload. To assess whether pathological phenotypes were manifested in the tissues under Afterload NoDC and whether Afterload DC can mitigate the pathological progression, smFISH staining was performed on a panel of gene markers associated with pathological hypertrophy and cardiac fibrosis (Figure 4). Aligned with previous study, tissues in the Afterload NoDC group showed significantly higher expression of pathological hypertrophy markers, including POSTN, TGF β 2, and COL5A2, compared to the static control. Surprisingly, despite being exposed to mechanical loading, EHTs in the Afterload DC condition showed similar marker expression to the static control. No significant difference among conditions was detected in FN1 expression.

Conclusion and Future Steps:

Our study highlights the promising potential of Afterload DC in promoting EHTs functionality by promoting cardiomyocyte maturation while preventing pathological phenotypes. To expand, assessing the effect of biomimetic loading on human induced pluripotent stem cell-derived cardiomyocyte will greatly facilitate the clinical translation of this novel mechanical stimulation regimen. Meanwhile, our bioreactor system could also serve as a platform for drug screening and disease modeling.

References:

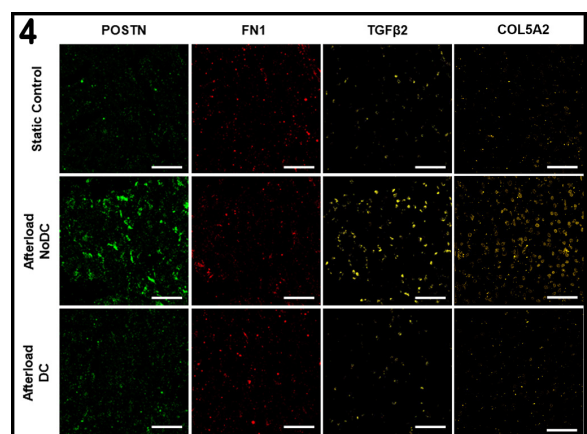
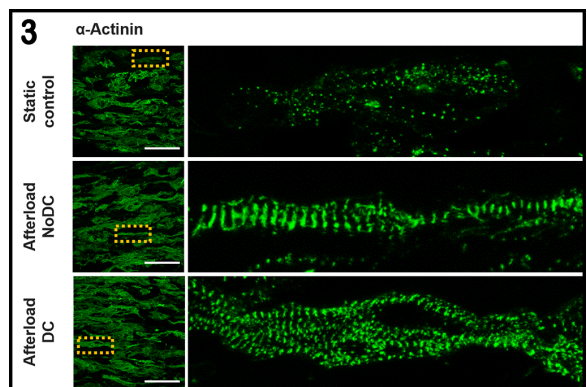
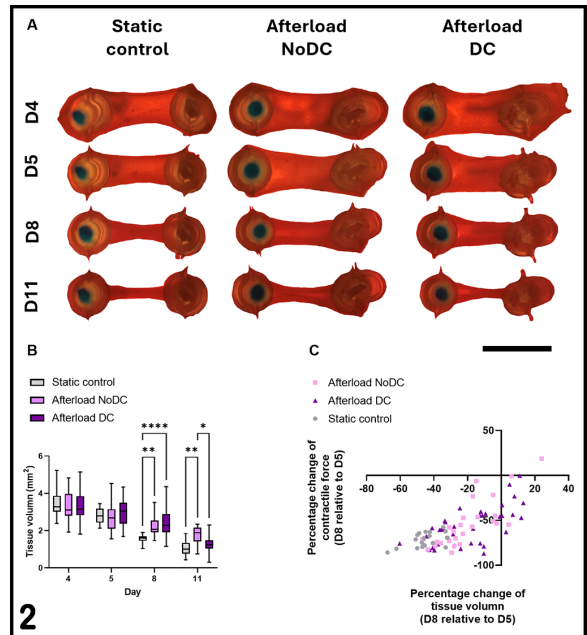
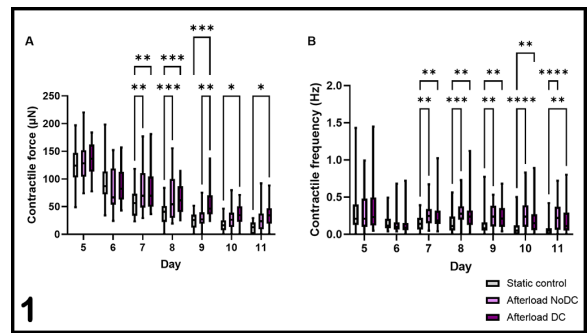
- [1] Leonard, Andrea, et al. "Afterload promotes maturation of human induced pluripotent stem cell derived cardiomyocytes in engineered heart tissues." *Journal of molecular and cellular cardiology* 118 (2018): 147-158.

Figure 1: Auxotonic contractile capacity of EHTs on post constructs across stimulation period. Contractile force (A) and frequency (B) across culture time for all three stimulation conditions.

Figure 2: Compaction of EHTs on post construct across stimulation period. (A) Bright field images of EHTs across culture time for all three stimulation conditions. (B) Quantitative measurement of tissue volume of EHTs across culture time. (C) Correlation between percentage change of contractile force and percentage change of tissue volume from D5 to D8 and D8 to D11.

Figure 3: Cardiomyocyte maturation in EHTs on Day 11. (A) Representative immunofluorescent images of α -actinin. Quantitative measurement of the sarcomere length (B) and the z-band length

Figure 4: Expression of gene markers associated with fibrosis and pathological hypertrophy in EHTs on Day 11.



Micro-Scale Optoelectronic Transduced Electrodes (MOTEs) for Chronic *in vivo* Neural Recording

CNF Project Number(s): 2657-18, 2836-19

Principal Investigator(s): Prof. Alyosha C. Molnar

User(s): Sunwoo Lee, Shahab Ghajari, Sanaz Sadeghi, Devesh Khilwani

Affiliation(s): Electrical and Computer Engineering, Cornell University

Primary Source(s) of Research Funding: National Institute of Health

Contact: am699@cornell.edu, sl933@cornell.edu, sg2367@cornell.edu, ss3842@cornell.edu, dk842@cornell.edu

Research Group Website: <https://molnargroup.ece.cornell.edu/>

Primary CNF Tools Used: ABM Contact Aligner, AJA Sputter, and Westbond 7400A Ultrasonic Wire Bonder, Oxford 100/81/82, UNAXIS Deep Si Etcher, Oxford PECVD/ALD, Anatech, P7 Profilometer, Zeiss SEMs

Abstract:

Elucidating how the brain functions requires chronic *in vivo* recording of neural activity in live animals. However, existing neural recording technologies have thus far failed to provide a tetherless and fully implantable neural recording unit that can function chronically. Instead, existing techniques typically require electrodes to be tethered to the outside world directly via a wire, or indirectly via an RF Coil [1], which is much larger than the electrodes themselves, causing irrevocable damages associated with the residual motions between electrodes and neurons as the brain moves. On the other hand, optical techniques, which are becoming increasingly popular, are often limited to subsets of neurons in any given organism, impeded by scattering of the excitation light and emitted fluorescence, and limited to low temporal resolution [2]. Here we heterogeneously integrate III-V optical devices on complementary metal-oxide-semiconductor (CMOS) via a layer transfer, creating Micro-scale Optoelectronic Transduced Electrodes (MOTEs), which are powered by and are communicating optically, combining many benefits of optical techniques with high temporal-resolution of electrical recording. Our work not only represents the smallest neural recorder to date but is also the first to be demonstrated to be functional *in vivo* and chronically (> 5 months) in awake mice.

Summary of Research:

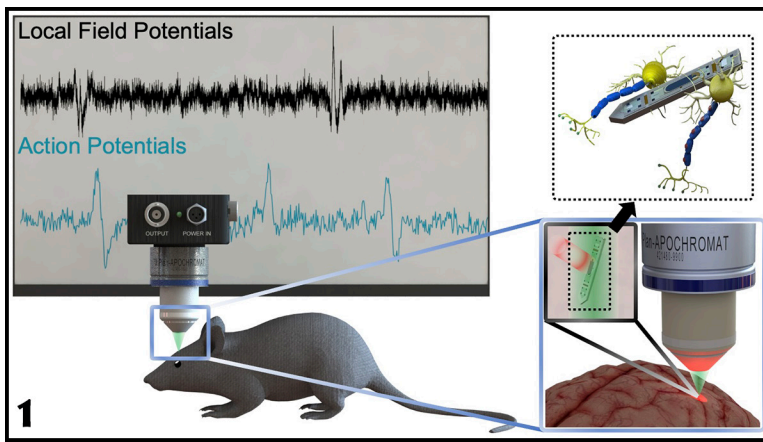
Our fabrication starts with about 5 mm x 5 mm, conventional 180 nm CMOS die, which contains the electronics for signal amplification, encoding, and transmission [3,4]. The CMOS die is then integrated with AlGaAs diode which acts as a photo-voltaic (PV) as well as light emitting diode (LED), hence the diode is abbreviated as PVLED [5]. The PVLED provides an optical link which powers the electronics and transmits

encoded signals in optical pulses. The MOTE utilizes Pulse Position Modulation (PPM) for signal encoding for its high information-per-photon efficiency, where the spacing between the output pulses is proportional to the measured electric field of neuronal signals across the measurement electrodes. Figure 1 depicts a conceptual deployment and system description of such MOTE, whereas Figure 2 shows the impressive scaling enabled through the MOTE's heterogeneous integration (< 1 nanoliter in volume and ~1 μ g in weight).

The MOTEs are completely untethered, hence free of any detrimental relative motion often observed in tethered or wired neural recording units. Instead, the MOTEs are powered optically, and through the PPM, emits the measured neural signals optically as well, at a longer wavelength than the "powering" wavelength. Figure 3 illustrates the measurement setup associated with the MOTEs where a 623 nm LED was used to power the MOTE, which in turn emits the PPM pulses that encode the neural activities at the 825 nm wavelength. The MOTEs have been implanted in mouse brains, and we were able to measure the neural activities chronically for more than 5 months (and counting), during which time the foreign body response seemed to be minimal thanks to their miniscule size, and the neural signals were quite stable. Figure 4 provides example measurements of action potential spikes from one such mouse brain where the MOTEs were embedded in its barrel cortex so that the recording can be done in a cause-and-effect fashion (i.e., a touch whisker activating barrel cortex responses).

Conclusions and Future Steps:

A MOTE is the smallest electrophysiological sensor of its kind, enabled through an ingenious heterogeneous integration approach that leverages multiple disciplines:



electronics, optics, nano/microfabrication, and electrophysiology. The next step would entail not only improving the circuits and the devices of the MOTEs but paving the path toward the mass production so to provide interested biolaboratories the MOTEs samples, and to examine the commercial viability. In parallel, applying existing MOTEs to biological studies previously unapproachable such as chronic in-organoid measurements is our near term goal.

References:

- [1] R. R. Harrison, et al., "A Low-Power Integrated Circuit for a Wireless 100-Electrode Neural Recording System," *IEEE J. Solid-State Circuits*, vol. 42, no. 1, pp. 123-133, Jan. 2007, doi: 10.1109/JSSC.2006.886567.
- [2] W. Yang and R. Yuste, "In vivo imaging of neural activity," *Nat Methods*, vol. 14, no. 4, Art. no. 4, Apr. 2017, doi: 10.1038/nmeth.4230.
- [3] S. Lee, A. J. Cortese, P. Trexel, E. R. Agger, P. L. McEuen, and A. C. Molnar, "A 330 μm x 90 μm opto-electronically integrated wireless system-on-chip for recording of neural activities," in 2018 IEEE International Solid-State Circuits Conference (ISSCC), Feb. 2018, pp. 292-294. doi: 10.1109/ISSCC.2018.8310299.
- [4] S. Lee, A. J. Cortese, A. P. Gandhi, E. R. Agger, P. L. McEuen, and A. C. Molnar, "A 250 μm x 57 μm Microscale Opto-electronically Transduced Electrodes (MOTEs) for Neural Recording," *IEEE Transactions on Biomedical Circuits and Systems*, vol. 12, no. 6, pp. 1256-1266, Dec. 2018, doi: 10.1109/TBCAS.2018.2876069.
- [5] S. Lee, et al., "Fabrication of Injectable Micro-Scale Opto-Electronically Transduced Electrodes (MOTEs) for Physiological Monitoring," *J. Microelectromech. Syst.*, vol. 29, no. 5, pp. 720-726, Oct. 2020, doi: 10.1109/JMEMS.2020.2999496.

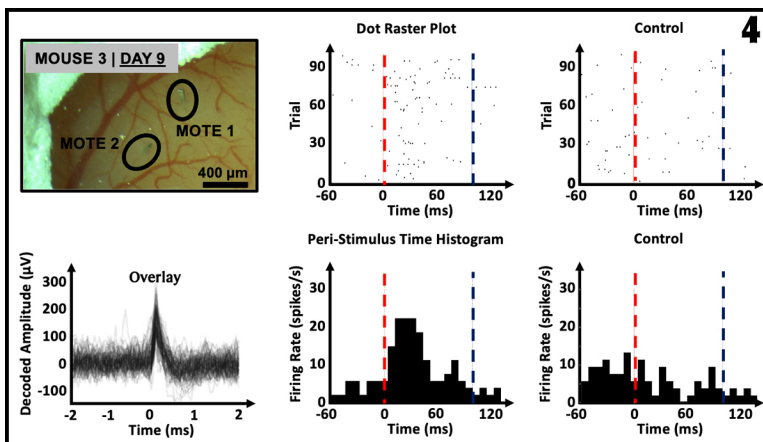
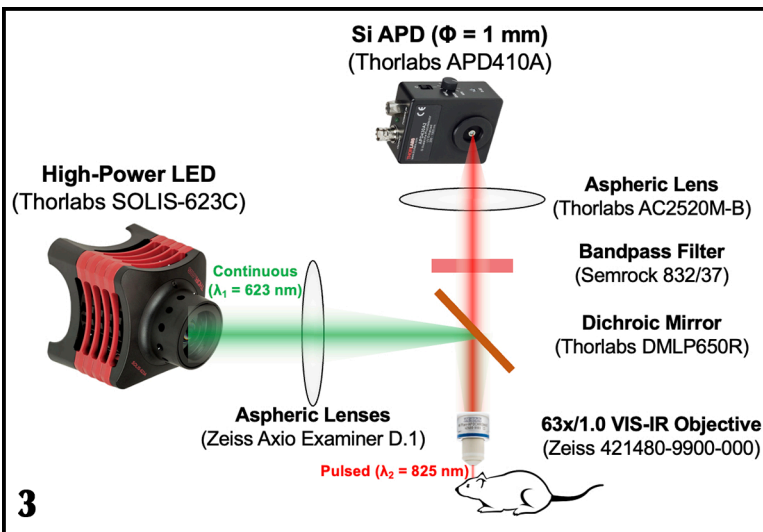
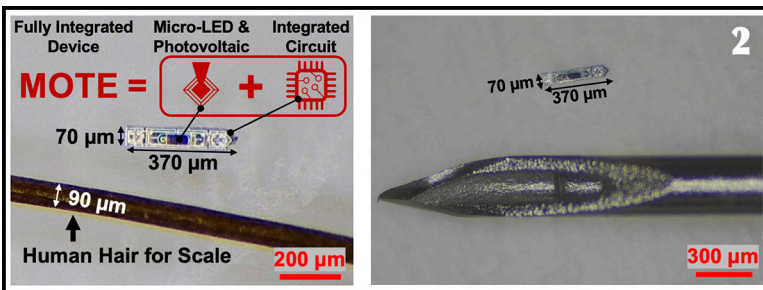


Figure 1: System level description of the micro-scale optoelectronic transduced electrodes (MOTEs) in a mouse brain.

Figure 2: Fully fabricated MOTEs next to S. Lee's hair (left) and a 31-gauge insulin needle (right).

Figure 3: Schematic of the MOTE-based measurement system, which the MOTE is powered and is communicating optically.

Figure 4: In vivo neural recording demonstrating that the MOTEs are indeed able to measure neural activities such as action potentials chronically.

On-Chip Cell Transportation and Rotation Using Vibration-Induced Flow

CNF Project Number: 2827-19

Principal Investigator(s): Alireza Abbaspourrad

User(s): Amirhossein Favakeh, Amir Mokhtare

Affiliation(s): Department of Food Science, Cornell University

Primary Source(s) of Research Funding: Ignite: Cornell Research Lab to Market, Center for Technology Licensing

Contact: alireza@cornell.edu, af446@cornell.edu, am2964@cornell.edu

Research Group Website: <https://abbaspourradlab.com/>

Primary CNF Tools Used: ABM Contact Aligner, Heidelberg Mask Writer - DWL2000, Dicing Saw - DISCO, P7 Profilometer

Abstract:

We present a system for cell manipulation based on vibration-induced flow (VIF), the science of acoustic streaming generated around the microstructure on a chip using circular vibration. This technique is easy to handle and applicable to an open-surface chip structure. It is a simple method involving a chip on an XY piezoelectric stage and is known for its simplicity. Thus, large cells can be manipulated by the applied flow velocity in the order of 100 $\mu\text{m/s}$ close to the micropillar arrays. We designed the micropillar array to control the mouse oocytes' transportation, rotation, and manipulation. The induced flow around the micropillars can be controlled by the applied frequency, amplitude, and shape/arrangement of the micropillar structure.

Summary of Research:

Recent advances in micro/nanofabrication and microfluidics have improved the manipulation of small biological objects, such as cells or microorganisms [1]. We present a transportation method based on vibration-induced flow (VIF) to move the mouse oocytes through the micropillar arrays on the open surface chip [2]. This chip is a candidate for being simple, low-cost, and easy to use, while offering accessible (open-structured) microfluidic channels for cell pickup. As shown in Figure 1, we fabricated the micropillars with a one-step photolithography process. First, SU-8 100 was poured on a fused silica wafer with a thickness of 500 μm and spun at 1500 rpm for 30 seconds. Next, the wafer was baked for 25 minutes at 65°C and for 70 minutes at 95°C. Then we exposed the baked wafer to UV light for

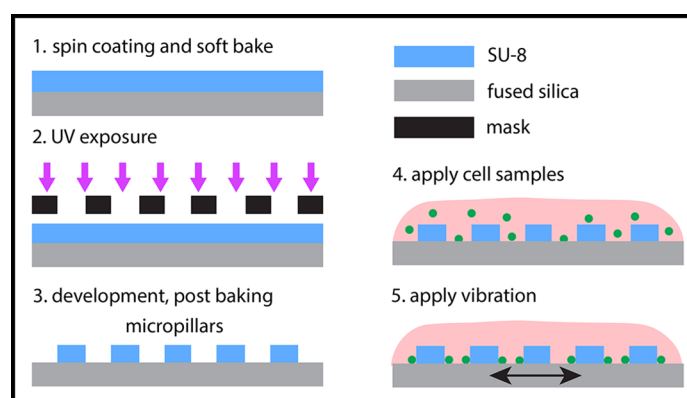


Figure 1: Schematic of fabrication process and experiment procedure.

one minute with an ABM contact aligner, followed by post-exposure baking at 95°C for 20 minutes. Finally, we submerged the wafer in SU-8 developer for 17 minutes before hard baking. The pillars' thickness was 200 μm , as measured by P7 Profilometer. Subsequently, the chips were separated using Dicing Saw DISCO, and a photograph of one of the chips is shown in Figure 2a. We fixed the chip on the XY piezoelectric stage. We generated the circular vibration with two sinusoidal wave signals with 90° offset in phase to the piezo driver via the waveform generator. The applied frequency and voltage were 200 Hz and 1 V, respectively. A culture medium containing mouse oocytes was directly dropped onto the chip (Figure 2b).

Figure 2c shows the concept of transporting and trapping cells into the center of the chip. By applying a circular vibration, a whirling flow is induced around each pillar, and since the pillars' pitch is designed to interfere with each other, a whirling flow is induced through the micropillar array. Since this system has enough power to generate fluid force to manipulate large cells, we can move the cells to any desired destination by adjusting the micropillar array and the distance between each pillar. For example, we fabricated the arrays in a spiral pattern to gather the mouse oocyte cells to the center of the chip. As a result, this technique can be utilized for flow control and cell transportation on an open-surface chip for any type of cell.

Conclusion:

We experimentally investigated the effect of VIF on mouse oocyte transportation and manipulation. Cells can be extracted easily since the chip has easy access to an external environment. Therefore, an operator can detect the cells with their eyes, collecting them with microinjectors, and there is no worry of losing the cells on the chip.

References:

- [1] Reyes, D. R., Iossifidis, D., Auroux, P.-A. & Manz, A. Micro total analysis systems. 1. Introduction, theory, and technology. *Anal. Chem.* 74, 2623-2636 (2002).
- [2] Hayakawa, T., Sakuma, S. & Arai, F. On-chip 3D rotation of oocyte based on a vibration-induced local whirling flow. *Microsystems & Nanoengineering* 1, 1-9 (2015).

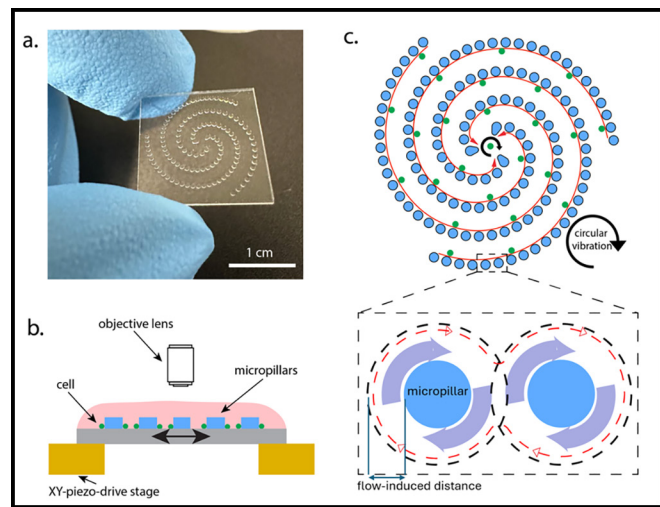


Figure 2: a. Photograph of the fabricated chip. b. Schematic of experimental setup. c. Concept of cell transportation using vibration-induced flow.

Fabrication of Microchip Devices for Organ-on-a-Chip and Lab-on-a-Chip Applications

CNF Project Number: 2857-19

Principal Investigator(s): Esak (Isaac) Lee, Ph.D.

User(s): Renhao Lu, Yansong Peng, Shufan Yin

Affiliation(s): Meinig School of Biomedical Engineering, Cornell University

Primary Source(s) of Research Funding: National Institutes of Health (NIH) R01 HL165135 and R01 CA279560

Contact: el767@cornell.edu, rl839@cornell.edu, yp255@cornell.edu, sy766@cornell.edu

Research Group Website: <https://leelab.bme.cornell.edu/>

Primary CNF Tools Used: Heidelberg Mask Writer DWL2000, ABM Contact Aligner, MVD100

Abstract:

Organ-on-a-chip is a microfluidic cell culture platform, integrated circuit (chip) that simulates the activities, mechanics, and physiological response of an entire organ or an organ system. Our lab aims to create organ-on-a-chip devices to study the mechanism of various diseases. In the past year, we mainly focused on two projects: (1) A 3D biomimetic model of lymphatics reveals cell–cell junction tightening and lymphedema via a cytokine-induced ROCK2/JAM-A complex; (2) Piezo1 regulates meningeal lymphatic vessel drainage and alleviates excessive CSF accumulation.

Summary of Research:

Project 1: A 3D biomimetic model of lymphatics reveals cell–cell junction tightening and lymphedema via a cytokine-induced ROCK2/JAM-A complex [1].

Impaired lymphatic drainage and lymphedema are major morbidities whose mechanisms have remained obscure. To study lymphatic drainage and its impairment, we engineered a microfluidic culture model of lymphatic vessels draining interstitial fluid. This lymphatic drainage-on-chip revealed that inflammatory cytokines that are known to disrupt blood vessel junctions instead tightened lymphatic cell–cell junctions and impeded lymphatic drainage. This opposing response was further demonstrated when inhibition of rho-associated protein kinase (ROCK) was found to normalize fluid drainage under cytokine challenge by simultaneously loosening lymphatic junctions and tightening blood vessel junctions. Studies also revealed a previously undescribed shift in ROCK isoforms in lymphatic endothelial cells, wherein a ROCK2/junctional adhesion molecule-A (JAM-A) complex emerges that is responsible for the cytokine-induced lymphatic junction zippering. To validate these in vitro findings, we further demonstrated in a genetic

mouse model that lymphatic-specific knockout of ROCK2 reversed lymphedema in vivo. These studies provide a unique platform to generate interstitial fluid pressure and measure the drainage of interstitial fluid into lymphatics and reveal a previously unappreciated ROCK2-mediated mechanism in regulating lymphatic drainage.

Project 2: Piezo1 regulates meningeal lymphatic vessel drainage and alleviates excessive CSF accumulation [2]

Piezo1 regulates multiple aspects of the vascular system by converting mechanical signals generated by fluid flow into biological processes. In this project, we utilize the lymphatic-on-chip devices to study the role of Piezo1 in lymphatics and its drainage functions. Together with our collaborators, we find that Piezo1 is necessary for the proper development and function of meningeal lymphatic vessels and that activating Piezo1 through transgenic overexpression or treatment with the chemical agonist Yoda1 is sufficient to increase cerebrospinal fluid (CSF) outflow by improving lymphatic absorption and transport. The abnormal accumulation of CSF, which often leads to hydrocephalus and ventriculomegaly, currently lacks effective treatments. We discovered that meningeal lymphatics in mouse models of Down syndrome were incompletely developed and abnormally formed. Selective overexpression of Piezo1 in lymphatics or systemic administration of Yoda1 in mice with hydrocephalus or Down syndrome resulted in a notable decrease in pathological CSF accumulation, ventricular enlargement and other associated disease symptoms. Together, our study highlights the importance of Piezo1-mediated lymphatic mechanotransduction in maintaining brain fluid drainage and identifies Piezo1 as a promising therapeutic target for treating excessive CSF accumulation and ventricular enlargement.

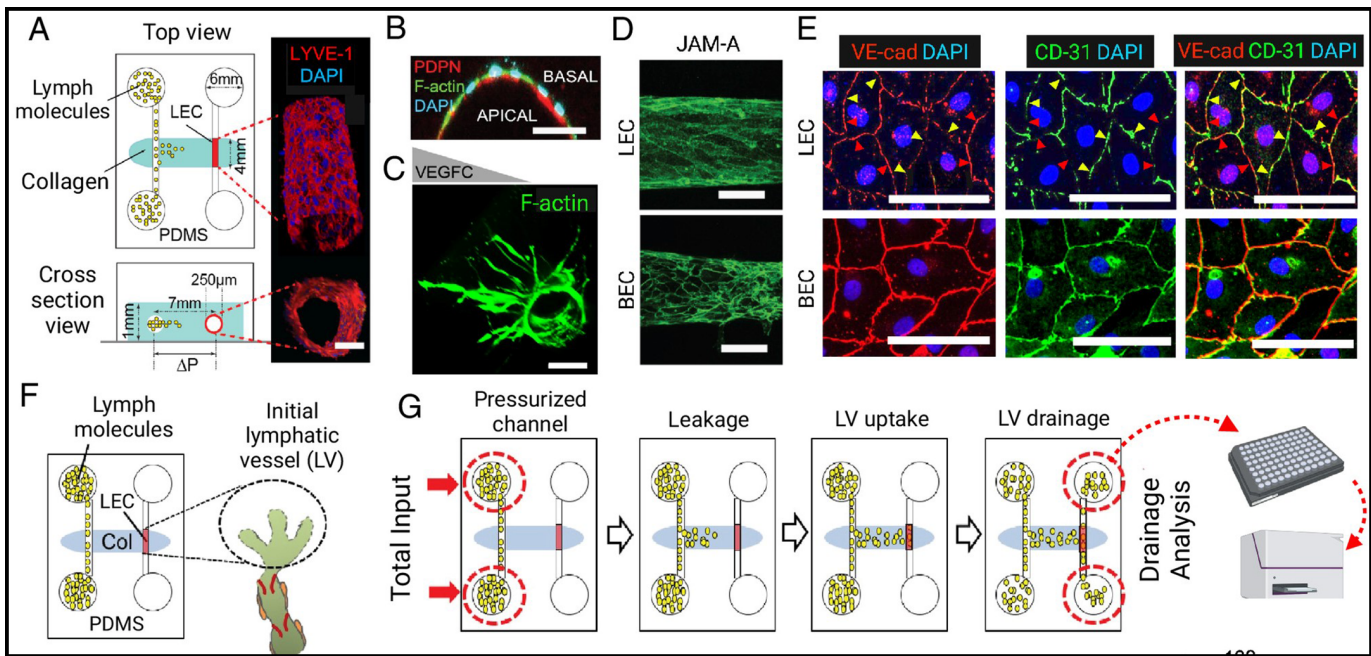


Figure 1, above: Lymphatic drainage-on-chip recapitulates lymphatic structure, drainage, and dysfunction. (A) A schematic of the lymphatic drainage-on-chip platform. (B) Apical podoplanin (PDPN) expression on the luminal side of the vessel. (C) Lymphatic sprouting in response to VEGFC stimulation. (D) Immunostaining of LEC-generated lymphatic vessels and BEC-generated blood vessels with a tight junction marker, JAM-A. (E) Immunostaining of lymphatic vessels and blood vessels with an adherens junction marker, VE-cadherin (VE-cad), and CD31. Red and yellow arrows indicate exclusive expression of VE-cad and CD31, respectively, showing interdigitated, discontinuous expression of VE-cad in LECs. (F) A schematic of a biomimetic lymphatic drainage-on-chip model system. The engineered lymphatic vessel (LV) in the right-side channel functions as an initial LV to drain interstitial lymph fluid that is introduced through the left-side channel. (G) Transport of lymph fluid. The left-side channel pressured with lymph fluid induces fluid transport. The pressure gradient between two channels results in fluid convection from the left channel to the engineered LV. The lymph fluid is drained by the engineered LV and accumulated in two right-side reservoirs. Total drained fluid is analyzed to obtain the number of drained lymph molecules.

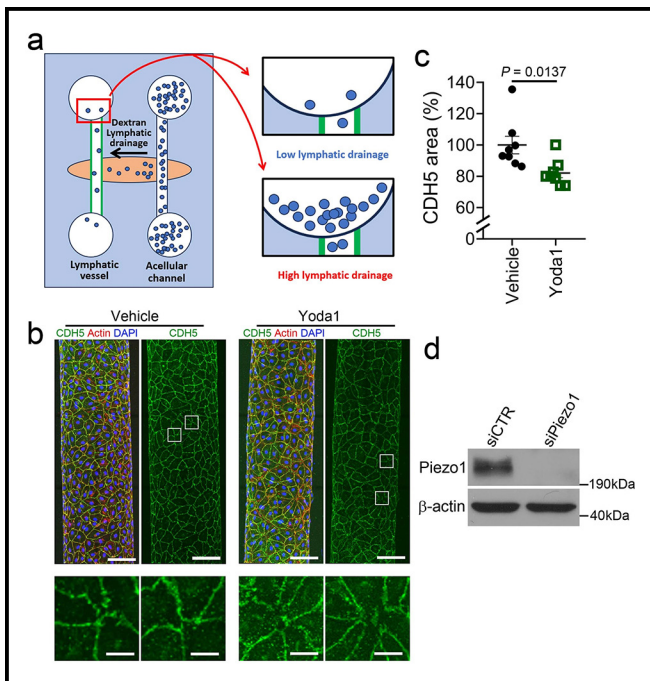


Figure 2, left: (a) Schematic illustration of the 3-D lymphatic vessel model used for this study. The outcome of the Yoda1-induced drainage increase is presented in Fig. 4c. (b) Fluorescence confocal images of the engineered lymphatic vessels stained for F-actin and CDH5. Enlarged CDH5 images (boxed) show more discontinuous junctions in the Yoda1-treated group than in the vehicle group. Scale bars: 100 μ m (10 μ m, enlarged images). Acellular channels are not shown. (c) The relative area of CDH5-stained cellular junctions ($n=8$ independent experiments). Statistics: two-tailed *t*-test. (d) Western blot assays verifying the efficient knock-down of Piezo1 in LECs prepared for the drainage measurement shown in Figure 4c ($n=4$ independent samples). Data are presented as mean values \pm SEM.

References:

- [1] Lee E, et al. A 3D biomimetic model of lymphatics reveals cell-cell junction tightening and lymphedema via a cytokine-induced ROCK2/JAM-A complex. *Proc Natl Acad Sci U S A*. 2023 Oct 10;120(41):e2308941120. doi: 10.1073/pnas.2308941120. Epub 2023 Oct 2. PMID: 37782785; PMCID: PMC10576061.
- [2] Choi D, et al. Piezo1 regulates meningeal lymphatic vessel drainage and alleviates excessive CSF accumulation. *Nat Neurosci*. 2024 May;27(5):913-926. doi: 10.1038/s41593-024-01604-8. Epub 2024 Mar 25. PMID: 38528202; PMCID: PMC11088999.

Investigating the Effect of the Tumor Microenvironment on Metastatic Progression Using Micro and Nano-Scale Tools

CNF Project Number: 2912-20

CNF Principal Investigator(s): Claudia Fischbach¹

User(s): Nicole Sempertegui¹, Garrett Beeghly¹, Jack Crowley²

Affiliation(s): 1. Biomedical Engineering, 2. Applied and Engineering Physics; Cornell University

Primary Source(s) of Research Funding: Breast Cancer Coalition of Rochester Trainee Grant,

Center on the Physics of Cancer Metabolism Award Number 1U54CA210184-01, National Cancer Institute

Contact: cf99@cornell.edu, nds68@cornell.edu

Primary CNF Tools Used: ABM Contact Aligner, Heidelberg DWL2000, Hamatech 9000, Malvern NS300 NanoSight

Abstract:

Breast cancer is the second leading cause of cancer-related death for women in the United States [1]. Breast cancer mortality is driven by metastasis, where cancer cells disseminate from the primary tumor to seed distant tissues such as the bone. During bone metastatic disease, cancer cells interact with their microenvironment consisting of a mineralized, collagen-rich extracellular matrix and other cell types including mesenchymal stem cells (MSCs), macrophages, and osteoclasts. These cells are known to participate in reciprocal signaling with cancer cells to influence tumorigenesis through the exchange of soluble factors [2,3] and extracellular vesicles (EV). However, the mechanisms by which soluble factor and EV signaling influence tumor cell invasion and the development of a pro-tumorigenic microenvironment remain unclear due to the lack of models that enable systematic study. To this end, CNF tools were used to investigate various stages in metastasis: EV-mediated formation of a pre-metastatic niche in bone and tumor cell invasion into bone. For pre-metastatic niche development studies, we leveraged EVs derived from breast cancer cells and bone-mimetic engineered substrates to investigate how EV binding to bone is regulated by components of their glycocalyx (sugar-coating on the outside of EVs) and matrix mineral content. For invasion studies into the bone, we developed a microfluidic model of the bone microenvironment with mineralized collagen microchannels and have shown that tumor cell invasion is inhibited when co-cultured with macrophages and osteoclasts seeded in a mineralized microchannel.

Summary of Research:

Isolation of Breast Cancer-Derived Extracellular Vesicles and Interactions with Bone Matrix. Prior to arriving at distant metastatic sites, tumor cells can release soluble factors and extracellular vesicles (EVs)

into circulation to prime the microenvironment of distant target organs for subsequent development of organotropic metastasis. EVs are gaining appreciation as stable vehicles of cell-derived cargo contributing to tumorigenesis and pre-metastatic niche (PMN) formation. In collaboration with Matt Paszek's Lab, we have successfully isolated and characterized EVs from murine 4T1s breast cancer cells using the Malvern NS300 NanoSight. Currently, we are investigating differences in 4T1 EV binding to bone-mimetic engineered substrates. These bone-mimetic models were developed at the CNF using SU-8 photolithography to create a micropatterned silicon wafer used to fabricate PDMS "microwells". These PDMS microwells are filled with a collagen type I matrix and subsequently mineralized using the polymer-induced liquid precursor (PILP) method to mimic bone extracellular matrix, as previously described [5]. Through this engineered system, we can systematically explore differences in EVs binding in the presence or absence of mineral in bone. Furthermore, we are examining how EV characteristics, such as glycocalyx composition, will affect binding to bone and whether this is dependent on matrix mineral content. Our preliminary data suggest that EV binding is increased in mineralized collagen substrates, and that removal of mucins from the glycocalyx reduces their ability to bind (Figure 1). Future work will incorporate MSCs in addition to EVs to probe the interplay between bone-resident cells, bone matrix and EVs. Overall, these studies will help unravel the mechanisms by which EVs and key components of the bone microenvironment regulate the onset of bone metastasis.

Effects of Mineralized Collagen on Breast Cancer Cell Invasion Using a Microfluidic Model of the Bone. During bone metastasis, tumor cell invasion and subsequent seeding of osteogenic niches [4] can be influenced by macrophages. Macrophages not only exert immunomodulatory effects, but also have the

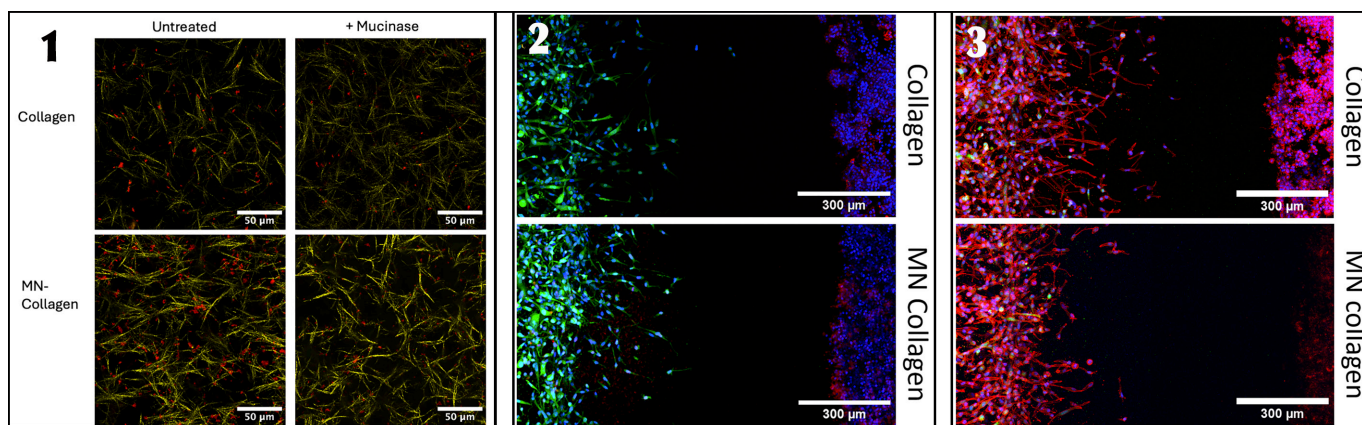


Figure 1, left: Confocal microscopy projection of 4T1 extracellular vesicles (EVs) stained with DiI lipophilic dye (red) in mineralized-collagen or collagen control microwells. Confocal reflectance was used to visualize collagen fibers (yellow). Scale bar: 50 μm .

Figure 2, middle: Fluorescent microscopy of non-mineralized collagen device (top) and mineralized (MN) collagen device (bottom) seeded with MDA-MB-231 breast cancer cells (green) and RAW264.7 macrophages (red). DAPI was used to stain nuclei (blue) Scale bar: 300 μm .

Figure 3, right: Fluorescent microscopy of non-mineralized collagen device (top) and mineralized (MN) collagen device (bottom) seeded with MDA-MB-231 breast cancer cells (green) and RAW264.7 osteoclasts. F-actin and nuclei are shown in red and blue, respectively. Scale bar: 300 μm .

potential to differentiate into osteoclasts, the primary cell type driving osteolysis in bone metastasis patients. Using SU-8 photolithography in conjunction with the ABM Contact Aligner and a photomask generated by the Heidelberg DWL2000, we have created a dual channel microfluidic devices that enables co-culture breast cancer cells and macrophages encapsulated in a 3D collagen matrix. To model these interactions within a bone-like microenvironment, the microfluidic device was modified using the PILP method to include selective and controlled collagen mineralization of the device microchannels [5]. We have shown that macrophages promote the invasion of breast cancer cells regardless of collagen mineralization and that this effect occurs without cell-cell contact, suggesting that it was caused by soluble factors secreted from macrophages. However, it was determined that collagen mineralization inhibits the ability of macrophages to promote tumor cell invasion compared to non-mineralized collagen co-culture conditions (Figure 2). Similarly, when macrophages were differentiated into osteoclasts within a mineralized collagen channel, tumor cell invasion was also inhibited compared to non-mineralized collagen devices (Figure 3). Future work includes device materials characterization and validating our findings by incorporating syngeneic breast cancer cells with primary macrophages and osteoclasts.

Funding Acknowledgements:

Breast Cancer Coalition of Rochester Trainee Grant (Nicole). The work described was supported by the Center on the Physics of Cancer Metabolism through Award Number 1U54CA210184-01 from the National Cancer Institute. The content is solely the responsibility of the authors and does not necessarily represent the official views of the National Cancer Institute or the National Institutes of Health.

References:

- [1] Siegel, R. L., et al. Cancer Statistics, 2021. CA. Cancer J. Clin. 71, 7-33 (2021).
- [2] Tan, M. L., et. al. Engineering strategies to capture the biological and biophysical tumor microenvironment in vitro. Adv. Drug Deliv. Rev. 176, 113852 (2021).
- [3] Zheng, P., and Li, W. Crosstalk Between Mesenchymal Stromal Cells and Tumor Associated Macrophages in Gastric Cancer. Front. Oncol. 10, 1-9 (2020).
- [4] Peinado, H., et al. Pre-metastatic niches: organ-specific homes for metastases. Nat. Rev. Cancer 17, 302-317 (2017).
- [5] Choi, S., et al. Intrafibrillar, bone-mimetic collagen mineralization regulates breast cancer cell adhesion and migration. Biomaterials. 198, 95-106 (2019).

Increasing Microfabrication Yield of Template-Based Carbon Nanotube Arrays for Gene Transfer

CNF Project Number: 3106-23

Principal Investigator(s): Michael Schrlau

User(s): Mujtaba Y.K. Siddiqui

Affiliation(s): Department of Mechanical Engineering, Kate Gleason College of Engineering; Rochester Institute of Technology

Primary Source(s) of Research Funding: New York State Fuzehub

Contact: mgseme@rit.edu, mys8553@rit.edu

Research Group Website: <https://people.rit.edu/mgseme/Site/Home.html>

Primary CNF Tools Used: AJA Ion Mill, PT 740 RIE, KLA P7 Profilometer, GCA AS200 i-line Stepper, OXFORD 81 RIE

Abstract:

Carbon nanotube (CNT) arrays template-based fabricated biomedical devices used for gene transfer, they can be used to transport novel gene therapies into cells which help combat illnesses such as HIV and some types of cancers. These devices are a more economical and efficient alternative for delivery of gene therapies as compared to conventional methods [1]. The Cornell NanoScale Facility (CNF) offers tools used to fabricate these devices, research conducted there has increased production yield and reduced production time.

Summary of Research:

CNT arrays produced using template-based fabrication have been shown in previous studies to possess the capability of supporting gene transfer. They have been reported to achieve 85% of plasmid DNA transfer into cells and show a three times higher efficiency for transfection in stem cells than standard lipofection methods [2]. Carbon nanotubes are produced on Anodic Aluminum Oxide (AAO) templates using a multistep fabrication process which involves cleanroom fabrication.

Etching tools at the CNF were utilized to create free standing tubes, Figure 1 shows Scanning Electron Micrograph (SEM) image of a CNT array device produced at CNF. The micrograph shows carbon tubes protruding from the surface of AAO, these tubes stand approximately 200 nm off the surface of the AAO substrate.

Commercially available AAO templates consist of self-aligned pores covered by an interconnected later of AAO creating a 'lattice'-like web of material that inhibits biomolecule transfer by creating a bottleneck —

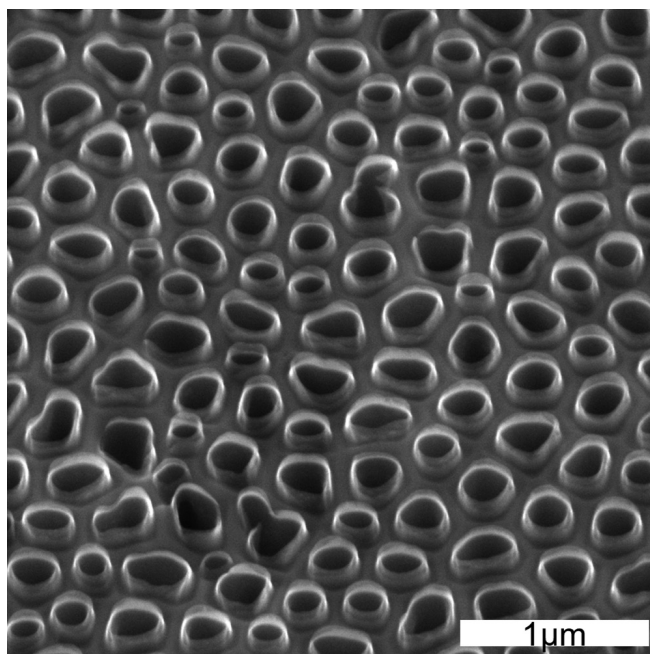


Figure 1: SEM of fabricated CNT.

this is referred as a lattice layer; during the fabrication of CNT arrays this layer needs to be removed, due to the size constraints and limitations of mechanical methods ion milling using the AJA ion mill at CNF was utilized to remove the top 1 μm of the AAO, exposing the pores.

Figure 2 shows a schematic visualizing from a side view the effects of ion milling on the AAO template, we noticed etch depth correlates to visible hydraulic pore diameter. The figure shows the AAO being etched away over time removing the lattice layer at the top to reveal the wider pores underneath. Ion mill time was

optimized 1hr after it was noted that the pore diameter at both times were reported to be statistically similar. This was reconfirmed by various repeats before being implemented into the standard procedure used to fabricate CNT arrays.

The devices are 13 mm disks with a thickness of 60 μm , these pieces are too small to fit into the CNF tools which are built to work with 4" and 6" wafers. A carrier wafer was designed and produced to hold multiple CNT arrays to increase production yield up to 60 devices at a time. Figure 3 shows a carrier wafer with CNT arrays placed into the square holders, the carrier consists of two silicon wafers patterned and etched to fit atop each other with windows exposing the CNT arrays placed between them, the carrier shown in Figure 3 is the bottom and will be covered by a top wafer to secure the wafers in place preventing any slippage into the cleanroom tools.

Conclusions and Future Steps:

Optimizing ion mill parameters and developing a carrier wafer to hold pieces led to an increase in production yield. Further studies are to be conducted to optimize other clean room processes that are utilized in the fabrication of these devices.

References:

- [1] Siddiqui, Mujtaba Yar Khan, "Application of ICP RIE Techniques to Produce CNT Arrays" (2023). Thesis. Rochester Institute of Technology. Accessed from: <https://repository.rit.edu/theses/11656>.
- [2] Golshadi, Masoud, "Carbon Nanotube Arrays for Intracellular Delivery and Biological Applications" (2016). Thesis. Rochester Institute of Technology. Accessed from: <https://repository.rit.edu/cgi/viewcontent.cgi?article=10360&context=theses>.

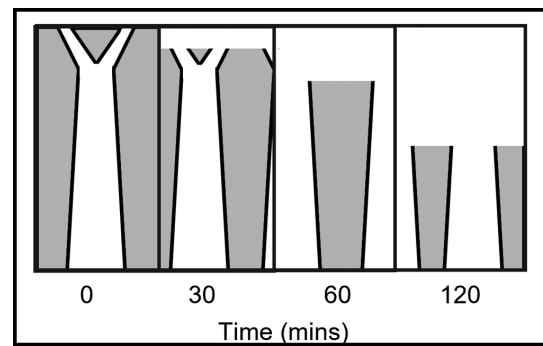


Figure 2: Schematic depicting effect of ion mill time on lattice layer evolution.

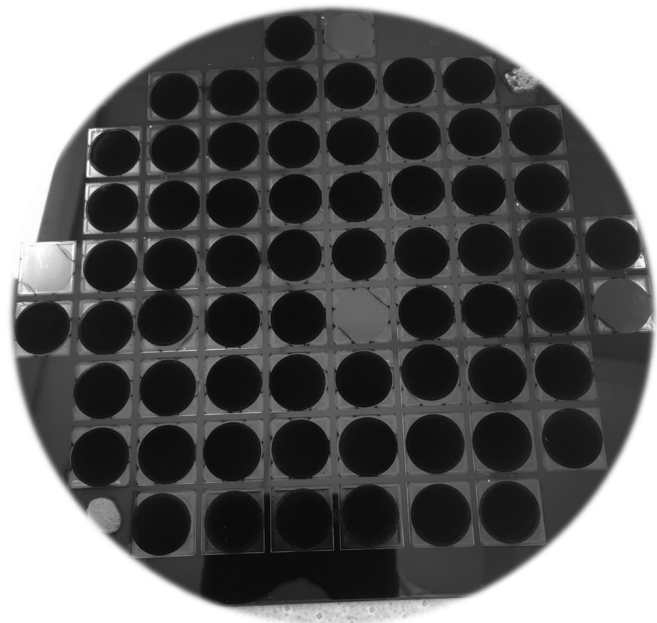


Figure 3: Silicon carrier wafer to hold CNT arrays during cleanroom fabrication.

High-Density, Integrated, Multi-Functional Neural Probe for Small Animals

CNF Project Number: 3135-23

Principal Investigator(s): Azahara Oliva Gonzalez, Antonio Fernandez-Ruiz

User(s): Lindsay Karaba, Jaehyo Park, Zifang Zhao

Affiliation(s): Neurobiology and Behavior, Cornell University

Primary Source(s) of Research Funding: DP2MH136496(NIH), R00MH120343(NIH), R00MH122582(NIH)

Contact: aog35@cornell.edu, afr77@cornell.edu, lak256@cornell.edu, jp2597@cornell.edu, zz833@cornell.edu

Research Group Website: braincomputation.org

Primary CNF Tools Used: Parylene Coater, SUSS MA6|BA6 Aligner, Nanoscribe GT2 Two-Photon Lithography System, Heidelberg DWL2000, CHA Mark 50 E-beam Evaporator

Abstract:

Micro-fabricated neural probes serve as an important tool for probing neural activities. There is an increasing need for developing high-density, multi-functional devices for monitoring electrical and electrochemical signals with minimal invasiveness and long-operation time in physiological environments. We have designed and fabricated high-density neural interfaces on conformable parylene-C substrates. Our probe has a cross-section of $3 \times 126 \mu\text{m}^2$, ensuring low damage to brain tissues. To achieve wireless neural activity recording in rodents during unrestrained behavior, we designed a light-weight wireless high-channel count headstage and performed parylene coating to ensure all-weather operations. We used a low-temperature solder bonding process to achieve high-density soft-hard circuit bonding, which enables connector-free, direct integration of the probe to a circuit board that allows a total system weight < 4 grams. With this system, we successfully recorded high-quality data from a freely moving animal in a naturalistic environment.

Summary of Research:

Recent advances in neural interfaces enabled recording of high-resolution neural activities up to a few thousand channels [1]. However, most high-density neural interfaces are built with rigid, silicon-based substrates [2].

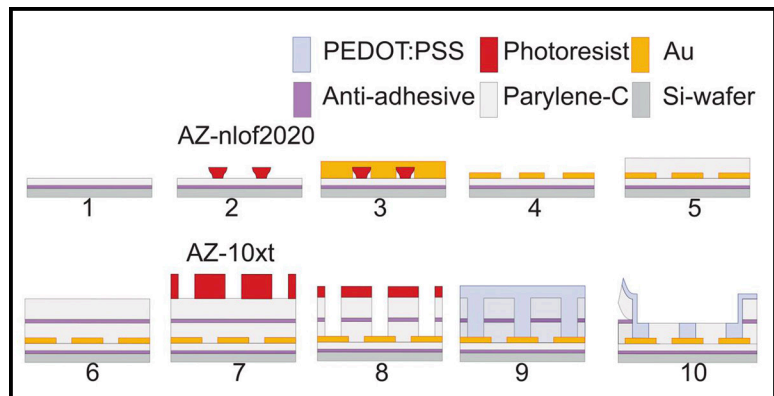


Figure 1: Microelectrode fabrication processes.

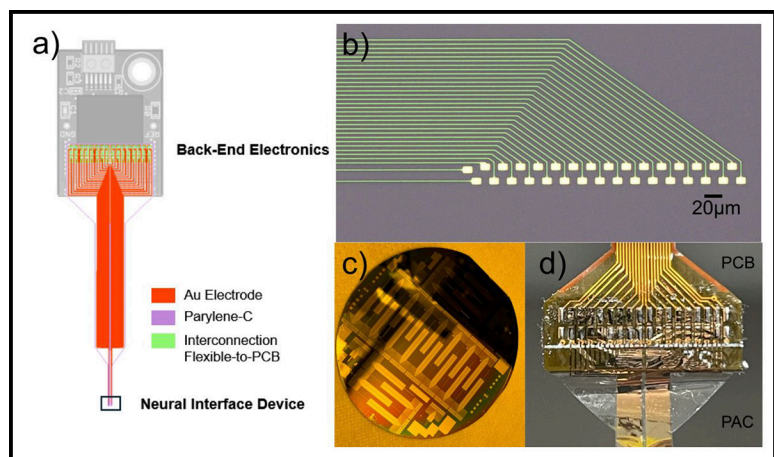


Figure 2: Light-weight, high-density neural probe. a) Illustration of wireless, light-weight neural monitor system. b) High-density, microelectrode on parylene substrate. c) 27 electrodes fabricated in a 4-inch wafer. d) soft-rigid electronic bonding with low-temperature solder.

This leads to physical damage to brain tissue during implantation and micro-electrode movement, and eventually degraded the signal quality. In order to solve this, we are building implantable microelectrodes with conformable, organic materials. We fabricated high-density conformable neural probe with parylene-C with similar process as previously reported [3] (Figure 1). In short, we used metal lift-off process to pattern a 150 nm Au layer on parylene-C substrate, then used dry etching process to pattern the opening in parylene-C passivation layer. We designed high-density neural probe with stackable design with 32ch in each probe unit to be directly bonded with back-end electronics (Figure 2a). Using CNF, we have optimized the lift-off process to reduced interconnect line width to 3 μm (Figure 2b). To achieve effective electrical bonding between parylene-C based neuro probe to a printed circuit board, we used a low-temperature solder bonding processing with a low melting point solder paste (137°C). We achieved reliable bonding without damaging parylene substrate (Figure 2c). Direct bonding of microelectrode and back-end circuit removed the need for complicated bonding process or bulky connectors and lead to a reduced form factor and system weight. We achieved 1.86 grams total system weight, with additional 2 grams for the lithium battery. This system could wirelessly record neural activity with a configurable channel number ranging from 64 channels to 256 channels. We used parylene-C for coating the back-end device for weather-proof coating. This allows us to record in freely moving rodents in outdoor, naturalistic environment in Liddell field campus. With this system, we have recorded high-quality electrophysiology signal in both rat and mouse hippocampus, to study the learning and memory function of related neural networks.

Conclusion and Future Steps:

We have fabricated conformable, high-density micro-electrodes with CNF tools and they have advanced our capability of study animal neural activity in traditionally challenging, unconventional environments. In the future, there are many possible directions we could work on to extend this work.

1) Multi-modal sensing: Currently, we are only using passive electrode to record electrical activity produced by neurons. Neural networks also rely on chemical signaling system, such as neurotransmitters. We are looking into how to effectively use different materials to electrically interact with neurotransmitters to actively sense the concentration of neurotransmitters, with multi-channel electrodes.

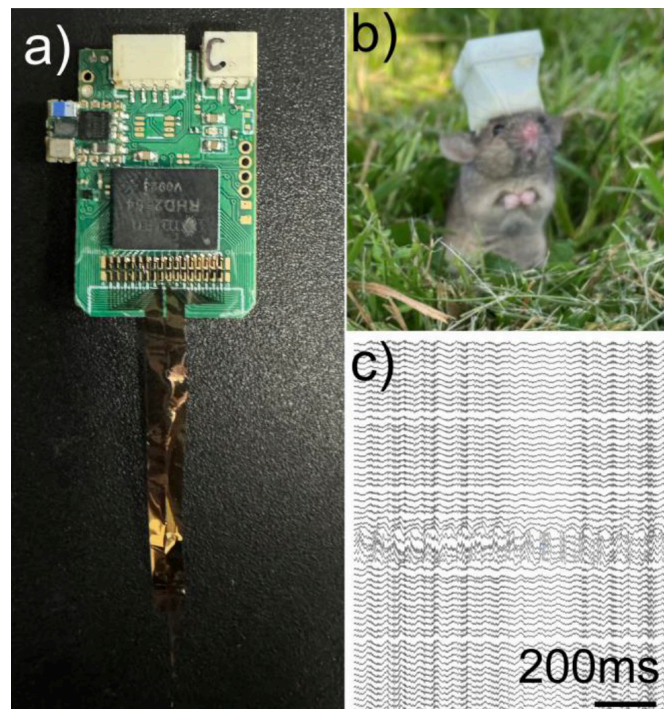


Figure 3: Wireless electrophysiology system for study unbounded animal behavior. a) Assembled wireless device with microelectrodes. b) A mouse with 3D printed carrier for wireless headstage. c) Recorded high quality electrophysiology during animal locomotion.

2) Neuro-modulations: Neuroscience also require tools to perturb neural circuits to investigate its functions. Importantly, optogenetics can modulate a subgroup neuron's function through opto-stimulation. We are currently exploring the possibility to build thin-membrane microelectrode on top of a thin wave-guide with the NanoScribe.

References:

- [1] Jun, J. J., et al. Fully integrated silicon probes for high-density recording of neural activity. *Nat.* 2017 5517679 551, 232-236 (2017).
- [2] Chen, R., Canales, A., and Anikeeva, P. Neural recording and modulation technologies. *Nat. Rev. Mater.* 2017 22 2, 1-16 (2017).
- [3] Zhao, Z., Cea, C., Gelinis, J. N., and Khodagholy, D. Responsive manipulation of neural circuit pathology by fully implantable, front-end multiplexed embedded neuroelectronics. *Proc. Natl. Acad. Sci. U. S. A.* 118, e2022659118 (2021).

Sequence-Defined Peptoids as Next-Generation EUV Photoresists

CNF Project Number: 2733-18

Principal Investigator(s): Christopher K. Ober

User(s): Chenyun Yuan, Rika Marui, Erina Yoshida

Affiliation(s): Materials Science and Engineering, Cornell University

Primary Source(s) of Research Funding: U.S. Department of Energy, Office of Science, Basic Energy Sciences

Contact: cko3@cornell.edu, cy479@cornell.edu

Research Group Website: <https://ober.mse.cornell.edu>

Primary CNF Tools Used: JEOL JBX-6300FS E-beam Lithography System, JEOL JBX-9500FS E-beam Lithography System, ASML DUV Stepper

Abstract:

Photoresists face substantial challenges as photolithography advances into the extreme ultraviolet (EUV) era. Traditional polymeric photoresists struggle with chemical randomness due to variations in polymer chains' molecular weight, composition, and sequence, as well as the unpredictable distribution and potential aggregation of photoacid generators (PAGs) within the polymer matrix. Additionally, the use of PAGs has sparked growing environmental concerns worldwide, especially since most commercially used PAGs are per- and polyfluorinated substances (PFAS). We have engineered sequence-defined polypeptoids to function as photoresists, addressing many existing limitations.

We developed a resist system that is a single-component monomolecular system composed solely of polypeptoids. The polypeptoids were synthesized by the solid-phase submonomer synthesis method [1]. The sequence typically includes phenol derivatives that induce solubility changes upon exposure to ionizing radiations including electronic beam (e-beam) or extreme UV (EUV), along with inactive building blocks, all precisely controlled at the molecular level. This design ensures uniform length, composition, and sequence, greatly minimizing compositional stochasticity. The developed photoresist platform, incorporating phenol derivatives, is inherently patternable under EUV or e-beam lithography, removing the need for PAGs or other additives in the resist formulation. This innovation addresses problems related to uneven PAG distribution and tackles environmental, health, and regulatory concerns associated with PAGs in photoresist formulations. EUV patterning experiments demonstrated that the photoresist could achieve patterning at a 14 nm half-pitch or smaller resolution using an aqueous tetramethylammonium hydroxide solution as the developer.

Summary of Research:

We have developed a novel sequence-defined polypeptoid photoresist to address challenges in EUV lithography. Traditional polymeric photoresists struggle with compositional stochasticity originated from the random nature of conventional polymers in terms of molecular weight, composition and sequence, and there are also environmental concerns due to the use of PAGs with are mostly fluorinated compounds [2]. The new polypeptoid photoresist system, synthesized via solid-phase submonomer synthesis, features precisely positioned functional groups and exhibits uniform chain length, composition, and sequence. This can be proven by liquid chromatography–mass spectrometry (LC-MS) measurements (Figure 1). The wide variety of building blocks we can choose also allows us to explore new patterning mechanisms that have not been applied in advanced EUV photoresist design. This system mitigates stochastic effects and allows for intrinsic patternability under EUV radiation, eliminating the need for PAGs and thereby addressing related environmental concerns.

Our research involves extensive screening of peptoid sequences with various building blocks, such as tBOC-protected phenols, t-butyl esters, and unprotected phenols. Initial testing revealed that certain peptoid sequences demonstrated a negative tone pattern when developed in highly dilute aqueous base solutions, despite being designed to mimic the composition of conventional chemically amplified photoresists. This negative tone was first observed in peptoid sequences during development in a diluted tetramethylammonium hydroxide (TMAH) solution, and further confirmed using atomic force microscopy (AFM) and scanning electron microscopy (SEM).

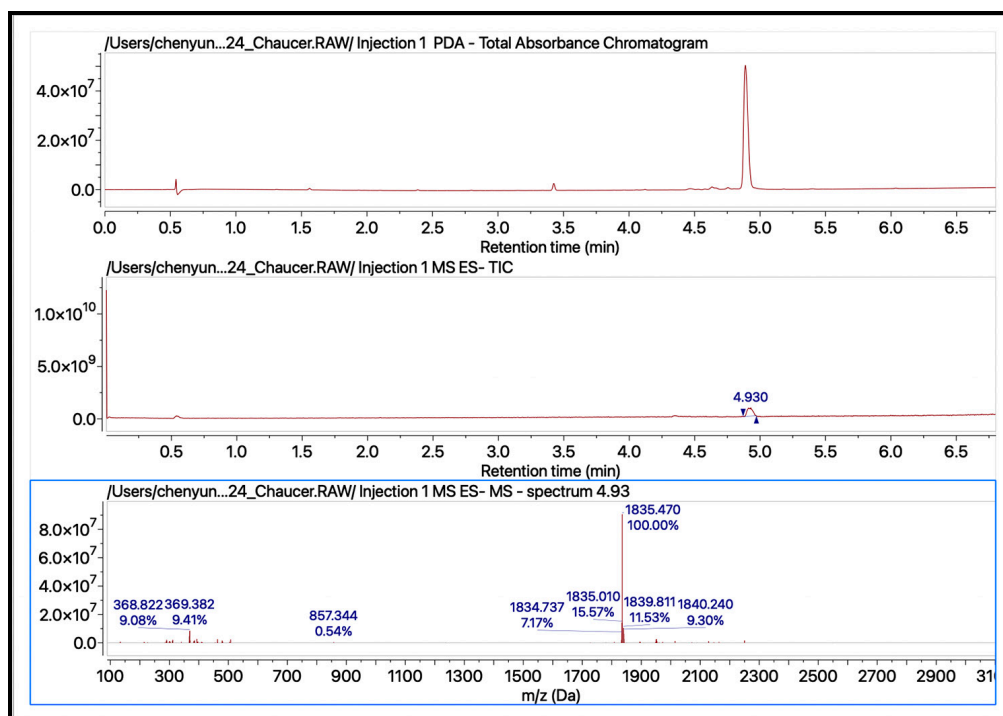


Figure 1: LC-MS data of one example polypeptoid sequence with theoretical molar mass 1836.96 g/mol.

Experiments indicated that these peptoids could be patterned in a negative tone under e-beam and EUV lithography, both with and without the presence of PAGs. However, the resolution improved significantly without PAGs, achieving a resolution of 24-nm half-pitch (hp) under e-beam lithography (Figure 2). Further testing at Lawrence Berkeley National Laboratory (LBNL) demonstrated that the peptoid sequences achieved a 14-nm hp resolution under EUV exposure without PAGs (Figure 3).

Our current efforts focus on understanding the underlying mechanisms and high-throughput synthesis of diverse peptoid sequences. The research confirmed that the negative tone mechanism is due to phenol groups in the structure, with chemistry occurring during exposure and potentially obviating the need for post-exposure baking (PEB). This phenol-based patterning mechanism has not been used in photoresist design previously, marking a significant advancement in photoresist technology.

References:

- [1] R. N. Zuckermann, J. M. Kerr, S. B. H. Kent, and W. H. Moos, "Efficient method for the preparation of peptoids [oligo(N-substituted glycines)] by submonomer solid-phase synthesis," *J. Am. Chem. Soc.*, vol. 114, no. 26, pp. 10646-10647, 1992, doi: 10.1021/ja00052a076.
- [2] C. K. Ober, F. Käfer, and C. Yuan, "Recent developments in photoresists for extreme-ultraviolet lithography," *Polymer*, vol. 280, 2023, doi: 10.1016/j.polymer.2023.126020.

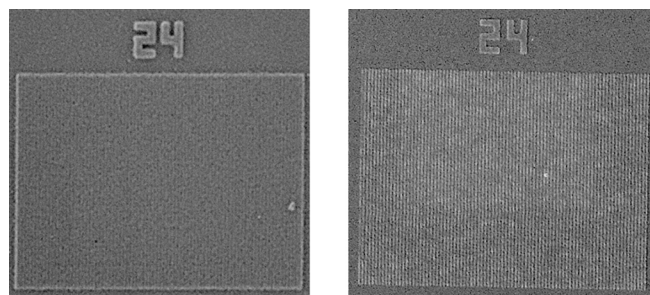


Figure 2: 24-nm half-pitch e-beam patterns of the polypeptoid resist. Left: with 10 wt% PAG. Right: without PAG. The no PAG sample required ~ 3 times dosage than the PAG containing sample.

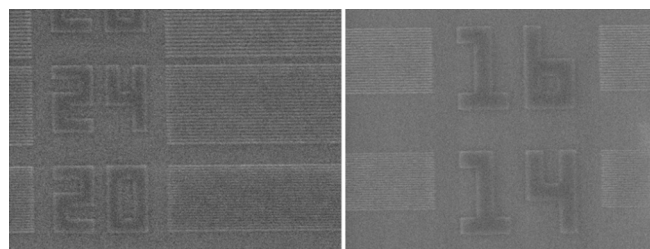


Figure 3: EUV patterns generated from the polypeptoid resist. Left: with 10 wt% PAG, 27 mJ/cm². Right: without PAG, 45 mJ/cm².

Direct Functionalization of Polyethylene Surfaces with High Density Polymer Brushes

CNF Project Number: 3040-22

Principal Investigator(s): Brett Fors

User(s): Anna Ringuette

Affiliation(s): Chemistry and Chemical Biology, Cornell

Primary Source(s) of Research Funding: This work was supported by the NSF under Award CHE-1752140

Contact: bpf46@cornell.edu, aer286@cornell.edu

Research Group Website: <https://fors.chem.cornell.edu/>

Primary CNF Tools Used: Ramé-Hart Goniometer

Abstract:

Introducing functionality into PE surfaces is a longstanding challenge in polymer science, driven by the need for polymer materials with improved adhesion and antifouling properties. Herein, we report surface-initiated hydrogen atom transfer-reversible addition-fragmentation chain transfer (SI HAT-RAFT) as a robust method to grow high-density brush polymers from PE surfaces. We demonstrate that under mild conditions, direct initiation from the C-H bonds of PE surfaces allows for the graft polymerization of a variety of (meth)acrylate monomers. The resulting polymer brushes reached several hundred nanometers in thickness with densities of ca. 0.62 chains/nm², compared to the current standard of ~ 0.28 chains/nm². Finally, we show that our method is capable of dramatically improving the adhesive properties of PE surfaces. This work enables the preparation of PE with diverse surface functionalities for potential use in biomedical, industrial, and battery applications.

Summary of Research:

Polyethylene (PE) is ubiquitous in our society, with over 100 million tons produced annually. The widespread use of PE is enabled by its superior bulk properties and low cost; PE is strong, tough, light weight, and chemically resistant. Despite these advantages, poor surface properties such as low adhesivity and wettability limit its use in applications such as battery membranes, packaging, and automotive materials, all of which require interfacing with other plastics, metals, and solvents. Furthermore, the surface of PE contains only unactivated C-C and C-H bonds, making it challenging to modify.

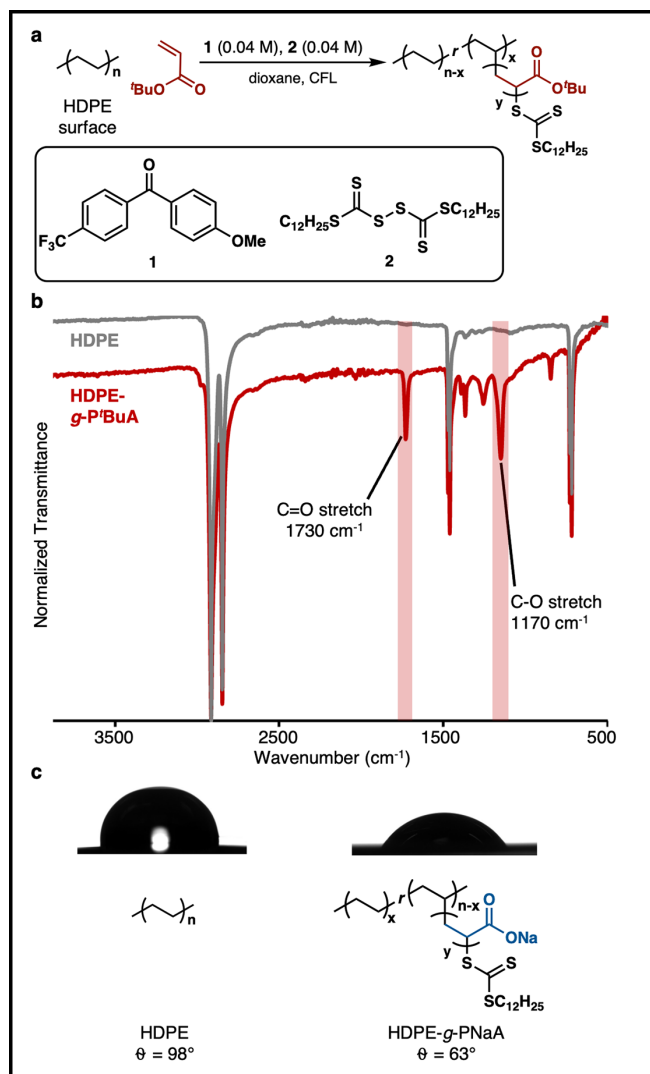


Figure 1: (a) Standard reaction conditions for SI HAT-RAFT from PE. (b) IR spectra of unfunctionalized HDPE and HDPE-g-PtBuA. (c) Static water contact angle for HDPE and HDPE-g-PNaA.

This difficulty in functionalization hampers the synthesis of PEs with high-performance surfaces such as antifouling biomedical implants, antibacterial high-touch surfaces, or chemically selective filtration membranes. A method to imbue PE surfaces with improved or novel properties would facilitate the development of next generation polymeric materials.

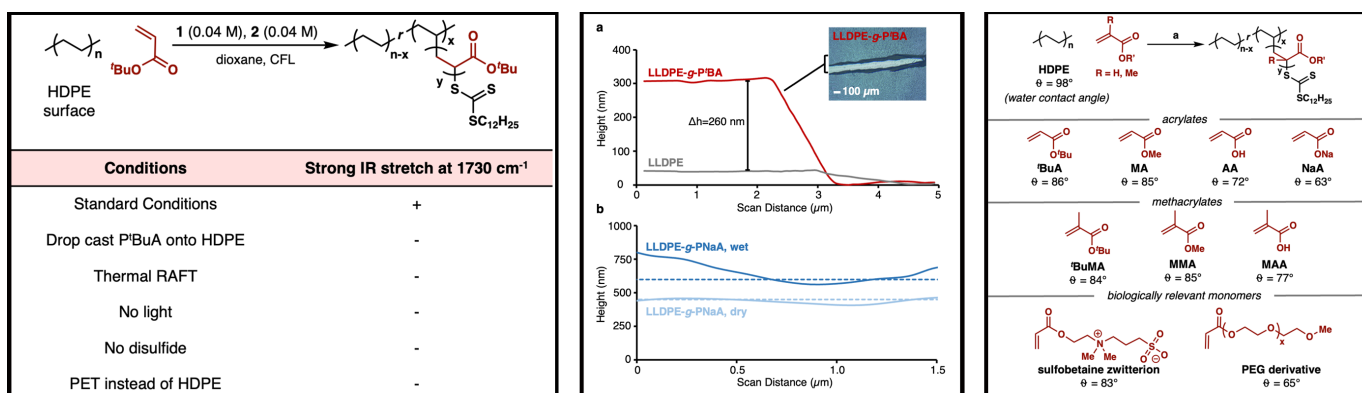


Table 1, left: SI HAT-RAFT Controls. **Figure 2, middle: (a)** AFM measurement of LLDPE-g-PtBuA brush thickness. Brush thickness is assessed by comparing the depth of a scratch (pictured here by optical microscopy) in an LLDPE film before and after grafting. **(b)** AFM swelling study of LLDPE-g-PNaA in pH 9 buffer solution shows the wet film swells 63% relative to the dry film. The dashed lines denote the average film height over the scan distance. **Figure 3, right: Monomer scope of SI HAT-RAFT, where a is the standard reaction condition: photocatalyst 1 (1 equiv.), CTA 2 (1 equiv.), monomer (200 equiv.), and dioxane (0.04 M in CTA) irradiated with a CFL at room temperature in a nitrogen atmosphere for 16 hours. For the sulfobetaine zwitterion and the PEG derivative, water was used in place of dioxane. For the sulfobetaine zwitterion, the reaction was run at half the overall concentration due to poor monomer solubility.**

We began our studies by layering a solution of benzophenone derivative [1], bis(trithiocarbonate) disulfide species [2], tert-butyl acrylate, and dioxane on top of a high-density polyethylene (HDPE) film and covering it with a glass slide before irradiating with visible light from a compact fluorescent light (Figure 2a, reaction setup depicted in SI). Following irradiation, we detected carbonyl and C-O bond stretches in the IR, indicating that poly(tert-butylacrylate) (PtBA) was successfully installed on the surface of PE (Figure 1). Upon basic hydrolysis of PtBA to poly(sodium acrylate) (PNaA), the static water contact angle of the surface decreased from 98° to 63°, indicating a dramatic increase in the hydrophilicity of the surface (Figure 1).

We then carried out a series of control experiments to verify that the polymer observed on the surface was in fact grafted covalently via the HAT-RAFT process. Free PtBA drop-cast onto an HDPE surface washed away easily, suggesting no adhesion of PtBA to HDPE in the absence of covalent bonds between the surface and the grafted polymer (Table 1). Additionally, subjecting HDPE to thermal RAFT polymerization conditions yielded no polymer on the surface, confirming that generation of radicals alone is not enough to graft from HDPE. We also found that under standard SI HAT-RAFT conditions but in the absence of light, polymerization does not proceed.

Having shown that we can grow acrylates from a PE surface, we set out to better characterize the brush polymers produced through microscopy experiments. A silicon wafer was spin-coated with linear low-density polyethylene (LLDPE) to form the substrate and then grafted with PtBA. Atomic force microscopy (AFM) was used to assess brush thickness (Figure 2). For our LLDPE-g-PtBA sample, we achieved a brush thickness

of 260 nm. We also used AFM to characterize brush density. Our SI HAT-RAFT method achieves a grafting density of 0.62 chains/nm². Currently, there are no other methods for grafting from PE surfaces that report such a high grafting density.

To demonstrate the diversity of PE surfaces accessible with SI HAT-RAFT, grafted polymer surfaces were prepared using a variety of acrylate and methacrylate monomers (Figure 3). Static water contact angles ranging from 63° to 86° are accessible, showing that hydrophilicity is tunable by the choice of monomer. Hydrophilicity can also be tuned by protonating or deprotonating the brushes. For example, in their protonated form, PAA brushes have a water contact angle of 72°. In their deprotonated, water-soluble PNaA form, the water contact angle falls to 63°. In the interest of synthesizing biomedically relevant surfaces, we examined a sulfobetaine zwitterion acrylate and a PEG acrylate.

Conclusions and Future Steps:

We developed a robust, highly diversifiable method to grow high density brush polymers from PE surfaces. The SI HAT-RAFT method presented achieved the highest reported brush thicknesses and densities grafting from PE surfaces, and we can access brush polymer surfaces composed of a wide variety of (meth)acrylate monomers. Improving the surface properties of PE opens the door to using PE in applications including battery science, antimicrobial surfaces, and filtration. This work addresses the long-standing challenge in polymer science of facile and robust access to PEs with enhanced surface properties.

New High-Resolution Resists for EUV Lithography

CNF Project Number: 3137-23

Principal Investigator(s): Christopher Kemper Ober

User(s): Madan Rajendra Biradar, Huseyin Cem Kiliclar

Affiliation(s): Department of Materials Science and Engineering, Cornell University

Primary Source(s) of Research Funding: DuPont and SK Hynix

Contact: cko3@cornell.edu, mrb348@cornell.edu, hck46@cornell.edu

Research Group Website: <https://ober.mse.cornell.edu/index.html>

Primary CNF Tools Used: ASML 300C DUV Stepper,

JEOL 6300 E-Beam Lithography, P10 Profilometer, Optical Microscope

Abstract:

The semiconductor industry depends on photoresists to manufacture advanced chips. To meet the industry's growing demands for precise pattern fidelity and resolution, scissionable polymeric materials with chain end groups that can trigger depolymerization are crucial. A promising solution is photodegradable polymer material based on poly(phthalaldehyde) (PPA), having acetal linkages highly sensitive to acids. When exposed to deep ultraviolet (DUV) or electron beam light, these end groups generate acids that induce depolymerization of PPA into its monomers. In this report, we describe the design and synthesis of bromo-substituted PPA and demonstrate its effectiveness as a photoresist through DUV lithography, achieving well-defined line-space patterns.

Summary of Research:

In 1983, IBM's research laboratory developed depolymerizable photoresists, including end-capped poly(phthalaldehyde) (PPA). These photoresists contain photolabile groups that generate acids when exposed to light. The acids then catalyze the chain cleavage of the PPA [1]. In the literature, various research groups have investigated the potential of PPA under DUV and EUV radiation. The Ober research group has demonstrated that functionalized poly(phthalaldehyde)s (PPAs) can serve as degradable polymer backbones. Additionally, this group has explored PAG-tethered phthalaldehyde to achieve exceptional results across several lithography techniques [2-4].

In this report, we have described the development of photoresists containing active end groups, which show high stability, low outgassing and extreme sensitivity under DUV exposure. The development and depolymerization mechanism of functionalized

linear Br-PPA is shown in Figure 1. After exposure of EUV radiation, the EUV active end group initiates depolymerization via a cascade mechanism.

Result and Discussion:

The synthesized Br-PPA polymer was examined with ¹H NMR spectroscopy to determine its structural confirmation and evaluate its stability, while its thermal stability was evaluated through thermogravimetric analysis. The molecular weight of the polymer was characterized via gel permeation chromatography.

For photoresist testing, 35 mg of the polymer was dissolved in 1 mL of cyclohexanone and spin-coated onto a silicon wafer at 2500 rpm for 60 seconds. The coated wafers were then subjected to DUV radiation using an ASML 300C DUV stepper. After radiation exposure, the film was baked at 90°C and developed in isopropyl alcohol for 30 seconds. The resulting line-space patterns were examined using Atomic Force Microscopy (AFM), as depicted in Figure 2.

Conclusions and Future Work:

In this work, we demonstrate the synthesis of bromo-substituted poly(phthalaldehyde) (Br-PPA) with active end groups and observed its potential as a photoresist for deep ultraviolet (DUV) lithography. The initial results with the Br-PPA are promising. Moving forward, we will further explore the lithographic performance of various functionalized PPA photoresists.

References:

- [1] Ito, H.; Willson, C. G. Chemical Amplification in the Design of Dry Developing Resist Materials, *Polym. Eng. Sci.* 23, 1983, 1012-1018.
- [2] Deng, J., Bailey, S., Jiang, S., Ober, C. K. High-Performance Chain Scissionable Resists for Extreme Ultraviolet Lithography: Discovery of the Photoacid Generator Structure and Mechanism. *Chem. Mater.* 2022, 34, 6170.6181.
- [3] Deng, J., Bailey, S., Ai, R., Delmonico, A., Denbeaux, G., Jiang, S., Ober, C. K. Synthesis of End-Cap Enabled Self-Immolative Photoresists For Extreme Ultraviolet Lithography. *Macro Lett.* 2022, 11, 1049.1054.
- [4] Deng, J., Bailey, S., Jiang, S., Ober, C. K. Modular Synthesis of Phthalaldehyde Derivatives Enabling Access to Photoacid Generator-Bound Self-Immolative Polymer Resists with Next-Generation Photolithographic Properties. *J. Am. Chem. Soc.* 2022, 144, 42, 19508-19520.

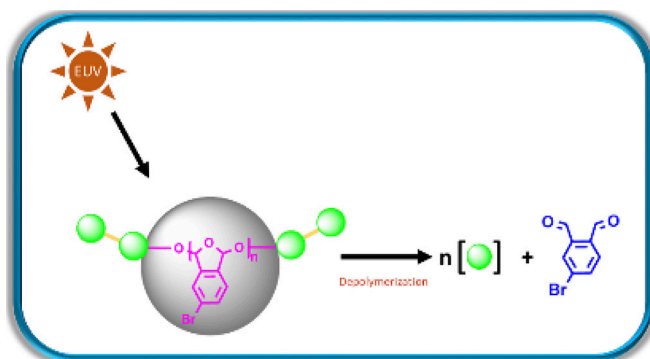


Figure 1: Functionalized linear Br-PPA with photoactive end groups.

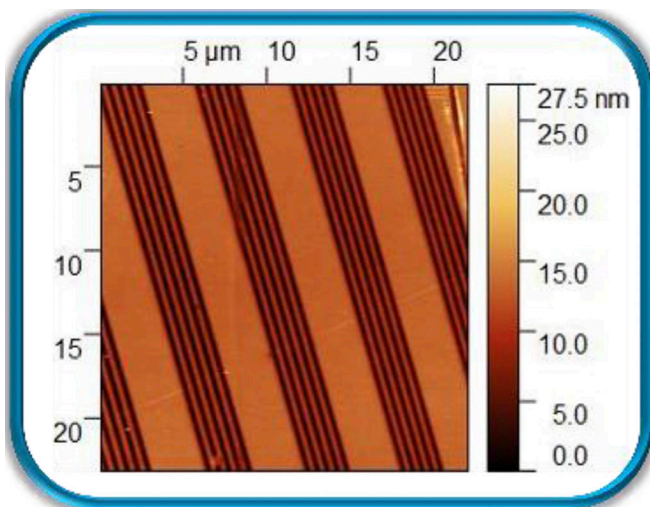


Figure 2: Line-space patterns characterized using AFM.

Fabrication of 2D-Material-Based Ionic Transistors

CNF Summer Student: Siyi (Cathy) Chen

**Student Affiliation: Materials Science and Engineering,
University of Illinois at Urbana-Champaign**

Summer Program(s): 2024 Cornell NanoScale Facility Research Experience for Undergraduates (CNF REU) Program

Principal Investigator(s): Yu Zhong, Assistant Professor, Materials Science and Engineering, Cornell University

Mentor(s): Kaushik Chivukula, Graduate Student, Materials Science and Engineering, Cornell University

Primary Source(s) of Research Funding: National Science Foundation under Grant No. NNCI-2025233

Contact: cathychen0915k@gmail.com, yz2833@cornell.edu, kc836@cornell.edu

Summer Program Website: <https://cnf.cornell.edu/education/reu/2024>

Primary CNF Tools Used: Heidelberg Mask Writer DWL-2000,

ABM Contact Aligner, Oxford 81 RIE, AJA Ion Mill, SC4500 Even-Hour Evaporator

Abstract:

Traditional electronic field-effect transistors (FETs), which utilize electrons and holes as charge carriers, are indispensable in modern electronic devices such as integrated circuits and microprocessors. They form the backbone of today's digital technology by enabling efficient information processing, storage, and transmission. Despite ongoing challenges in the miniaturization of electronic transistors, ionic FETs offer distinct advantages, particularly biocompatibility and tunable conductance. Our project aims to fabricate ionic transistors using advanced 2D materials and address the limitation of low on-off current ratios in these devices.

Summary of Research:

The human brain, with its highly selective ionic transmission system, processes vast amounts of information and facilitates neural communication daily. To mimic the ultra-functional capabilities of the brain, nano-channeled ionic field-effect transistors that use ions like Na^+ and Ca^{2+} as carriers, similar to those in neural processes, show great potential for future applications. Such transistors are promising for artificial brain systems and memory devices like neuromorphic memristors due to their unique ability to maintain discrete conductivity states, which serve as memory storage units.

In order to replicate the ultra-selectivity of brain ionic channels and increase the on-off ratio, we focused on fabricating ionic transistors with nanochannels approaching the Debye length. Conventional microchannels, characterized by their short Debye

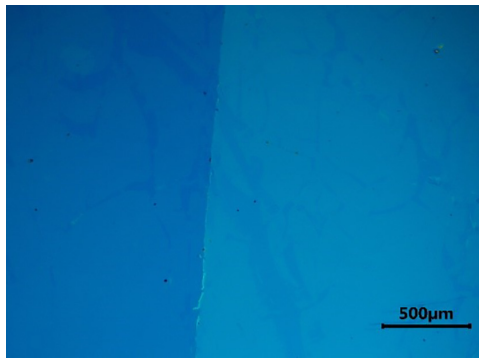
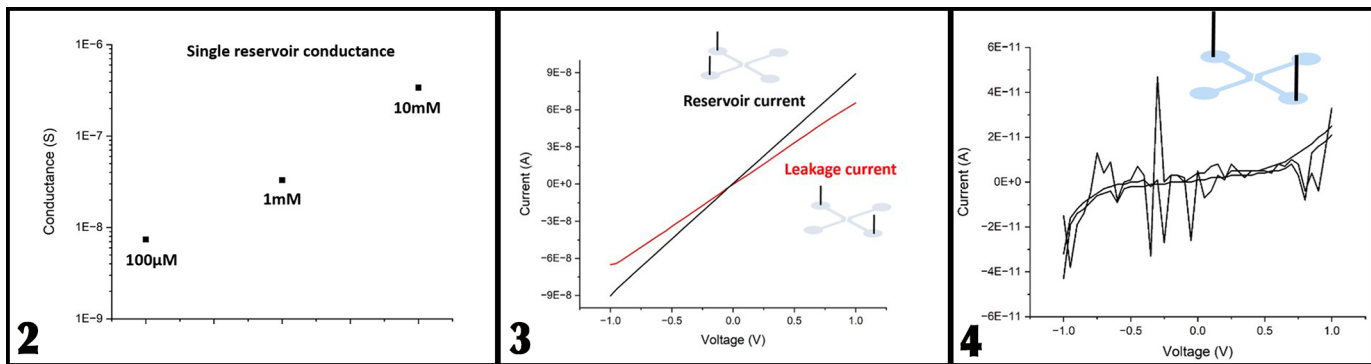


Figure 1: Stable 2D heterostructure.

lengths and discontinuous electric field effects, often result in the undesirable coexistence of both negative and positive ions. In contrast, the nanochannel design allows the electric field to penetrate the entire channel, predominantly permitting the passage of only a single ion type. This ensures a low energy consumption in the transistor, mirroring brain functions.

We began by preparing a silicon wafer with a 300 nm thermal oxide layer, cutting it into 1-inch by 1-inch pieces. To create the nanochannel ionic pathway, we deposited a monolayer of 2D Copper-Tetrakis (4-carboxyphenyl) porphyrin (CU-TCPP) by immersing the wafer pieces in a Copper Nitrate solution, capping them with Hexane, and injecting TCPP solution using a syringe pump. After allowing the Hexane to evaporate, the remaining solution was drained. Thereafter, a monolayer of Molybdenum disulfide (MoS₂) was exfoliated and transferred onto the CU-TCPP-coated pieces, resulting in the formation of a stable 2D heterostructure, as illustrated in Figure 1.

To etch the MoS₂ monolayer into a 100 μm by 100 μm pattern, photolithography and the AJA ion mill at the Cornell NanoScale Facility were employed. Oxygen plasma then removed the photoresist cleanly. Next, we deposited 50 nm of silicon dioxide using the Oxford Atomic Layer Deposition FlexAL machine to serve as the insulating layer of the ionic field effect transistor. The gate electrode was fabricated by depositing 10 nm of titanium and 50 nm of gold with the Thermal/E-gun Evaporation System, followed by a lift-off process using hot N-Methylpyrrolidone (NMP) stripper. The



source and drain channels were defined using SU-8 and photolithography, and subsequently etched with the Oxford reactive ion etching tool. Finally, capping the pieces with Polydimethylsiloxane (PDMS) completed the fabrication process.

For the measurement of Single Reservoir Conductance, four holes were made in the PDMS, into which sodium chloride (NaCl) electrolyte was injected. Two silver electrodes were placed in the same reservoir. With ions flowing freely within the unobstructed single fluid channel, conductivity was observed, confirming the successful fabrication of the single reservoir. Figure 2 shows the relationship between the NaCl solution concentration and its conductance, indicating that as the concentration increases, the number of ions available for carrying electric current also increases, leading to higher conductance.

During the leakage test, electrodes were placed in two separate fluid channels rather than in the same one. Without a nanochannel allowing current to flow between the channels in this case, no current should have been detected when applying voltage if there was no leakage. However, as shown in Figure 3, when voltage ranging from -1V to 1V was applied, a leakage current of approximately 10^{-7} A was detected. This current is of the same order as that of a single connected reservoir, suggesting that some leakage was indeed occurring between the two fluid channels.

To address this issue, we applied Vapor Phase (3-Aminopropyl) triethoxysilane (APTES) treatment [1] to the PDMS to induce covalent bonding between SU-8 and PDMS, enhancing the sealing of the fluid channels.

After this optimization, we repeated the leakage test under identical conditions. This time, the current was around 10^{-11} A, which is three orders of magnitude lower than the previous leakage current, and no linear trend

was observed in Figure 4. This minor current, likely due to the open holes, was close enough to zero to indicate that there was no leakage, confirming the successful fabrication of a leakage-free device, ready for future experiments and innovations.

Conclusions and Future Steps:

In conclusion, our 2D material-based ionic field effect transistors demonstrate potential for applications in future Neuromorphic Computing systems by simulating brain functions. The use of Oxygen Plasma effectively removed the photoresist, while Hot NMP facilitated the lift-off process. The leakage between source and drain channels was minimized through APTES treatment of PDMS, resulting in a non-leakage current of approximately 10^{-11} A under a voltage range of -1V to 1V. Future work should focus on testing and measuring the conductance of different organic molecule cages, which could lead to the selective manipulation of ion types passing through the transistors.

Acknowledgements:

Special thanks to the 2024 Cornell NanoScale Science & Technology Facility Research Experiences for Undergraduates (CNF REU) Program funded by the National Science Foundation under Grant No. NNCI-2025233, and the National Nanotechnology Coordinated Infrastructure. I would also like to thank Prof. Yu Zhong and Kaushik Chivukula for their mentorship, as well as the CNF staff and program coordinators for their support.

References:

- [1] *Micromachines* 2015, 6(12), 1923-1934.

Optimizing Annealing Temperature for Ohmic Contacts to AlGaIn/GaN

CNF Summer Student: Timothy Walsh

Student Affiliation: Chemical Engineering, Cornell University

Summer Program(s): 2024 Xing Army Educational Outreach Program (AEOP), 2024 Cornell NanoScale Science & Technology Facility Research Experience for Undergraduates (CNF REU) Program

Principal Investigator(s): Huili (Grace) Xing, Electrical and Computer Engineering, Cornell University

Mentor(s): Aaron Windsor, Cornell NanoScale Facility, Cornell University; Joseph Dill, Applied Engineering Physics, Cornell University; Jimmy Encomendero, Electrical and Computer Engineering, Cornell University

Primary Source(s) of Research Funding: Xing Army Educational Outreach Program (AEOP), National Science Foundation under Grant No. NNCI-2025233

Contact: tpw29@cornell.edu, grace.xing@cornell.edu, ajw49@cornell.edu, jed296@cornell.edu, jje54@cornell.edu

Summer Program Website: <https://cnf.cornell.edu/education/reu/2024>

Primary CNF Tools Used: GCA AS200 i-line Stepper, Glen 1000 Resist Strip, SC4500 Odd-Hour Evaporator, Rapid Thermal Annealer (RTA), Zeiss Supra SEM, Bruker Energy-dispersive X-ray Spectrometer (EDS), Optical Microscope

Abstract:

As ultra-wide bandgap semiconductor research progresses, the need for reliable, low-resistivity ohmic contacts becomes more essential. To ensure high contact quality and reproducibility, process conditions must be carefully optimized. This project specifically analyzed the impact of various annealing temperatures on a Ta/Al/Ni/Au metal stack to minimize contact resistance. Previously, annealing at 830°C under N₂ ambient showed lateral metal diffusion, known as contact spreading, leading to the transistor short-circuiting and preventing the measurement of contact resistance. GaN pieces were first coated with photoresist, onto which transfer length method patterns were transferred using the GCA AS200 i-line stepper. The SC4500 Odd-Hour evaporator was then used for e-beam evaporation of 20 nm tantalum, 50 nm aluminum, 100 nm nickel, and 40 nm gold. After liftoff, the samples were analyzed and measured under the Zeiss Supra Scanning Electron Microscope (SEM). The samples were then annealed in N₂ ambient at temperatures ranging from 500, 600, 700, 800, and 900°C. Using the SEM and its Energy Dispersive Spectroscopy (EDS), the spreading of the metals was measured. Lastly, using the transfer length method, the optimal annealing conditions for the lowest contact resistance were explored.

Summary of Research:

Silicon Process and Results. The spreading under investigation was seen previously on a 20 nm tantalum, 150 nm aluminum, 50 nm nickel, and 50 nm gold stack on GaN. Thus, the process started by recreating this metal stack onto four 8 x 8 mm Si pieces in order to trial the process. First, each piece was cleaned with

sonication in acetone, isopropyl alcohol, and deionized water for 5 minutes each. Then, to remove any excess moisture, the pieces were placed on a hotplate at 110°C for five minutes. From there, AZ NLOF 2020 negative photoresist was spun onto each piece, with a target width of 1.1 μm, and then they were baked at 115°C for 60 seconds. The GCA AS200 i-line stepper exposed each piece in four spots with an Ohmic contact mask. After baking these pieces again at 115°C for 60 seconds on a hotplate, they developed in 726 MIF for 60 seconds, removing the unexposed photoresist. The Glen 1000 Resist Strip removed any excess organic matter or resist on the pieces. To deposit the metal stack, the SC4500 Odd-Hour electron beam evaporator was used. Liftoff consisted of 10 minutes in Microposit Remover 1165, five minutes isopropyl alcohol, both in sonication, then a rinse with deionized water. Under the Zeiss Supra SEM, the Circular Transfer Length Method (C-TLM) spacings were measured, and EDS baseline images were taken. Then, the four pieces were annealed at 700, 750, 800, and 850°C for 60 seconds under N₂ ambient in the Rapid Thermal Annealer (RTA). Again, the pieces were analyzed under the SEM with EDS to examine any spreading.

Before annealing, the circle lines were crisp, as seen in Figure 1(a). After annealing, visual spreading of aluminum could be seen under both the optical microscope and the SEM, as in Figure 1(b). Additionally, annealing induced nickel clumping. This can be seen in the EDS images in Figure 2. This effect is likely due to the high surface energy of nickel. Since aluminum melts at 660°C, it likely forms a liquid at an annealing temperature above this. Because the nickel sits atop this aluminum liquid, to reduce its surface energy, the nickel

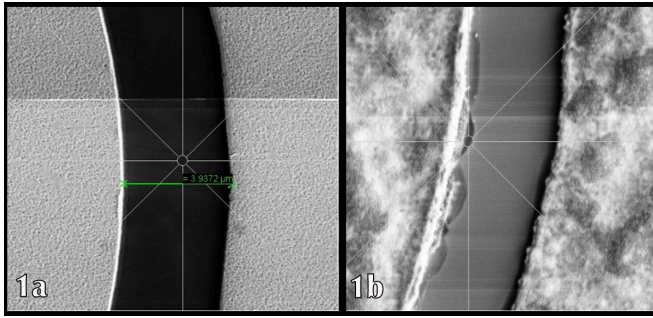


Figure 1: (a) Si Sample 2 μm Gap Pre-anneal. (b) Si Sample 2 μm Gap Annealed at 850°C.

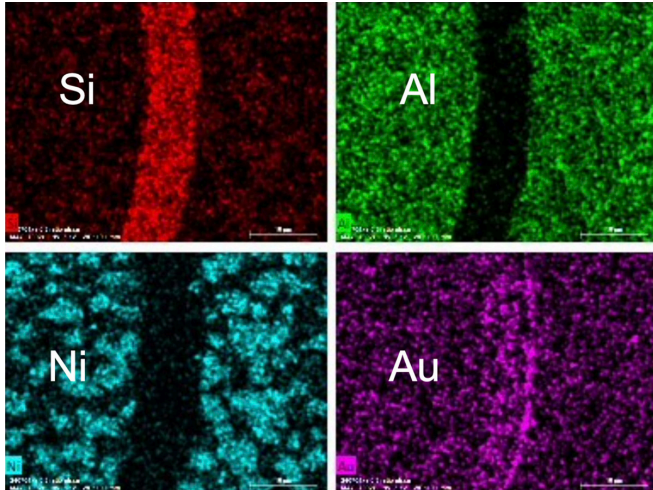


Figure 2: Si Sample 2 μm Gap Annealed at 700°C.

obtains a lower surface energy by forming spheres. This causes the clumping effect.

GaN Process and Results. The fabrication process with five 10 x 10 mm GaN pieces was identical to that of the Si pieces, except before the electron beam deposition, the pieces were cleaned in HCl, deionized water, BOE, and deionized water again for 60 seconds each. Additionally, the Ta/Al/Ni/Au metal stack was changed to 20 nm tantalum, 50 nm aluminum, 100 nm nickel, and 40 nm gold. The intention was to reduce the amount of aluminum liquid that the nickel layer sits atop to prevent the nickel clumping. Also, the thickness of nickel was doubled to encourage it to remain flat instead of clumping and forming spheres. The five GaN pieces were annealed at 500, 600, 700, 800, and 900°C, and the 800°C sample was measured on a probe station.

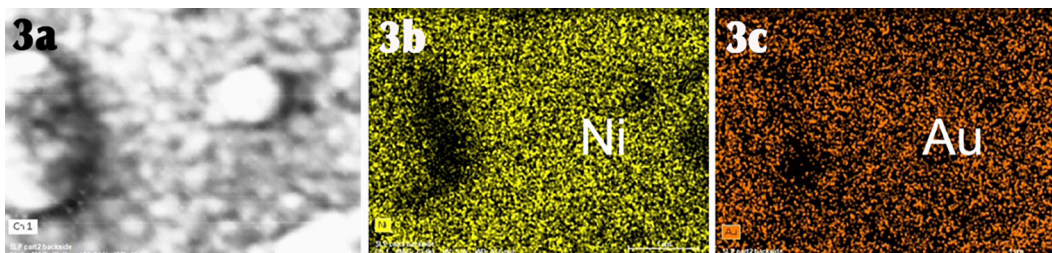


Figure 3: (a) GaN SEM. (b): Ni EDS. (c) Au EDS.

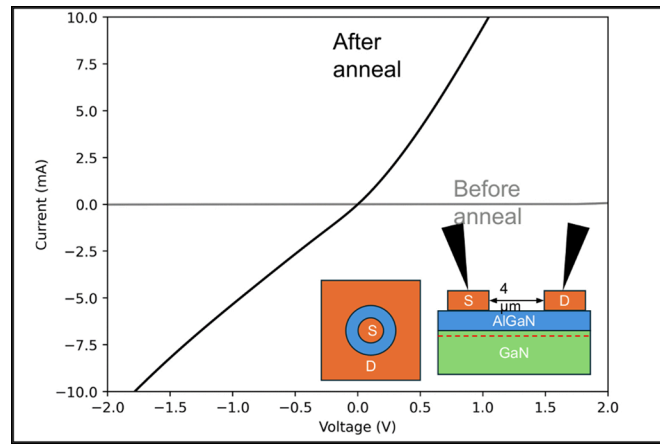


Figure 4: TLM Measurement for 800°C GaN Sample.

On GaN, there was no visual spreading as there was on the Si, but a “bubbling” effect was observed. This bubbling is evident in Figure 3(a). Figure 3(b) and 3(c) show that these bubbles are actually voids of gold and nickel, so they are different from the nickel clumps seen on Si. Annealing the GaN at 800°C increased the amount of current that could pass through the contact by roughly two orders of magnitude, as shown in Figure 4. Although, the contact is still not Ohmic, as Current vs Voltage is not linear.

Conclusion and Future Steps:

Varying the annealing temperature of the Ta/Al/Ni/Au stack on GaN from 500 to 900°C showed minimal spreading but an increasing “surface bubbling” effect as temperature increases. Nickel clumping as well as spreading on the Si pieces was evident after annealing, and future TLM measurements on the GaN pieces will determine the annealing temperature with the lowest contact resistance.

Acknowledgements:

The author would like to thank: the Army Educational Outreach Program; the Cornell NanoScale Facility Research Experiences for Undergraduates program; Professor Grace (Huili) Xing; Aaron Windsor.

Fabrication of Interdigitated Electrodes for use in a Homebuilt Electron Force Microscope

CNF Project Number: 863-00

Principal Investigator(s): John A. Marohn

User(s): Azriel Finsterer, George DuLaney

Affiliation(s): Chemistry and Chemical Biology, Cornell University

Primary Source(s) of Research Funding: NSF Award # DMR-2113994

Contact: john.marohn@cornell.edu, af482@cornell.edu, grd44@cornell.edu

Primary CNF Tools Used: Hamatech Hot Piranha Cleaner, Class II Resist Spinners, Edge Bead Removal System, ABM Contact Aligner, Hamatech Wafer Processor, SC4500 Odd-Hour Evaporator, DISCO Dicing Saw

Abstract:

Interdigitated electrodes are under development for applications in electron force microscopy. These devices will be employed in the investigation of charge recombination dynamics in organic photovoltaic devices.

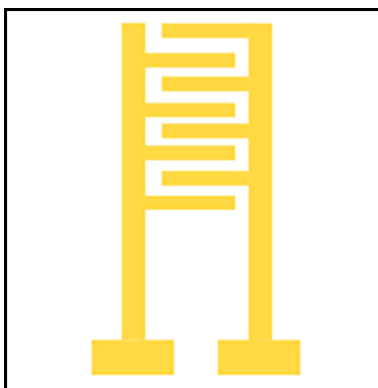


Figure 1: An Interdigitated Electrode. Interdigitated electrodes (IDEs) have a comb-like structure that increases the sensitivity of charge detection.

Summary of Research:

The fabrication of interdigitated electrodes (IDEs) for application in the homebuilt electron force microscopes (EFMs) of the Marohn group will be facilitated by the tools provided by the Cornell NanoScale Facility (CNF). The electrodes will be made utilizing basic photolithography and thin film deposition techniques. These devices will be used in the analysis of charge recombination dynamics in organic photovoltaic (OPV) films using a novel EFM method invented in the Marohn Lab: phase kick electron force microscopy (pk-EFM) [1]. The comb-like structure of the IDEs as shown in Figure 1 will greatly enhance the sensitivity of the new method, allowing us to make measurements with space-charge limited current.

The process of fabricating the interdigitated electrodes will begin in photolithography room 106. Lift-off resist (LOR) will be spin-coated on a cleaned, dehydrated 100 mm quartz wafer. A soft bake will be performed at 150. by direct contact on a hot plate. Once the soft bake is complete, a compatible imaging resist will be spin-coated on top of the LOR resist and will be baked per the imaging resist's requirements. Edge beads will be removed after each spin coating step and film uniformity will be checked with the Filmetrics F50.

The IDE pattern will be written using the ABM Contact Aligner. Rachel Cohn of the Marohn Group has already written the mask for this application, so the Heidelberg Mask writers will not be utilized. Exposure conditions for this application have yet to be optimized; therefore an exposure array will be performed to determine the optimal conditions for writing the IDEs onto the stack. Once the optimal conditions have been determined, exposed stacks will be placed in the SC4500 Odd-Hour Evaporator where chromium and gold will be deposited into the pattern left behind by the mask. Microchem Remover PG will lift the resist stack

and excess gold from the quartz wafer, leaving behind the gold IDEs. The devices will be removed from the wafer using the DISCO dicing saw and will be brought back to Baker Laboratory for thin film deposition. No thin film deposition onto the IDEs will be conducted in the CNF cleanroom.

Fully fabricated interdigitated electrodes will be used as substrates for the deposition of OPV materials. One particular system of interest is the known OPV blend of poly-(3-hexylthiophene) (P3HT) and [6,6] phenyl-C61-butyric acid methyl ester (PCBM), which has been studied with time-resolved microwave conductivity (TRMC) [2][3], time-resolved photoluminescence spectroscopy (TRPL) [4] and has shown to have power conversion efficiency of up to six percent when thermally annealed [5]. The added sensitivity provided by the IDEs will allow our group to better compare the experimental results of the EFM method – shown

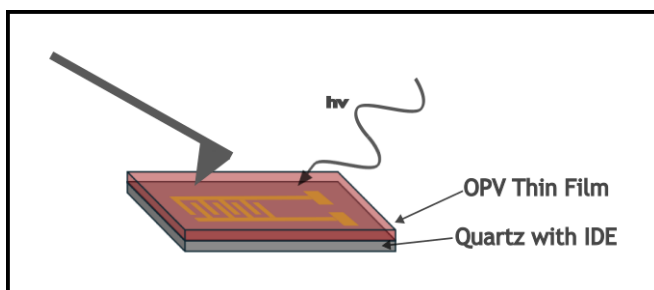


Figure 2: Schematic of Electron Force Microscope Experiment Using Interdigitated Electrodes. Interdigitated electrodes deposited on quartz substrates (bottom layer) will have an organic photovoltaic layer deposited on top of them (top layer). A conductive cantilever tip is brought close to the sample surface as it is irradiated with light. The cantilever's motion is modified by the electrostatic forces arising from the generation of charge carriers within the sample.

in Figure 2 – to those of other methods and potentially allow for the screening of promising OPV materials for incorporation into devices.

Conclusions and Future Steps:

Organic photovoltaic materials will be spin-coated on quartz substrates containing the fabricated IDEs. These samples will be inserted into Marohn Group microscopes where pk-EFM experiments will be conducted. The incorporation of the IDEs into the experiment will allow for space-charge-limited measurements of conductivity to be collected, improving the sensitivity of the experiment.

References:

- [1] “Microsecond Photocapacitance transients observed using a charged microcantilever as a gated mechanical integrator”; Dwyer, R.P.; Nathan, S.R. and Marohn, J.A. *Sci Adv.* 3 (6), 2017.
- [2] “Dark Carriers, Trapping, and Activation Control of Carrier Recombination in Neat P3HT and P3HT:PCBM Blends”; Ferguson, A.J.; Kopidakis, N.; Shaheen, S.E. and Rumbles, G. *J. Phys. Chem. C*, 115, 23134-23148 (2011).
- [3] “Revealing the Dynamics of Charge Carriers in Polymer:Fullerene Blends Using Photoinduced Time-Resolved Microwave Conductivity”; Savenije, T.J.; Ferguson, A.H.; Kopidakis, N. and Rumbles, G. *J. Phys. Chem. C*, 117, 24085-24103 (2013).
- [4] “Time-Resolved Charge-Transfer State Emission in Organic Solar Cells: Temperature and Blend Composition Dependences of Interfacial Traps”; Arndt, A.P.; Gerhard, M.; Quintilla, A.; Howard, I.A.; Kock, M. and Lemmer, U. *J. Phys. Chem. C*, 119, 13516-13523 (2015).
- [5] “Roles of donor and acceptor nanodomains in 6% efficient thermally annealed polymer photovoltaics”; Kim, K.; Liu, J.; Namboothiry, M.A.G. and Carroll, D.L. *Applied Physics Letters*, 90, 163511 (2007).

Ferroelectric Hafnium Zirconium Oxide Under the Gate of AlN/GaN High Electron Mobility Transistors

CNF Project Number: 2801-19

Principal Investigator(s): Debdeep Jena

User(s): Akshey Dhar

Affiliation(s): Materials Science and Engineering, School of Electrical and Computer Engineering; Cornell University

Primary Source(s) of Funding: Semiconductor Research Corporation

Contact: djena@cornell.edu, ald99@cornell.edu

Research Group Website: <https://jena-xing.engineering.cornell.edu/>

Primary CNF Tools Used: GCA AutoStep 200 DSW i-line Wafer Stepper, SC4500 Odd-Hour Evaporator, PT770 Etcher, Rapid Thermal Anneal - AG Associates Model 610, Arradiance ALD Gemstar-6, JEOL JBX-6300FS

Abstract:

Gallium nitride-based high electron mobility transistors (GaN HEMTs) are at the cutting edge of technological innovation. Renowned for their high speed and power capabilities, GaN HEMTs are utilized across a diverse array of sectors, including telecommunications, power electronics, aerospace, defense, industrial, medical, and consumer electronics. Integrating GaN with an aluminum nitride (AlN) barrier enhances speed, power output, and thermal management. However, traditional HEMTs are reaching their physical limits. The work in the CNF investigates the addition of a ferroelectric hafnium zirconium oxide (HZO) layer beneath the gate of AlN/GaN HEMTs to overcome these limitations. This is achieved through the use of the remnant polarization of ferroelectrics to modulate the threshold voltage and demonstrate the ability for memory, giving GaN HEMTs improved device performance and more functionality. Through the development of multiple HEMT devices with varying HZO thicknesses, hysteresis in device output currents is verified and alterable, with preliminary results exhibiting a threshold voltage tuning range of 0.5-1.2 V. Overall, the work lays the foundation for the benefits of incorporating ferroelectric layers under the gate of AlN/GaN HEMTs.

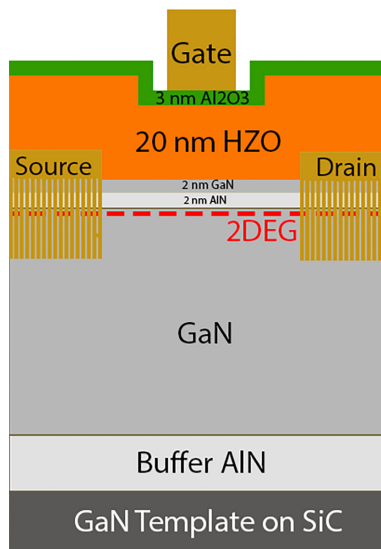


Figure 1: Schematic image of processed HEMT device with alloyed contacts and an HZO layer.

Summary of Research:

As the demand for higher performance devices grows and transistors continue to scale down, discovering new materials to enhance device performance or introduce new functionalities becomes increasingly critical. One promising approach is integrating a ferroelectric layer beneath the gate of High Electron Mobility Transistors (HEMTs). When combined with the polarization-induced two-dimensional electron gas (2DEG) of an AlN/GaN heterostructure, the ferroelectric layer's ability to switch polarization can modify the device's threshold voltage. This modification is achieved through ferroelectric polarization, which alters the polarization at the heterostructure interface.

To demonstrate this feature, HEMT devices were fabricated at the CNF. Figure 1 presents a schematic of the processed device. The fabrication process involves the following steps: (1) device isolation, (2) ohmic contact metallization, (3) HZO deposition, (4) annealing, and (5) gate metallization. Steps 1, 2, and 4 employ the GCA AutoStep 200 DSW i-line Wafer Stepper to define optical patterns for subsequent steps. Additionally, Step 4 uses the JEOL JBX-6300FS for defining electron beam lithography (EBL) gates. Device isolation is performed via etching in the PT770 Etcher, while ohmic and gate metallizations are conducted in the SC4500 Odd-Hour Evaporator. HZO and Al₂O₃ layers are deposited using the Arradiance ALD Gemstar-6 and annealed in the

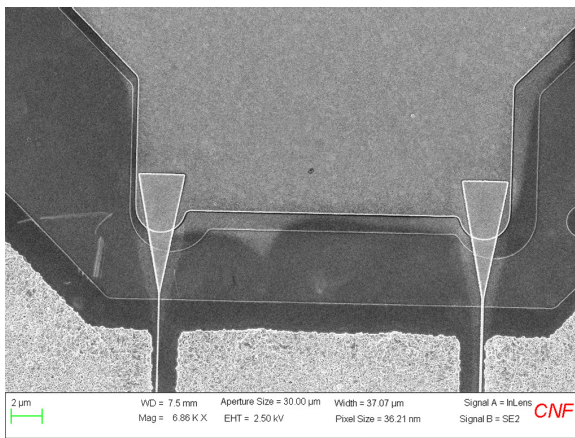


Figure 2: SEM of EBL deposited gate.

Rapid Thermal Anneal - AG Associates Model 610. Figure 2 shows scanning electron microscope (SEM) images of the deposited EBL gates between the source and drain contacts.

The ferroelectric properties of the HZO layer can be evaluated using a polarization-electric field (P-E) loop. Figure 3 illustrates the P-E loop of the deposited HZO layer. The remnant polarization of the HZO films was measured at $14.155 \text{ } \mu\text{C}/\text{cm}^2$, which is slightly lower than the typical values reported in the literature ($\sim 17 \text{ } \mu\text{C}/\text{cm}^2$).

Due to the ferroelectric properties, the drain current versus gate voltage graphs display a counterclockwise hysteresis loop during dual sweeping of the gate voltage. Adjusting the sweep range of the gate voltage results in a threshold voltage modulation. Figure 4 demonstrates a 1 V threshold voltage tuning range, which is achieved by varying the gate voltage sweep ranges.

Conclusions and Future Steps:

Five different devices were fabricated, each with varying thicknesses of HZO. Through these devices, the study aimed to demonstrate the ability to modulate the threshold voltage, reduce gate leakage, and exhibit memory storage capabilities. The transfer curves of the devices exhibited distinct counterclockwise hysteresis. This hysteresis, along with the modulation of the gate voltage, demonstrated a 1 V threshold voltage tuning range, as well as indicating the memory capabilities of the device. Additionally, the gate leakage current in samples with HZO was reduced by approximately six orders of magnitude compared to those without HZO.

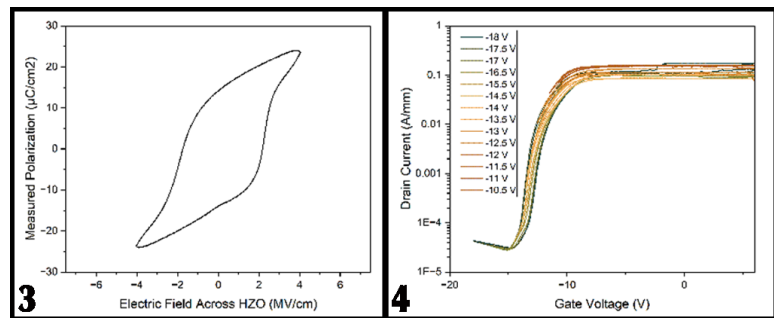


Figure 3, left: P-E loop of the deposited HZO layer in a metal-ferroelectric-metal structure.

Figure 4, right: Transfer Curve of HEMT device with HZO at multiple gate voltage sweeps, demonstrating threshold voltage modulation.

Given the slight decrease in the remnant polarization of the HZO layer compared to in literature, future work should focus on analyzing devices with a more robust HZO layer. This improvement could result in a larger memory window in the transfer curves and a greater threshold voltage tuning range.

In addition to perfecting the deposition of the HZO layer, exploring other ferroelectric materials could yield better interaction with the AlN/GaN heterostructure. Currently, significant research is focused on ferroelectric aluminum scandium nitride (AlScN). As AlScN is a nitride and can be deposited using Molecular Beam Epitaxy, it is possible to develop an all nitride ferroelectric HEMT heterostructure in-situ. This approach could result in cleaner interfaces, larger hysteresis curves, and improved device performance.

References:

- [1] Chunlei Wu, Hansheng Ye, Nikhita Shaju, Jeffrey Smith, Benjamin Grisafe, Suman Datta, and Patrick Fay. Hf_{0.5}Zr_{0.5}O₂-based ferroelectric gate hemts with large threshold voltage tuning range. *IEEE Electron Device Letters*, 41(3):337–340, March 2020.
- [2] O. Ambacher, J. Smart, J. R. Shealy, N. G. Weimann, K. Chu, M. Murphy, W. J. Schaff, L. F. Eastman, R. Dimitrov, L. Wittmer, M. Stutzmann, W. Rieger, and J. Hilsenbeck. Two-dimensional electron gases induced by spontaneous and piezoelectric polarization charges in n- and ga-face algan/gan heterostructures. *Journal of Applied Physics*, 85(6):3222–3233, March 1999.

Improving Interface Quality and Repeatability in Contacts to β -Ga₂O₃ by Metal-First Processing

CNF Project Number: 2802-19

Principal Investigator(s): Huili Grace Xing¹, Debdeep Jena¹

User(s): Kathleen Smith²

Affiliation(s): 1. School of Electrical and Computer Engineering,

2. Department of Applied and Engineering Physics; Cornell University

Primary Source(s) of Research Funding: Air Force Office of Scientific Research (AFOSR),

Semiconductor Research Corporation (SRC), Defense Advanced Research Projects Agency (DARPA)

Contact: grace.xing@cornell.edu, djena@cornell.edu, kts57@cornell.edu

Primary CNF Tools Used: SC4500 Odd-Hour E-Beam Evaporator, Angstrom E-Beam Evaporator, ABM Contact Aligner, AS200 i-Line Stepper, AJA Ion Mill, Glenn 1000 Resist Strip, PT720/740, PT770, RTA AG610

Abstract:

A metal-first process for forming contacts to β -Ga₂O₃ is developed that demonstrates improved contact repeatability compared to conventional liftoff processing by minimizing surface modification and results in non-alloyed contact resistances as low as 70 m Ω -mm. The metal-first process is further applied to a range of ohmic and Schottky metals with varied work functions to demonstrate that metal-first processing results in a high-quality interface that at least partially alleviates Fermi-level pinning in contacts to β -Ga₂O₃.

Summary of Research:

β -Ga₂O₃ is an ultra-wide bandgap semiconductor (~4.8 eV) with a high critical electric field, wide range of demonstrated, controllable n-type doping, sufficient electron mobility, and low-cost, native substrates that makes it potentially suitable for kilovolt device applications. Metal-semiconductor interfaces in Ga₂O₃ devices, however, are complex and inconsistent: in Schottky contacts, the Fermi-level is dramatically pinned (ie. the Schottky barrier height Φ_B does not trend linearly with the metal work function Φ_M) and measures of Φ_B can vary by over 1 eV for the same contact metal [1]. Similar variation of contact quality is observed in ohmic contacts.

The contacts reported here are formed by a metal-first process, in which the contact metal is blanket-deposited on the as-grown semiconductor surface, then patterned with photoresist (Figure 1a). The metal between the contact pads is then removed by wet and/or dry etching. This contrasts with conventional liftoff processing, where the contact area is first exposed to photoresist during patterning, then metal is deposited and the excess metal between the pads is lifted off in solvent (Figure 1b).

We fabricated both metal-first and lifted-off Ti/Au (10/110 nm) transfer length method (TLM) patterns on n+ ($> 5 \times 10^{19} \text{ cm}^{-3}$) Si-doped (010) β -Ga₂O₃ by electron-beam evaporation. For the metal-first contacts, TLM measurements have linear-ohmic IV behavior with a contact resistance (R_c) of 0.73 Ω -mm.

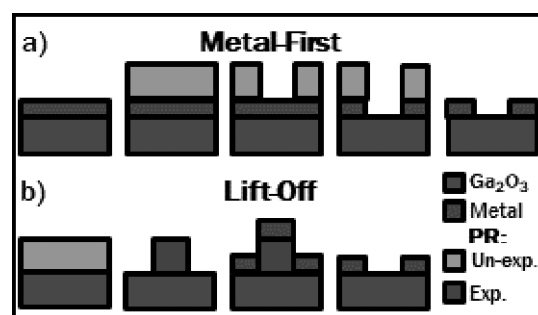


Figure 1: Process flow schematic for a) metal-first and b) liftoff contact processing.

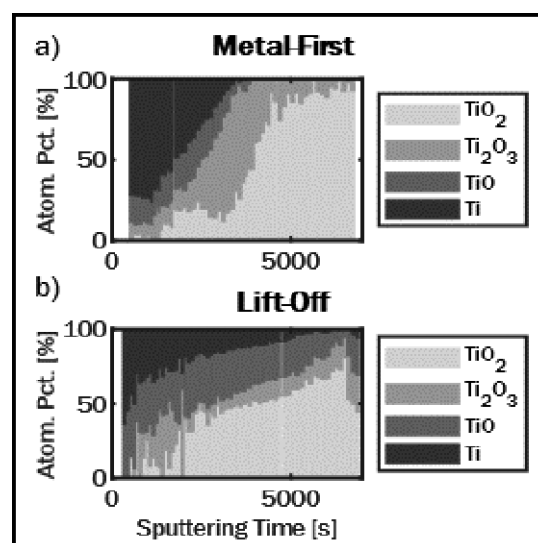


Figure 2: Comparison of Ti oxidation state from depth-resolved XPS for a) metal-first and b) lifted off Ti/Au ohmic contacts. For the metal-first contacts, Ti is fully oxidized to Ti⁴⁺ near the Ga₂O₃ interface, while for the lifted-off contacts, Ti is only partially oxidized.

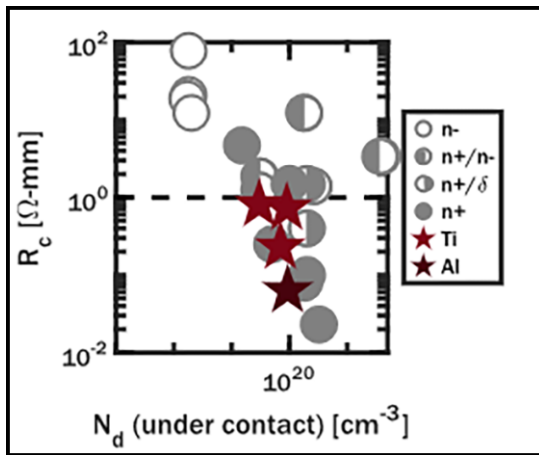


Figure 3: Bench-marking of ohmic contacts to Ga_2O_3 from literature (grey) and this work (red). The non-alloyed metal-first contacts are highly competitive with existing reports.

The lifted-off contacts, however, are non-conductive. Depth-resolved x-ray photoelectron spectroscopy (XPS) measurements of the oxidation state of titanium near the metal-semiconductor interface for the metal-first contacts demonstrate a smooth transition from metallic Ti to fully-oxidized TiO_2 near the Ga_2O_3 surface (Figure 2a). In the lifted-off contacts, however, the oxidation state of Ti is far more disordered, and the Ti layer is not fully oxidized even at the Ga_2O_3 surface (Figure 2b).

This implies that liftoff processing can detrimentally modify the $\beta\text{-Ga}_2\text{O}_3$ surface and inhibit ohmic contact formation.

The metal-first process was then applied to fabricate TLM patterns with three ohmic (low Φ_M) metals (Al, Ti, and Cr). TLM measurements have linear-ohmic IV behavior for Al and Ti contacts, with highly-leaky Schottky behavior for Cr contacts due to the higher Φ_M . The Al contacts have an ultra-low contact resistance of $70 \text{ m}\Omega\text{-mm}$, which is among the lowest reported values of R_c (Figure 3). Metal-first anode Schottky barrier diodes were also fabricated with three Schottky (high Φ_M) metals (Ni, Pd, and Pt). For the ohmic metals, Φ_B was extracted from the specific contact resistance using the thermionic field emission (TFE) model. For the Schottky metals, Φ_B was extracted from C-V, forward I-V fitting with the TFE model, and reverse I-V fitting with a numerical reverse leakage model developed by W. Li, et al [2]. The resulting barrier heights have a linear

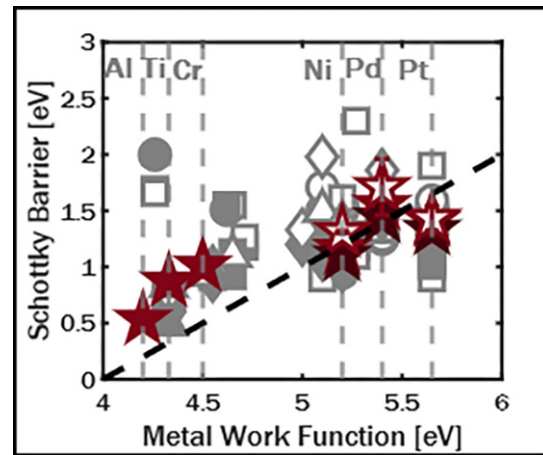


Figure 4: Measured Φ_B vs. Φ_M for contacts to Ga_2O_3 from literature (grey) and this work (red). The extracted Φ_B in this work increases with increasing Φ_M with a slope of 0.46 and R2 of 0.986, while reports from literature show significant Fermi-level pinning with very little dependence of Φ_B on Φ_M .

dependence on Φ_M with a slope of 0.46 and reasonable R2 value of 0.986, indicating that the Fermi-level is at least partially un-pinned by using metal-first contact processing to minimize damage or modification of the $\beta\text{-Ga}_2\text{O}_3$ surface (Figure 4).

Conclusions and Future Steps:

In this work, we demonstrate that metal-first contact processing decreases surface modification in $\beta\text{-Ga}_2\text{O}_3$ compared to liftoff processing and results in ultra-low non-alloyed contact resistances ($70 \text{ m}\Omega\text{-mm}$). Further, metal-first processing can at least partially un-pin the Fermi level in ohmic and Schottky contacts to $\beta\text{-Ga}_2\text{O}_3$, leading to an S value of 0.46. The surface orientation dependence of Fermi-level pinning bears further investigation, as this work included only a limited set of orientations, as does the temperature stability of these metal-first contacts, which is critical for high voltage device performance.

References:

- [1] L. A. M. Lyle, J. Vac. Sci. Technol. A, 40, 060802 (2022).
- [2] W. Li, D. Saraswat, Y. Long, K. Nomoto, D. Jena, and H. G. Xing, Appl. Phys. Lett., 116, 192101 (2020).

Transparent Dual Polarized Antenna

CNF Project Number: 2865-20

Principal Investigator(s): Amal El-Ghazaly¹

User(s): Rabia Yahya², Haosen Yin¹, Amal El-Ghazaly¹

Affiliation(s): 1. Electrical and Computer Engineering, Cornell University;

2. Department of Physics, Nouakchott University, Nouakchott, Mauritania

Primary Source(s) of Research Funding: NSF grant no. 2239066

Contact: ase63@cornell.edu, ry355@cornell.edu, hy584@cornell.edu, ase63@cornell.edu

Research Group Website: vesl.ece.cornell.edu

Primary CNF Tools Used: ABM Contact Aligner, PV75 Sputtering System, Even/Odd Hour Evaporators

Abstract:

Herein, we present a novel transparent antenna with ultra-wideband (UWB) performance along with polarization diversity through four ports allowing MIMO operation. The antenna design can be of a great interest for a vehicular applications and Internet of Things (IOT) where the dual polarization and multiple ports allows as well as medical glasses and vehicular windows where transparency is needed for visibility. The proposed antenna provides compact size with dimensions of 50 mm x 50 mm, through the employment of CPW, dual orthogonal-polarization, isolation level of 20 dB, and envelope correlation coefficient (ECC) of 0.0016 as well as MIMO performance.

Summary of Research:

The structure of the proposed antenna, as shown in Figure 1, is a circular slot fed by four coplanar waveguide (CPW) lines through four semi-circular patches placed in a perpendicular arrangement to achieve orthogonal polarization. Four strips are inserted between the semi-circular patches to enhance the isolation between the ports and maximize the polarization purity of the antenna. The conductive layer of the antenna is composed of a thin film of Silver (Ag) inserted between two layers of Indium Tin Oxide (ITO). The conductor stack was deposited onto a glass substrate with approximate structure of ITO (48 nm)/Ag (17.5 nm)/ITO (42 nm)/Glass (0.7 mm) as reported in [1], where a transparency of 88% and sheet resistance of 3.1 Ω/sq are achieved. A Corning Eagle XG glass substrate is used, having a relative permittivity of 5.27, loss tangent of 0.001, and thickness of 0.7 mm.

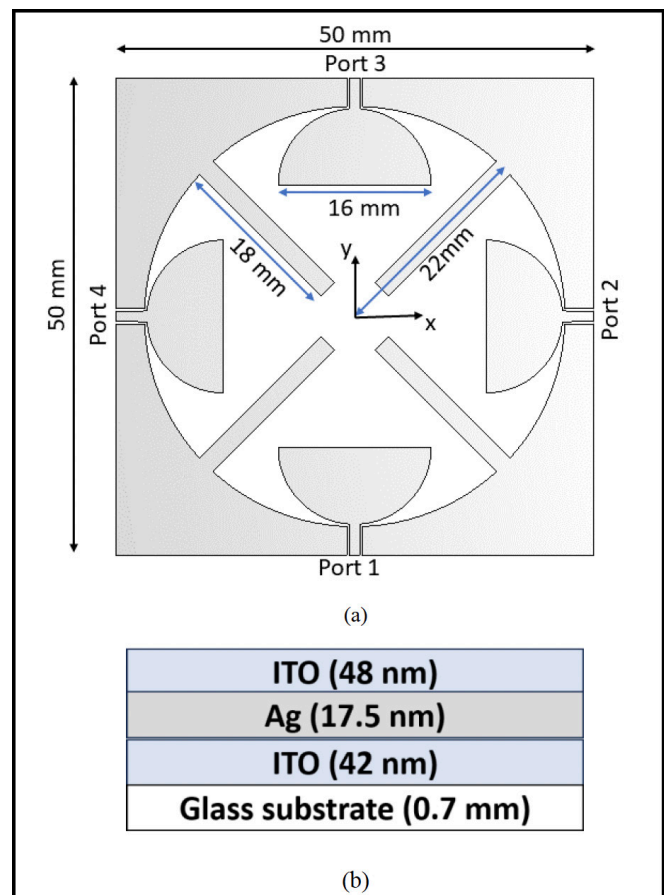


Figure 1: Structure of the proposed antenna. a) Perspective view and b) side view of the antenna design.

The proposed structure has been fabricated in the Cornell NanoScale Facility (CNF) and a picture of the fabricated antenna is included in Figure 2.

The fabrication process began by first, cleaning the glass substrate with acetone and isopropyl alcohol, then prebaking it before coating it with LOR-3A and S1813 photoresists. The antenna design was then exposed onto the substrate using a contact aligner and the pattern was developed. ITO was then sputtered onto the glass substrate on one side using an Indium-Tin target in a Kurt J. Lesker PVD 75 sputtering tool with a partial pressure of oxygen and a substrate temperature of 100°C. The composition of the ceramic sputtering target used is 90% Indium/10% Tin.

After sputtering the ITO, a layer of Ag with thickness of 17.5 nm was e-beam evaporated using a CHA evaporator. Later, the process of ITO deposition was repeated.

Subsequently, the substrate was soaked in Microposit Remover 1165 and sonicated to lift-off the photoresist and achieve the desired pattern. The substrate was then diced in a Disco wafer saw to extract the precise square antenna piece.

As a final step, 50 Ω SMA ports were connected to the antenna CPW feed lines using a conductive epoxy to prepare the antenna for measurement.

Conclusions:

An ultra-wide band transparent antenna with features suitable for MIMO is proposed for various applications across automotive, IOT, and medical industries, among others. The performance of the antenna has been proven through simulation as well as primarily measurement results with return loss below -10 dB and an isolation level of 20 dB. The proposed antenna provides high transparency, a symmetric and compact structure, dual orthogonal polarization with similar radiation patterns, and diversity characteristics with ECC less than 0.0016 and DG on the order of 10 dB over the entire UWB.

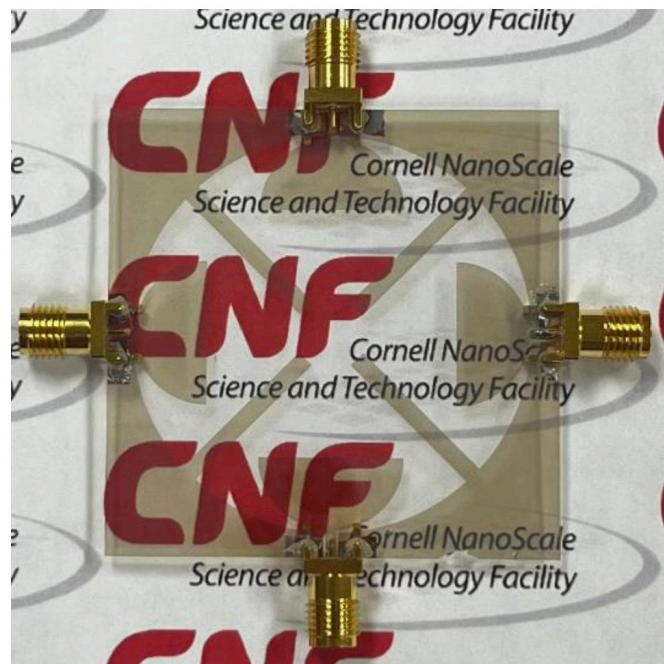


Figure 2: Image of the fabricated transparent antenna prototype.

References:

- [1] J. -W. Kim, J. -I. Oh, K. -S. Kim, J. -W. Yu, K. -J. Jung and I. -N. Cho, "Efficiency-Improved UWB Transparent Antennas Using ITO/Ag/ITO Multilayer Electrode Films," *IEEE Access*, vol. 9, pp. 165385-165393, 2021, doi: 10.1109/ACCESS.2021.3131868.

Superconducting Microwave Devices at the CNF

CNF Project Numbers: 2998-22, 3117-23

Principal Investigator(s): Valla Fatemi

User(s): LuoJia Zhang, Haoran Lu, Kushagra Aggarwal, Saswata Roy

Affiliation(s): School of Applied and Engineering Physics, Cornell University

Primary Source(s) of Research Funding: Lab start-up account, AFOSR

Contact: vf82@cornell.edu, lz282@cornell.edu, hl2396@cornell.edu, ka543@cornell.edu, sr938@cornell.edu

Research Group Website: <https://fatemilab.aep.cornell.edu/>

Primary CNF Tools Used: Heidelberg DWL2000, ABM contact aligner, AJA sputterer, AJA ion mill, Glen 1000, Angstrom e-beam deposition, both JEOL systems

Abstract:

The Fatemi Lab is interested in a spectrum of nanodevice research ranging from low dimensional materials to quantum circuits, with a focus on superconductivity, including novel superconductors or device physics enabled by superconductors. In the last year we have advanced our capability in superconducting qubit and resonator fabrication, as well as in graphene Josephson junctions.

much higher contact transparency than Ti/Nb contacts deposited by magnetron sputtering. This could be due to work function mismatch or interface damage. We are continuing to investigate improved contacts by leveraging this observation. Preliminary Josephson devices, both two- and multi-terminal have been successfully tested in our lab.

Summary of Research:

We have developed high quality resonators and Josephson junctions for superconducting microwave qubits. With the transmon qubit and readout resonator fabricated partially at CNF, we demonstrated a new quantum control protocol [1]. We are also leveraging these skills to investigate novel materials and fabrication methods for superconducting qubits, aiming for higher performance.

Additionally, in our graphene mesoscopic superconductivity efforts, we have recently found that Ti/Al contacts deposited by e-beam evaporation have

Conclusions and Future Steps:

We have developed useful qubit and graphene Josephson junction fabrication at the CNF. Moving forward, we anticipate development of superconducting qubits and other novel microwave-frequency devices based on novel materials and graphene Josephson devices.

References:

[1] <https://arxiv.org/abs/2405.15695>

System-on-Foil

CNF Project Number: 3028-22

Principal Investigator(s): Shane McMahon, Graeme Houser

User(s): Dylan Richmond, Marcus Gingerich, Chad Moore

Affiliation(s): Lux Semiconductors Inc.

Primary Source(s) of Research Funding: NSF SBIR Grants

Contact: smcmahon@luxsemiconductors.com, ghouser@luxsemiconductors.com, drichmond@luxsemiconductors.com, mgingerich@luxsemiconductors.com, cmoore@luxsemiconductors.com

Research Group Website: luxsemiconductors.com

Primary CNF Tools Used: Electron-beam Evaporator (Odd & Even Hour), AJA Sputter, PT740, Trion III Minilock, SEM Supra & Ultra, Logitech CMP Orbis, Oxford PECVD, Heidelberg Mask Writer DWL2000, DISCO Dicing Saw, Oxford FlexAL, Savannah ALD

Abstract:

Lux Semiconductors is developing a new system-level advanced packaging technology, System-on-Foil, designed to overcome limitations of current packaging technologies. This architecture integrates a patterned metal core substrate, facilitating high-speed signal transmission between redistribution layers on the top and backside. Copper transmission lines are patterned in silicon wafer toolsets to achieve interposer-like densities, enabling high bandwidth, low latency routing for chiplet-based heterogeneous integration. The rigid metal substrate allows for thicker dielectric layers that enable low loss high speed transmission lines, leveraging the metal substrate as reference ground. High speed signal can be routed through the metal core in impedance matched coaxial vias with near zero crosstalk. The metal core also provides good thermal conductivity, CTE compatibility with silicon, and durability even in ultra-thin form factors.

Summary of Research:

Layers of circuitry containing oxides and metals are deposited and processed onto thin, metal wafers to

realize interposer chiplets with 2.5D architecture. These chiplets act as intermediaries in the signal routing and delivery between transistor and PCB domains.

Conclusions and Future Steps:

We have realized thin, metal foil interposers, and integrated them with traditional and flexible hybrid electronics to demonstrate our technology. Our more recent work has been focused on increasing the number of layers with applications toward integrating high bandwidth memory with compute modules, photonics, and nurturing the chiplet ecosystem. Our future steps are to continue to deliver on our customer's needs. At the CNF, we look to learn and adapt to the challenges that are associated with layering thick oxides and metals together to achieve several-micron tall layer stacks. Development of our platform is also taking place at other NNCI institutions, such as Georgia Tech and U Penn.

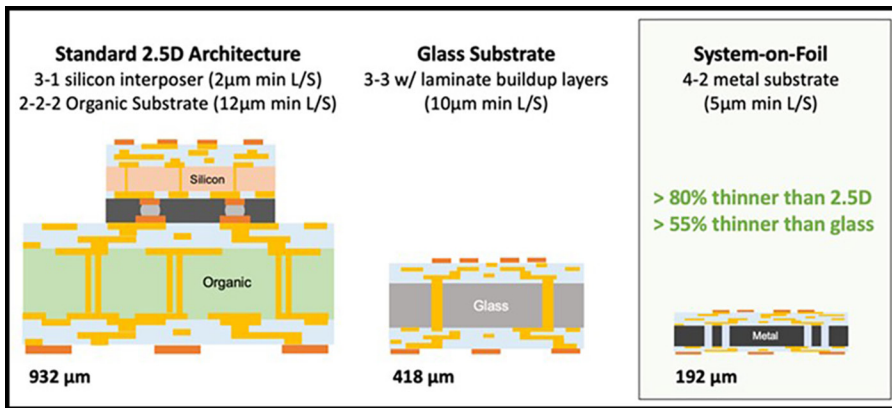


Figure 1: Advanced packaging cross sectional comparison.

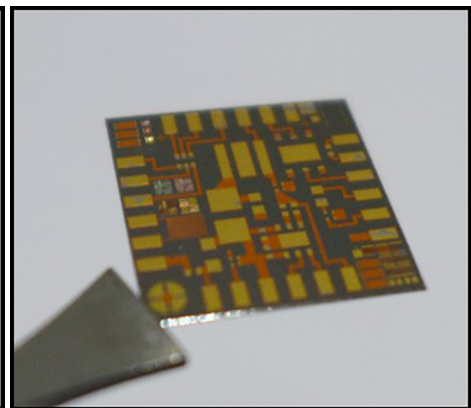


Figure 2: Completed metal foil interposer.

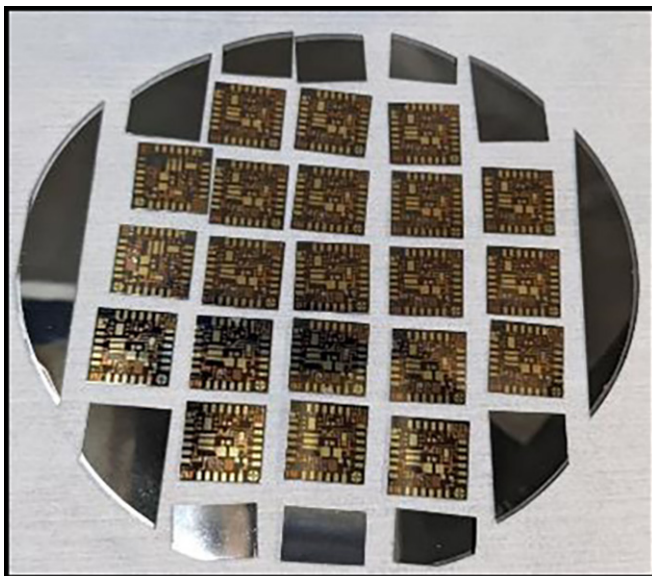


Figure 3: Completed 100 mm diameter metal foil substrate containing 21 interposers.

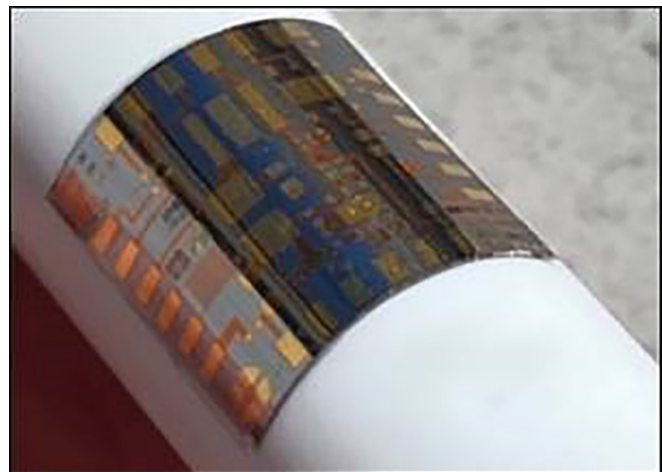


Figure 4: Metal foil interposer wrapped around a tube of Chapstick.

ASIC Design for a Fast X-Ray Pixel Array Detector

CNF Project Number: 3065-23

Principal Investigator(s): Julia Thom-Levy

User(s): Nicholas Brown, Mark Tate, Sixuan Li

Affiliation(s): Laboratory of Atomic and Solid-State Physics, Cornell University

Primary Source(s) of Research Funding: United States Department of Energy

Contact: jt297@cornell.edu, njb234@cornell.edu, mwt5@cornell.edu, sl2536@cornell.edu

Primary CNF Tools Used: Cadence Virtuoso Software

Abstract:

The first Keck X-ray pixel array detector (Keck-PAD) was developed at Cornell University in the late 2000s. It is a high speed, high flux, photon burst detector that can take and store eight images at an image rate of roughly 10 MHz. It was designed to study fast condensed matter physics processes, such as crack propagation and materials failure, via x-ray diffraction at synchrotron storage ring x-ray sources, such as the Cornell High Energy Synchrotron Source (CHESS). However, synchrotron sources continue to advance in speed and brilliance thereby opening opportunities to study processes that require imaging at rates that exceed 10 MHz. Methods to create the K3 test chip (K3TC) — a chip with faster pixel electronics that follows in the footsteps of the original Keck detector — are presented in this report.

Summary of Research:

The K3TC ASIC is organized as a 16 x 16 imaging array. A block diagram of the K3TC pixel can be seen in Figure 1. Incoming X-rays strike a semiconductor sensor, represented with a reverse biased diode in the diagram. This creates a correlated number of electron-hole pairs that are then separated by a large high voltage bias. K3TC can collect either electrons or holes, depending on the sensor. Once the charge has been collected, it is then integrated across CF1. A corresponding voltage is then produced at the output node of the amplifier. If this output voltage crosses an externally set threshold, VTH, then the pixel triggers adaptive gain, closing .AG, and adding more capacitance to the integrator. This, in turn, decreases the gain of the integrator, allowing it to collect

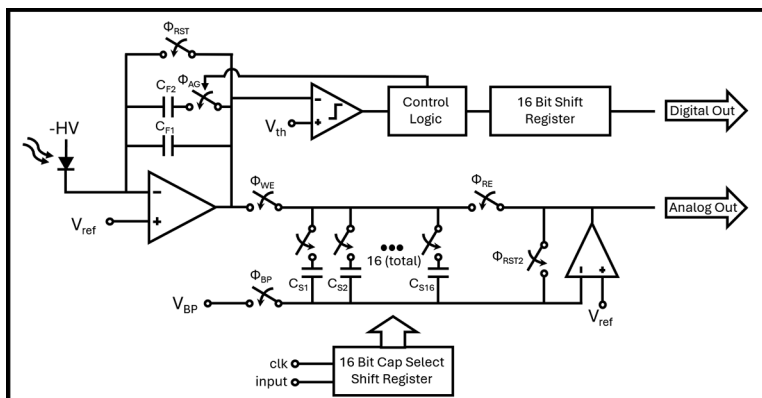


Figure 1: Block diagram of a single pixel for the K3TC.

more X-rays before saturating. At the end of an image the voltage is stored on a storage capacitor (CS1, CS2, etc.) and if the adaptive gain has been triggered, a digital “1” is added to the 16-bit shift register. The front end is then reset via .RST, and the next storage capacitor is switched in. The process is then repeated until all sixteen images have been taken.

After all sixteen images have been collected, the data is read off chip at a much slower rate. The analog and digital data is streamed from the chip in different channels and the analog data is converted to digital off chip. It is then passed into an FPGA, processed, and passed into a computer.

The first step of the current project was to identify the pain points in the previous Keck PAD. Real world tests found that the original Keck PAD could run at about 10 MHz (100ns per frame), but image quality began to break down at higher speeds [1]. Simulations performed in Cadence Virtuoso were used to identify limitations in the front-end amplifier and the reset switch. As can be seen in Figure 1, the design relies on an integrating op-amp, which needs to be fast to allow for the detector to keep up with all the large amount of signal. A new amplifier was drafted and simulated. It sacrifices DC gain for speed, while maintaining similar amounts of power draw. A new simple redesign of the reset switch reduced the on resistance, which speeds up resets.

Next, elements from another ASIC designed in the group, the Mixed-Mode PAD (MM-PAD) — a continuous imager designed for longer time scale, higher flux experiments than K3TC [2] — were incorporated and a K3TC test chip was submitted and fabricated in TSMCs 180 nm node size.

Conclusions and Next Steps:

A first step towards a fast X-ray pixel array detector was achieved, opening opportunities to study processes

that require imaging at rates that exceed 10 MHz. A fast front-end amplifier was designed and a 16 x 16 pixel ASIC was fabricated in TSMC's 180 nm node size. Next, the functionality of the ASIC will be tested. For this purpose, a PCB has been developed to hold, power, and control parts of the chip. Data processing and finely tuned digital control will be done on an FPGA. Tests will focus primarily on speed, as well as noise performance, power consumption, and readout. Multiple test structures have been built into the chip and will be used to verify functionality of its components. Additionally, X-ray sensors will be bonded to the ASIC and tests will be conducted using optical pulsed lasers and X-rays sources.

References:

- [1] L. Koerner, "X-ray analog pixel array detector for single synchrotron bunch time-resolved imaging," Cornell University, 2010.
- [2] K. S. Shanks, Characterization of a Small-Scale Prototype Detector with Wide Dynamic Range for Time-Resolved High-Energy X-Ray Applications, Cornell University: IEEE, 2021.

Preferential Electro spray Deposition onto Interdigitated Electrodes

CNF Project Number: 3109-23

Principal Investigator(s): Paul Chiarot

User(s): Bryce Kingsley

Affiliation(s): Mechanical Engineering Department, State University of New York at Binghamton

Primary Source(s) of Research Funding: SUNY Binghamton IEEC Grant

Contact: pchiarot@binghamton.edu, bkingsl1@binghamton.edu

Research Group Website: <https://sites.google.com/binghamton.edu/mmfl>

Primary CNF Tools Used: AJA Sputter System(s), Heidelberg DWL2000, Hamatech Wafer Processor(s), SUSS MA6-BA6 Contact Aligner, YES Image Reversal Oven, YES Vapor Prime Oven, DISCO Dicing Saw, Photoresist Spinners/Hotplates

Abstract:

Electrospray deposition is an additive process that uses strong electric fields to atomize a liquid solution into a fine spray of charged microdroplets. Solute material dispensed in the liquid will be contained in the droplets, which undergo rapid in-flight solvent evaporation until dry particles of solute remain and are deposited on a surface to create a film. In this work, we investigate the preferentiality of electro spray deposition onto substrates with conductive and insulative components. Micro-scale devices were fabricated at the Cornell NanoScale Facility (CNF) that consisted of interdigitated metal electrodes on glass substrates. Fluorescent nanoparticles were electro spray-deposited onto the devices and imaged with fluorescent microscopy to evaluate the preferentiality of deposition onto the conductive electrodes versus the insulative glass substrate.

Summary of Research:

In this work we investigated the preferentiality of electro spray-deposited polymer films on multi-material substrates (i.e., substrates with conductive and insulative components). Figure 1 contains a schematic of the electro spray deposition process, which begins from a precursor solution composed of a solute material (polymer) in a volatile carrier solvent. The precursor solution is pumped through an emitter and charged with a high electric potential (3-5 kV) causing the liquid meniscus at the tip of the emitter to deform into a cone (Taylor Cone). A charged microjet is emitted from the tip of the conical meniscus which breaks up into a spray of nano- and micro-sized droplets. The volatile carrier solvent rapidly evaporates from the droplets, rendering a spray of dry (solvent-free) solute particles that are delivered to the substrate to create a film.

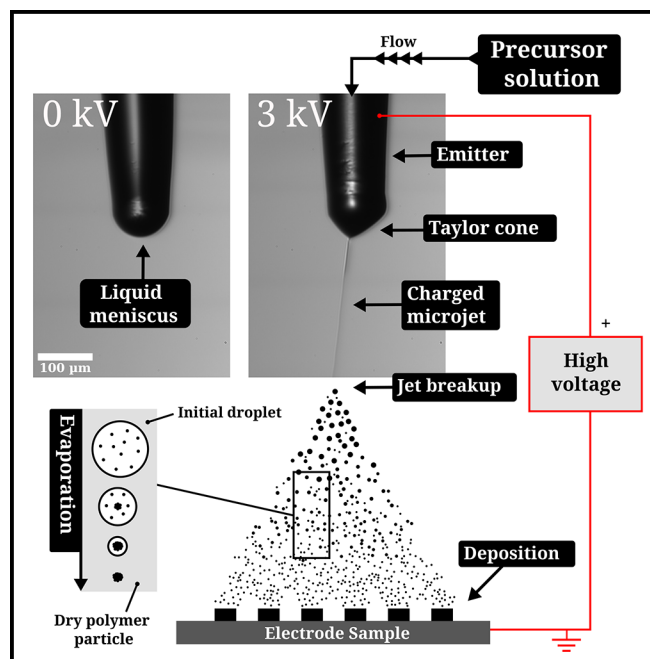


Figure 1: Schematic of electro spray deposition.

The deposition pattern of an electro spray is governed by the electric field formed between the emitter and the substrate. The charged droplets/particles follow the electric field lines to the target which preferably terminate on grounded conductive surfaces, allowing for preferential deposition of material onto conductive surfaces (versus neighboring insulative surfaces). In this work, we probed the geometric limits of preferential electro spray deposition by fabricating micro-scale devices at the CNF that were composed of interdigitated metal electrodes on glass substrates.

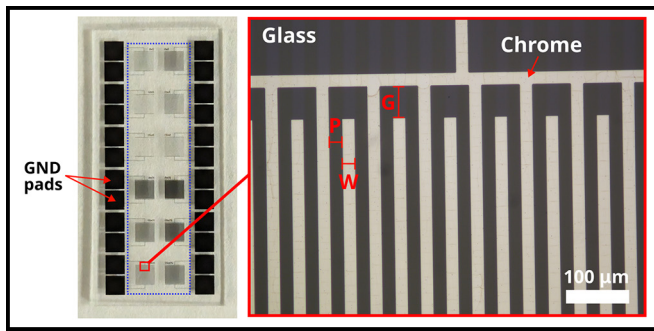


Figure 2: Optical and microscopic images of the electrode devices fabricated at CNF.

Figure 2 contains a photo and microscope image of a single device with 12 arrays of interdigitated chrome electrodes on a glass substrate. Each array on the device had a different electrode width (W) and pitch (P), with widths of 2, 5, 10, 20 μm and pitches of 5, 10, 20 μm . The microscope image outlined in red shows the 20 x 20 μm ($W \times P$) array. All arrays used a uniform channel gap (G) of 50 μm . The interdigitated electrode devices were fabricated at the CNF.

The electrode pattern was designed using a python GDSII library (phidl) and converted to a mask using the mask writer at the CNF. Following mask fabrication, the device fabrication process was as follows: (1) sputter deposition of chrome (200 nm) onto glass substrate, (2) photoresist (S1805) spin-coating and baking, (3) expose with contact aligner, (4) NH_3 image reversal, (5) flood exposure and develop, and (6) wet-etch chrome to reveal pattern.

The preferentiality of deposition onto the electrodes was evaluate by electro spraying fluorescent polystyrene nanoparticles (~ 100 nm diameter) and imaging with fluorescent microscopy. Figure 3 contains fluorescent microscope images of polystyrene deposition onto the electrodes. The image on the left is of the device that was fabricated (at CNF) using soda-lime (SL) glass as the substrate, and the device in the right image was fabricated on Borofloat (BF) glass. Notably, there is a

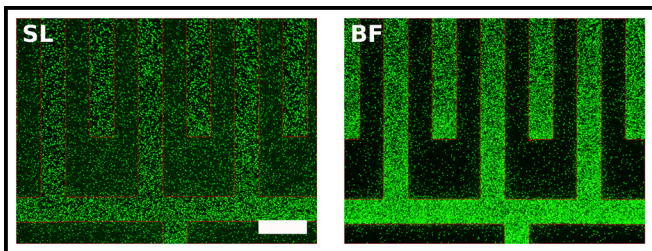


Figure 3: Fluorescent microscopy images showing the effect of glass substrate on preferentiality of electro spray deposition. Soda-lime glass is denoted by SL and Borofloat glass is denoted by BF. Scale bar in 40 μm .

significant difference in the deposition on the SL glass versus the BF glass. The device with SL glass (left) received a significantly greater amount of material on the glass substrate (the black area) compared to the device with BF glass (right) which received a minimal amount of material on the glass. The deposition onto the glass of the SL device (left) results in decreased coverage on the electrodes (outlined in red), as material is “lost” to the glass substrate. In contrast, the device with BF glass (right) has much greater coverage on the electrodes since less material was delivered (lost) to the glass substrate.

Figure 4 plots the preference ratio (ratio of deposition onto electrodes vs. glass) versus metallization ratio (ratio area of electrodes vs. glass). Larger metallization ratios equate to electrodes with less glass area, resulting in preference ratios near or exceeding 0.9 (90%). Over all metallization ratios, the devices with BF glass substrate have greater preferentiality than those with SL glass. The difference in preferentiality between the SL and BF glass can be attributed differences in their dielectric properties. Electro spray deposition is highly sensitive to the electrical properties of the target material. For dielectric materials, the rate of charge decay governs the deposition onto the substrate. For preferential deposition, dielectrics with low rate of charge decay (BF glass) are beneficial as charge that is delivered (from the charged particles of the electro spray) to the surface of the dielectric will remain for a longer period of time and inhibit other charged particles from landing. Deposited charge will dissipate faster on dielectric with high charge decay (SL glass), resulting in greater accumulation of material on the glass.

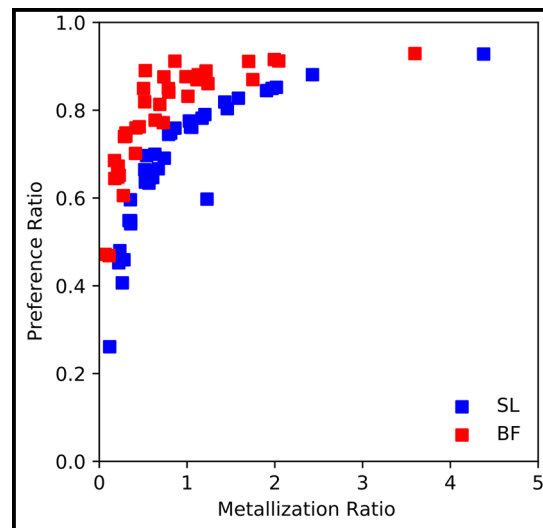


Figure 4. Plot of preference ratio vs. metallization ratio for SL glass (blue) and BF glass (red) substrates.

Micro-Scale Ceramic Additive Manufacturing for Aerospace Applications

CNF Summer Student: Elizabeth Quansah

Student Affiliation: MSE, University of Illinois at Urbana-Champaign

Summer Program(s): 2024 Cornell NanoScale Facility Research Experience for Undergraduates (CNF REU) Program

Principal Investigator(s): Sadaf Sobhani, Department of Mechanical and Aerospace Engineering, Cornell University

Mentor(s): Giancarlo D'Orazio, Department of Mechanical and Aerospace Engineering, Cornell University

Primary Source(s) of Research Funding: National Science Foundation under Grant No. NNCI-2025233

Contact: elizaq99@gmail.com, sobhani@cornell.edu, gd373@cornell.edu

Summer Program Website: <https://cnf.cornell.edu/education/reu/2024>

Primary CNF Tools Used: Nanoscribe Photonic Professional GT2, Zeiss Ultra Scanning Electron Microscope

Abstract:

This paper suggests mechanisms for producing silica glass microscale electro-spray emitters for spacecraft propulsion systems and prefaces the potential of these methods for producing microscale ceramics. The following research is conducted in an effort to replace tungsten needles currently used as emitters and explore micro-scale additive manufacturing. This work relies on two-photon photolithography for additive manufacturing green bodies that undergo thermal processing to produce silica glass, silicon carbide (SiC), or silicon oxycarbide (SiOC). GP Silica, a polymer-based resin containing glass nanoparticles, is converted into emitter-shaped green bodies using the Nanoscribe Photonic Professional GT2. Conversion of SiC and SiOC precursor resins into green bodies using the Nanoscribe is also attempted as in previous works [1-3], and the SiOC precursor exhibits success. Thermally processing green bodies is completed in an air furnace to produce glass and a microwave furnace to produce SiC and SiOC. Characterization of resulting structures suggests high potentials for additively manufacturing glass and thermally processing ceramics in the microwave furnace, although further optimizations remain necessary.

Summary of Research:

Additive manufacturing demonstrates increasing promise for device fabrication, making identifying technological limitations of interest. The Nanoscribe Photonic Professional GT2, a micro-additive manufacturing technology utilizing two-photon photolithography, fires a 780 nm femtosecond laser that is re-emitted at 390 nm after striking a molecule within the resin it is printing with. This provides sufficient energy to cure the resin. This paper explores the Nanoscribe's ability to micro-additively manufacture green bodies for thermal processing to make silica glass, silicon carbide (SiC), and silicon oxycarbide (SiOC).

GP Silica is a polymer-based resin containing glass nanoparticles. Developing emitter green bodies with this resin requires optimizing print parameters using the 10X large feature objective. This was completed by printing a 4 x 4 array of 150 μm cubes on a silicon substrate. Scan speed varied along one axis and laser power along the other. 60% laser power and 80,000 $\mu\text{m}/\text{s}$ scan speed produced the smoothest edges and fewest bubbles.

The array was placed in a Nabertherm air furnace for thermal processing according to NanoGuide's standard curve [4], which peaks at 1300°C with 3 hour holds at 90°C, 150°C, 230°C, and 280°C. Following sintering, the array was imaged under the scanning electron microscope (SEM), revealing that 14/16 cubes survived, 12 of which were smooth without cracks or bubbles (Figure 1).

Due to this success, solid glass emitters with a 1000 μm base, 700 μm height, and 20° cone angle were attempted using the same process (Figure 2). Many emitters survived, although deformed, as signified by an estimated 55% shrinkage instead of the expected 30%. Next, a new batch of solid emitters and emitters with porous exteriors were printed and heated for 20 hours in the air furnace according to NanoGuide's fast curve4, which ramps to 1300°C at 180°C/hr, saving approximately 40 hours compared to the standard curve. These emitters were more successful, as demonstrated by an estimated 24% shrinkage (Figure 3).

To determine whether a similar process is possible for producing SiC and SiOC emitters, SiC and SiOC precursor resins were developed for printing on the Nanoscribe with 63X oil immersion on glass substrates. Starfire SMP-10 and Starfire SPR-688 were homogenized into resins by mixing in 1%/wt 2-Isopropylthioxanthone and 9%/wt 1,6-Hexanediol diacrylate. Attempting to print with the SiC precursor Starfire SMP-10 based resin using a 10,000 $\mu\text{m}/\text{s}$ scan

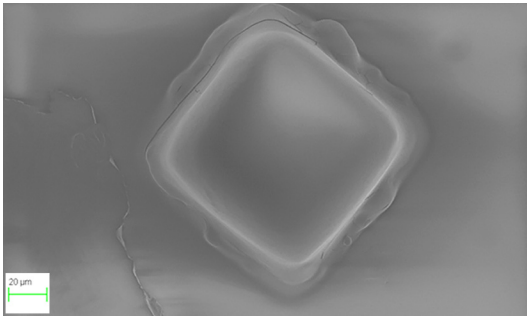


Figure 1: A successful glass cube has a smooth surface without cracks and bubbles.

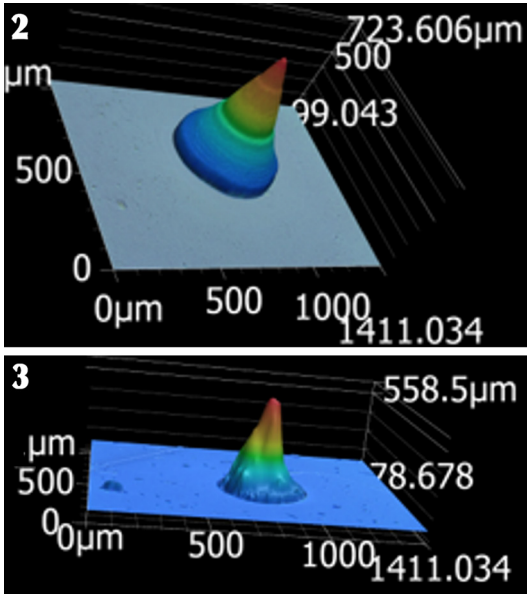


Figure 2: Keyence image of a GP Silica solid emitter green body. Figure 3: Keyence image of a solid glass emitter.



Figure 4: The alumina crucible is lined with SiC and goes inside of a 1 kW microwave.

speed with laser power ranging from 30% to 80%, as well as a 20,000 $\mu\text{m/s}$ scan speed with 70% and 80% laser power produced no parts due to the resin's low viscosity. Significant motion during printing prevented proper curing and substrate adhesion. When printing with the SiOC precursor Starfire SPR-688 based resin, bubbling occurred at laser powers above 50% with a 10,000 $\mu\text{m/s}$ scan speed, suggesting that printing is possible with the SiOC precursor but not the SiC precursor for the formulations and settings tested.

Lastly, the microwave furnace, an alumina crucible lined with SiC within a 1 kW microwave that ramps at 150°C/min, was evaluated for thermal processing ceramics. SiC precursor Starfire SMP-10 cured at 200°C and SiOC precursor Starfire SPR-688 cured at 445°C were placed into the microwave furnace independently for 2, 3, 4, and 5 minutes. Examining 4-minute thermally converted SiC precursor optically and using the SEM revealed consistency with SiC and an amorphous silicate phase. Similarly, 3-minute thermally converted SiOC precursor appeared consistent with SiOC after optical examination.

Conclusions and Future Steps:

In conclusion, GP Silica is useful for micro-additively manufacturing glass emitters with the Nanoscribe. The fast heating curve [4] proves effective as demonstrated by the emitters' 24% shrinkage. Additionally, printing was achieved with the SiOC precursor resin, but not the SiC precursor resin.

Finally, the microwave furnace may present an option for sintering ceramics, but further research is required. In the future, optimizing thermal processing glass emitters and developing emitters using the SiOC precursor resin is necessary, along with testing this process with a more viscous SiC precursor resin.

Acknowledgements:

Many thanks to the CNF REU Program of the National Nanotechnology Coordinated Infrastructure funded by National Science Foundation grant no. NNCI-2025233. Special thanks to Sadaf Sobhani, Giancarlo D'Orazio, Giovanni Sartorello, and Melanie-Claire Mallison for their guidance.

References:

- [1] J. Bauer, et al., "Additive manufacturing of ductile, Ultrastrong polymer-derived nanoceramics," *Matter*, vol. 1, no. 6, pp. 1547–1556, Dec. 2019. doi:10.1016/j.matt.2019.09.009.
- [2] G. Konstantinou, et al., "Additive micro-manufacturing of crack-free PDCS by two-photon polymerization of a single, low-shrinkage Pre-ceramic Resin," *Additive Manufacturing*, vol. 35, p. 101343, Oct. 2020. doi:10.1016/j.addma.2020.101343.
- [3] L. Brigo et al., "3D Nanofabrication of SiOC Ceramic Structures," *Advanced Science*, vol. 5, (12), 2018/12//. Available: <https://www.proquest.com/scholarly-journals/3d-nanofabrication-sioc-ceramic-structures/docview/2262718647/se-2>.
- [4] NanoGuide Professional Photonic Series. (n.d.). Retrieved July 8, 2024, from <https://support.nanoscribe.com/hc/en-gb/articles/4402084033810-Printing-with-the-Glass-Printing-Explorer-Set-GP-Silica>.

Synthesis of Temperature-Responsive Hydrogel Particles for Hydraulic Control of Cooled Short Circuits

CNF Project Number: 1356-05

Principal Investigator(s): Ulrich Wiesner

User(s): Danni Tang

Affiliation(s): Department of Materials Science and Engineering, Cornell University

Primary Source(s) of Research Funding: U.S. Department of Energy (DOE),

Office of Energy Efficiency and Renewable Energy (EERE),

Office of Technology Development, Geothermal Technologies Program (DE-EE0009786.000)

Contact: ubw1@cornell.edu, dt427@cornell.edu

Research Group Website: <http://wiesner.mse.cornell.edu/>

Primary CNF Tools Used: Heidelberg DWL2000, ABM Mask Aligner, AMST MVD100

Abstract:

The “short circuit” issue is one of the major challenges that prevents Enhanced Geothermal Systems (EGS) from being commercially successful. In this work, temperature-responsive poly(N-isopropylacrylamide) (pNIPAM)-based hydrogel particles were designed to mitigate the issue by reducing the local permeability of “short circuit” regions. To understand the particle jamming behavior, we fabricated a parallel step emulsifier device at CNF to produce particles with narrow size distribution to conduct fundamental rheology tests.

Summary of Research:

The “short circuit” issue arising from uneven permeability distributions within fracture systems is one of the major challenges in Enhanced Geothermal Systems (EGS). When a fluid gets injected underground, it preferably flows through highly permeable paths. As a result, these regions are rapidly drained of heat, leading to a premature thermal breakthrough and system failure [1]. To alleviate this problem, we designed temperature-responsive nanocomposite poly(N-isopropylacrylamide) (pNIPAM)-based microgel particles. As one of the most studied thermosensitive hydrogel, pNIPAM exhibits a reversible entropy-driven volume phase transition, leading to particle expansion at low temperatures and particle contraction at high temperatures [2]. With careful design, these pNIPAM-based particles can expand to up to several hundred

times their original volume when the temperature of their local environment falls below a threshold. This could effectively diminish short circuits by decreasing local channel permeability.

Particles with varying compositions were successfully synthesized through inverse suspension polymerization (Figure 1a). Single-particle studies conducted under an optical microscope demonstrated the particle’s responsiveness to temperature changes (Figure 1b). However, studying the rheological property of jammed particles remained challenging since inverse suspension polymerization yields highly polydisperse particle sizes (Figure 2). With the aim of better understanding this complex hydrogel particle system, it is desirable to also study a simpler case consisting of monodisperse particles. To facilitate particle production with a narrow size distribution, we fabricated a parallel step emulsifier device using CNF tools.

At CNF, the Heidelberg DWL2000 was used to create photomasks based on the CAD design (Figure 3) adapted from Stolovicki, et al. [3]. Next, a two-layer SU-8 master mold was fabricated in the Class II photoresist room following the procedure described in Figure 4. The resulting mold was subsequently treated with (1H,1H,2H,2H-perfluorooctyl) trichlorosilane (FOTS) to increase its hydrophobicity. Lastly, the device was obtained by casting PDMS onto the master mold. In the next step, microgels with different compositions will be produced using this device for rheology tests.

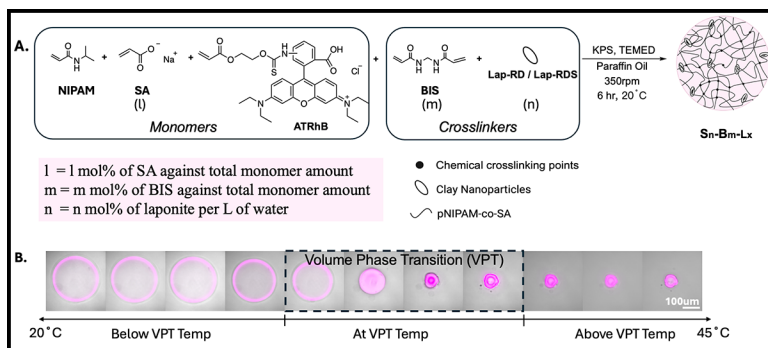


Figure 1: Synthesis of the poly(*N*-isopropylacrylamide) (pNIPAM)-based nanocomposite microgel. (A) General synthesis scheme of the hydrogel particles. (B) Typical volume phase transition observed under the confocal microscope.

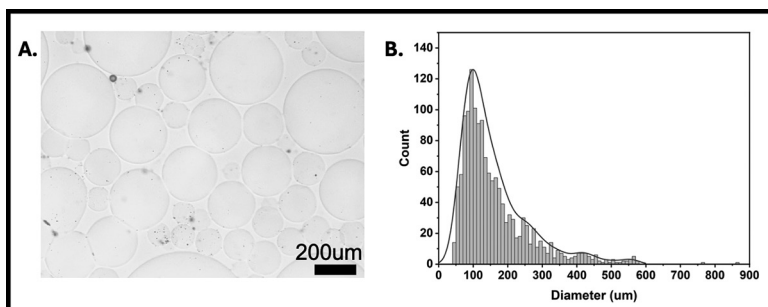


Figure 2: Particle size distributions from batch synthesis. (A) Typical optical images of resulting microgels (Scale bar: 200 μm). (B) Typical size distribution of microgels.

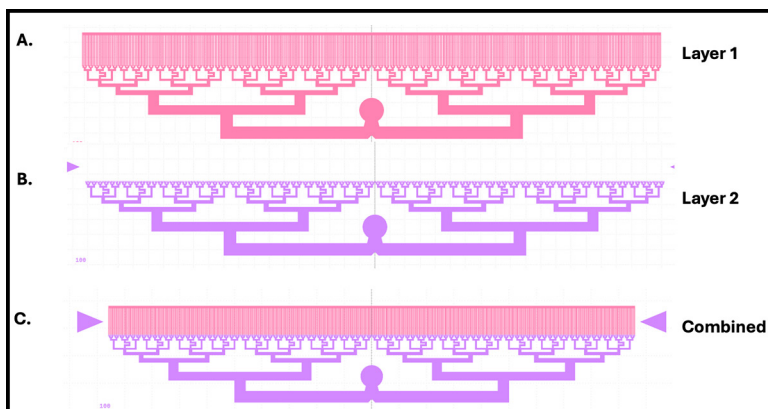


Figure 3: CAD design of the parallel step emulsifier device adapted from the Weitz group [3]. (A) Layer 1; (B) Layer 2; (C) merged images.

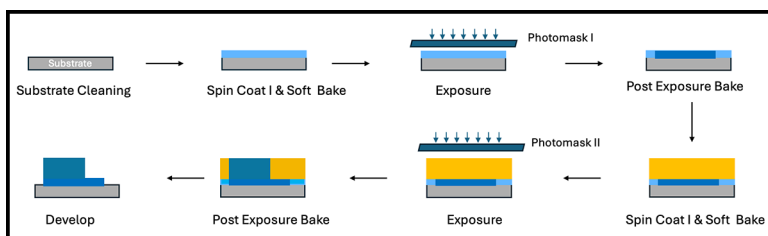


Figure 4: General process flow of the double layer SU-8 master mold fabrication.

Conclusions and Future Steps:

Overall, we synthesized hydrogel particles via inverse suspension polymerization and demonstrated their temperature responsiveness under the microscope. To further understand how individual microgel particles' properties affect the macroscopic rheology properties of the jammed particles, a simple system composed of monodispersed particles was proposed as an alternative. At the CNF, we were able to fabricate an emulsifier device to achieve this goal. In the future, particles with varying compositions will be produced using this device and studied for their rheological behavior.

References:

- [1] Oh, K. W.; Lee, K.; Ahn, B.; Furlani, E. P. Design of Pressure-Driven Microfluidic Networks Using Electric Circuit Analogy. *Lab Chip* 2012, 12 (3), 515–545. <https://doi.org/10.1039/c2lc20799k>.
- [2] Hirotsu S.; Hirokawa, Y.; Tanaka, T. Volume-Phase Transitions of Ionized *N*-Isopropylacrylamide Gels. *Journal of Chemical Physics* 1987, 87 (2), 1392–1395. <https://doi.org/10.1063/1.453267>.
- [3] Stolovicki, E.; Ziblat, R.; Weitz, D. A. Throughput Enhancement of Parallel Step Emulsifier Devices by Shear-Free and Efficient Nozzle Clearance. *Lab on a Chip* 2017, 18 (1), 132–138. <https://doi.org/10.1039/C7LC01037k>.

Low Loss Superconducting LC Resonator for Strong Coupling with Magnons

CNF Project Number: 2126-12

Principal Investigator(s): Gregory David Fuchs

User(s): Srishti Pal, Qin Xu

Affiliation(s): Department of Applied Physics & Engineering, Department of Physics; Cornell University

Primary Source(s) of Research Funding: Department of Energy (DOE),
Center for Molecular Quantum Transduction (CMQT)

Contact: gdf9@cornell.edu, sp2253@cornell.edu, qx85@cornell.edu

Research Group Website: <https://fuchs.research.engineering.cornell.edu/>

Primary CNF Tools Used: AJA Sputter Deposition, Heidelberg Mask Writer - DWL2000, GCA 6300 DSW 5X g-line Wafer Stepper, YES Asher, PT770 Etcher - Left Side, P7 Profilometer, Zeiss Supra SEM, Nability Nanometer Pattern Generator System (NPGS), JEOL 6300, Dicing Saw – DISCO, Westbond 7400A Ultrasonic Wire Bonder

Abstract:

We present a hybrid system based on strongly coupled microwave photons hosted by a microstructured resonator and magnon modes of the molecular ferrimagnet vanadium tetracyanoethylene (V[TCNE]_x). Using Cornell NanoScale Facility (CNF), we develop a process to integrate the fabrication of high quality-factor (Q-factor) superconducting LC resonators and the deposition of lithographically patterned V[TCNE]_x films. We improve the encapsulation of the V[TCNE]_x film using atomic layer deposition (ALD) of alumina (Al₂O₃). We also discuss the design and fabrication of new broadband structures capable of exploring high-power parametric processes in V[TCNE]_x films.

Summary of Research:

This research is focused on studying two systems.

(i) A strongly coupled hybrid photon-magnon system where the coupling strength between the two sub-systems exceeds the mean energy loss in either of them. The key figure-of-merit of this hybrid system is its cooperativity $C=4g^2/k_m k_r$, where g is the coupling strength between magnons and photons, and k_m and k_r are the damping rates for magnons and photons, respectively. The system operates in strong-coupling regime if $C > 1$. (ii) The non-linear excitation of magnons in V[TCNE]_x waveguides using high microwave powers.

As a cavity for microwave photons for the coupled photon-magnon system, we use lumped-element planar LC resonators fabricated on superconducting niobium thin-film offering high Q-factor and thus low The basic steps for patterning our LC resonators using photolithography are shown in Figure 1(a).

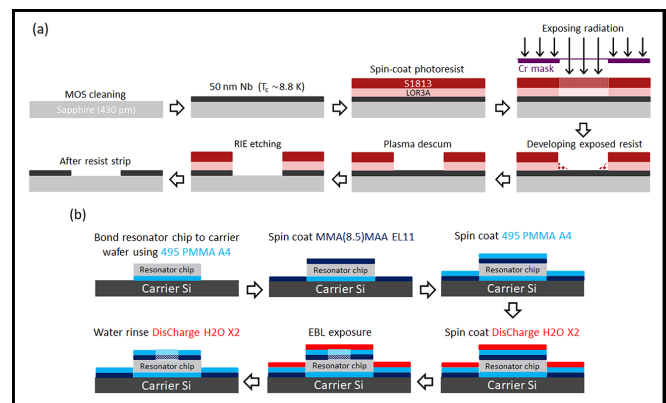


Figure 1: Process flow for (a) patterning the LC resonator using photolithography, and (b) e-beam patterning for V[TCNE]_x deposition.

First, we sputter a 50 nm thick niobium film (thickness measured using P7 profilometer) on a MOS cleaned sapphire substrate using the AJA sputter deposition tool. The superconducting transition temperature (T_c) of our niobium film is ~ 8.8 K, which is high enough to offer low damping in our operating temperature range of 0.4 - 4 K. The resonator design, patterned on a photomask using Heidelberg Mask Writer-DWL2000, is then cast onto the resist coated wafer (we spin-coat a resist bilayer of LOR3A and S1813) using 5X g-line Wafer Stepper. The developed resist (in AZ726MIF) is descummed in YES Asher followed by dry etching of niobium in PT770.

Finally, we strip the resist in 1165 and dice the wafer using Dicing Saw–DISCO to separate the chips patterned on the wafer. For the magnon sub-system, we use the low-loss organic ferrimagnet V[TCNE]_x with a low

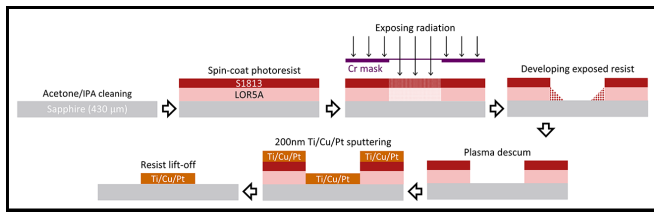


Figure 2: Process flow for fabricating broadband chips with Ti/Cu/Pt tri-layer.

Gilbert damping $\alpha \sim 10^{-4}$ offering long magnon lifetime and thus low k_m . Using e-beam lithography in JEOL 6300 or Naby Nanometer Pattern Generator System (NPGS) connected to Zeiss Supra SEM, we pattern a $6 \mu\text{m}$ wide and $600 \mu\text{m}$ long bar on the $10 \mu\text{m}$ wide and $600 \mu\text{m}$ long inductor wire using the steps shown in Figure 1(b). We then ship the exposed resonator chips to our collaborators in Ohio State University for V[TCNE]x growth and liftoff.

To avoid saturation of the superconducting niobium film due to formation of vortices at high microwave powers, we chose to fabricate the broadband chips with low resistivity Ti/Cu/Pt tri-layer. The steps for this fabrication are illustrated in Figure 2. First, we coat clean (with acetone followed by IPA) sapphire wafers with bilayer of LOR5A and S1813. The resist coated wafer is then exposed in 5X g-line Wafer Stepper to be patterned with the design written on a photomask using Heidelberg Mask Writer-DWL2000. The developed resist (in AZ726MIF) is descummed in YES Asher followed by deposition of 200 nm thick Ti/Cu/Pt tri-layer in the AJA sputter deposition tool. Finally, we lift-off the resist using 1165 and then dice the wafer using Dicing Saw-DISCO.

The degradation of the organic ferrimagnet V[TCNE]x when exposed to air has necessitated its encapsulation, primarily with epoxy and cover glass as also adopted in our earlier studies [1,2]. Despite offering protection against air exposure, this encapsulation suffers from the demerit of exerting large inhomogeneous strain on V[TCNE]x as the sample is cooled down due to the disparate thermal expansion coefficients of sapphire and epoxy. A solution to this problem is to encapsulate with a material that has a similar thermal expansion coefficient to sapphire, like alumina (Al_2O_3). To test the performance of the hybrid resonator-magnon system with alumina as the encapsulation material, we collaborated with Ohio State University for V[TCNE]x growth and Northwestern University for the atomic layer deposition (ALD) of alumina. Figure 3(a)-(c) showcases the microscope images and the schematic cross-section of the alumina encapsulation on the

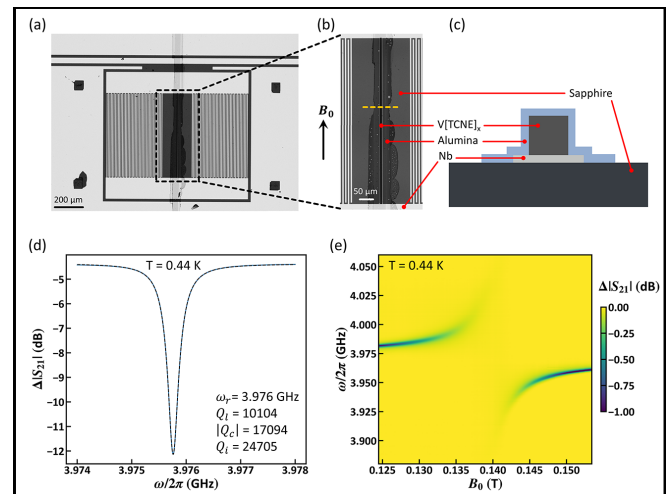


Figure 3: (a) Microscope image of LC resonator device with patterned V[TCNE]x and ALD encapsulation. (b) Magnified microscope image around the region marked with black dashed rectangle in (a). (c) Illustration of the cross section of the device along the yellow dashed line in (b). (d) Fitted (black dashed line) resonator response (blue curve) with extracted Q -factors at 0 T at 0.44 K. (e) 2D colormap of $|S_{21}|$ as a function of static magnetic field and microwave frequency at 0.44 K.

V[TCNE]x bar grown on the inductor wire of our LC resonator. The fitted resonator response at 0.44 K as shown in Figure 3(d) reveals the internal Q -factor as high as 24705. The anti-crossing obtained for the coupled resonator-magnon system is shown in Figure 3(e). The uniaxial anisotropy field H_k , a quantitative measure of the inhomogeneous strain on the V[TCNE]x, extracted from the anti-crossing turns out to be 6.8 mT which is an order of magnitude lower than that obtained for our previous epoxy encapsulated sample [2].

Conclusions and Future Steps:

We have demonstrated our successful upgradation of the V[TCNE]x encapsulation to reduce the strain and hence the magnetocrystalline anisotropy at the cryogenic temperature. We will integrate the broadband chips with V[TCNE]x encapsulated with alumina to explore high-power non-linear instability processes in V[TCNE]x.

References:

- [1] H. F. H. Cheung, et al, "Raman Spectroscopy and Aging of the Low-Loss Ferrimagnet Vanadium Tetracyanoethylene", The Journal of Physical Chemistry C 125, 20380 (2021).
- [2] Q. Xu, et al, "Strong Photon-Magnon Coupling Using a Lithographically Defined Organic Ferrimagnet", Advanced Science 11, 2310032 (2024).

Investigation of Dry Chemical Actuators Using Palladium Thin Films

CNF Project Number: 2736-18

Principal Investigator(s): Nicholas Lawrence Abbott¹

User(s): Hanyu Alice Zhang²

Affiliation(s): 1. Chemical and Biomolecular Engineering, 2. Applied and Engineering Physics; Cornell University

Primary Source(s) of Research Funding: Cornell Center for Materials Research with funding from the National Science Foundation Materials Research Science and Engineering Centers program (DMR-1719875)

Contact: nla34@cornell.edu, hz496@cornell.edu

Research Group Website: <https://nlabbottcornell.weebly.com/>

Primary CNF Tools Used: Heidelberg DWL2000 Mask Writer, ABM Contact Aligner, Oxford 81/82/100 Etchers, AJA Sputter Deposition Tools, Plasma-Therm Takachi HDP-CVD, SC4500 Odd-Hour Evaporator, PT770 Etcher (Left Side), OEM Endeavor Aluminum Nitride Sputtering System, Leica CPD300 Critical Point Dryer, DISCO Dicing Saw

Abstract:

The goal of this work is to design microscale systems that enable the conversion from chemical to mechanical energy via chemomechanical transduction. Previously, by making use of the surface chemistry of platinum, we have demonstrated that a platinum-titanium bimorph can respond to changes in its environment and actuate [1]. In contrast to platinum's surface reactions with gaseous hydrogen and oxygen, palladium is a material known to absorb atomic hydrogen in bulk. In this work, we demonstrate that we can use both surface and bulk properties of palladium to drive actuation.

Summary of Research:

Palladium is well-known for its ability to absorb hydrogen in bulk, thus enabling it to be a material of choice for sensing [2-4], hydrogen purification [2], and storing hydrogen [2,5].

While hydrogen is diffusing into bulk palladium, the material can undergo a phase transition from a hydrogen-poor α phase to a hydrogen-rich β phase depending on the concentration of hydrogen that the palladium is exposed to. The $\alpha \rightarrow \beta$ phase transition causes a lattice expansion which can induce a large amount of strain. This is normally undesirable for sensing and storage purposes, however, in this project we present a novel way to utilize this strain to drive microscopic actuators, enabling the development of mechanisms such as small mechanical switches that can not only sense the presence of hydrogen, but also control the amount of hydrogen present by closing and opening a valve.

Figure 1A shows an array of fabricated hinges post release, and Figure 1B shows an individual hinge. To

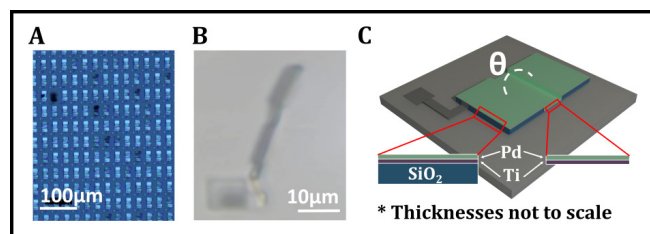


Figure 1: Optical micrographs and 3D rendering of individual hinges.

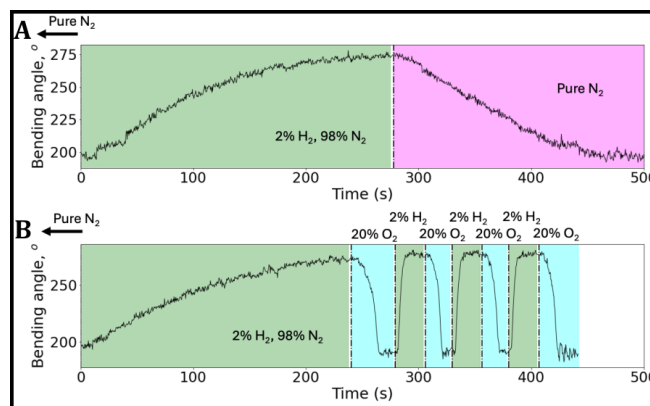


Figure 2: Actuation data upon exposing a hinge to cycling between A) 2 v% H_2 and 20 v% O_2 (All counterbalanced to 1 atm with N_2) and B) 2 v% H_2 and ultra high purity N_2 .

fabricate these hinges, a sacrificial layer of aluminum nitride is used, and rigid 600 nm thick silicon dioxide panels are deposited on top of the aluminum nitride via chemical vapor deposition. After the rigid panels are patterned, a thin layer of titanium is sputtered to act as a tether, after which the bimorph consisting of 20 nm of sputtered titanium and 20 nm of sputtered palladium is deposited, completing the fabrication process. A 3D

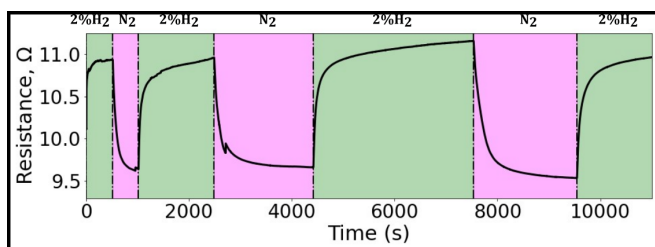


Figure 3: Resistance data upon exposing a palladium film to cycling between 2 v% H₂ and ultra high purity N₂.

rendering of an individual hinge with all the layers is shown in Figure 1C. The chips are then diced, released, dried in the critical point drier, and brought to the lab for experimentation.

Upon exposing the devices to 2 v% H₂, 20 v% O₂, or ultra pure nitrogen (all at 1 atm, H₂ and O₂ counter-balanced with N₂), we observe an actuation of around 100 .on our 3 μm long hinges, as shown in Figure 2.

We also notice that the application of oxygen instead of nitrogen drives faster actuation not only while oxygen is turned on, but also the oxygen affects the rate of actuation while hydrogen is applied.

We think that actuation in 2 v% H₂ and ultra pure nitrogen is driven by the formation of palladium hydride as atomic hydrogen is diffusing into the palladium lattice. Upon the application of oxygen gas to the palladium hydride system, oxygen molecules can dissociate and react with atomic hydrogen in the palladium lattice to form OH. and eventually water. This provides an additional chemical pathway for atomic hydrogen to be removed from the palladium lattice.

To test the formation of palladium hydride, we have conducted additional experiments via the measurement of electrical resistance, as shown in Figure 3.

In addition, because the formation of palladium hydride is known to be a temperature-dependent process, we were able to show that we can drive a similar actuation by cycling the temperature in a 2 v% H₂ environment.

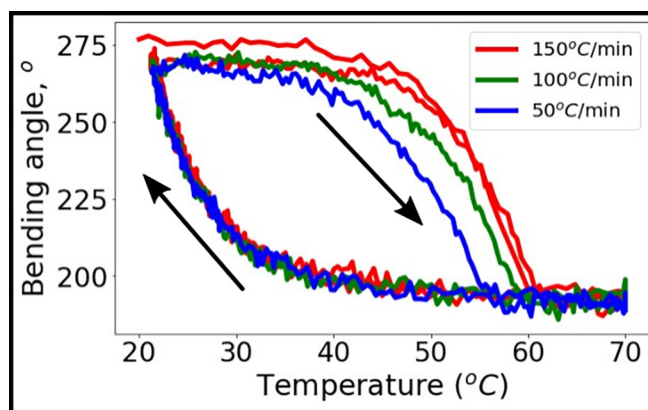


Figure 4: Temperature driven actuation of the palladium hinge under different temperature ramp rates.

Conclusions and Future Steps:

Through numerous analyses and fabrication runs, we have shown that the devices actuate reliably and reproducibly. We are currently in the process of understanding the material science and chemistry behind these actuators and running experiments to test our theoretical models and hypotheses.

References:

- [1] N. Bao, et al. Gas-phase microactuation using kinetically controlled surface states of ultra-thin catalytic sheets. *PNAS*, 120(19), 2023.
- [2] B.D. Adams and A. Chen. The role of palladium in a hydrogen economy. *Materials Today*, 14(6):282-289, 2011.
- [3] I. Darmadi, F. A. A. Nugroho, and C. Langhammer. High-performance nanostructured palladium-based hydrogen sensors—current limitations and strategies for their mitigation. *ACS sensors*, 5(11):3306-3327, 2020.
- [4] C. C. Ndaya, N. Javahiraly, and A. Brioude. Recent advances in palladium nanoparticles-based hydrogen sensors for leak detection. *Sensors*, 19(20):4478, 2019.
- [5] S. K. Konda and A. Chen. Palladium based nanomaterials for enhanced hydrogen spillover and storage. *Materials Today*, 19(2):100-108, 2016.

Metal-Organic Framework-Inspired Metal-Containing Clusters for High-Resolution Patterning

CNF Project Number: 2751-18

Principal Investigator(s): Christopher Kemper Ober

User(s): Emma Hester

Affiliation(s): Department of Materials Science and Engineering, Cornell University

Primary Source(s) of Research Funding: Office of Naval Research (ONR)

Contact: cko3@cornell.edu, egh66@cornell.edu

Research Group Website: <https://ober.mse.cornell.edu/index.html>

Primary CNF Tools Used: Molecular Vapor Deposition (MVD), Atomic Force Microscope (AFM)

Abstract:

In order to treat surfaces for resistance of a wide range of marine organisms, surface chemistry, physical properties, durability, and attachment scheme must all be considered in the synthesis and design of a coating. By synthesizing a hydrophobic polymer backbone and modifying it to contain different functional groups with varying degrees of hydrophilicity, it is possible to achieve an overall amphiphilic material that is resistant to settlement and will promote removal of certain marine species. Surface characterization of these thin films suggests that buffered and zwitterionic species are capable of interfering with calcareous and non-calcareous foulers.

Summary of Research:

PS-PVMS is a block copolymer that was synthesized to high purity using a method previously established by the Ober group [1]. The polymer contains a vinyl group that is reactive and is later utilized in thiol-ene click chemistry in order to attach different chemical functionalities that are thought to be useful in generating antifouling and foul resistant surfaces. The following buffers were synthesized (Figure 1) with corresponding water contact angles. Generally speaking, the goal is to have more hydrophilic character as most foulers are more attracted to hydrophobic materials. In this case, however, it was found that the more hydrophobic materials better resisted fouling.

The process of coating the slides starts with molecular vapor deposition of a thin single layer of APTMS on piranha cleaned slides. This prepares the substrate for the following layers: Ma-SEBS, SEBS, and finally, the PS-PVMS modified antifouling coating. (Figure 2). With the addition of each layer, water contact angle is once again measured prior to addition of the following layer. Ma-SEBS and SEBS are thermally annealed to the surface post drying in a 120°C oven for 12 hours,

which helps with thermal stability and increases the durability of the materials in the water. The final layer is then spray coated on to the surface. Synthetic methods adapted from [2-4].

AFM was used to characterize the surface morphology of each of the coatings. AFM gave a better idea of the uniformity of the coatings (Figure 3). In the images it was noted that ImZ-PVMS had some crater-like formations. It is not totally clear what caused this, but it is important to note as this can impact the results of fouling. One theory is that because the permanent zwitterionic imidazole group contains two opposite charges within a close proximity to one another, it is possible that intermolecular entanglement becomes higher resulting in an overall rougher surface [5].

References:

- [1] Zhang, Z.; Chaudhuri, K.; Kaefer, F.; Malanoski, A. P.; Page, K. A.; Smieska, L. M.; Pham, J. T.; Ober, C. K. Controlling Anti-Penetration Performance by Post-Grafting of Fluorinated Alkyl Chains onto Polystyrene-block-poly(vinyl methyl siloxane). *ACS Applied Materials and Interfaces* 2024, 16(15).
- [2] Leonardi, A. K.; Medhi, R.; Zhang, A.; Düzen, N.; Finlay, J. A.; Clarke, J. L.; Clare, A. S.; Ober, C. K. Investigation of N-Substituted Morpholine Structures in an Amphiphilic PDMS-Based Antifouling and Fouling-Release Coating. *Biomacromolecules* 2022, 23, 2697–2712.
- [3] Leonardi, A. K.; Ober, C. K. Polymer-Based Marine Antifouling and Fouling Release Surfaces: Strategies for Synthesis and Modification. *Annu. Rev. Chem. Biomol. Eng.* 2019, 10, 241–264.
- [4] Leonardi, A. K.; Zhang, C.; Düzen, N.; Aldred, N.; Finlay, J. A.; Clarke, J. A.; Clare, A. S.; Segalman, R.; Ober, C. K. “Amphiphilic nitroxide bearing siloxane-based block copolymer coatings for enhanced marine fouling release”, *Appl. Mater. Int.*, (2021), 13(24), 28790-28801
- [5] Lin, C. H.; Luo, S. C. Zwitterionic Conducting Polymers: From Molecular Design, Surface Modification, and Interfacial Phenomenon to Biomedical Applications. *Langmuir* 2022, 38(24), 7383-7399.

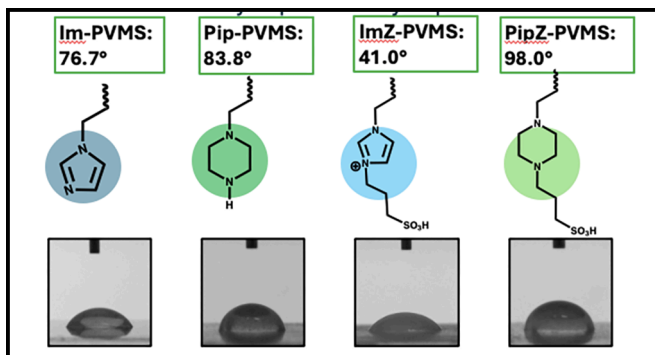


Figure 1: Four buffers were synthesized and attached to a PS-PVMS backbone via thiol-ene click chemistry. Once adhered, corresponding water contact angles were measured to gauge effectiveness of reaction and to test surface presence.

Image Depiction of Layer	Chemical Identification	Water contact angle
	Piranha cleaned slides	 4.7±0.9 °
	APTMS	 45.9±3.5°
	Ma-SEBS	 97.8±1.1°
	SEBS	 99.6±2.4°

Figure 2: Visual depiction of each layer and water contact angles post adhesion/thermal annealing.

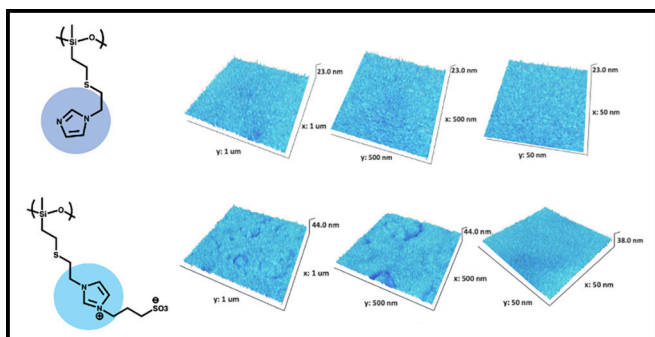


Figure 3: Imidazole family of buffered PS-PVMS AFM surface characterization.

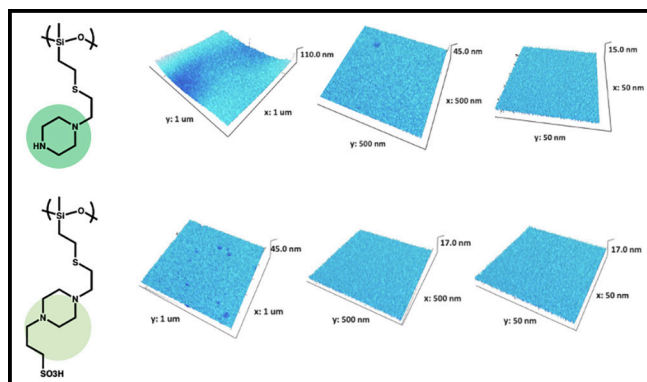


Figure 4: Piperazine family of buffered PS-PVMS AFM surface characterization.

Thiol-Norbornene Photopolymer for Two-Photon Photopolymerization

CNF Project Number: 2754-18

Principal Investigator(s): Yadong Wang

User(s): Warrick Ma

Affiliation(s): Chemistry and Chemical Biology, Cornell University

Primary Source(s) of Research Funding: Cornell Startup Fund; Ignite Innovation Acceleration Grant

Contact: yw839@cornell.edu, ym464@cornell.edu

Research Group Website: <https://biofoundry.bme.cornell.edu>

Primary CNF Tools Used: Nanoscribe Photonic Professional GT2 Two-Photon Lithography System

Abstract:

Carbic anhydride is an underappreciated starting material for 3D-printable, non-hydrogel photopolymers. Compared with other norbornene precursors, carbic anhydride is cheaper and reactive via aminolysis. As a result, the generalized and efficient functionalization with carbic anhydride can increase the utilization of thiol-norbornene photopolymers. Here, we report carbic anhydride's catalyst-free condensation with two commodity polymers: amine-functionalized polypropylene glycol and polydimethylsiloxane. The reaction completes in 1h, produces water as the only byproduct, and does not require purification. It is therefore affordable, facile, and green. Mixing the product with thiol cross-linkers and the appropriate photo-additives produces photopolymers, which have the potential to be used for microfabrication with two-photon photopolymerization (2PP). The simple yet versatile platform will benefit additive manufacturing of soft materials and beyond.

Summary of Research:

Thiol-norbornene photopolymers are excellent for additive manufacturing. Nevertheless, scalable thiol-norbornene photopolymers need a more affordable starting material and a more scalable synthesis. Among the norbornene precursors, carbic anhydride (CA) is the cheapest and greenest. CA reacts via alcoholysis or aminolysis, thermodynamically favorable processes that can occur without a catalyst. If water is removed from the reaction mixture, CA's reaction with amine yields norbornene dicarboximide [1-3]. Adapting this strategy will make the synthesis of thiol-norbornene photopolymers greener and more economical.

The norbornene dicarboximide-functionalized polymers are synthesized from amine-functionalized PPG and PDMS (Figure 1). Proton nuclear magnetic resonance (¹H-NMR) indicates the clean formation of norbornene dicarboximide from the singlet at 6.0-6.1 ppm (Figure 2).

Except for 7kPDMS-5CA, all products are transparent liquids. 7kPDMS-5CA's opacity potentially arises from the partial crystallinity of the pendant norbornene dicarboximide propyl side chains.

Two thiol cross-linkers, pentaerythritol tetrakis(3-mercaptopropionate) (PETMP) and 4.6% (mercapto-propyl)methylsiloxane]-dimethylsiloxane copolymer (polySH), are used to study photopolymerization. PETMP is miscible with PPG-based polymers but not with PDMS-based polymers. As a result, 0.9kPDMS-2CA:PETMP is a milky-white mixture. We attempted to solubilize PDMS-based polymers with polySH. However, only 5kPDMS-2CA:polySH is transparent. All immiscible mixtures remain stable emulsions after overnight storage without agitation. Aggregate formation may lead to a heterogeneous network and affect the mechanical properties of 3D-printed materials [4].

To assess the printability of norbornene dicarboximide photopolymers, we investigated their photorheology with 400-500 nm light to capture the effect of 2PP cross-linking. Judging by the cross-over point of loss and storage modulus, only 5kPPG-3CA:PETMP cross-links too slowly (385 nm or 405 nm). Cross-linked 5kPPG-3CA:PETMP is also extremely soft and tacky, indicative of a weak network not suitable for additive manufacturing. All other photopolymers cross-link quickly, with various cross-over points (Figure 3) reflecting the structure-property relationships.

After rheological studies identified four printable formulations, they were tested for 2PP. PDMS-based photopolymers are unsuitable for 2PP due to light scattering resulting from the heterogeneous mixture. 2kPPG-2CA:PETMP shows the best solubility in isopropyl alcohol, and thus is used as a proof-of-concept for 2PP (Figure 4). The cured photopolymer in the camera view suggests the photopolymer's feasibility.

The catalyst-free condensation between amine-functionalized PPG or PDMS and CA affords a family of

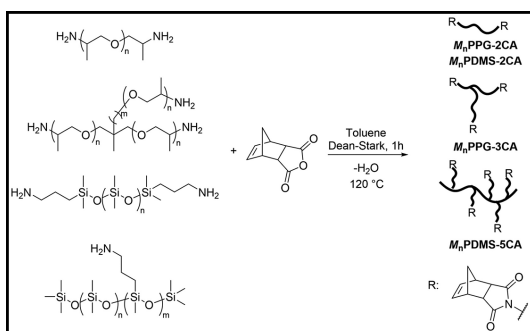


Figure 1: Synthesis of norbornene dicarboximide polymers from amine-functionalized polypropylene glycol (PPG) or polydimethylsiloxane (PDMS). The prefix M_n represents the average molecular weight of the amine-functionalized starting material. The number preceding CA represents the number of norbornene dicarboximide groups in a single chain. For example, amine-terminated PPG ($M_n = 2$ kDa) affords 2kPPG-2CA.

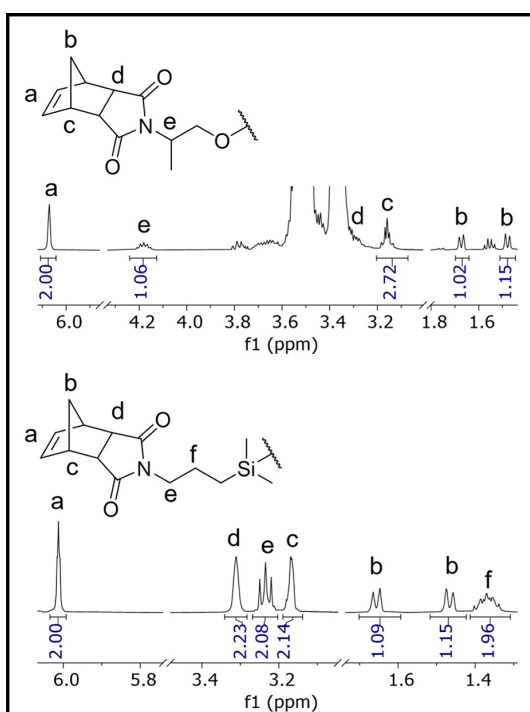


Figure 2: $^1\text{H-NMR}$ spectra of norbornene dicarboximide-functionalized polymers showing their end group structure (500 MHz, CDCl_3).

norbornene dicarboximide functionalized polymers—with water as the only byproduct. The reaction is affordable and green and occurs at a 100-g scale without purification. The resultant photopolymers have potential in microfabrication with 2PP. Cheap but versatile, our method can benefit additive manufacturing of soft materials and beyond. In the future, the 2PP parameter should be systematically fine-tuned for successful fabrication.

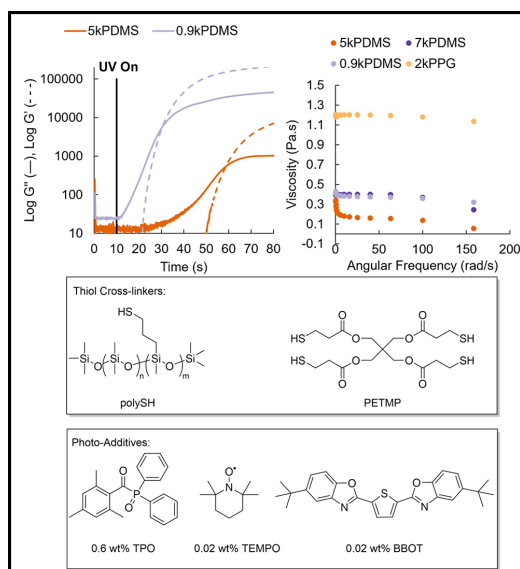


Figure 3: Photorheology and viscosity of representative photopolymers (names are abbreviated to their respective backbone). The photorheology data of 2kPPG and 7kPDMS are in Figure S3. Ultraviolet (UV) radiation (400–500 nm, 10 mW/cm^2) is switched on at 10 s (G' : storage modulus; G'' loss modulus).

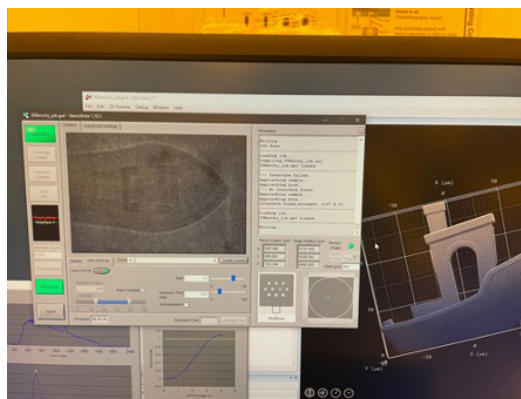


Figure 4: 2PP on Nanoscribe Photonic Professional GT2 Two-photon Lithography System with 2kPPG-2CA:PETMP showing cured 3D object on the substrate. Solvent washing during post-printing obliterated the object, potentially due to rapid solvent swelling of the partially cured photopolymer.

References:

- [1] Wang, H., et al. *Polym Chem-Uk* 2024, 15 (6), 534-543. DOI: 10.1039/d3py01278f.
- [2] Majchrzak, M., et al. *Polymer* 2012, 53 (23), 5251-5257. DOI: 10.1016/j.polymer.2012.09.033.
- [3] Pawloski, A. R., et al. *J Photopolym Sci Tec* 2002, 15 (5), 731-739. DOI: DOI 10.2494/photopolymer.15.731.
- [4] Abdilla, A., et al. *J Polym Sci* 2021, 59 (19), 2114-2128. DOI: 10.1002/pol.20210453.

Influence of Ligand for Metallo-Elastomer Design

CNF Project Number: 2754-18

Principal Investigator(s): Yadong Wang

User(s): Chia-Wei Yeh, Simon Van Herck

Affiliation(s): Biomedical Engineering, Cornell University

Primary Source(s) of Research Funding: NIH

Contact: yw839@cornell.edu, cy465@cornell.edu, sbv25@cornell.edu

Research Group Website: <https://biofoundry.bme.cornell.edu/>

Primary CNF Tools Used: Rame-Hart 500 Goniometer

Abstract:

Metal-ligand coordination is an appealing strategy pursued to achieve crosslinking in the design of elastomers for biomedical applications. A variety of ligands, like catechols and imidazole groups, can be employed to achieve this and have been reported in literature. However, material property comparisons are usually done on a single ligand with variations in ligand density or complexation metal. Here, we intend to expand our understanding of ligand-metal coordination crosslinking in elastomer design via a head-to-head comparison of different ligands. We designed a modular polymer platform that allowed for easy conjugation with a Salen-, pyridoxal- or catechol based ligand. These polymers are used to evaluate the influence of the ligand on chelation strength, mechanical properties, catalytic activity and biological interaction.

Summary of Research:

The experimental work done in collaboration with CNF for this project is limited to contact angle measurements, using the Rame-Hart 500 Goniometer.

Thin films were prepared of polymer only or polymer crosslinked with Cu-salts on glass slides. The contact angle between a water droplet and the hydrophobic surface was analyzed. Overall, we observed a clear trend with a decrease in contact angle for films crosslinked with Cu compared to uncrosslinked films, indicating a more hydrophilic surface. We hypothesize that this is due to the crosslinking chemistry of these ligands that occurs via the formation of a phenolate anion that will chelate with the Cu-ion, the thereby generated ionic content increased hydrophilicity. This hypothesis is supported by the largest decrease for catechol (SuCat10 and SuCat25) based polymer due to deprotonation of both phenolic protons and higher anionic surface. An overview of the results is given in Figure 1 and 2.

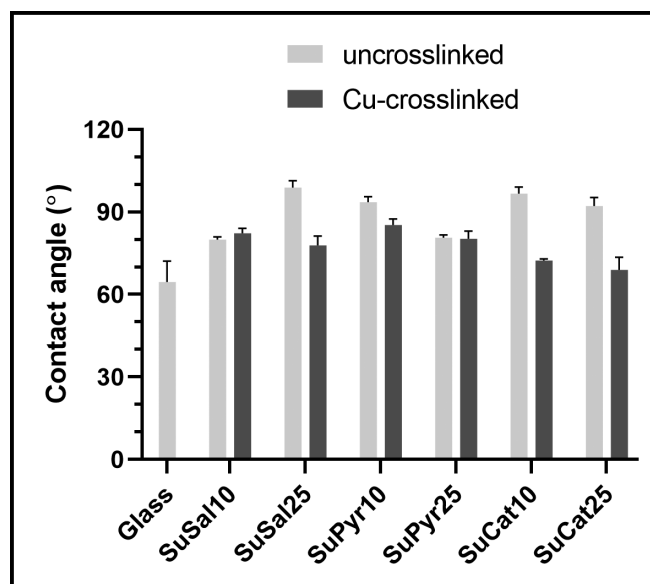


Figure 1: Plot of contact angles of water droplet on polymer surface for polymer only (= no Cu) and Cu-crosslinked polymer films.

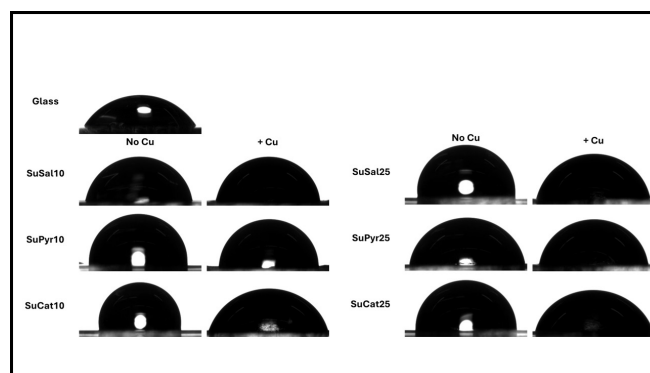


Figure 2: Visual presentation of change in contact angle upon Cu-crosslinking of films.

Fabrication of Polymer Grafted Core-Shell Nanoparticles

CNF Project Number: 2955-21

Principal Investigator(s): Christopher Ober

User(s): Yu Shao

Affiliation(s): Materials Science and Engineering, Cornell University

Primary Source(s) of Research Funding: NSF

Contact: cko3@cornell.edu, ys2295@cornell.edu

Primary CNF Tools Used: Zetasizer

Abstract:

Polymer-grafted nanoparticles (PGNs) possess the advantages of both polymers and inorganic cores, and demonstrate superior magnetic, optical, electronic, and mechanical properties. PGNs were synthesized by mini-emulsion polymerization and the brush canopy size, graft density and molar mass of the grafted polymer chains could be controlled by modifying the monomer feeding rate, the monomer concentration, and other parameters. Through combined technologies we are about to fabricate a series of inorganic-inorganic core-shell nanoparticles based on unique silicon-containing polymer precursor and unfold the structure-property relationship towards cutting edge magnetic and photoresponsive materials.

Summary of Research:

In this research, it is critically important to obtain stable colloidal emulsion systems that create a nano-encapsulation environment and then be able to graft uniform polymer brushes on the surface of NPs. To characterize the colloidal suspension, we use mainly dynamic light scattering (DLS) technique to monitor the emulsion condition before and after polymerization. As shown in Figure 1, particle size and distribution can be varied due to different monomer feeding ratio. Morphology of core-shell NPs is uniform with PDI close to 0.1 according to DLS and also confirmed by STEM (Figure 2). However, when it comes to preceramic polymer coating, it's tricky to make a uniform emulsion system.

As shown in Figure 3, even though the data file says good quality, the curve shows an asymmetric peak profile which means that the size distribution is not uniform. In addition, concentration and temperature will influence the colloidal system a lot. Progress needs more of modification.

Conclusions and Future Steps:

DLS is a facile tool to characterize the emulsion condition of colloidal system. For emulsions with nanoparticles and multiple ingredients, it's a challenge to make ideally uniform nano-encapsulation environments. Concentration and temperature play critical roles and need to be modified systematically in the future.

References:

- [1] Chenyun Yuan, Florian Kafer, and Christopher K. Ober. (2021). Polymer-Grafted Nanoparticles (PGNs) with Adjustable Graft-Density and Interparticle Hydrogen Bonding Interaction.
- [2] Alicia Cintora, Florian Kafer, Chenyun Yuan, and Christopher K. Ober. (2021). Effect of monomer hydrophilicity on ARGET-ATRP kinetics in aqueous mini-emulsion polymerization.
- [3] Roselynn Cordero, Ali Jawaid, Ming-Siao Hsiao, Zoe Lequeux, Richard A. Vaia, Christopher K. Ober, "Mini Monomer Encapsulated Emulsion Polymerization of PMMA in Aqueous ARGET ATRP", ACS Macro Letters, 7, 4, 459-463.

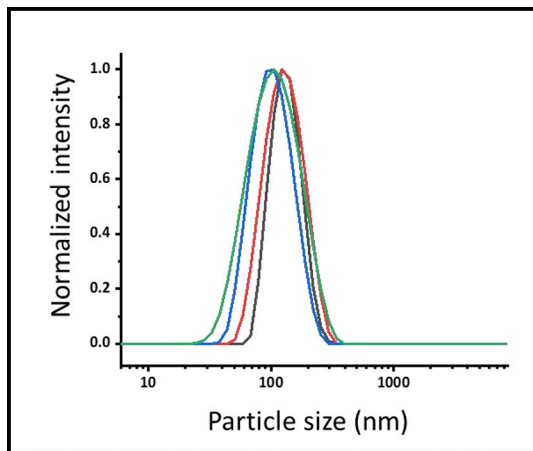


Figure 1: DLS overlay of CdS nanoparticles coated with silica shell.

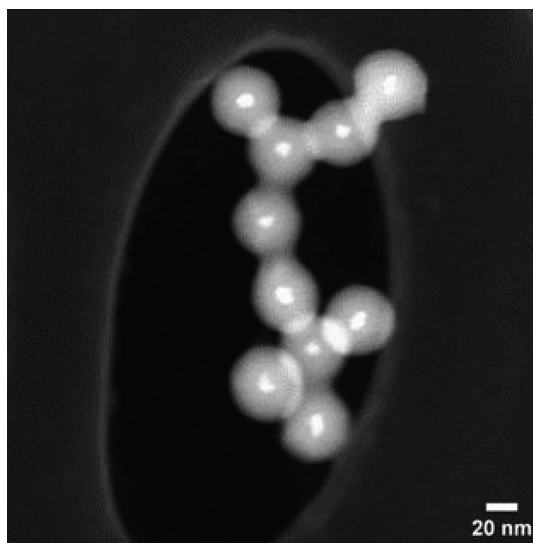


Figure 2: STEM image of CdS nanoparticles coated with silica shell.

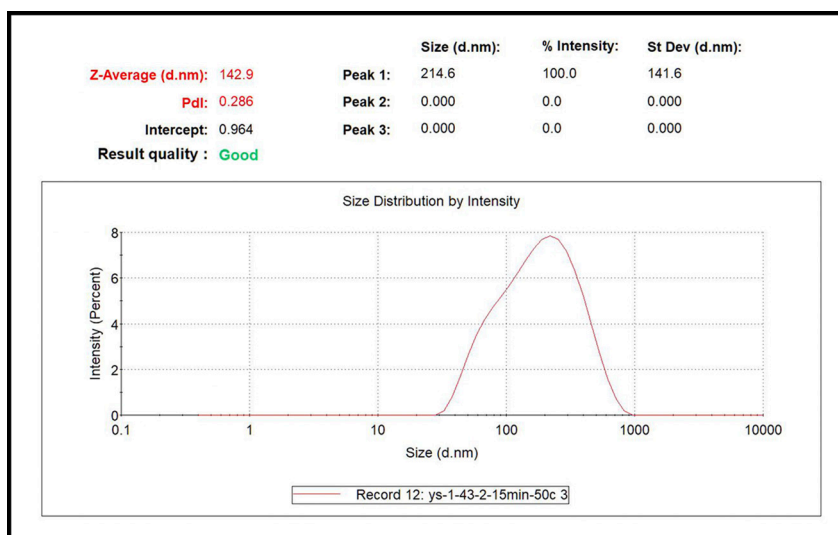


Figure 3: DLS of emulsion made by CoFe_2O_4 NPs and preceramic precursors at 50°C .

Quasi-2D Materials for Ultra-Low Resistance Electrical Interconnects

CNF Project Number: 3007-22

Principal Investigator(s): Hair P. Nair

User(s): Bilal Azhar

Affiliation(s): Department of Materials Science and Engineering, Cornell University

Primary Source(s) of Research Funding: Semiconductor Research Corporation (SRC)

Contact: hn277@cornell.edu, ba428@cornell.edu

Primary CNF Tools Used: General Materials Anneal Furnace, Veeco Savannah ALD, Woollam RC2 Spectroscopic Ellipsometer, AJA Sputter Deposition, ABM Contact Aligner, GCA AutoStep 200 DSW i-Line Wafer Stepper, Heidelberg Mask Writer, YES Vapor Prime Oven, AJA Ion Mill, Glen 1000 Resist Strip, Dektak XT Profilometer, Zeiss Ultra SEM

Abstract:

The dramatic increase in the resistivity of interconnect lines with decreasing dimensions presents a significant bottleneck for further downscaling of integrated circuits [1]. This is because current interconnects use 3-dimensional metals that experience increased interface electron scattering as the interconnect dimensions approach their electron mean free path. A possible solution is to use metals with much lower electron mean free paths such as: W, Mo, and Ru. Metallic delafossite oxides are an alternative solution because of their inherent advantages over traditional metals such as: ultra-low room temperature resistivity, potential mitigation of interface/surface scattering due to their 2D Fermi surface, potentially decreased likelihood of electromigration, and potentially better compatibility with low-K oxide dielectrics. Metallic delafossite can prove to be a disruptive new material for ultra-scaled electrical interconnects.

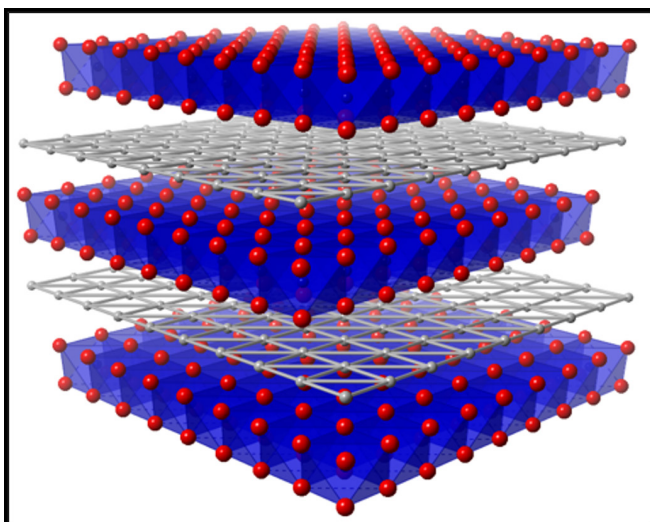


Figure 1: Layered crystal structure of delafossite PtCoO₂.

Delafossites are layered oxides with the formula ABO₂ where A is a metal cation that forms 2D sheets separated by the BO₂ transition-metal oxide octahedra, Figure 1. In this study we focus on metallic delafossites PtCoO₂ and PdCoO₂ because of their ultra-low room temperature resistivity of 2.1 $\mu\Omega\cdot\text{cm}$ and 2.6 $\mu\Omega\cdot\text{cm}$, respectively, which is comparable to the current semiconductor industry standard interconnect metal, Cu, Figure 2 [2]. The metallic delafossite structure has an anisotropic nature with resistivity along the c-axis a factor of 500 higher than resistivity within the Pt/Pd sheet. Due to the layered crystal structure, the Fermi surface of the metallic delafossites is cylindrical as for a 2D metal. This quasi-2D crystal structure can potentially mitigate interface and surface scattering since the electron Fermi velocity does not have components perpendicular to the Pd/Pt sheets. This can potentially overcome the resistivity penalty encountered by conventional 3D metals in ultrathin films (< 20 nm). Additionally, the unique Fermi surface topology allows for an electron-phonon coupling constant that is a factor of 3 lower than copper [3].

Our focus has been to demonstrate metallic delafossites as a disruptive new material for ultra-scaled electrical interconnects, for which we have two goals. The first goal is to realize their unique electrical properties and the second goal is to demonstrate the growth of highly quality delafossite thin films via atomic layer deposition (ALD) a back-end-of-the-line (BEOL) compatible synthesis technique.

Summary of Research:

To realize the unique electrical properties of delafossite thin films we have been investigating the structural and electrical properties of PdCoO₂ thin films grown via molecular beam epitaxy (MBE). MBE has been shown to achieve highly crystalline films which is critical for electrical property characterization due to the structure-property relation [4,5]. We used high-resolution X-Ray diffraction (HRXRD) to confirm that the films are phase-pure. We measured the resistivity of the films using a van der Pauw geometry and modelled the resistivity scaling with film thickness using Fuchs-Sondheimer (FS) and Mayadas-Shatzkes (MS) model. The upshot being that a 50 nm thick PdCoO₂ film has a resistivity of $\sim 8 \mu\Omega\cdot\text{cm}$. It should be noted that while our XRD phi scans did reveal in-plane twinning our resistivity fitting did not find twin boundaries to be a significant contributor to resistivity.

In addition to modeling the resistivity scaling with thickness, we are also modeling the line-width resistivity scaling into the sub 100 nanometer regime. Towards this we have fabricated micron wide wires via the contact aligner and are fabricating sub-micron wires via the i-line stepper. It is important to scale down incrementally so to check for any lithography-related degradation of the delafossite wires which would make it difficult to isolate the dimension dependent resistivity change.

We are also investigating back-end-of-the-line (BEOL) compatible growth of these materials via Atomic Layer Deposition (ALD) and Sputtering. To guide this effort we have created a thermodynamic model of the PdCoO₂ system and are validating it via ex-situ anneals in relevant ambients, temperatures, and time scales to find BEOL conditions in which these materials are stable.

Conclusions and Future Steps:

We have three main goals: (1) Characterize the line-width resistivity scaling of these delafossite materials, (2) map out their stability in BEOL conditions, and (3) find a BEOL compatible growth method.

References:

- [1] D. Gall, J. Appl. Phys. 127, 050901 (2020).
- [2] V. Sunko, P.H. McGuinness, C.S. Chang, E. Zhakina, S. Khim, C.E. Dreyer, M. Konczykowski, M. König, D.A. Muller, and A.P. Mackenzie, Phys. Rev. X 10, 021018 (2020).
- [3] C.W. Hicks, A.S. Gibbs, A.P. Mackenzie, H. Takatsu, Y. Maeno, and E.A. Yelland, Phys. Rev. Lett. 109, 116401 (2012).
- [4] J. Sun, M.R. Barone, C.S. Chang, M.E. Holtz, H. Paik, J. Schubert, D.A. Muller, and D.G. Schlom, APL Mater. 7, 121112 (2019).
- [5] Q. Song, J. Sun, C.T. Parzyck, L. Miao, Q. Xu, F.V.E. Hensling, M.R. Barone, C. Hu, J. Kim, B.D. Faeth, H. Paik, P.D.C. King, K.M. Shen, and D.G. Schlom, APL Mater. 10, 091113 (2022).

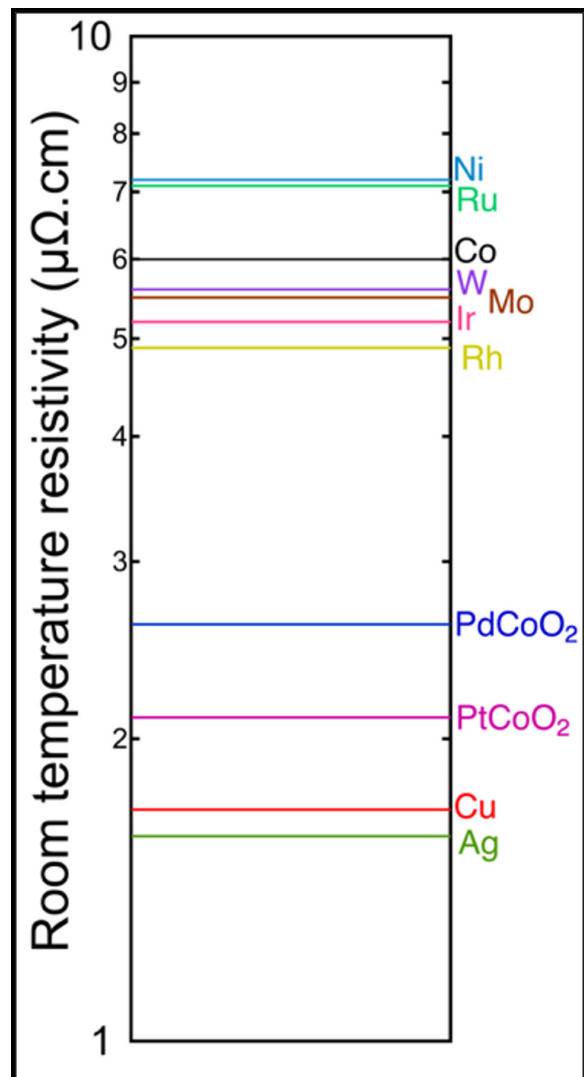


Figure 2: Comparison of room temperature resistivity of PdCoO₂ and PtCoO₂ to conventional interconnect metals.

Lithiation Induced Phases in 1T'-MoTe₂ Nanoflakes

CNF Project Number: 3035-22

Principal Investigator(s): Jeeyoung Judy Cha

Users(s): Natalie Williams, Sihun Lee

Affiliations(s): Materials Science and Engineering, Chemistry and Chemical Biology; Cornell University

Primary Source(s) of Research Funding: The Gordon and Betty Moore Foundation's EpiQS Initiative #9062.01, The National Science Foundation, CBET-CAREER #2240944

Contact: jc476@cornell.edu, nlw49@cornell.edu, sl2859@cornell.edu

Research Group Website: cha.mse.cornell.edu

Primary CNF Tools Used: Heidelberg Mask Writer - DWL2000, SC4500 Odd-Hour & Even-Hour Evaporator

Abstract:

Molybdenum ditelluride (MoTe₂) is a layered, two-dimensional (2D) crystal that naturally exists in three different structural phases. Each phase exhibits distinct optical and electronic properties. One way to induce new phases in 2D materials is through the reversible insertion of ions, atoms, or molecules into the gaps of crystalline materials, otherwise known as intercalation. Here we report electrochemical intercalation of lithium (Li) into the distorted octahedral or 1T'-phase of MoTe₂ nanoflakes, leading to the discovery of two previously unreported lithiated phases [1].

Summary of Research:

We assembled coin-type cells with 1T'-MoTe₂ powder to induce two, distinct and reversible phase transitions upon lithium intercalation. These phases are denoted as lightly lithiated phase I and heavily lithiated phase II (Figure 1). We also fabricated electrochemical cells on individual nanodevices using exfoliated crystals (Figure 2), which allowed for investigations into structure and electrochemical property changes in situ as we directly control intercalation of lithium ions into the 2D crystal. Structural differences between the 1T' and lithiated phase of MoTe₂ were characterized by in situ Raman spectroscopy, and a change from the previously metallic to semiconducting phase upon lithiation was revealed

through in situ transport measurements (Figure 3). In situ Hall measurements indicated bandgap opening in the lithiated phases, as evidenced by a significantly reduced Hall carrier density, and increasing resistance with decreasing temperature. Changes in structure for the heavily lithiated phase II was further analyzed using in situ angle-resolved Raman spectroscopy, in situ single-crystal x-ray diffraction (XRD), and in situ transition electron microscopy (TEM).

Conclusions and Future Steps:

Successful application of in situ experiments enabled detailed investigations of crystal structure and electronic properties of MoTe₂ nanoflakes during electrochemical lithium intercalation. The discovery of new phases in initially metallic 1T'-MoTe₂ highlights the effectiveness of electrochemical intercalation in adjusting phase stability and electron density in 2D materials.

References:

- [1] S. Xu, K. Evans-Lutterodt, S. Li, N. L. Williams, B. Hou, J. J. Huang, M. G. Boebinger, S. Lee, M. Wang, A. Singer, P. Guo, D. Y. Qiu, and J. J. Cha, Lithiation Induced Phases in 1T'-MoTe₂ Nanoflakes, DOI: 10.1021/acsnano.4c06330.

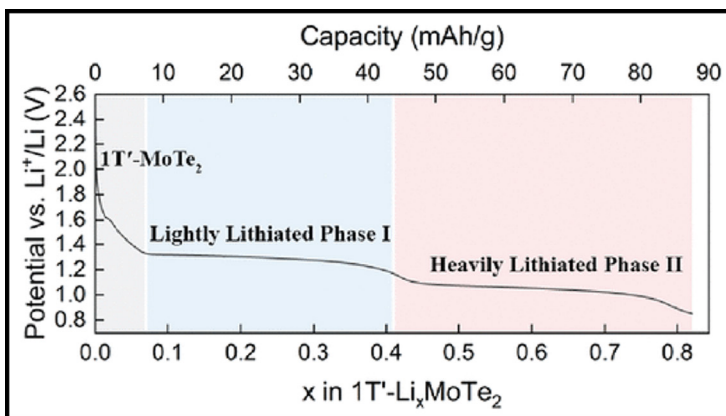


Figure 1: Galvanostatic discharging of 1T'-MoTe₂ powder in a coin cell showing two distinct, intermediate phases upon 1T'-MoTe₂ lithiation.

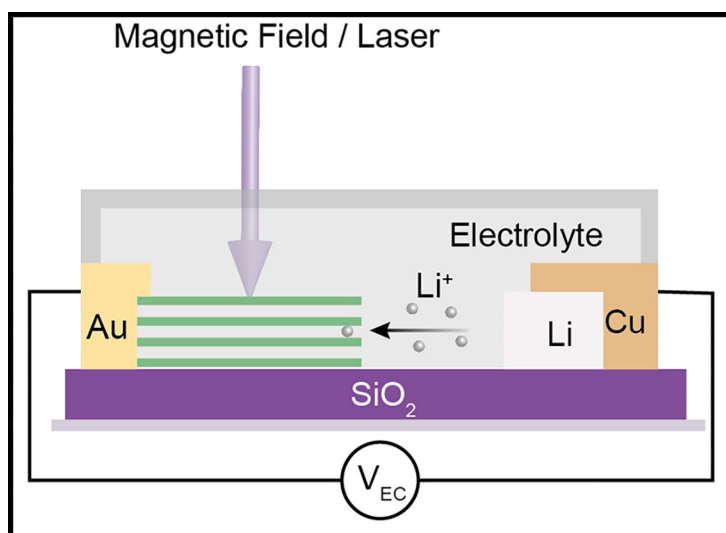


Figure 2: A schematic of a planar electrochemical intercalation cell capable of in situ experiments, such as for Raman spectroscopy, single-crystal XRD, and transport measurements.

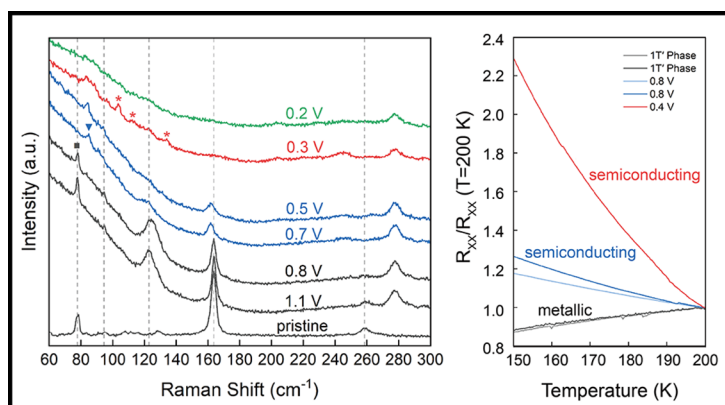


Figure 3: (Left) New structures of lithium intercalated 1T'-MoTe₂, namely lightly lithiated phase I and heavily lithiated phase II. (Right) Initially metallic 1T'-MoTe₂ is transformed into lithiated, semiconducting phases as confirmed by transport measurements, showing increasing resistance with decreasing temperature.

Measuring Microplastic Migration Through Human Intestinal Mucus

CNF Project Number: 3058-23

Principal Investigator(s): Meredith Silberstein

User(s): Max Tepermeister, Ellen van Wijngaarden

Affiliation(s): Sibley School of Mechanical and Aerospace Engineering, Cornell University

Primary Source(s) of Research Funding: College of Engineering Sprout Award

Contact: meredith.silberstein@cornell.edu, mt845@cornell.edu, ewv8@cornell.edu

Research Group Website: silbersteinlab.com

Primary CNF Tools Used: Harrick Plasma Generator, Malvern Nano ZS Zetasizer

Abstract:

Microplastic accumulation in the body has become a growing concern due to widespread harmful physiological effects. This research is focused on understanding how the intestinal mucus layer prevents the migration of ingested microplastics. We studied how size and surface charge of microplastics of different compositions, functionalization and size alter particle movement through mucus. Previous studies have used alternative mucus models such as porcine gastric mucus and have focused primarily on one plastic composition. Our study uses mucus derived from a human colonic cancer cell line, HT29MTX, and tests a broad range of plastic compositions and sizes. Results highlight the importance of the mucus layer in hindering the migration of particles > 200 nm and identify compositions diffuse more easily through mucus.

Summary of Research:

Over 400 million tons of plastic are produced every year [1]. Many of these plastics end up in the environment, gradually breaking down into microplastics. Microplastics are defined as plastic particles under 5 mm and can be found in the water soil and air. Ingestion of these particles has been linked to negative health impacts including metabolic disorders, neurotoxicity and intestinal inflammation [2]. The mucus layer within the intestine acts as a protective barrier against harmful substances however, studies have demonstrated that microplastics often travel through intestinal mucus and end up in other organs [3]. The goal of this research project is to characterize microplastic migration through intestinal mucus to identify key factors contributing to microplastic migration and understand the role of the mucus layer. Previous work has looked at particle migration in various mucus models such as porcine gastric mucus [4], hydrogels, human lungs, human cervix

and various animal sources [4,5]. Most studies focus on polystyrene microplastics however a broad array of particle compositions are often ingested [2]. We used particle characterization techniques and microrheology to study the migration of different compositions, surface functionalizations and sizes in intestinal mucus produced by HT29MTX human colorectal adenocarcinoma cells.

HT-29MTX cells were chosen due to their high mucus production and common use in human intestinal studies. Cells were grown as a monolayer in growth media for 21 days for a mature mucus layer. Zeta potential was used to measure the effective surface charge of particles in solution. Zeta potential was measured using a Malvern Nano Zs Zetasizer (Malvern Pananalytical, Malvern, U.K.). A total of three measurements were taken for each particle type. Each particle composition and functionalization was tested with values ranging from -43 mV to 14 mV, as shown in Figure 1.

Cells were cultured in 6-well plates on circular cover glasses for microrheology to determine particle diffusivity. The particle of interest was added to the culture media at a concentration of 1 μ l/ml and left to equilibrate for 15 minutes. The diffusion of particles through the mucus layer was imaged on an Elyra Super Resolution Microscope. A time series was collected with a step of 0.05 s with at least three biological replicates and at different locations over the cell monolayer. Images were analyzed using ImageJ Trackmate and Matlab to determine mean squared displacements and diffusion coefficients [6].

Diffusivity was determined to compare the effects of size, composition and surface functionalization. Diffusivity increased as microplastic size decreased, as shown in Figure 2. Polyethylene and polystyrene particles had the highest diffusivity out of all particle compositions tested, while silica particles had the lowest diffusivity. The diffusivity of 500 nm particles could not be determined

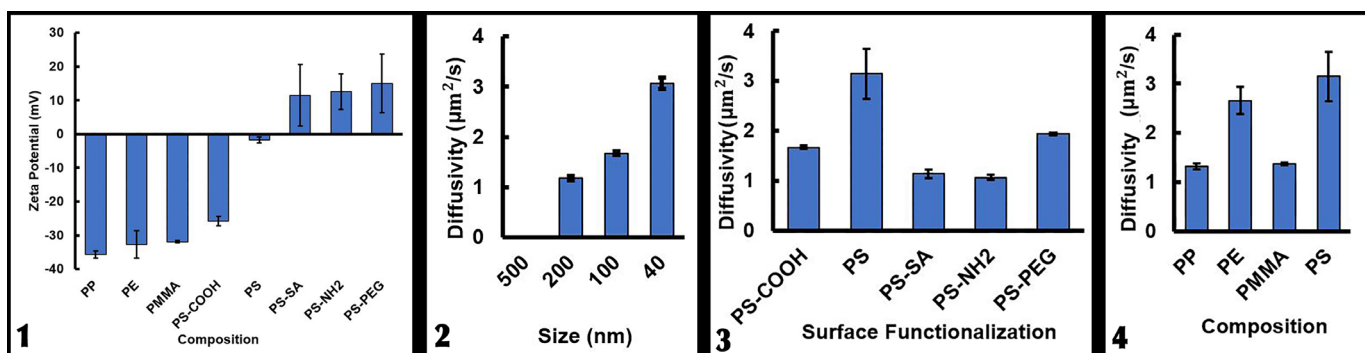


Figure 1: Zeta potential for each particle composition and surface functionalization.

Figure 2: Diffusivity for each particle size.

Figure 3: Diffusivity for each particle composition at 100 nm for PS, PP, PE, and PMMA.

Figure 4: Diffusivity for each surface functionalization of for PS 100 nm particles.

as these particles did not migrate through the mucus. Mucus has a pore size of approximately 200 nm, which prevented these particles from passing through [7]. In contrast, 40 nm particles were able to diffuse much more easily through the mucus layer. Figures 3 and 4 indicate that unfunctionalized polystyrene had the highest diffusivity. These results highlight the role of the mucus layer in preventing the migration of particles > 200 nm and indicate that certain compositions present a greater health threat. Further study is needed to understand how diffusivity might be related to negative health effects such as inflammation and cell death.

Conclusions and Future Steps:

The tools and technical expertise provided at the CNF was essential to the rapid testing necessary for biological samples. Future work will investigate how the mucus layer structure and mechanical properties alter cell uptake of particles through the design of microfluidic chips for cell growth and imaging. We will also expand on our preliminary tests to include particles carrying other environmental pollutants which may alter surface properties and change particles migration through the mucus.

References:

- [1] Y. Li, L. Tao, Q. Wang, F. Wang, G. Li, M. Song, *Environ. Health* 2023, 1, 249.
- [2] G. Visalli, A. Facciola, M. Pruiti Ciarello, G. De Marco, M. Maisano, A. Di Pietro, *Int J Environ Res Public Health* 2021, 18, 5833.
- [3] M. M. Garcia, A. S. Romero, S. D. Merkle, J. L. Meyer-Hagen, C. Forbes, E. E. Hayek, D. P. Scieszka, R. Templeton, J. Gonzalez-Estrella, Y. Jin, H. Gu, A. Benavidez, R. P. Hunter, S. Lucas, G. Herbert, K. J. Kim, J. Y. Cui, R. R. Gullapalli, J. G. In, M. J. Campen, E. F. Castillo, *Environmental Health Perspectives* 2024, 132, 047005.
- [4] P. Georgiades, P. D. A. Pudney, D. J. Thornton, T. A. Waigh, *Biopolymers* 2014, 101, 366.
- [5] A. Cobarrubia, J. Tall, A. Crispin-Smith, A. Luque, *Frontiers in Physics* 2021, 9.
- [6] J.-Y. Tinevez, N. Perry, J. Schindelin, G. M. Hoopes, G. D. Reynolds, E. Laplantine, S. Y. Bednarek, S. L. Shorte, K. W. Eliceiri, *Methods* 2017, 115, 80.
- [7] J. McCright, A. Sinha, K. Maisel, *Cell Mol Bioeng* 2022, 15, 479.

Fabrication of Non-Volatile Memory Transistors Using Hybrid Two-Dimensional Materials

CNF Project Number: 3064-23

Principal Investigator(s): Yu Zhong

User(s): Haolei Zhou, Qiyi Fang, Kaushik Chivukula, Ashutosh Garudapalli

Affiliation(s): Department of Materials Science and Engineering, Cornell University

Primary Source(s) of Research Funding: Cornell Startup Funding

Contact: yz2833@cornell.edu, hz595@cornell.edu, qf52@cornell.edu, kc836@cornell.edu, ag2289@cornell.edu

Research Group Website: <https://zhong.mse.cornell.edu/>

Primary CNF Tools Used: Oxford 100 PECVD, DWL 2000 Mask Writer, DWL 66FS Writer, Odd Hour Evaporator, Even Hour Evaporator, ABM Contact Aligner

Abstract:

This project is focused on the fabrication of electrolyte-gated nonvolatile memory transistors based on hybrid two-dimensional (2D) materials. The goal is to understand how the hysteresis changes under various measurement conditions for a memory transistor made from a hybrid MoS_2 -crown ether thin film. The retainability of ions inside the film is the main factor of such a hysteresis phenomenon. Previous research shows that the MoS_2 -based transistors may have a small hysteresis at high gate voltage or due to factors such as high moisture absorption [1]. In our experiment, we used liquid electrolytes instead of typical solid-state electrolytes. By applying this change, we found a much lower turn-on voltage and a much larger hysteresis. In addition, by adding a thin layer of a 2D crown ether polymer (CEP) film on top of monolayer MoS_2 , the retention time of ions seems to increase and hence increases the hysteresis. Such hysteresis is critical for neuromorphic computing such as potentiation or depression.

Summary of the Research:

To synthesize CEP films, we used a method called laminar assembly polymerization in a homemade Teflon reactor [2]. The CEP films were grown at the interface between water and pentane. In the bottom of the reactor, 2,4,6-trihydroxybenzene-1,3,5-tricarbaldehyde was dissolved in deionized water. For the injected solution, 6,7,9,10,17,18,20,21-octahydrodibenzo[b,k]

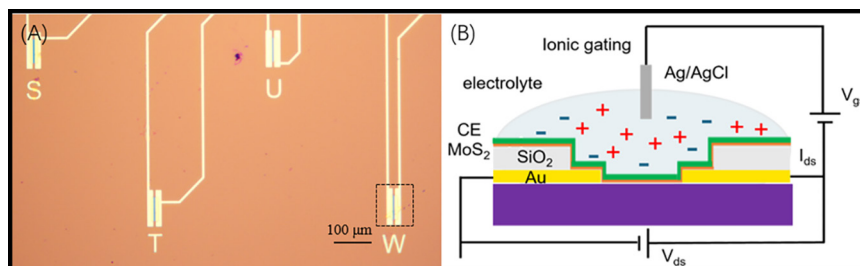


Figure 1: (A) Optical image of fabricated FET device covered with MoS_2 single layer film and (B) Schematic of the memory transistor.

[1,4,7,10,13,16]hexaoxacyclooctadecine-2,13-diamine dissolved in a solution of mixed chloroform and methanol with a ratio of 3:1 was delivered through the top pentane phase. By gradually injecting the solution, the CEP film was formed at the interface.

For the device fabrication, a set of lithographic tools at Cornell NanoScale Facility was used. Figure 1 shows an optical image and schematic of the device. To make the device, a contact alignment mask was first made. The patterns of masks were tested via DWL 66FS writer. There are two masks made by DWL 2000 mask writer. The first mask is for defining the metal contacts, the basic structure of the device with a channel length of 150 micrometers and a channel width of 10 micrometers.

A 280 nm silicon dioxide is deposited on the p-doped pure silicon by the plasma-enhanced chemical vapor deposition. Then S1813 was spin-coated on the substrate with a recipe of 5000 rpm – 40s. ABM contact aligner is then used for exposing the photoresist. MIF-726 60s recipe was applied to develop the photoresist. The deposition of a 10 nm Ti/ 100 nm Au electrode was accomplished by the odd-hour evaporator with a ratio of

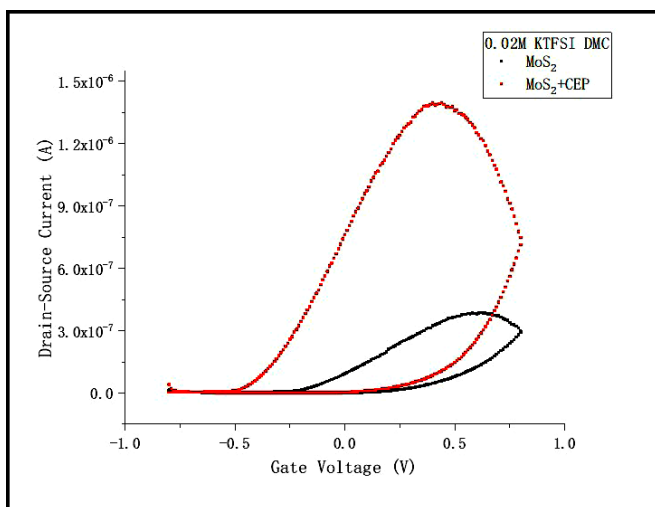


Figure 2: Transfer curve of MoS₂ devices with (red) and without CEP film (black).

one angstrom per second at a power of approximately 10%. The liftoff process was done with 20 minutes of S1165 remover, 20 minutes of acetone and five minutes of isopropanol. The second mask is designed for the insulating layer. The same processes were done except for the deposition part. 80nm of silicon oxide was deposited on the device with the even-hour evaporator. The rate was approximately 3.5 angstrom per second at a power of 3%.

To complete the device fabrication, we first transferred MoS₂ on the prepatterned electrode mentioned above followed by transferring the CEP film on MoS₂. We compared the transfer curve of MoS₂ transistors with and without CEP film. The device with a CEP film shows a more significant hysteresis than that without a CEP film (Figure 2). Our hypothesis is that the presence of CEP film can increase the retention time of ions on the MoS₂ surface due to the strong interaction between the cations and crown ether units (Figure 3). Further investigations are underway to reveal the mechanisms for the memory effect.

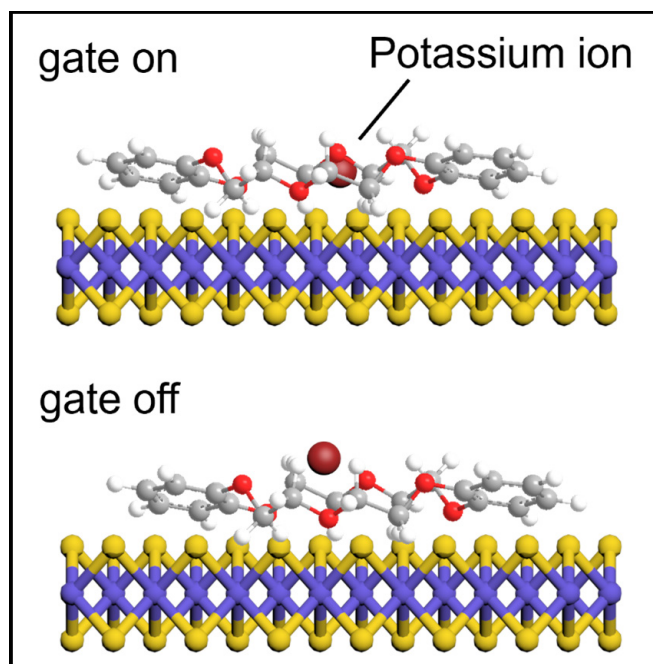


Figure 3: Schematic of memory effect from a MoS₂-CEP film.

Conclusions and Future Plans:

The MoS₂ device exhibits some hysteresis intrinsically in the liquid electrolyte. Such hysteresis is closely correlated with the concentration of the liquid electrolyte and the dielectric constant of the solvent. The addition of CEP film will increase the retainability of ions on the films because of strong cation-crown ether interactions. In the future, a device with better performance (lower channel width) can be designed to reduce the effect of the leakage current.

References:

- [1] Late, D. J.; Liu, B.; Matte, H. S. S. R.; Dravid, V. P.; Rao, C. N. R., *Acs Nano* 2012, 6 (6), 5635-5641.
- [2] Zhong, Y.; Cheng, B.; Park, C.; Ray, A.; Brown, S.; Mujid, F.; Lee, J.-U.; Zhou, H.; Suh, J.; Lee, K.-H.; Mannix, A. J.; Kang, K.; Sibener, S. J.; Muller, D. A.; Park, J. *Science* 2019, 366 (6471), 1379-1384.

FuSe Internship

CNF Project Number: CNF Summer Internship

Principal Investigator(s): Ron Olson¹, Lynn Rathbun¹

User(s): Sherri Ellis²

Affiliation(s): 1. Cornell NanoScale Science & Technology Facility (CNF), Cornell University;

2. Engineering Program, Tompkins Cortland Community College

Primary Source(s) of Research Funding: Cornell NanoScale Science & Technology Facility (CNF), a member of the National Nanotechnology Coordinated Infrastructure (NNCI), which is supported by the National Science Foundation (Grant NNCI-2025233)

Contact: olson@cnf.cornell.edu, rathbun@cnf.cornell.edu, see43@cornell.edu

Research Group Website: <https://www.cnf.cornell.edu/>

Primary CNF Tools Used: Hamatech Hot Piranha & Wafer Processors, YES EcoClean Asher, SÜSS Microtec Gamma Cluster System, Heidelberg DWL 2000 Mask Writer, ABM Contact Mask Aligner, ASML PAS 5500/300C DUV Wafer Stepper, Oxford 1000 Plasma Enhanced Chemical Vapor Deposition (PECVD) System, FilMetrics F50, Zeiss Scanning Electron Microscopes (SEMs), Veeco Icon Atomic Force Microscope (AFM).

Abstract:

I am participating in the Future of Semiconductors (FuSe) internship, a new collaboration between the Cornell Nanoscale Facility (CNF), Tompkins Cortland Community College (TC3), the University of Chicago and the University of Wisconsin-Madison. This internship includes learning about micro and nano fabrication, using CNF's cleanroom tools and processes, assisting with tasks in the photolithography areas, and providing support to a research project focused on new resist polymers. I have completed seven weeks of the 16-week internship.

Summary of Research:

I began with learning about cleanroom tools through CULearn's online courses and participating in CNF's short course "Technology & Characterization at the Nanoscale." This was followed by hands-on training and practice with some of CNF's cleanroom tools and assisting with daily and weekly tasks in the photolithography areas.

The processes and tools that I have been trained in and utilized include the following: For cleaning wafers, I used the hot strip bath, spin rinse dryers, Hamatech Hot Piranha, YES EcoClean Asher, and Glen 1000. For applying wafer coating by hand, I used spinners, hotplates, and the FilMetrics F50 to measure the photoresist film thickness. For automated wafer coating and post exposure developing, I ran the SUSS Microtec Gamma Cluster System.

For making masks, I learned how to use KLayout / L-edit CAD software to create the design, and the Heidelberg DWL 2000 Mask Writer to create the masks. To expose the coated wafers with a mask, I operated the ABM Contact Mask Aligner (figure 1) and the ASML PAS 5500/300C DUV Wafer Stepper. For developing the photoresist after exposure, I used the Hamatech Wafer Processors. I was also trained on the Oxford 1000 Plasma Enhanced Chemical Vapor Deposition (PECVD) system for thin film deposition.

For microscopy, I have operated basic optical microscopes, Zeiss Scanning Electron Microscopes (SEMs) (figure 2), and the Veeco Icon Atomic Force Microscope (AFM). I may also still receive training on the JEOL 6300 Electron Beam Lithography System.

I was offered the opportunity to prepare wafers for use in training, using a specific recipe through a multistep process. Some of the wafers were previously used, so I first cleaned them by spinning with acetone/IPA, using the hot strip bath, the spin rinse dryer, the EcoClean, and the Hot Piranha. Once prepared, I coated the wafers on a spinner, baked them, assessed thickness with FilMetrics F50, exposed them using the ABM Contact Aligner, developed them in a Hamatech, and completed the process with a hard bake. I appreciated being able to engage in a multistep photolithography process in service of a useful finished product.

Regarding assisting with daily and weekly tasks in the photolithography rooms, this included cleaning, refilling and restocking chemicals and supplies, refilling



Figure 1: Ellis at the ABM Contact Mask Aligner.



Figure 2: Ellis at the Zeiss Scanning Electron Microscope (SEM).

chemicals in the Hamatechs and Hot Piranha, and refilling water in the Gamma, ASML, and DWL 2000.

For the second half of my internship, I will continue to help with tasks in the photolithography areas and assist a Ph.D. student with research focused on developing a new resist polymer. Per the student, the project “focuses on using a block copolymer with an ideally high χ (chi) value to improve etching contrast, applying directed self-assembly as a strategy to increase pattern density.”

This internship has been a valuable learning experience so far. I am so grateful for this opportunity to learn about photolithography processes and tools, and to have so many hands-on experiences in the cleanroom.

I’m looking forward to further training, continuing to assist in the photolithography areas, and participating in the innovative research project.

Acknowledgements:

Special thanks to the following CNF staff for their supervision, training, and support: Ron Olson, Garry Bordonaro, Giovanni Sartorello, John Treichler, Xinwei Wu, Aaron Windsor, Jeremy Clark, and Alan Bleier, and to Ph.D. student Chaoqiuyu (Rachel) Wang for the opportunity to assist in her research.

Harnessing Magnetic-Field Driven Actuation for Microscale Motion in MEMS-Inspired Device

CNF Project Number: 2866-20

Principal Investigator(s): Amal El-Ghazaly

User(s): Ludovico Cestarollo, Zexi Liang, Conrad Smart

Affiliation(s): Electrical and Computer Engineering, Materials Science and Engineering, Lab of Atomic and Solid State Physics; Cornell University

Primary Source(s) of Research Funding: National Science Foundation

Contact: ase63@cornell.edu, lc942@cornell.edu, zl467@cornell.edu, cs2239@cornell.edu

Research Group Website: <https://vesl.ece.cornell.edu>

Primary CNF Tools Used: Heidelberg Mask Writer – DWL2000, SUSS MicroTec Gamma Cluster Tool, ASML PAS 5500/300C DUV Wafer Stepper, Oxford ALD FlexAL, Plasma-Therm Takachi HDP-CVD, Oxford 81/82/100 ICP and PT770 Etchers, Xactix XeF₂ Isotropic Silicon Etch System, DISCO Dicing Saw, Zeiss Ultra SEM, AFM – Veeco Icon, P7 Profilometer

Abstract:

Accurate small-scale control of magnetic actuation necessitates exact tuning of the magnetic fields and gradients that drive movement. In this study, two control magnets create the local magnetic fields needed to induce microscale deflections of a shuttle (in a micromechanical system) equipped with a soft magnetic element. The magnetization orientation and anisotropy of the magnetic element are optimized to maximize deflection in the ON state and its contrast with the OFF state. To demonstrate the effectiveness of the actuation force, a double-folded beam MEMS structure integrated with the control magnets is designed and fabricated.

Summary of Research:

Magnetic actuation stands out in mechanical systems as it allows the generation of large forces in a contactless manner. Various forms of magnetic actuators exist, including magnetic elastomers for millimeter-scale actuation [1-3] and programmable actuators with nanoscale magnets for creating microscale robots [4]. These studies typically use large NdFeB permanent magnets or electromagnetic coils to generate the necessary magnetic fields. However, integrated solutions are needed where both the actuation driver (generating the magnetic field) and actuated mechanism (moving in response to the field) exist within the same micrometer-scale device. Challenges include miniaturizing the switchable magnetic controls and fabricating microscale devices that respond mechanically to magnetic fields. Thin-film magnets produce fields that extend only short distances, requiring precise design of the geometry of

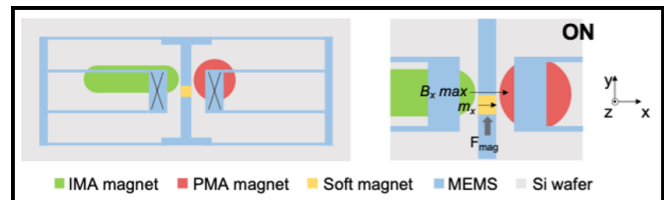


Figure 1: Integrated MEMS featuring a system of beams and magnetic controls.

the actuating mechanism to meet structural constraints. Despite these challenges, magnetic actuation offers a compact, low-power solution for micro-actuators.

This research tackles these issues and presents a tenable design for high-resolution, programmable MEMS micro-actuator. Our novel device uses micro-magnetic controls interacting with a soft magnetic element on a flexible beam system to induce deflection. By programming the magnetization of the control magnets and the soft magnetic element, the system can switch between ON and OFF states. The proposed design features a pair of IMA (in-plane magnetic anisotropy) and PMA (perpendicular magnetic anisotropy) control magnets, as shown in Figure 1.

A double folded beam MEMS is elevated over the magnets, anchored to them by the two supports, each denoted with a cross. The MEMS center shuttle is equipped with a soft magnetic element. This magnet, in response to the field exerted by the two control magnets, imparts a force to the shuttle, causing motion along the y-direction. In the current setup, the presence of a

magnetic field coupling between the control magnets above (or below) their surface corresponds to the ON (and OFF) states.

The control magnets were engineered to obtain the desired anisotropies. The IMA magnet is deposited as a single layer of pure Co in the shape of an elongated ellipse, forcing magnetization along its long dimension purely through shape anisotropy. The PMA magnet, instead, is grown as a Co/Pt heterostructure with 20 repeating layers of nanometer-thick Co and patterned to a circular shape. In the ON state, the IMA and PMA magnets are magnetized in the +x and -z directions, respectively, to concentrate the magnetic flux between them just above their surface. This strong magnetic flux density localization between the two magnets (separated by 1 μm) creates a significant B_{xy} ($\partial B/\partial y$) flux density gradient component, inducing a powerful actuation force on the soft magnet (an analytical model was developed to guide the device design). In the complete MEMS actuator, the beams can deflect if the magnetic force overcomes the mechanical restoring force. The mechanical restoring force from the MEMS is calculated by treating it as a system of fixed-guided beams [5]. By fabricating beams with a width (y-direction) of 30 nm and a thickness of 300 nm, and by depositing a soft magnet being 125 nm thick, large deflections up to 1 μm can be achieved.

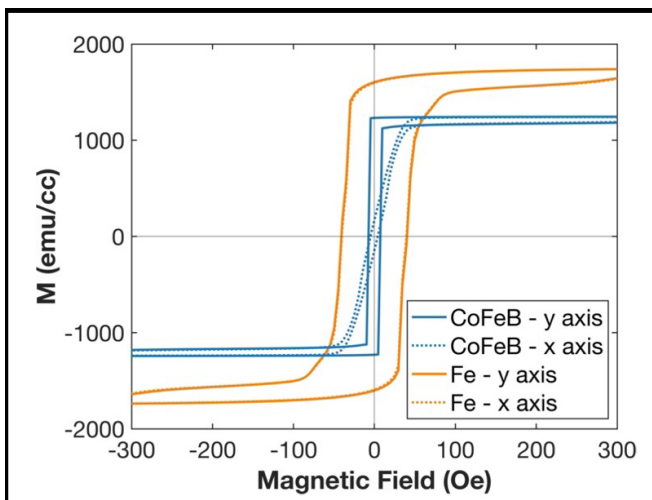


Figure 2: M vs H hysteresis loops along the x and y axes for Fe and CoFeB magnets deposited in the presence of an in-plane magnetic field.

The soft magnetic element was engineered to orient its easy axis along the y -direction in the OFF state, while allowing magnetization in the x -direction when exposed to small fields in the ON state. By depositing a square magnet using $\text{Co}_{43}\text{Fe}_{43}\text{B}_{14}$ in an in-plane field of 200 Oe along the y -direction, the desired behavior with a switching field (H_k) of 40 Oe was achieved, as shown in Figure 2 (this switching can be obtained with the system of IMA/PMA magnets). This switching behavior cannot be replicated with pure Fe, where magnetocrystalline anisotropy is not induced with the application of a field during deposition. As a result, Fe shows identical behavior along the x and y axes due to the absence of shape anisotropy in the square pattern.

Conclusions and Future Steps:

This research paves the way for high-resolution micrometer-scale magnetic actuators. By integrating the magnetic controls (actuating driver) with the MEMS featuring an embedded magnet (actuated mechanism), we are pioneering the development of the first fully-integrated magnetic actuator. Our innovative magnetic design maximizes the contrast in actuation between ON and OFF states. The resulting device, comprising control magnets, a soft magnetic element, and a folded beam MEMS structure, will be the first example of a fully-integrated magnetic actuation system.

References:

- [1] L. Cestarollo, S. Smolenski, and A. El-Ghazaly, "Nanoparticle-based magnetorheological elastomers with enhanced mechanical deflection for haptic displays," *ACS Applied Materials & Interfaces*, vol. 14, no. 16, pp. 19002-19011, 2022.
- [2] Y. Chen, K. Srinivasan, M. Choates, L. Cestarollo, and A. El-Ghazaly, "Enhanced Magnetic Anisotropy for Reprogrammable High-Force-Density Microactuators." *Advanced Functional Materials*, 2305502, 2023.
- [3] S. Marchi, A. Casu, F. Bertora, A. Athanassiou, and D. Fragouli, "Highly magneto-responsive elastomeric films created by a two-step fabrication process", *ACS Applied Materials & Interfaces*, vol. 7, no. 34, pp. 19112-19118, 2015.
- [4] K. Dorsey, T. Pearson, E. Esposito, S. Russell, B. Bircan, Y. Han, M. Miskin, D. Muller, I. Cohen, and Paul L. McEuen, "Atomic layer deposition for membranes, metamaterials, and mechanisms," *Advanced Materials*, vol. 31, no. 29, 1901944, 2019.

Fabrication of Micro Scale Triboelectric Microphone

CNF Project Number: 2929-21

Principal Investigator(s): Shahrzad Towfighian

User(s): Mohammad Alzgoool

Affiliation(s): Mechanical Engineering, Binghamton University

Primary Source(s) of Research Funding: National Science Foundation Grant

Contact: stowfigh@binghamton.edu, malzgoo1@binghamton.edu, mmalzgoool14@gmail.com

Primary CNF Tools Used: Unaxis PT770, OEM AlN Sputtering, AJA Sputter Deposition, Heidelberg DWL-2000 Mask Writer, Oxford PECVD, Oxford 81 Etcher, PT770 Etcher, DISCO Dicing Saw, SÜSS MA6-BA6 Contact Aligner, YES Polyimide Curing Oven, Primaxx Vapor Etcher

Abstract:

In our project, we are trying to fabricate and optimize a microphone that operates by using the mechanical structure and the triboelectric property of polyimide and aluminum with a back-etched wafer with aluminum nitride-aluminum layer as our diaphragm. The back-plate consists of polyimide, aluminum, and amorphous silicon. The motivation of this project comes from the promising results acquired from the MEMS triboelectric accelerometer that gave high signal-to-noise ratio, and the high and linear response of the output voltage [1]. The design from the previous work was optimized for sensitivity by manipulating the dimensions of the serpentine springs of the back-plate, and a back-etch was incorporated into the design to make the device act as a microphone.

Research Summary:

There are many advantages of triboelectric generators over piezoelectric generators such as lower cost, high flexibility, and superior electrical output. The operation of triboelectric generators depends on contact of a metal and a dielectric material with different affinity to electrons, the contact will result in charged conductive plates and separation with high impedance in between the plates will result in high voltage. In this work, we optimized our previous design of triboelectric accelerometers for maximum sensitivity with genetic algorithm [1]. The optimized triboelectric accelerometer was fabricated (Figure 1) and mounted on a shaker. The triboelectric excitation of 2-10 g was applied while the voltage was acquired. Frequency was swept from 0.5- 4 kHz and voltage produced was measured.

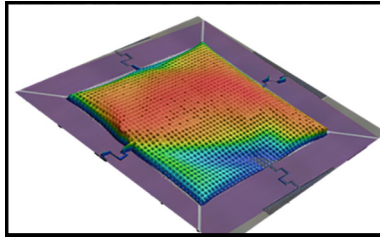


Figure 1: Fabricated triboelectric accelerometer.

Fabrication:

The fabrication process (Figure 2) for triboelectric generator starts with 500 nm aluminum nitride, recipe used for this operation utilized the heater provided with the machine and required seasoning of the wafer for many depositions before continuing with the real wafer. The minimum stress from the nitride layer acquired

with low-stress recipe was -50 MPa while it was more than 1 Gpa for the normal recipe. 500 nm of aluminum is sputtered and patterned for bottom electrode at 3 mtorr with titanium nitride adhesive layer. This is followed by high-rate silicon oxide PECVD layer that is one micron thick to create the gap between upper and lower electrode.

The process is then followed by back etching of the wafer to create inlet for the sound waves, the first aluminum nitride layer acts as a perfect stop-layer for the etching. This is done by cycling 200 loops of etching with five minutes of release to clean black silicon deposits, this process was finalized after 1000 loops. Then, polyimide spin-coating at 5000 rpm for one minute was done, curing by polyimide oven for one hour at 300°C is optimal, and patterning is carried out using RIE oxford 81 with CF_4/O_2 mixture of 15/45 sccm. Then, the top layer is finished by sputtering 200 nm aluminum, which is patterned by PT770 ICP machine, and depositing amorphous silicon for proof-mass with 200°C under 20 mtorr for 20 minutes to ensure stress is within tensile region, the amorphous silicon resulted is one micron thick and is etched with SF_6/O_2 mixture for one minute with RIE machine Oxford 81. Then, release of the top and bottom layers is done by vapor HF etching which is done using slow speed for 2 μm etch followed by 8 μm etch using faster recipe to etch oxide layer sideways. Finally, the wafer is diced and wire-bonded for testing.

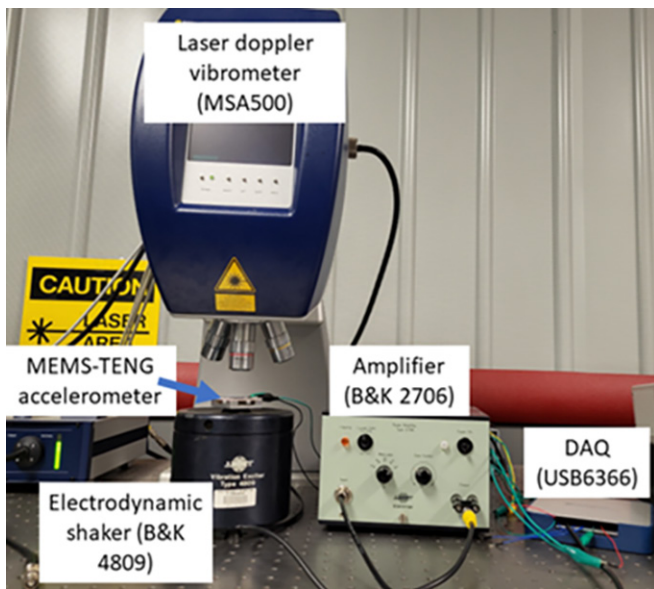


Figure 2: Fabrication process overview.

Results:

The accelerometer was tested at 0.5-4 kHz with excitation amplitude 2-10g with sinusoidal input. The frequency response (Figure 3) shows a noticeable resonance peak at 1.25 kHz with 1.8 V generated at the highest end as a response to excitation of 10g. The frequency response for the rest of the tested bandwidth is relatively flat for every tested acceleration amplitude. The residual stresses during deposition processes of spin-coating the polyimide and from the sputtering deposition of the aluminum layer caused shift in resonance between expected and acquired results. These stresses cause the released membranes to buckle up which creates undesired differences between the designed and the actual device.

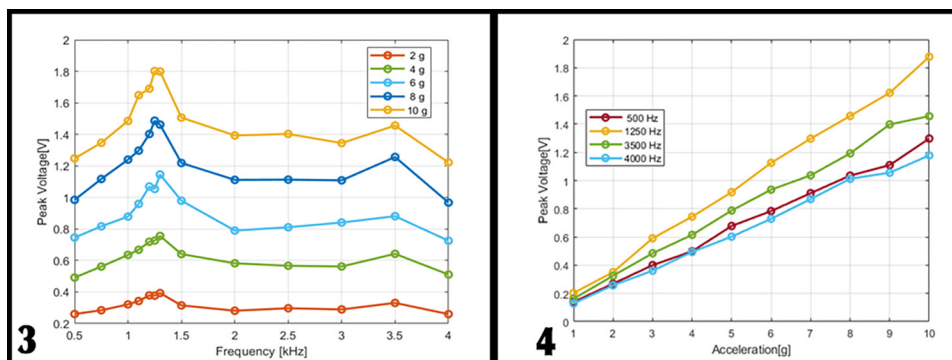


Figure 3: Frequency response of the triboelectric accelerometer.

Figure 4: Excitation amplitude-triboelectric accelerometer output voltage.

Generated voltage-excitation amplitude (Figure 4) still shows linear relation with the highest sensitivity of 187 mV/g. The sensitivity is an improvement over our previous design which has 68 mV/g sensitivity with only 0.7 V as the highest produced voltage [1]. It is also noticed that there is a linear relationship between the measured acceleration and the produced voltage for the fabricated accelerometer at each frequency. Results present a promising design that can be suitable for self-powered MEMS motion sensors or microphones.

Conclusions and Future Work:

In this work, we were able to significantly enhance the performance of a triboelectric accelerometer by applying genetic algorithm to the design and by modifying the fabrication process. We targeted maximum sensitivity in our optimization and changed the placement of the dielectric layer from the bottom to top. The changes made to the fabrication process alongside the changes in the design have improved the device output.

Currently, we are trying to test the device with back-etched volume to act as a microphone. Such work requires complete investigation of both diaphragm and back-plate separately to understand their integration.

References:

- [1] Alzgoool, M., Tian, Y., Davaji, B., and Towfighian, S. (2023). Self-powered triboelectric MEMS accelerometer. *Nano Energy*, 109, 108282.

Magnetically Programmed Diffractive Robotics

CNF Project Number: 2964-21

Principal Investigator(s): Itai Cohen, Paul L. McEuen

User(s): Conrad Smart, Zexi Liang, Melody Xuan Lim, Weiyi Li

Affiliation(s): Kavli Institute at Cornell for Nanoscale Science, School of Applied and Engineering Physics, Laboratory of Atomic and Solid-State Physics, Department of Physics; Cornell University

Primary Source(s) of Research Funding: National Science Foundation, Alfred P. Sloan Foundation

Contact: itai.cohen@cornell.edu, plm23@cornell.edu, cs2239@cornell.edu, zl467@cornell.edu, mxl3@cornell.edu, wl689@cornell.edu

Primary CNF Tools Used: Oxford 81/82 etcher, YES EcoClean Asher, ASML DUV Stepper, Gamma Automatic Coat-Develop Tool, JEOL 9500 EBL, JEOL 6300 EBL, SC 4500 Odd-Hour Evaporator, AJA Sputter Deposition, Heidelberg DWL2000, PT770 Etcher (left side), Unaxis 770 Deep Silicon Etcher, Oxford FlexAL, Oxford PECVD, Plasma-Therm Takachi HDP-CVD, Zeiss SEM, Veeco AFM

Abstract:

We introduce a new class of magnetically controlled microscopic robots (microbots) that operate at the visible-light diffraction limit, which we term diffractive robots. We combine nanometer-thick mechanical membranes, programmable nanomagnets, and diffractive optical elements to create untethered microbots small enough to diffract visible light and flexible enough to undergo complex reconfigurations in millitesla-scale magnetic fields. We demonstrate applications including sub-diffractive imaging using a novel variant of Structured Illumination Microscopy (Robot-SIM, or R-SIM), tunable diffractive optical elements for beam steering and focusing, and force sensing with piconewton sensitivity. This platform offers a powerful new tool for high-resolution imaging, tunable optics, and ultra-small force sensing, merging robotics and optical technologies at the microscale.

Summary of Research:

Microscopic robots with features comparable to the wavelength of light introduce diffractive optical effects, creating exciting new opportunities at the intersection of robotics and optics for probing the microscopic world and controlling light. Although the intersection of diffraction and tunable mechanics have been pioneered in the fields of micro-optical MEMS [1-3], these systems have never been miniaturized into a microscopic robotics package.

The two key elements that enable diffractive robots are programmable nanomagnets and ALD hinges. The nanomagnet arrays consist of single-domain cobalt nanomagnets ~ 100 nm

wide with varying aspect ratios. The coercive fields and magnetic dipole directions of these nanomagnet arrays are controlled by shape anisotropy [4,5]. The moments align along each magnet's long axis, and higher shape anisotropy (aspect ratio) magnets have higher coercive fields.

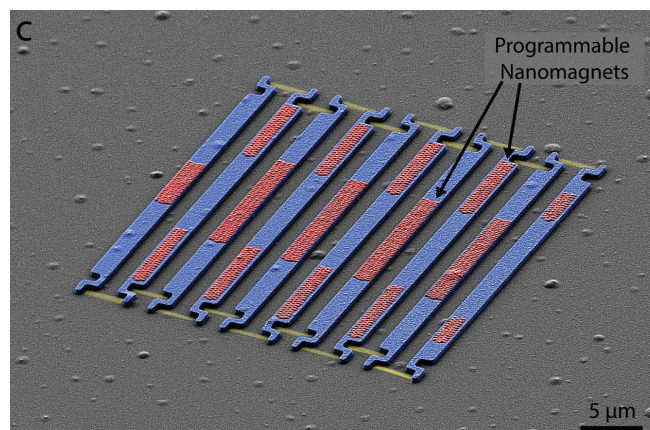


Figure 1: False-color scanning electron microscope image of a diffractive robot, consisting of (yellow) ALD silicon oxide hinges, (red) programmable cobalt nanomagnets, and (blue) rigid silicon oxide panels.

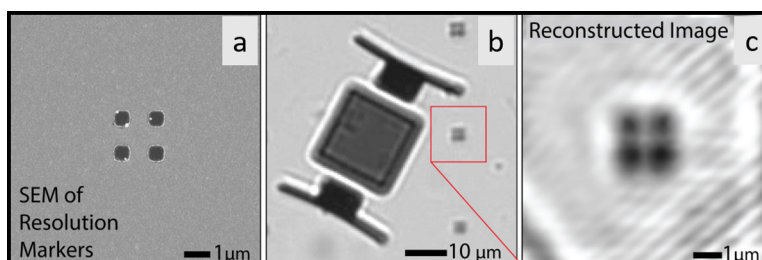


Figure 2: (a) SEM of the 2D resolution markers, (b) micrograph of diffractive robot near markers, (c) R-SIM reconstruction of the markers using the diffractive robot.

Using the disparate coercive fields, we sequentially magnetize the nanomagnet arrays in opposite directions to program the microbot magnetic control. The nanomagnets are embedded in 300 nm thick silicon dioxide panels and capped with chromium. Finally, 5 nm-thick ALD SiO₂ membranes connect the panels (Figure 1) to form a durable flexible joint [6].

As an illustration of the possible applications of diffractive robotics, we use a diffractive robot as a mobile optical element to image beyond the standard diffraction limit of a microscope. We do this using a variant of Structured Illumination Microscopy (SIM), where we use the body of a diffractive robot to create a structured light field, as well as to sample the rotated images for reconstruction. We call this technique Robotic SIM, or R-SIM. Our robot consists of a diffraction grating (1000 lines/mm) body connected to two magnetized panels. We implement R-SIM by walking the robot across the features to be imaged and collecting a series of images at a variety of angles and phases. We demonstrate the power of R-SIM by imaging a pattern of four metal dots spaced 600 nm apart (shown in the SEM in Figure 2a) that cannot be resolved using standard optical microscopy.

The robot is scanned across the feature to collect three angles and five phases per angle, with an overall acquisition time of ~ 30 seconds. The diffraction-limited object in Figure 2b is reconstructed in Figure 2c, demonstrating that R-SIM can resolve the four isolated dots.

To demonstrate beam steering, we fabricate microscopic diffraction gratings with magnetically tunable periodicities as shown in Figure 3. At zero magnetic field, the grating has a periodicity of 500 lines/mm. As the field increases (i-iii) the panels compress. In the corresponding diffraction images, three bright spots are seen: a central bright peak and lesser bright peaks to the left and right which move away from the central peak with increasing magnetic field (i-iii). These peaks are the zeroth, -1, +1 diffractive orders of the grating, corresponding to beams deflected by angles $\theta = \arcsin(n\lambda/a)$, where a is the grating spacing. The mechanical structure of the robot thus allows us to magnetically beam steer the diffractive orders. These gratings can also locomote across the surface to enable mobile, local control of light fields.

Inversely, this coupling between the internal configuration and the optical properties can be used

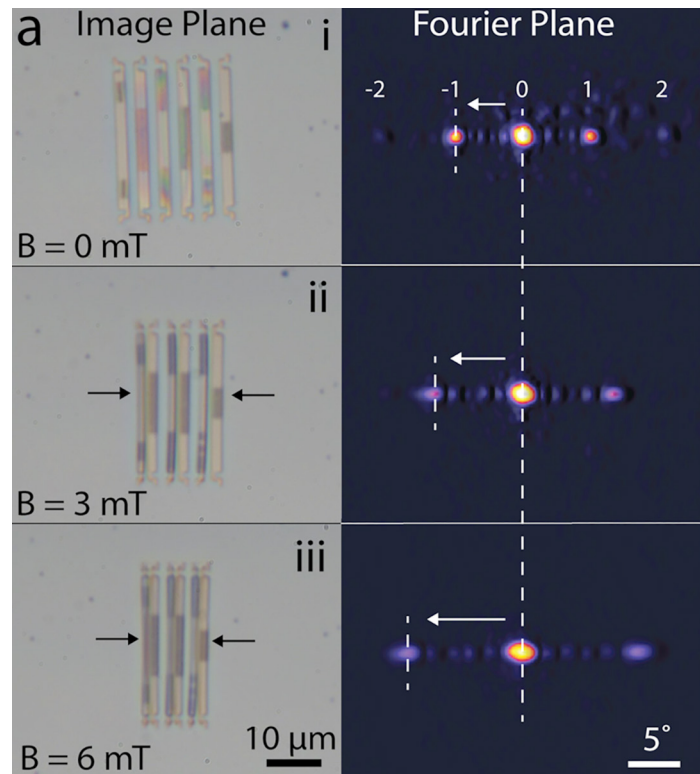


Figure 3: Image plane (left) and Fourier plane (right) of the diffraction grating in a uniform magnetic field of 0 mT, 3 mT, and 6 mT.

to measure small forces acting on the microbot, by measuring the location of the +1 diffractive order. We measure a noise floor of $5 \mu\text{T}$ at a 30 Hz bandwidth, with a force sensitivity of 1 pN.

References:

- [1] Z. Yang, T. Albrow-Owen, W. Cai, T. Hasan, Miniaturization of optical spectrometers. *Science* 371, eabe0722 (2021).
- [2] J. Chai, K. Zhang, Y. Xue, W. Liu, T. Chen, Y. Lu, G. Zhao, Review of MEMS Based Fourier Transform Spectrometers. *Micromachines* 11, 214 (2020).
- [3] O. Solgaard, A. A. Godil, R. T. Howe, L. P. Lee, Y.-A. Peter, H. Zappe, Optical MEMS: From Micromirrors to Complex Systems. *Journal of Microelectromechanical Systems* 23, 517-538 (2014).
- [4] J. Cui, T.-Y. Huang, Z. Luo, P. Testa, H. Gu, X.-Z. Chen, B. J. Nelson, L. J. Heyderman, Nanomagnetic encoding of shape-morphing micromachines. *Nature* 575, 164-168 (2019).
- [5] R. P. Cowburn, Property variation with shape in magnetic nanoelements. *J. Phys. D: Appl. Phys.* 33, R1 (2000).
- [6] K. J. Dorsey, T. G. Pearson, E. Esposito, S. Russell, B. Bircan, Y. Han, M. Z. Miskin, D. A. Muller, I. Cohen, P. L. McEuen, Atomic Layer Deposition for Membranes, Metamaterials, and Mechanisms. *Advanced Materials* 31, 1901944 (2019).

Microwave Frequency Acoustic Resonators for Quantum Applications

CNF Project Number: 3042-22

Principal Investigator(s): Andrew Cleland

Affiliation(s): Pritzker School of Molecular Engineering, University of Chicago

Primary Source(s) of Research Funding: AFOSR

Contact: anc@uchicago.edu

Primary CNF Tools Used: OEM Endeavour

Abstract:

We are exploring the low temperature mechanical performance of thin-film, oriented AlN deposited on silicon and sapphire substrates. We are using this material to make bulk acoustic wave and surface acoustic wave devices for quantum applications. These are ultimately for applications in quantum acoustics, to be measured using superconducting qubits as single phonon sources and detectors. The goal is to quantify loss in these devices at low temperatures and low phonon excitation powers.

Summary of Research:

The oriented AlN films we are using are remotely grown by reactive sputter deposition at Cornell's CNF, targeting typically 300 nm thick oriented AlN films. These are then post-deposition patterned with thin-film aluminum at UChicago's PNF, where the patterned aluminum film defines either surface acoustic wave transducers or bulk wave acoustic resonators, with design frequencies in the microwave frequency band (1-10 GHz). At these frequencies, measured at mK temperatures on a dilution refrigerator, these systems will be in their mechanical ground states, so loss and performance can be measured at single phonon powers. The device patterns involve either using geometries with in-plane surface acoustic wave transducers as delay lines or SAW resonators, or using single-sided capacitively-coupled transducers to couple to thickness-mode bulk acoustic wave resonator modes. Devices are measured at low temperatures (10-100 mK) using either microwave frequency vector network analyzers or using superconducting qubits for quantum (single phonon) measurements.

We have demonstrated we can use the AlN films on double-side polished silicon wafers to make high quality factor (1-10 million Q) bulk acoustic wave resonators (BAWs) as measured using a vector network analyzer. We have also integrated similar design BAWs with superconducting qubits to perform measurements in the quantum limit; these experiments are still on-going, with no conclusive results to date.

Conclusions and Future Steps:

Work is still in progress. We may order additional films grown if and when we run out of the existing material.

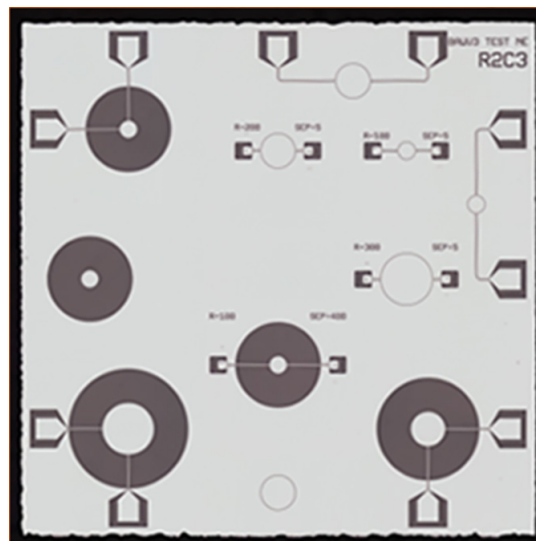


Figure 1: Image of set of bulk acoustic wave resonator structures; silver is aluminum metallization, darker areas are underlying AlN on silicon.

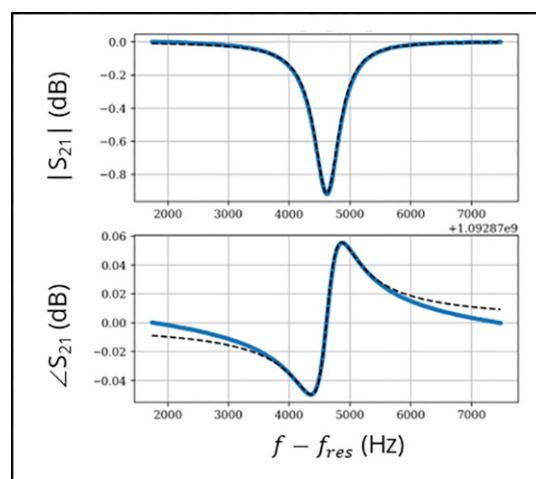


Figure 2: Vector network analyzer measurements of one bulk acoustic wave resonance, with a mechanical Q of about 2 million measured at about 3 GHz and a temperature of 3K.

High Efficiency Fiber-Chip Coupling

CNF Project Number: 2524-17

Principal Investigator(s): Jaime Cardenas

User(s): Sushant Kumar

Affiliation(s): The Institute of Optics, University of Rochester

Primary Source(s) of Research Funding: National Science Foundation - PFI

Contact: jaime.cardenas@rochester.edu, skumar31@ur.rochester.edu

Research Group Website: <https://www.hajim.rochester.edu/optics/cardenas/>

Primary CNF Tools Used: JEOL9500, ASML PAS 5500/300C DUV Stepper, Oxford PECVD, LPCVD Furnace, Oxford 100 Etcher, Unaxis 770 Deep Silicon Etcher, Plasma-Therm Versaline Silicon Etcher, Xactix Xenon Difluoride Etcher

Abstract:

We design and fabricate silicon photonic chips for high efficiency Polarization Maintaining optical fiber-chip coupling.

Summary of Research:

The need for increasingly large amounts of data and bandwidths has been driving the growth of Silicon Photonics for telecom and data-center applications. But this has also led to an increasing share of power consumption in the optical data-networks leading to development of more energy efficient designs like co-packaged optics [1], ring-based modulators [2], etc. These designs while being energy efficient are very sensitive to polarization. To ensure clean polarization devices can integrate laser sources on chip [3], which increases heat density on chip and introduces associated thermal instability and cross coupling issues that require more expensive cooling and careful design. More modern system designs [4] include external laser sources to reduce the heat density on chip but require PM fiber connections to the chip. To our knowledge there are no good industry level solutions for PM fiber connections.

Most widespread packaging solutions for PM fibers rely on micro lens assemblies and some recent work on angle thin polished PM fiber connection uses on chip gratings and epoxy [5], which makes the connection limited in bandwidth and heavily temperature dependent due to the use of epoxy. In this project we designed high efficiency couplers for PM-fiber-chip coupling and measured to verify any depolarization effects caused by the connection itself.

We designed the SiO₂ Mode Converter (MC) by matching the optical mode at the MC-fiber interface. This is done by optimizing the dimensions for the MC at the interface. This allows not only for efficient coupling

of optical power due to minimized mode matching, but also increases the alignment tolerance of the fiber-chip connection by making the mode 10 μm in diameter as compared to regular waveguide tapers which have 3-4 μm diameter optical modes. On the other end of the MC, the dimensions of the MC and waveguide taper are optimized to maximize the power transfer. Since at this interface everything is lithographically designed, misalignment is not a concern and only the power coupling efficiency is of import. The input and output ports are offset laterally to eliminate any scattered light polluting the measurements.

We start with 5.75 μm of OXFORD-PECVD SiO₂ on a blank Si wafer and then use a 300 nm thick OXFORD-PECVD deposited Si₃N₄ layer for waveguide layer. The waveguides are defined using the ASML-PAS-500 stepper and etched using the OXFORD-100 ICP-RIE. We deposit 5.75 μm SiO₂ via OXFORD-PECVD and then pattern the SiO₂ (MC) using the ASML PAS-5000. The SiO₂ is etched using the OXFORD-100. Fiber grooves are etched into the chip using either UNAXIS 770 or the Plasma-Therm Versaline Deep Silicon Etcher. Once the grooves are etched the chips are undercut using the Xactix Xenon Difluoride Etcher to optically isolate the mode while it propagates in the SiO₂ mode converter. The wafer is diced into chips using the DISCO dicing saw. Further details on the design and fabrication of devices can be found in the published paper [6].

For testing the coupling efficiency and the polarization extinction ratio (PER), light coming out of the PM fiber is used as baseline and the fiber is aligned to TE orientation using a free-space linear polarizer. Then the light is launched onto the chip and collected at the output using a high NA microscope objective to estimate the propagation loss of the chip. At this point the pre-fusion PER is also estimated and largely matches the

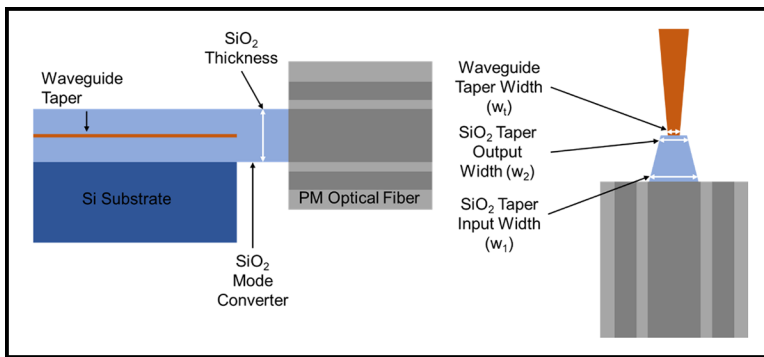


Figure 1: Chip design and material configuration.

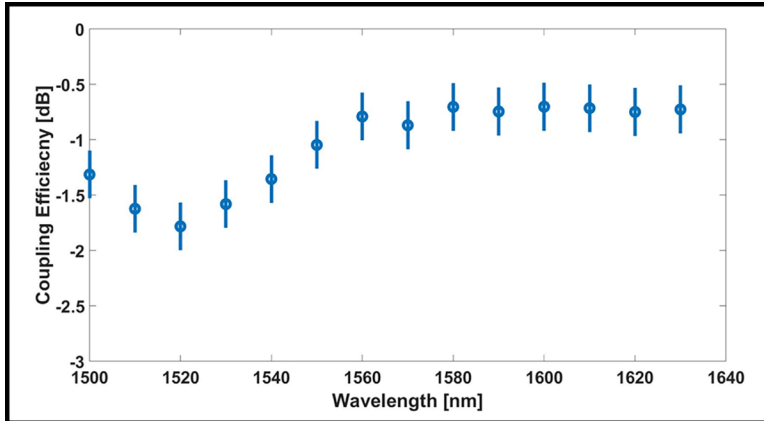


Figure 2: Coupling data for fused fiber-chip connection.

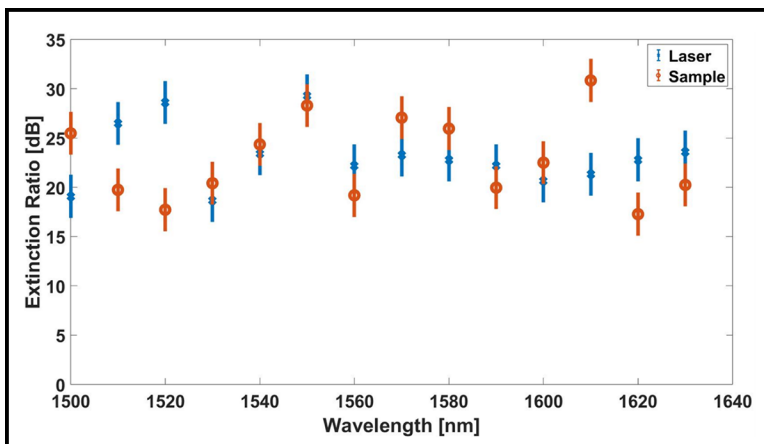


Figure 3: PER data for post-fusion PM-fiber-chip connection.

baseline established from the PM fiber. This indicates that the light coming out of the PM fiber doesn't depolarize as it couples to and travels through the chip. Then the objective is replaced with another optical fiber to estimate a pre-fusion coupling efficiency of 1.2dB. Then the fiber is fused to the chip using a CO2 laser and the light is again collected using the optical fiber at the other end and the post fusion coupling is estimated to be 1dB per facet. Then the fiber at the output is replaced with the high NA objective with a liner polarizer in the optical path, to again estimate the PER. As shown in Figure 2.

The PER post fusion also largely follows the baseline established from the PM fiber light leading to the conclusion that the fusion doesn't lead to any damage to the PM fiber structure or any depolarization of the light.

Conclusions and Future Steps:

In conclusion, we demonstrate efficient fiber to chip connection via CO2 laser fusion and show no degradation in polarization of the light that is being couple onto the chip. This demonstrates that the MC design and the laser fusion process are a viable option not only for standard single mode fibers-chip coupling but also for PM fibers. Further design, fabrication and testing is underway for other fiber configurations.

References:

- [1] John Williamson, "Co-packaged optics, putting the pieces together," OpticalInterconnectNews.com, Issue 30, pp 20-21.
- [2] M. Kim, M. Kim, Y. Jo, H. Kim, S. Lischke, C. Mai, L. Zimmermann, and W. Choi, "A Fully Integrated 25 Gb/s Si Ring Modulator Transmitter with a Temperature Controller," in Optical Fiber Communication Conference (OFC) 2020, OSA Technical Digest (Optica Publishing Group, 2020), paper T3H.7.
- [3] P. J. Winzer, "Optical Networking Beyond WDM," in IEEE Photonics Journal, vol. 4, no. 2, pp. 647-651, April 2012, doi: 10.1109/JPHOT.2012.2189379.
- [4] W. Zhou, Y. Zhu, J. Wang, M. Moewe, R. Zhu, W. Zhao, V. Rossin, H. Liu, J. Wang, T. Zhu, P. Yalamanchili, T. Pham, R. Chen, V. Zeng, and J. Stewart, "High Power CW Laser for Co-Packaged Optics," in Conference on Lasers and Electro-Optics, Technical Digest Series (Optica Publishing Group, 2022), paper SS2D.3.
- [5] B. Snyder and P. O'Brien, "Packaging Process for Grating-Coupled Silicon Photonic Waveguides Using Angle-Polished Fibers," in IEEE Transactions on Components, Packaging and Manufacturing Technology, vol. 3, no. 6, pp. 954-959, June 2013, doi: 10.1109/TCPMT.2012.2237052.
- [6] J. Nauriyal, M. Song, R. Yu, and J. Cardenas, "Fiber-to-chip fusion splicing for low-loss photonic packaging," Optica 6, 549-552 (2019).

Programmable Poling for Electric Field Induced Second Harmonic Generation

CNF Project Number: 2971-21

Principal Investigator(s): Peter McMahon^{1,2}

User(s): Ryotatsu Yanagimoto^{1,3}, Benjamin Ash^{1,3}

Affiliation(s): [1] School of Applied and Engineering Physics, Cornell University; [2] Kavli Institute at Cornell for Nanoscale Science, Cornell University; [3] NTT Physics and Informatics Laboratories, NTT Research, Inc.

Primary Source(s) of Research Funding: NSF Award CCF-1918549, David and Lucile Packard Foundation Fellowship, NTT Research, Air Force Office of Scientific Research Award Number FA9550-22-1-0378

Contact: pmcmahon@cornell.edu, ry338@cornell.edu baa77@cornell.edu

Primary CNF Tools Used: Oxford 100 PECVD, Even-Hour Evaporator, Woollam RC2 Spectroscopic Ellipsometer, Lesker PVD75 Sputter

Abstract:

Programmable photonics plays a vital role in modern technologies because of its low power consumption, high spatial parallelism, and high bandwidth. For most traditional devices, features are etched onto the device during fabrication, defining the device's utility. Recent device improvements enable programmability over a high number of spatial features, allowing a device to move beyond the one device, one function paradigm. Using this device, we demonstrated optical computation with spatially programmable index of refraction, but the same approach underlying this device can be extended into the nonlinear regime by performing electric-field induced second harmonic (E-Fish) generation. This work demonstrates proof-of-concept material development for a nonlinear lithography-free waveguide that converts 1550 nm light into 780 nm light with the ability to shape the wavefront of the generated signal. In the long term, this nonlinear programmability could enable light generation at nontraditional frequencies and spatially parallel computation.

Summary of Research:

Lithography-free photonics has attracted considerable attention in the field of programmable photonics because the large number of programmable parameters allows the device to move beyond the one device, one function paradigm. This means lithography-free devices can perform a large range of tasks and compensate for fabrication error [1]. Recent advances in lithography-free technology have enabled a device with real index of refraction modulation on-chip. In this device, a photoconductor and waveguiding layer with high native χ^2 nonlinearity are stacked in series and placed under high voltage, allowing the two layers act as a voltage divider. Because the index of refraction of the

waveguiding layer depends on the electric bias, the index of refraction can be spatially controlled by shining different patterns of light onto the photoconductor [2]. Using the same device concept, the core material can be replaced with a material that displays large induced χ^2 during an electric-field induced second harmonic (E-Fish) process. Silicon nitride has previously demonstrated large induced χ^2 under a large electric bias, and our work successfully reproduced these results [3]. Furthermore, devices fabricated in the CNF displayed programmable E-Fish, showing that we can program the poling period and measure the increased second harmonic signal at the output. Finally, potential doped oxynitride claddings have been fabricated on the PECVD system which have the potential to make a more efficient, continuous-operation device.

Silicon-Rich Silicon Nitride Development. Using a PECVD system, we deposit silicon nitride films with low optical loss over a wide range of visible and infrared wavelengths. By adjusting the silane flow during deposition, we can tune the index of refraction from 1.9 to 2.4 at a wavelength of 1 μm . Moreover, these films display high photoconductivity, with a 100X conductivity switching ratio when pumped with a 532 nm laser. To characterize the film's induced χ^2 , we deposit our SiNx films onto conductive Si substrates with 1.4 μm of thermal oxide. After sputtering ITO onto the SiNx layer, we pump the sample with 1535 nm light and record the power of 776 nm light generated as a function of applied DC voltage. By comparing this signal to the signal generated by LiNbO3 (which has a well-characterized native χ^2), we can estimate the effective χ^2 in our films as we increase the applied electric field.

Figure 1 shows the measured χ^2 for our silicon nitride and other similar films, which are consistent with

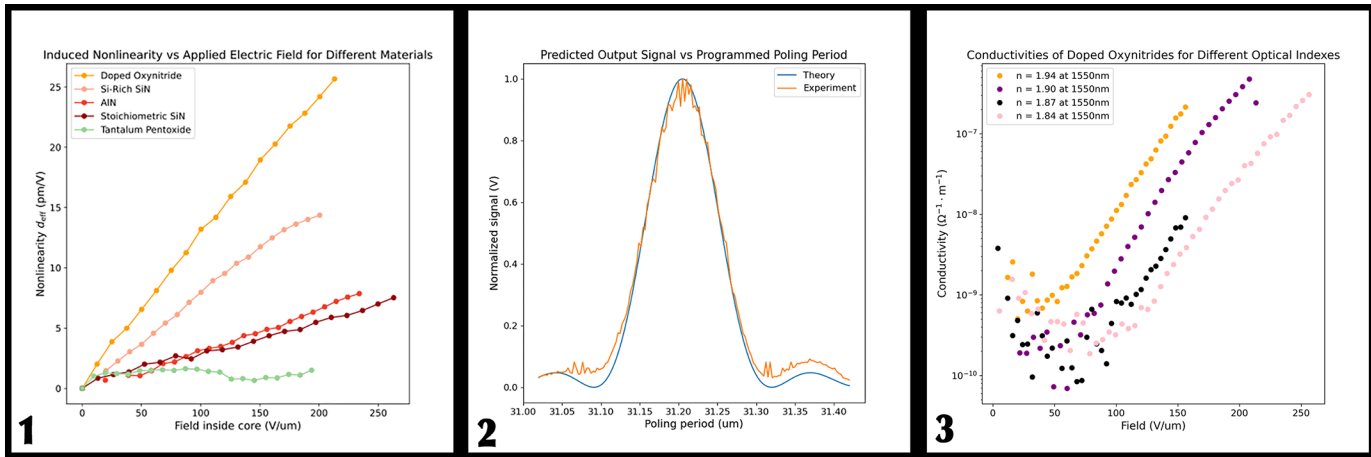


Figure 1: Silicon-rich nitride shows exceptionally high induced nonlinearity under large applied electric fields. When compared to other materials, silicon-rich silicon nitride has high induced nonlinearity. Its high optical index and low optical loss over a wide range of visible and infrared frequencies make it a desirable core material for a programmable nonlinear device.

Figure 2: Comparison of the predicted generated output power versus the experimental output power for different applied poling periods. The close agreement between experiment and theory proves that we can program the poling period to satisfy the phase matching condition for E-Fish. This procedure can be executed for different wavelengths and waveguide dispersions.

Figure 3: Characterization of the electric conductivity of boron-doped silicon oxynitrides. Doped oxynitrides display exceptionally high conductivities given their low optical indexes. Moreover, these conductivity curves show that both index and conductivity can be tuned by adjusting the N₂O or B₂H₆ flow. These characteristics, combined with losses below 5 dB/cm across a broad range of infrared frequencies, make these films ideal claddings for a continuous operation device.

recent measurements on similar materials [3]. When these films are integrated into a programmable device, we can apply different poling periods to satisfy the phase-matching condition for E-Fish. Our device design consisted of SiN_x waveguide cores with SiO₂ claddings. By applying a low-AC bias to the film, we could optimize the impedance of each film to achieve the highest field contrast between SiN_x in the bright and dark state. Figure 2 demonstrates a device where we apply varying poling periods and optimize this period to achieve the largest output signal.

Doped Oxynitride Development. In our current device configuration, there is an impedance mismatch between the cladding and core layers of the device at DC. This means the higher impedance layers (specifically the oxides) will dominate the impedance of the stack at DC and reduce the switching ratio. While we can apply AC voltage to correct for this issue, this causes our devices to have lower modulation efficiencies and to operate non-continuously. One solution to this problem is fabricating low-loss, low-index, conductive cladding materials where we can change the deposition parameters to tune the index and conductivity. Films have already been demonstrated to achieve these types of parameters using boron-doped silicon oxynitrides, so we modified these recipes to integrate them into our devices [4]. Figure 3 shows the characterized conductivities of these films, which are repeatable across different depositions. In the future, we hope to integrate our SiN_x and doped

oxynitride films to make a continuous operation nonlinear programmable waveguide which can perform E-Fish generation and optical parametric amplification to generate different frequencies.

Acknowledgements:

The authors wish to thank National Science Foundation funding (award CCF-1918549). PLM gratefully acknowledges financial support from a David and Lucile Packard Foundation Fellowship. The authors wish to thank NTT Research for their financial and technical support. We gratefully acknowledge the Air Force Office of Scientific Research for funding under Award Number FA9550-22-1-0378. This work was performed in part at the Cornell NanoScale Facility, a member of the NNCI, which is supported by NSF Grant NNCI-2025233.

References:

- [1] P. L. McMahon, Nature Reviews Physics 5, 717 (2023).
- [2] T. Onodera, et al, Scaling on-chip photonic neural processors using arbitrarily programmable wave propagation (2024), arXiv:2402.17750.
- [3] E. Timurdogan, C. V. Poulton, M. J. Byrd, and M. R. Watts, Nature Photonics 11, 200 (2017).
- [4] N. Brinkmann, D. Sommer, G. Micard, G. Hahn, and B. Terheiden, Solar Energy Materials and Solar Cells 108, 180 (2013), selected publications from the 22nd Space Photovoltaic Research and Technology (SPRAT) Conference.

HfO₂-Based Platform for High Index Contrast Visible and UV Integrated Photonics

CNF Project Number: 2985-21

Principal Investigator(s): Karan Kartik Mehta²

User(s): Oscar Jaramillo^{1,2}

Affiliation(s): 1. Applied and Engineering Physics, 2. Electrical and Computer Engineering; Cornell University

Primary Source(s) of Research Funding: NSF, Corning

Contact: karanmehta@cornell.edu, oj43@cornell.edu

Primary CNF Tools Used: Metritcon, Zeiss Ultra SEM, JEOL 9500, PT770 Etcher, Woollam RC2 Spectroscopic Ellipsometer, AFM, Furnaces, Oxford PECVD, Keyence VHX-7100 Digital Microscope, Oxford FlexAL

Abstract:

We investigate photonic devices fabricated within a HfO₂/Al₂O₃ platform for high-index visible/ultraviolet photonics. Our findings show bulk optical losses of 2.8 ± 1.4 dB/cm and single-mode (SM) waveguide losses of 7.9 ± 1.7 dB/cm at a wavelength (λ) of 375 nm. At $\lambda = 405$ nm, SM waveguides show 2.6 ± 0.45 dB/cm. For $\lambda = 730$ nm, we measure a loaded quality factor (Q) of 1,840,000 bounding (SM) waveguide losses to <0.4 dB/cm. These results highlight the potential of (HfO₂)_x(Al₂O₃)_{1-x} devices and systems for visible and ultraviolet photonics.

Summary of Research:

Photonic integration at visible and UV wavelengths has applications in trapped-ion systems, spectroscopy, and other fields [1-3]. However, most common material platforms for integrated photonics absorb strongly in the UV, and increased surface and sidewall scattering at shorter wavelengths (scaling roughly as $\sim \lambda^{-4}$) pose a challenge in achieving low-loss waveguide structures. Silicon nitride (SiN) is a well-developed material with a high refractive index (~ 2.06 at $\lambda = 405$ nm), but experiences bulk optical losses of approximately 2.5 dB/cm at $\lambda = 461$ nm [4] and higher at shorter wavelengths [5]. Another material, aluminum oxide (Al₂O₃), has been used to demonstrate propagation losses of ~ 1.35 dB/cm at 369 nm [6,7], but suffers from a relatively low refractive index (~ 1.68 at $\lambda = 405$ nm). Hafnium dioxide (HfO₂), a CMOS compatible material, offers a high refractive index (~ 2.1 at $\lambda = 405$) and a wide band-gap

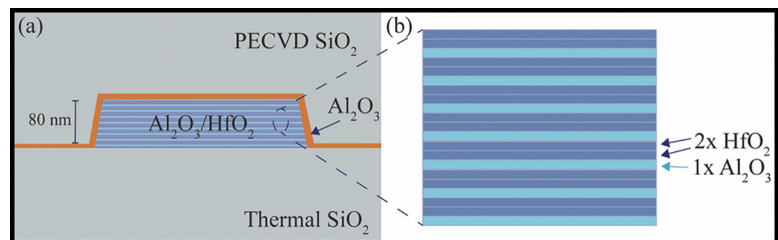


Figure 1: Waveguide cross-section showing an HfO₂-based core, a 4 nm thick Al₂O₃ diffusion barrier and PECVD SiO₂ cladding.

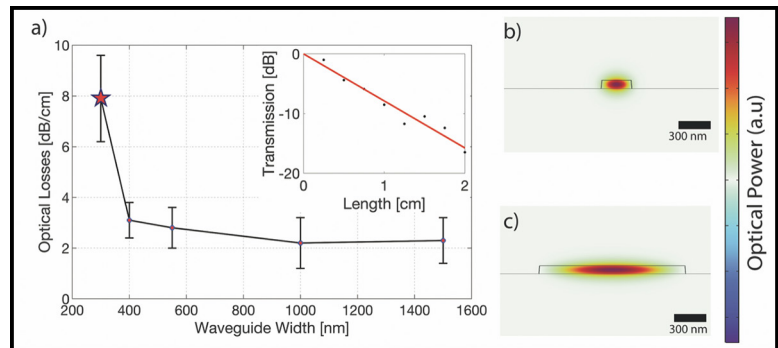


Figure 2: Optical micrograph of a representative device used to measure optical losses. To the right, an SEM image of a grating coupler used to couple light into the device.

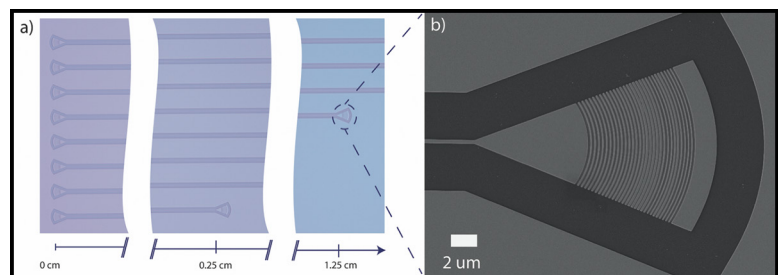


Figure 3: Measured optical losses for varying widths at 375 nm. Inset shows data obtained for a width of 300 nm.

material (5.65 eV) [8], but its tendency to crystallize limits its use in photonics to interaction lengths of ~ 100 nm [9,10]. Here we fabricate fully-cladded single mode (SM) and multimode (MM) waveguides using a low loss and high index HfO_2 -based composite (~ 1.97 at $\lambda = 405$), composed of alternating layers of HfO_2 and Al_2O_3 deposited via Atomic Layer Deposition (ALD) [11,12]. We demonstrate an optical loss at $\lambda = 375$ nm of 7.9 ± 1.7 dB/cm for SM waveguides and measure bulk optical loss associate to bulk material loss to be 2.8 ± 1.4 dB/cm at $\lambda = 375$ nm, and bound losses < 0.4 dB/cm at 730 nm from resonator measurements, indicating potential for this single high-index platform to span devices from the near UV to visible range.

Our platform consists of an 80nm-thick composite material deposited via ALD on a silicon wafer with $3 \mu\text{m}$ of thermally grown wet silicon oxide (Figure 1a). The composite material consists of single atomic layers of HfO_2 and Al_2O_3 with a duty cycle (DC) of 1/3 and a period (P) of 3, deposited via ALD at 300°C (Figure 1b). The characterization and choice of specific P and DC are discussed elsewhere [11,12]. After ALD deposition, we dice the wafer into pieces and anneal them at 800°C in a nitrogen environment for one hour. Each chip is processed separately by defining a pattern with electron beam lithography (JEOL9500) using ZEP520-A resist and etching with an inductively coupled plasma (ICP) etch using a BCl_3/Ar chemistry. The samples are then cleaned with a standard RCA clean. We deposit a ~ 4 nm layer of Al_2O_3 as a diffusion barrier and anneal again at 800°C for one hour. Finally, we deposit ~ 800 nm of plasma enhanced chemical vapor deposition (PECVD) SiO_2 as cladding.

We design and fabricate grating couplers to measure optical losses through a cutback configuration. Figure 2 shows subsections of a 4 cm long chip with input couplers and two output couplers at 0.25 cm and 1.25 cm, used to couple light in and out of the device from single-mode fibers. Figure 2b shows an SEM image of a representative grating for $\lambda = 405$ nm. We vary the width of the waveguide and measure the optical losses of each structure in order to discern sidewall scattering and bulk absorption. Figure 3a shows the measured optical loss as a function of width, with the inset showing a measurement obtained for a waveguide width of 300nm (indicated with a star on the plot). With increasing width, optical loss associated with sidewall scattering decreases and becomes dominated by bulk material loss. Quasi-TE optical modes measured for widths of 300 nm and 1500 nm are shown in Figure 3b and 3c, respectively.

A linear regression analysis [4] enables us to differentiate the fraction of optical loss arising from surface scattering vs. bulk loss. We find material loss to be 2.8 ± 1.4 dB/cm at $\lambda = 375$ nm.

Conclusions and Future Steps:

This work demonstrates that HfO_2 can be used to obtain competitive optical loss at $\lambda = 375$ and a higher refractive index than Al_2O_3 . We observe that optical loss is dominated by sidewall scattering, indicating that fabrication optimization can enable even lower optical losses in SM waveguides. This work may lead to significantly more efficient grating devices, compact footprints, and micro-resonant structures, among others, for photonics at blue/UV wavelengths as compared to platforms in pure Al_2O_3 or SiN. Future work will determine the ultimate loss at shorter wavelengths.

References:

- [1] D.J. Blumenthal. Photonic integration for UV to IR applications. *APL Photonics* 5, 020903, 2020.
- [2] G. Moody, et al. Roadmap on integrated quantum photonics. *J. Phys. Photonics* 4 012501. 2022.
- [3] Mehta, K., et al. Integrated optical addressing of an ion qubit. *Nature Nanotech* 11,1066-1070, 2016.
- [4] M. Corato-Zanarella, et al, "Absorption and scattering limits of silicon nitride integrated photonics in the visible spectrum," *Opt. Express* 32, 5718-5728 (2024).
- [5] C. Sorace-Agaskar, et al., "Versatile Silicon Nitride and Alumina Integrated Photonic Platforms for the Ultraviolet to Short-Wave Infrared," in *IEEE Journal of Selected Topics in Quantum Electronics*, vol. 25, no. 5, pp. 1-15, Sept. Oct. 2019, Art no. 8201515, doi: 10.1109/JSTQE.2019.2904443.
- [6] Kwon, J., et al. Multi-site integrated optical addressing of trapped ions. *Nat Commun* 15, 3709 (2024). <https://doi.org/10.1038/s41467-024-47882-5>
- [7] G.N. West, et al. Low-loss integrated photonics for the blue and ultraviolet regime. *APL Photonics* 4, 026101, 2019.
- [8] L. Kang, B. H. Lee, W.-J. Qi, Y. Jeon, R. Nieh, S. Gopalan, K. Onishi, and J. C. Lee. Electrical characteristics of highly reliable ultrathin hafnium oxide gate dielectric. *IEEE Electron Device Letters*, vol. 21, no. 4, pp. 181-183, 2000.
- [9] P. Torchio, A. Gatto, M. Alvisi, G. Albrand, N. Kaiser, and C. Amra. High-reflectivity $\text{HfO}_2/\text{SiO}_2$ ultraviolet mirrors. *Applied Optics*, vol. 41, no. 16, pp. 3256-3261, 2002.
- [10] Zhang, C., et al. Low-loss metasurface optics down to the deep ultraviolet region. *Light Sci Appl* 9, 55, 2020.
- [11] O. Jaramillo, L. Massai, and K. Mehta, "HfO₂-based Platform for High Index Contrast Visible and UV Integrated Photonics," in *CLEO 2023, Technical Digest Series* (Optica Publishing Group, 2023), paper STh10.6.
- [12] Leonardo Massai. High Polarization Purity and Short-wavelength Optics for Trapped-ion Quantum Systems. Master's thesis, ETH, 2021.

Metamaterial Spectrometer: A Low SWaP, Robust, High Performance Hyperspectral Sensor for Land and Atmospheric Remote Sensing

CNF Project Number: 3003-22

Principal Investigator & User: Lori Lepak

Affiliation(s): Phoebus Optoelectronics LLC

Primary Source(s) of Research Funding: National Aeronautics and Space Administration (NASA)

Contact: llepak@phoebusopto.com

Research Group Website: www.phoebusopto.com

Primary CNF Tools Used: ASML DUV Stepper, Oxford ALD, Oxford PECVD, Ultra and Supra SEM, CHA Evaporator, Oxford 81 Etcher, Logitech CMP

Abstract:

Since 2003, Phoebus Optoelectronics has enabled custom R&D solutions in the fields of Plasmonics, Metamaterials, Antennas, and Sensors. We work closely with our customers throughout device development, from simulation and design, to prototype realization, testing, and small volume manufacturing. Our R&D portfolio spans the spectral ranges of visible light, infrared, terahertz (THz), and microwave radiation, for applications in high resolution imaging systems, wavelength and polarization filtering, tunable optical components, beam forming and steering, solar cells, renewable energy devices, and chemical and biological toxin sensors. We routinely partner with large, industry-leading businesses to develop products in all of these areas, jointly performing advanced testing and working together to scale up to medium- and large-volume manufacturing. Our agile team makes extensive use of the resources at the CNF for our nano/micro fabrication and testing, to provide cost efficiency and rapid turnaround.

In the present report, we discuss the ongoing development of a metamaterial-based hyperspectral imaging filter.

Summary of Research:

Phoebus uses the resources of the CNF to fabricate plasmonic chips patterned with a metamaterial surface to enable Extraordinary Optical Transmission (EOT), a phenomenon unique to metastructures in which light is transmitted through apertures much smaller than the incident wavelength, at anomalously large intensities relative to the predictions of conventional aperture theory. EOT was first observed by T.W. Ebbesen in 1998 [1]. Since its founding in 2003, Phoebus has successfully harnessed EOT by incorporating metasurfaces into

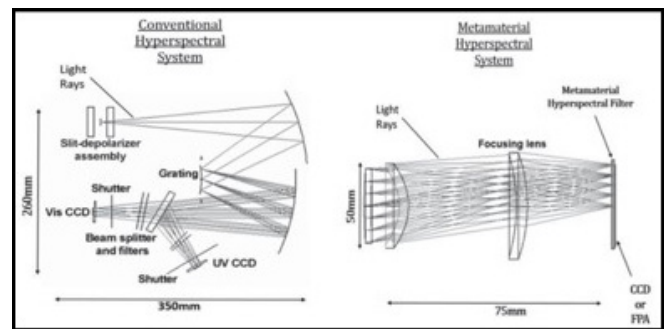


Figure 1: Phoebus's Metamaterial Spectrometer (MS) technology (right) eliminates much of the size and weight of conventional hyperspectral spectrometer technologies (left). Note the significant difference in scale of the two images.

devices used to perform light filtering [2-3], photon sorting [4-5], polarimetric detection [6], high speed optical detection [7], and SPR plasmonic sensor chips [8].

In our current project, we are developing a hyperspectral imaging system, shown schematically in Figure 1. Our technology (Figure 1b) uses a metasurface to precisely target very narrow spectral bands of interest, enabling a significant reduction in the size and number of optical components relative to current state-of-the-art imaging systems (Figure 1a), which in turn will enable the integration of our high-performance sensor onto weight-sensitive platforms (ie. satellites) far more readily than existing systems. Our initial goal is to detect and image trace gases in the Earth's atmosphere in the midwave infrared (MWIR), defined as 3-5 μm wavelength, while minimizing dependence on the Angle of Incidence (AoI) of light upon the sensor, up to an angle of 12° off-normal.

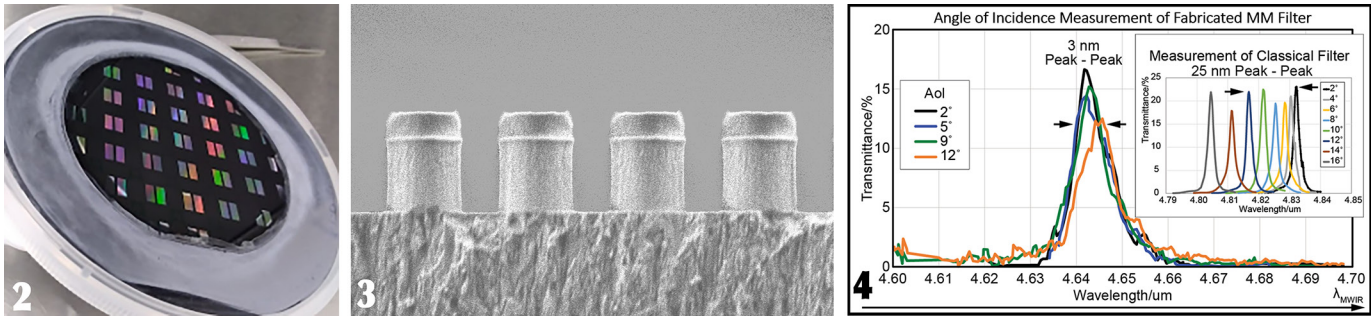


Figure 2: Wafer lithographically patterned with optical metastructures, using the ASML DUV stepper

Figure 3: SEM image (cross section) of etched pillars with near-vertical sidewalls. Imaged at ~ 15kX in the Ultra SEM, the grain structure of the etch stop layer is clearly visible.

Figure 4: Measured optical performance of fabricated metamaterial filter showing the angle of incidence independence up to a cone of 12° (f/2.4). (Inset) Same measurement performed on a classical Fabry-Pérot filter. Reproduced from reference 9.

Using the ASML DUV stepper, entire wafers can rapidly be lithographically patterned with highly uniform, large-area arrays of metastructures, as shown in Figure 2. In general, the optimal feature size and period of these metastructures depends primarily upon the desired wavelength of operation and the refractive indices of the constituent materials. In the MWIR, typical feature sizes are on the order of $\sim 1 \mu\text{m}$. Equally critical for minimizing optical losses in photonics applications, the relatively narrow spaces between features can be etched to form high-aspect-ratio structures with nearly vertical sidewalls, as shown in Figure 3.

Conclusions and Future Steps:

With strong, ongoing support from the National Aeronautics and Space Administration (NASA), we have successfully completed three generations of MWIR devices. As shown in Figure 4, they demonstrated the desired AoI insensitivity up to 12°. As we finish optimizing a few key process improvements in our fourth generation devices, we are beginning to integrate pixelated versions of our MWIR devices with commercially available ROIC's, for incorporation into a full camera system.

In addition, we are adapting our metasurface technology to other spectral ranges, from the visible to the microwave, by substituting appropriate materials, and scaling feature sizes as appropriate to the imaging wavelength. The extensive resources of the CNF are enabling us to rapidly develop our Metamaterial Spectrometer technology for a broad range of imaging and sensing applications.

References:

- [1] Ebbesen, T.W., et al. "Extraordinary optical transmission through sub-wavelength hole arrays." *Nature*, (1998). 391(6668): p. 667-669.
- [2] Crouse, D. "Numerical modeling and electromagnetic resonant modes in complex grating structures and optoelectronic device applications." *Electron Devices, IEEE Transactions on* 52.11 (2005): 2365-2373.
- [3] Crouse, D., et al. "Polarization independent enhanced optical transmission in one-dimensional gratings and device applications." *Optics Express* 15.4 (2007): 1415-1427.
- [4] Lansley, E., et al. "Light localization, photon sorting, and enhanced absorption in subwavelength cavity arrays." *Optics Express* 20.22 (2012): 24226-24236.
- [5] Jung, Y.U., et al. "Dual-band photon sorting plasmonic MIM metamaterial sensor." *Proc. SPIE 9070, Infrared Technology and Applications XL, 90702X* (June 24, 2014); doi:10.1117/12.2050620.
- [6] Crouse, D., et al. "A method for designing electromagnetic resonance enhanced silicon-on-insulator metal-semiconductor-metal photodetectors." *Journal of Optics A: Pure and Applied Optics* 8.2 (2006): 175.
- [7] Mandel, I., et al. Theory and Design of A Novel Integrated Polarimetric Sensor Utilizing a Light Sorting Metamaterial Grating. *Sensors Journal, IEEE*, (2012): Vol. PP, 99
- [8] Lepak, L., et al. "Handheld chem/biosensor using extreme conformational changes in designed binding proteins to enhance surface plasmon resonance (SPR)" *Proc. SPIE 9862, Advanced Environmental, Chemical, and Biological Sensing Technologies XIII, 9862-7* (April 17, 2016); doi:10.1117/12.2222305.
- [9] Bendoy, I., et al. "Low SWaP-C hyperspectral metamaterial spectrometer (MMS) for narrow-band, wide angle-of-incidence MWIR atmospheric sensing," *Proc. SPIE 12091, Image Sensing Technologies: Materials, Devices, Systems, and Applications IX, 120910J* (30 May 2022); <https://doi.org/10.1117/12.2632794>.

optiXphere Sensor Development

CNF Project Number: 3101-23

Principal Investigator & User: Tom Dunbar

Affiliation(s): tomPhyxx.LLC

Primary Source(s) of Research Funding: tomPhyxx.LLC, NYS Advanced Materials Grant (NYSTAR-AMT MEP)

Contact: tom@tomPhyxx.com, tom@uvcPhyxx.com

Research Group Website: tomPhyxx.com

Primary CNF Tools Used: CHA Evaporators, ABM Contact Aligner, Heidelberg DWL2000, YES Polyimide Oven

Abstract:

The optiXphere project aims to develop an omnidirectional UV-C detector. This report summarizes the progress made in substrate development, coating methods, and photolithographic techniques over the past year. Key advancements include refining the aluminum evaporation process, developing a wax resist etching technique, and constructing a projection lithographic system. These efforts have significantly improved the uniformity of photocurrent response across the substrate, moving closer to achieving a nearly flat detection curve.

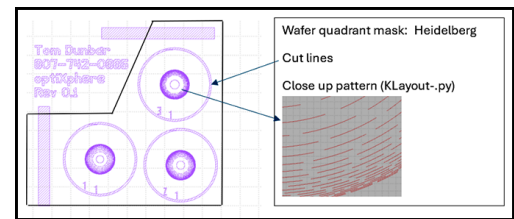


Figure 1: Quadrant mask design used for initial pattern transfer attempts.

Summary of Research, 2023-2024 Progress:

Substrate Development. Initial substrates were received from a Vermont Lampworker. A contract for substrate molding production was undertaken, resulting in near production-quality components. The refinement in the lampworker's process has ensured that the substrates are of high quality and suitable for subsequent experimental phases. The ability to produce substrates that meet the desired specifications has been a critical step in advancing the project.

Coating Methods. Various coating methods and CHA evaporations were evaluated, reducing UV-C photocurrent non-uniformity from four to two orders of magnitude. This significant improvement highlights the effectiveness of the refined coating techniques, paving the way for consistent and reliable substrate performance in future experiments. The evaluation of different methods has allowed for optimization of the coating process, ensuring that the substrates meet the necessary quality standards.

Nanoimprint Pattern Transfer Attempts. Initial attempts using SU-8 photoresist and Sylgard 185 molds for pattern transfer were abandoned due to mold press issues and limitations in feature size. The process aimed to create diffractive patterns, Figure 1, on the substrate but faced challenges in achieving the desired precision and resolution. Despite these challenges, valuable insights were gained, leading to the development of alternative approaches for pattern transfer.

New Approach 1, Projection Photolithography. Aluminum evaporation over the full substrate using the ODD-hour evaporator and a custom-built projection photolithographic stepper was pursued. A simplistic rotator system was developed as an accessory for the CHA Thermal evaporator to improve substrate coating uniformity.

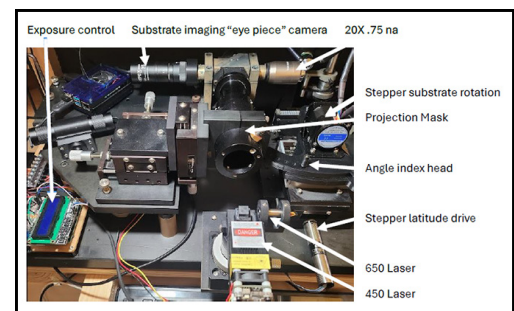


Figure 2: Custom-built projection photolithographic stepper system.

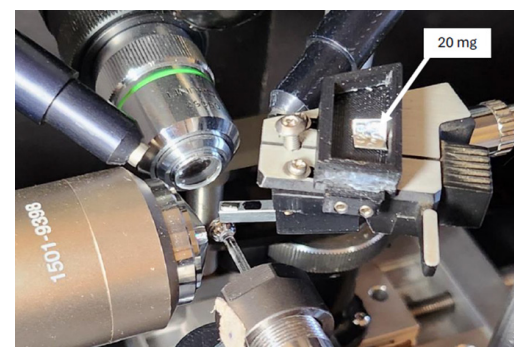


Figure 3: Custom-built wax scribing system.

This new approach addressed the limitations of previous methods, allowing for more precise control over the coating process and resulting in better substrate uniformity. The ability to achieve uniform coatings has been crucial in improving the overall performance of the substrates.

System Construction, Figure 2. A projection system with on-axis imaging was constructed to evaluate focus on spherical substrates. Exposures were made using a Young's double slit pattern, revealing resolution limitations. The system included a 650 nm dimmable diode laser for focusing and a 450 nm laser for exposure, controlled by an Arduino microcontroller. This setup enabled detailed examination of the substrate surface and the quality of the photolithographic process, providing critical insights for further refinements. The construction of this system has been a key development, allowing for precise control and evaluation of the photolithographic process. Resolution limitations using the current system components have shelved this approach for now.

New Approach 2, Wax Resist Etching. Inspired by Renaissance glassmaking techniques, wax-coated substrates were scribed and etched, creating thin horizontal features. Initial experiments using atomic force microscope probes were unsuccessful, leading to the planned use of microtome blades for more robust scribing. This wax resist technique, dubbed "Plow Lithography," involved detailed scribing of the wax layer followed by etching to expose the underlying aluminum, creating the desired patterns. The development of this technique should provide a reliable method for creating the necessary patterns on the substrates, Figure 3.

Funding and Collaboration:

Supplemental funding was secured through the NYS Advanced Materials Initiative Grant with MEP partnership with the Alliance for Manufacturing and Technology. Collaboration with Glassomer for substrate development is ongoing, with the first prototypes expected soon. The grant supplies in part CNF experiment expenses. These collaborations have provided essential resources and expertise, enabling significant progress and ensuring that the project stays on track. The funding and collaborative efforts have been instrumental in advancing the project and overcoming various challenges.

Experimental Results:

The first set of suitably coated substrates provided promising photocurrent results, showing a significant reduction in non-uniformity, Figure 4. The raw uncoated

substrate had a four orders of magnitude non-uniformity, which was reduced to two orders with aluminum coating. This marked improvement validates the new coating and patterning techniques and demonstrates their potential for producing high-quality detectors. The experimental results have been encouraging, providing a strong foundation for further development.

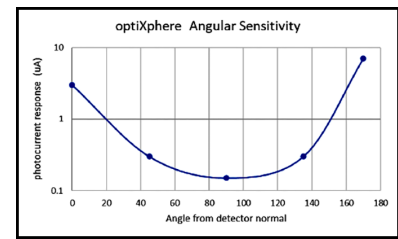


Figure 4: Photocurrent response versus latitude location on the substrate.

Process Challenges:

The initial pattern transfer approach faced challenges with mold pressing and achieving sub-micron feature sizes. The wax resist etching process also encountered difficulties, particularly with the surface roughness and speed limitations using atomic force microscope probes. These issues prompted the development of a more robust scribing technique using microtome blades. Addressing these challenges is crucial for achieving the desired precision and consistency in the substrate features, ensuring the final product meets the stringent requirements for UV-C detection. The challenges encountered have highlighted the need for continuous refinement and adaptation of the techniques used.

Conclusions and Future Steps:

The optiXphere project has made significant strides in substrate coating and patterning techniques. However, challenges remain in achieving the desired feature sizes and uniformity. Future efforts will focus on refining the wax resist etching process, developing stronger scribing tools, and exploring reflow transfer techniques for conformal 3D microprinting. Continued collaboration with CNF and external partners will be crucial in advancing the project towards a commercial-ready detector. Achieving a nearly flat photocurrent response across the substrate remains the ultimate goal, ensuring consistent and reliable detection of UV-C light, which is essential for practical applications in various fields. The future steps outlined will build on the progress made and address the remaining challenges to achieve the project's goals.

References:

- [1] Zabow, G. (2022). Reflow Transfer for conformal 3-dimensional microprinting. NIST patent pending.

Dual-Band Metalenses for Imaging and Absolute Temperature Detection

CNF Project Number: 3105-23

Principal Investigator(s): Jason G. Valentine

User(s): Rahul Shah

Affiliation(s): Mechanical Engineering, Vanderbilt University

Primary Source(s) of Research Funding: Federal Grant

Contact: jason.g.valentine@vanderbilt.edu, rahul.shah.1@vanderbilt.edu

Primary CNF Tools Used: Gamma, ASML DUV Stepper, Heidelberg 2000, Oxford 81/82, Anatech Strip Resist, SEM

Abstract:

The project focuses on developing a novel dual-band metalens system, engineered for precise detection and identification of unknown aerial objects, with potential military applications. The design incorporates two metalenses that operate in distinct mid-infrared bands designed using a hyperbolic phase profile for diffraction-limited focusing enabling maximum angle resolution [1]. The metalenses are integrated with wavelength-selective filters for enhanced performance and compactness.

Summary of Research:

Trip 1: 2/4/24 – 2/10/24

- Orientation and training on the Gamma, ASML DUV Stepper, Heidelberg 2000, E beam deposition tool and in general chemistry.
- Generated mask for two lenses and patterned multiple wafers.
- The process aimed to deposit a hard mask and perform lift-off at The Vanderbilt Institute of Nanoscale Science and Engineering (VINSE). However, due to the large diameter of the lens (20 mm), lift-off proved challenging, resulting in incomplete liftoff and rendering the samples unusable for further processing and testing as seen in Figure 1.

Trip 2: 3/11/24 – 3/21/24

- Training on Oxford 81/82, Oxford Cobra, Anatech Resist Strip, and Scanning Electron Microscope (SEM).
- Employed a new strategy of depositing mask material (SiO₂) on wafer before patterning to avoid having to lift-off of the hard mask.

- Generated mask for two samples and patterned multiple wafers.
- Post-processed the wafers to etch the anti-reflective coating (ARC), etch hard mask using a CHF₃/Ar recipe, and then ash-etch the rest of the resist and ARC, preparing the sample for Si etch.
- Attempted to Si etch using multiple recipes on the Oxford Cobra; however, a straight edge etch was not achieved as seen in Figure 2.
- Using a CHF₃/O₂ etch recipe for the hard mask, samples were Si etched at VINSE, achieving a vertical edge etch as seen in Fig. 3.
- Characterization revealed significant reduction in the size of the fabricated pillars compared to the designed ones due to diffraction effects during exposure and edge etching during mask and Si etch. The smallest design features were not patterned, leaving empty spaces on the wafer, as seen in Figure 2 and Figure 3.

Trip 3: 5/16/24 – 5/22/24

- To account for the discrepancy between fabricated pillar and designed pillar sizes, a bias was added to the design to compensate for the shrinkage during patterning and etching.
- Generated new masks incorporating the bias and patterned multiple wafers.
- Post-processed the samples, preparing them for Si etch at VINSE.
- After Si etch at VINSE, the lenses were characterized, and pillars covered entire lens surface as seen in Figure 4.

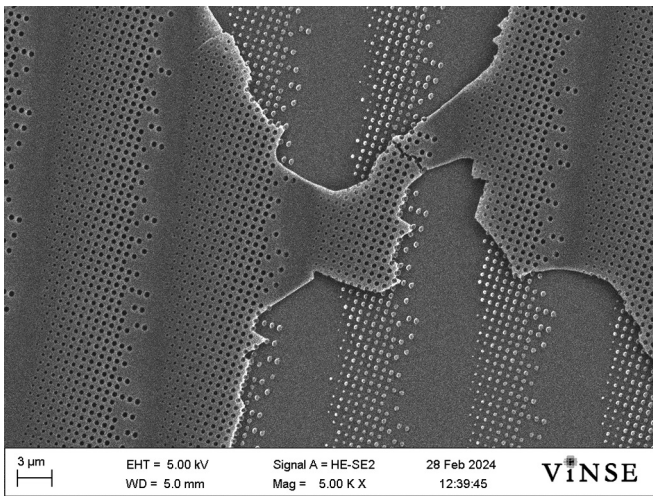


Figure 1: SEM images of the lens showing incomplete lift-off of the mask from the lens.

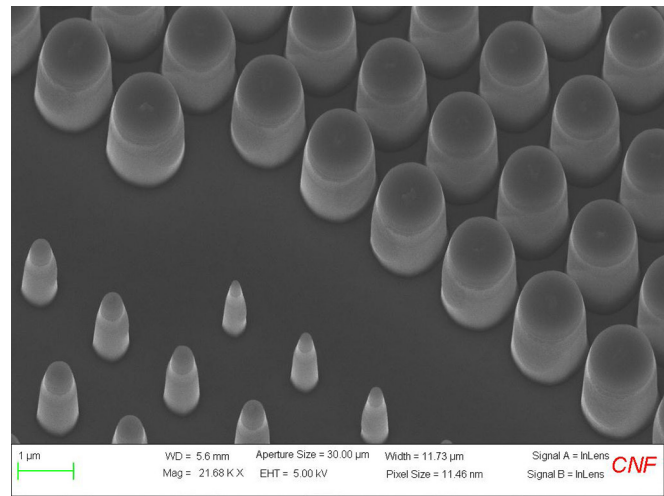


Figure 2: SEM image of the lens after Si etch at CNF showing pillars without perfectly vertical side walls. Rows of missing pillars visible.

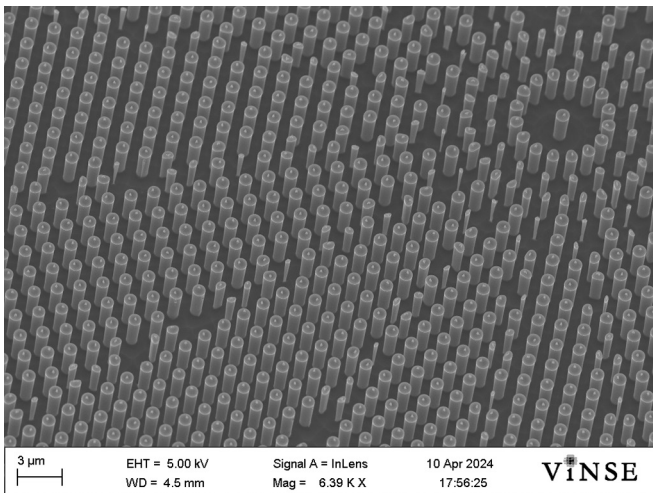


Figure 3: SEM image of the lens after Si etch at VINSE using a different mask etch recipe, showing improved side wall profile. Rows of missing pillars visible.

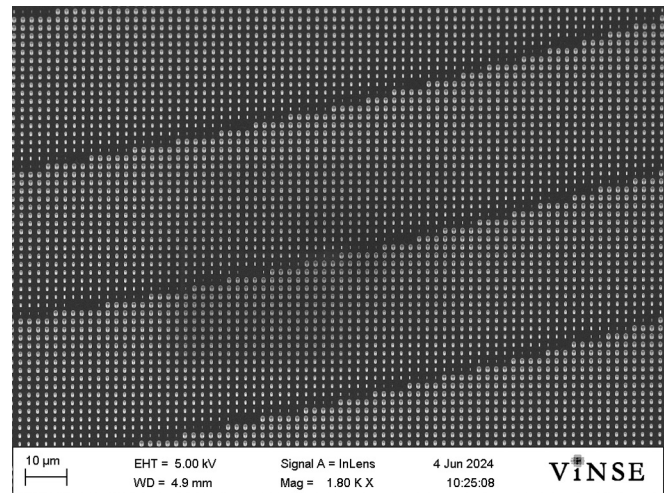


Figure 4: SEM image of the lens patterned after biasing, and after Si etch at VINSE with complete lens surface covered with pillars.

Conclusion and Future Steps:

The two lenses are designed to operate at a narrow band, and to ensure optimal performance, both lenses need to be equipped with a narrow band filter. We aim to design and fabricate a distributed Bragg reflector (DBR)-cavity-DBR based band pass filter on one side of the wafer and pattern and etch the lens on the other side of the wafer to achieve a seamless, compact design for our metalens. After fabrication and characterization, the lenses will undergo extensive testing to ensure they meet the necessary performance standards for the desired application.

References:

[1] Mohammadreza Khorasaninejad, et al., Metalenses at visible wavelengths: Diffraction limited focusing and subwavelength resolution imaging. *Science* 352,1190-1194(2016). DOI:10.1126/science.aaf6644.

Diffractive Optical Element Manufacturing Feasibility

CNF Project Number: 3141-24

Principal Investigator(s): Chris Poulsen

User(s): Chris Poulsen, Alex Beam

Affiliation(s): Applied Image Inc.

Primary Source(s) of Research Funding: Applied Image Inc.

Contact: cpoulsen@appliedimage.com, abeam@appliedimage.com

Primary CNF Tools Used: GCA 5x g-line Stepper, Oxford 100 Plasma Etcher, YES Eco-Clean Asher, KLA P7 Profilometer

Abstract:

The purpose of this project is to investigate the feasibility of manufacturing a specific diffractive optical element (DOE) pattern using equipment available at both the Cornell NanoScale Facility (CNF) and at Applied Image, Inc. The pattern in question is a computer-generated hologram that acts as a high angle (170+ degrees) dot grid type beam splitter with $0.9 \mu\text{m}$ elements for use in an optical instrument.

Summary of Research:

Applied Image has set out to investigate whether it will be feasible to manufacture high quality DOEs using our current lithography equipment and resources like the Oxford 100 plasma etcher at CNF. Our test pattern that we are attempting to reproduce is a $49 \times 49 \times 0.900 \mu\text{m}$ binary pixel array with a pi phase shift, repeated over an entire 100 mm fused silica wafer.

Our first attempt to pattern our resist was using CNF. We used S1805 resist and a master made on our own lithography equipment with reticle markings for our GCA 5x G-Line stepper. Our stepper is nearly identical to the one at CNF, so we attempted to pattern our wafer using the stepper at CNF. The stepper at CNF is configured differently than ours and was unable to focus correctly on a clear substrate. The autofocus system on our stepper appears to be a completely different design, which allows it to focus properly.

One of our next tasks was to take the processes and training we received from CNF regarding resist spinning back to Applied Image. We completely redesigned the processes for our spin lab to mirror the best practices we learned during our training at CNF. Major changes were using pipettes for depositing resist, methods for depositing HMDS, increasing our accelerations and using a copper plate for cooling. Another important process related note, we have also launched a project to overhaul our safety procedures and documentation using CNF's safety manual as a gold standard.

After producing several wafers that were successfully patterned with AZ3312 resist, we took these back to CNF for processing in the Oxford 100 Plasma Etcher. We used two etch processes CHF_3/O_2 oxide etch (etch rate:150nm/min Selectivity 2.5:1), and $\text{C}_4\text{F}_6/\text{high He}$ oxide etch (etch rate:225nm/min selectivity 4:1) [1]. An etch depth of 690 nm was targeted to create a pi phase shift in 632.7 nm He/Ne laser light.

An attempt was made to measure the etch depth of the pattern with the KLA P7 Profilometer. This did not turn out to be successful as the features were not quite big enough to get a good reading from the stylus. Most readings with the profilometer returned 125-275 nm etch depths. It was difficult to line up larger features ($2 \mu\text{m} \times 6 \mu\text{m}$) as the viewing lens did not resolve these features very well. For better process control test patches with a larger cross-sectional area of at least $50 \times 50 \mu\text{m}$ would need to be added to make better measurements on either a profilometer or an ellipsometer.

Despite the inability to measure or control the etch depth, reliance on the suggested etch rates seemed to be good enough to produce favorable results. Both etch methods produced an acceptable diffraction efficiency of around 90%. Although diffraction efficiency in terms of zero order energy to total beam energy were high, some undesirable artifacts were present in the form of lines between the desired dots in the resulting diffraction pattern. More investigation will be ongoing to attempt to resolve this issue.

Further work is being done to optimize the process including switching to ChemLab 5305 High-Resolution resist, that has so far shown superior resolution to Shipley S1805, AZ1505 and AZ3312 resists.

References:

- [1] CNF Users. "Oxford 100 ICP Dielectric Etcher." Cornell NanoScale Science & Technology Facility. Etch Baseline Data. Accessed July 2, 2024.

Nanomolding of Topological Materials for Interconnects

CNF Summer Student: Richard A. Remias

Student Affiliation: Physics, University of Rhode Island

Summer Program(s): 2024 Cornell NanoScale Facility Research Experience for Undergraduates (CNF REU) Program

Principal Investigator(s): Judy Cha, Materials Science and Engineering, Cornell University

Mentor(s): Quynh Sam, Khoan Duong; Materials Science and Engineering, Cornell University

Primary Source(s) of Research Funding: National Science Foundation under Grant No. NNCI-2025233

Contact: risikoalbi@live.com, jc476@cornell.edu, qps2@cornell.edu, nd399@cornell.edu

Summer Program Website: <https://cnf.cornell.edu/education/reu/2024>

Primary CNF Tools Used: Oxford FlexAl ALD, Zeiss Supra SEM, Bruker EDX, Veeco Icon AFM, Woollam RC2 Ellipsometer

Abstract:

The increasing resistivity of copper (Cu) interconnects with decreasing dimensions poses many challenges for the continued downscaling of integrated circuits and computer chips. At the nanoscale, electron scattering at grain boundaries and surfaces of the interconnects causes an increase in resistivity leading to higher energy consumption and signal delay in computer chips. Conversely, topological materials may show decreasing resistivity with decreasing size at nanoscale dimensions due to their topologically protected band structures that are predicted to suppress electron scattering. Thus, transport studies of topological materials at the nanoscale are critical to find alternative metals to Cu interconnects. Nevertheless, current nanowire synthesis methods such as molecular beam epitaxy (MBE) and chemical vapor transport (CVT) struggle to create uniformly sized nanowires.

We use nanomolding to fabricate nanowires of topological materials, where a bulk material is pressed into a porous anodic aluminum oxide (AAO) mold to create high aspect ratio nanowires. To promote more facile nanomolding and to prevent oxidation of the molded nanowires, we coat the AAO mold pore walls with a thin film of aluminum nitride (AlN) and tantalum nitride (TaN). The CNF's Oxford FlexAl atomic layer deposition (ALD) tool is used to deposit precise and uniform films due to its self-limiting reactions. Through energy dispersive X-ray spectroscopy (EDX), we determine the infiltration depth of AlN in our pores. Additionally, InBi is a topological material which may exhibit interesting quantum properties at few-layer thicknesses.

We use nanomolding to compress InBi into thin flakes by encapsulating the InBi with hexagonal boron nitride (hBN). The CNF's AFM Veeco Icon tool is used to determine the resulting thickness of the InBi flake.

Summary of Research:

ALD was first used to deposit 20 nm of AlN onto the AAO mold which had a pore diameter of 120 nm. This deposition was done at 400°C for 334 cycles at 0.6 Å/cycle, using trimethylaluminum (TMA) and H₂/N₂ plasma as precursors. These precursors were pulsed for 0.02 seconds and 5 seconds, respectively. To estimate deposition thickness, a blank silicon substrate was placed next to the mold in the ALD chamber and ellipsometry was used to determine the thickness of AlN deposited onto the substrate. The resulting thickness was estimated to be about 18.02 ± 0.027 nm. A scanning electron microscope (SEM) was then used to take a cross-sectional image of the AAO mold which was combined with EDX to map the elements deposited within the mold channel walls. However, due to low film thickness and low atomic weight of nitrogen, the infiltration depth of AlN in our pores was inconclusive as no nitrogen was detected on the pore walls (Figure 1).

Next, we used ALD to deposit 10 nm of TaN onto a mold of identical pore diameter. This deposition was done at 250°C for 250 cycles at 0.4 Å/cycle, using tris(diethylamido)(tert-butyrimido)tantalum(V), or TBTDET, and ammonia (NH₃) as precursors. The pulse time for these precursors was 6 seconds and 15 seconds, respectively. The same method was used to estimate the deposited film thickness, which was determined to be 6.87 ± 0.081 nm. SEM was used to take a cross-sectional image and EDX was used for element mapping. Unfortunately, no tantalum was detected in the pores so the infiltration depth of TaN is inconclusive (Figure 2). Through improvements in ALD parameters, we may be able to determine infiltration depth using EDX.

Additionally, we used nanomolding to press InBi into thin flakes. This was done by placing an hBN flake both on top of and underneath the InBi piece to create an hBN-InBi-hBN stack. The stack was made using tape

exfoliation and the desired flakes of uniform thickness were found under a microscope and transferred using a glass slide with an epoxy drop. We used a hot press to compress the InBi stack at 80°C for 15 minutes. The resulting stack is shown in Figure 3.

To determine the final thickness, we used atomic force microscopy to create a line profile over the stack. We measured the thickness of InBi to be 35.9 nm (Figure 4). Different nanomolding parameters were also used on different stacks, such as pressing for 30 minutes at 100°C, however, no flakes were pressed to be thinner than 35.9 nm.

Conclusions and Future Steps:

EDX results after deposition of AlN and TaN show that a more sensitive elemental mapping method may be needed for accurate determination of infiltration depth into AAO channel pores. A method such as X-ray photoelectron spectroscopy may be more sensitive to thinner films as well as lighter elements. Also, increasing precursor pulse time in ALD processes may allow more time for gases to travel into high aspect ratio features, increasing infiltration depth. Increasing gas flow rates may also prove useful as it will increase delivery of gases deeper into the pores.

Results also show that nanomolding can be used to create sub 40 nm thin InBi flakes. Future work would include removing the top hBN flake and testing the resistance of the InBi flake.

Acknowledgements:

This work was made possible by the Cornell NanoScale Facility and funded by the National Science Foundation via grant no. NNCI-2025233. Special thanks to Judy Cha, Quynh Sam, Khoan Duong, Sihun Lee, and Melanie-Claire Mallison for their great help and guidance.

References:

- [1] Chen, L., Wu, A.X., Tulu, N., et al. Exceptional electronic transport and quantum oscillations in thin bismuth crystals grown inside van der Waals materials. *Nat. Mater.* 23, 741–746 (2024). <https://doi.org/10.1038/s41563-024-01894-0>.
- [2] Kiani, M. T., Sam, Q. P., Jin, G., Pamuk, B., Han, H. J., Hart, J. L., Stauff, J., and Cha, J. J. (2023). Nanomolding of metastable Mo4P3. *Matter*, 6(6), 1894–1902. <https://doi.org/10.1016/j.matt.2023.03.023>.

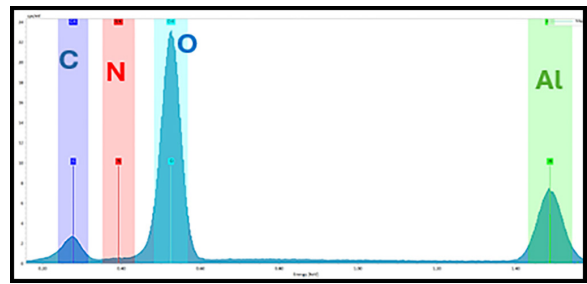


Figure 1: Cross-sectional EDX Spectrum of AAO Channels Post AlN ALD.

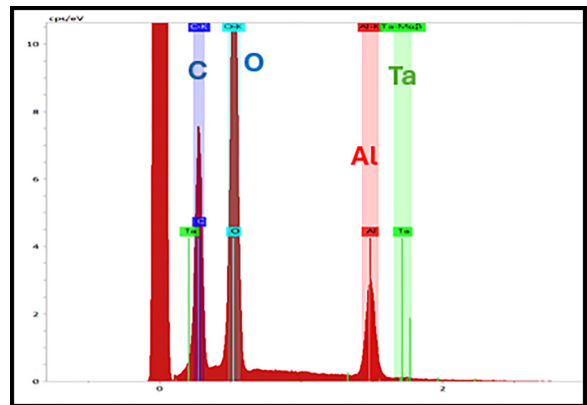


Figure 2: Cross-sectional EDX Spectrum of AAO Channels Post TaN ALD.

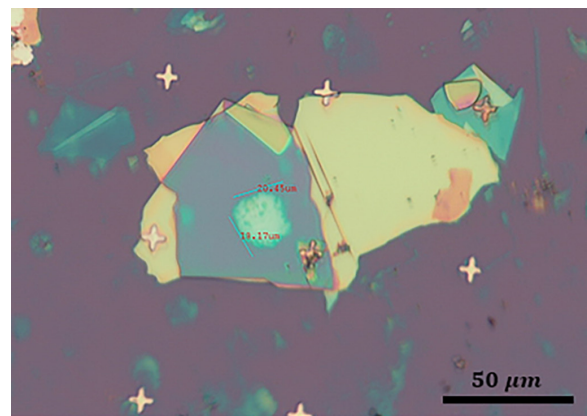


Figure 3: Optical Microscope Image of Compressed InBi Stack.

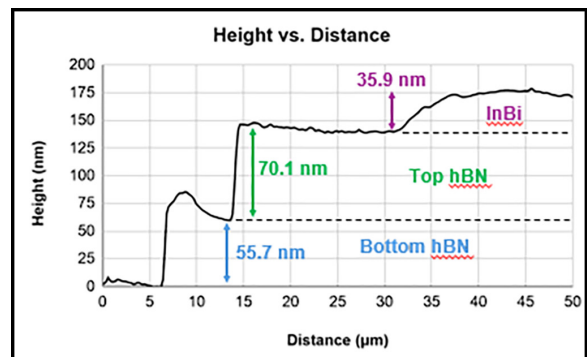


Figure 4: AFM Line Profile Graph of Compressed InBi Stack.

Micro-Additive Manufacturing Processes for Electrochemical CO₂ Reduction

CNF Summer Student: Hunter Saylor

Student Affiliation: Electrical and Computer Engineering, Morgan State University

Summer Program(s): 2024 Cornell NanoScale Science & Technology Facility

Research Experience for Undergraduates Program with Morgan State University (CNF REU MSU)

Principal Investigator(s): Sadaf Sobhani, Mechanical and Aerospace Engineering, Cornell University

Mentor(s): Giancarlo D'Orazio, Mechanical and Aerospace Engineering, Cornell University

Program and Primary Source(s) of Research Funding: Cornell College of Engineering (CNF REU MSU), National Science Foundation under Grant No. NNCI-2025233 (CNF REU)

Contact: husay1@morgan.edu, sobhani@cornell.edu, gd373@cornell.edu

Summer Program Website: <https://cnf.cornell.edu/education/reu/2024>

Primary CNF Tools Used: Nanoscribe GT2, AJA Sputter, Zeiss Ultra SEM

Abstract:

This work investigates the application of micro-additive manufacturing in the development of gas diffusion electrodes (GDEs) for electrochemical CO₂ reduction reactors. This technology relies on the principles of electrochemistry to convert CO₂ into useful chemical products. A key focus of this work is the reactor design and fabrication, as these elements impact the overall efficiency and functionality of the system. The gas diffusion electrode is identified as a common failure point in such reactors. To enhance the performance and durability of the GDE, we utilize the Nanoscribe Photonic Professional GT2 two-photon lithography 3D printer to print a microporous layer atop a carbon paper electrode. This effort aims to mitigate electrolyte flooding in our vapor-fed reactor. A copper catalyst will be deposited onto the microporous layer using the AJA sputter system. Subsequent analysis of the GDE surface will be conducted using a scanning electron microscope (SEM) to ensure structural integrity and optimal surface characteristics. To evaluate the performance of the CO₂ reduction reactor, measurements of open-circuit potential, electrochemical impedance spectroscopy, and cyclic voltammetry will be scrutinized. The results will highlight common failure modes, such as catalyst delamination and

electrolyte flooding. Additionally, a long-duration, steady-state test will be performed to measure changes in potential at a fixed current, providing insights into the long-term performance and lifespan of the GDE. Our findings will deliver quantitative insights into the optimization of gas diffusion electrode synthesis, advancing the efficiency of electrochemical CO₂ reduction processes. This research underscores the potential of micro-additive manufacturing in addressing critical challenges in renewable energy and carbon capture technologies.

Summary of Research:

In the effort to optimize the fabrication and design of the CO₂ reduction reactor's Gas Diffusion Electrode (GDE), we addressed common failure modes such as catalyst degradation and flooding of the electrolyte into the vapor-fed reactor. To minimize these failure modes, we had to [1] characterize the reactor before and after long-duration trials, [2] design and print a microporous layer on the GDE, and [3] test the effect of electrolyte mixing into the reactor's expected liquid products.

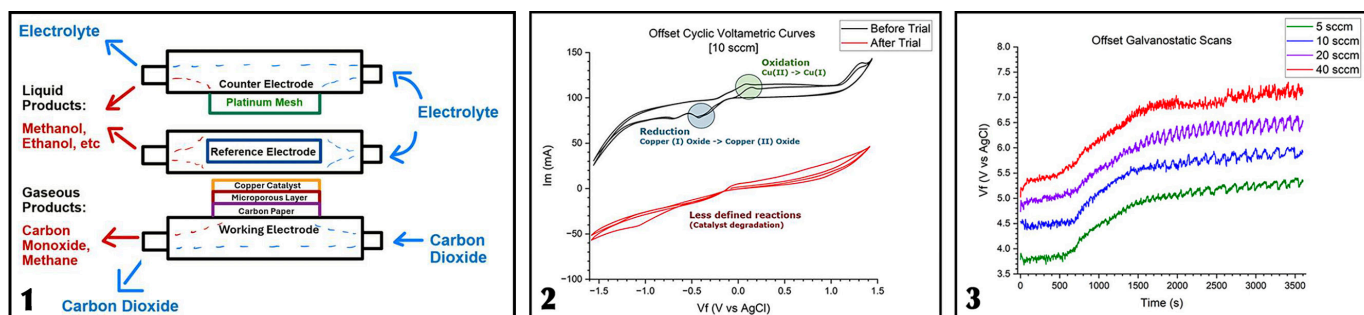


Figure 1, left: Diagram of CO₂ reduction reactor. Figure 2, middle: Offset cyclic voltammetric scans taken of reactor cell before and after long-duration trial. Figure 3, right: Offset galvanostatic scans of reactor cell at different CO₂ flow rates.

The rate of degradation of the gas diffusion electrode's copper catalyst and the rate of flooding of electrolyte into the vapor-fed reactor are both dependent on the flow rate of CO₂ into the reactor. In order to measure these effects, we employed the characterization of the reactor before and after an hour long run of the reactor at different flow rates. Our characterization involved taking cyclic voltametric scans of the reactor, in which a voltage is applied across the working and reference electrodes, and its current density is measured. These scans display the reduction and oxidation reactions occurring at the copper catalyst of the GDE. Over the course of the long-duration trial, a galvanostatic scan was taken, in which a steady current of 350 mA/cm² was applied and the voltage across the reactor was measured. The galvanostatic scan measures the rate of electrochemical reaction. Multiple trials were conducted at varying CO₂ flow rates of 5, 10, 20, and 40 standard cubic centimeters per minute (SCCM). The operating conditions in which we applied to our long-duration trials were influenced by previous literature, which concluded that 5 SCCM of CO₂ at an applied current density of 350 mA/cm² outputs the best reactor performance and efficiency [1].

3D-printing the microporous layer (MPL) offers control of the GDE's pore size and density. The MPL is printed on a layer of carbon paper using the Nanoscribe GT2, then a ~300 nm layer of copper is deposited on top of the MPL using AJA Sputter system. This design of the gas diffusion electrode allows the copper layer to be used as a catalyst for the CO₂ conversion, and the microporous layer to be used to prevent flooding of electrolyte into the vapor-fed reactor.

Another facet in the effort to optimize the design of the GDE involved measuring the effect that of electrolyte mixing into the liquid products of the CO₂ reduction reactor. To address this, we performed a test involving measuring the rise velocity of the various samples through a capillary tube. The samples included deionized water to act as a control, the electrolyte (KHCO₃), the alcohol and acid products, as well as the alcohol and acid products mixed with KHCO₃.

Conclusions and Future Steps:

The cyclic voltametric scans taken before and after the long-duration trials suggest that the copper catalyst degrades more rapidly if there is a higher CO₂ flow rate input.

This can be determined because the reduction and oxidation reactions that are present in the characterization of the reactor before the long-duration trial are no longer present afterwards. The galvanostatic scans taken over the course of the trial also show that the CO₂ reduction reactor reaches steady-state operation after approximately half an hour.

Our 3D-printed microporous layer has pores approximately 1-5 microns in diameter, and also improves upon the previous method of 3D-printing the entire GDE. In comparison, printing the MPL takes ~6-9 hours, whereas printing the entire GDE takes ~35-55 hours.

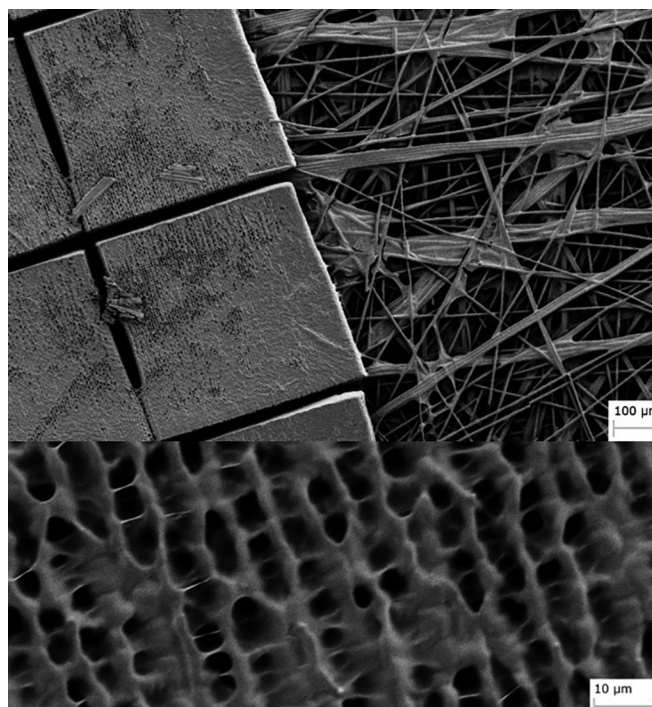


Figure 4: Scanning electron microscope (SEM) images of the microporous layer printed on carbon paper.

Results from measuring the rise velocity of electrolyte and liquid products through capillary tubes suggest that KHCO₃ has relatively low hydrophobicity, as it has the lowest rise velocity from our tests, and it lowers the rise velocity of the alcohol and acid products when they are mixed together. The results of these experiments will influence the hydrophobic coating used on the microporous layer.

Future work involves coating the printed microporous layer with a hydrophobic coating. The coated microporous layer will then be tested and its effectiveness against electrolyte flooding and catalyst degradation will be measured.

Acknowledgements:

Many thanks to 2024 Cornell NanoScale Facility Research Experience for Undergraduates Program with Morgan State University and the National Science Foundation Grant No. NNCI-2025233. Special thanks to my principal investigator Dr. Sadaf Sobhani for the wonderful opportunity, to my mentor Giancarlo D'Orazio for his patience and guidance, to my staff host Giovanni Sartorello for his support, and to Melanie-Claire Mallison for being an excellent host.

References:

- [1] D. Corral, et al., "Advanced manufacturing for electrosynthesis of fuels and chemicals from CO₂," *Energy Environ. Sci.*, vol. 14, no. 5, pp. 3064-3074, May 2021, doi: 10.1039/D0EE03679J.

Study Unconventional Spin-Orbit Torque Generation on Micron-Sized Devices Fabricated with Photolithography

CNF Project Number: 598-96

Principal Investigator(s): Daniel C. Ralph

User(s): Xiaoxi Huang

Affiliation(s): Department of Physics, Cornell University

Primary Source(s) of Research Funding: Semiconductor Research Corporation-Superior Energy-efficient Materials and Devices

Contact: dcr14@cornell.edu, xh384@cornell.edu

Primary CNF Tools Used: DWL 66fs, AJA Sputter Deposition

Abstract:

Micron-sized devices made with DWL 66fs direct writer and AJA sputter system were used to study spin currents generated with magnetic ordering. We experimentally observed that antiferromagnetic ordering plays a significant role in enhancing spin current generation efficiency in PdCrO_2 thin films and canted magnetic moment produces out-of-plane damping-like torque in SrRuO_3 thin films.

Summary of Research:

Magnetic materials with perpendicular magnetic anisotropy (PMA) are the most promising materials for high-density magnetic memory; and the efficient magnetization switching of PMA-magnets are enthusiastically pursued by Spintronics researchers, as it has the potential to realize energy-efficient high-density information storage. Fortunately, out-of-plane spin component borne by a spin current is theoretically predicted and experimentally demonstrated to be able to drive the efficient anti-damping switching of magnetization of a PMA-magnet [1]. Our primary research goal is to find materials that efficiently produce spin currents with out-of-plane spin component and ultimately demonstrate the efficient switching of magnetization of PMA-magnet pillars with diameters as small as 100 nm. Our search for such materials has been centered around materials that have magnetic orderings, including both ferromagnetic and anti-ferromagnetic orderings.

Two successful trials have been made on PdCrO_2 , which is an anti-ferromagnet below 37 K, and SrRuO_3 , which is a ferromagnet below 150 K. To detect spin current generation and the specific spin orientations allowed in these materials, micron-sized devices such as spin-torque ferromagnetic resonance (ST-FMR) devices and Hall bar devices are patterned on these materials.

The devices for ST-FMR and Hall measurements—established techniques for spin-orbit torque characterization [2] is shown in Figure 1 and Figure 2. Bar structures with dimensions of

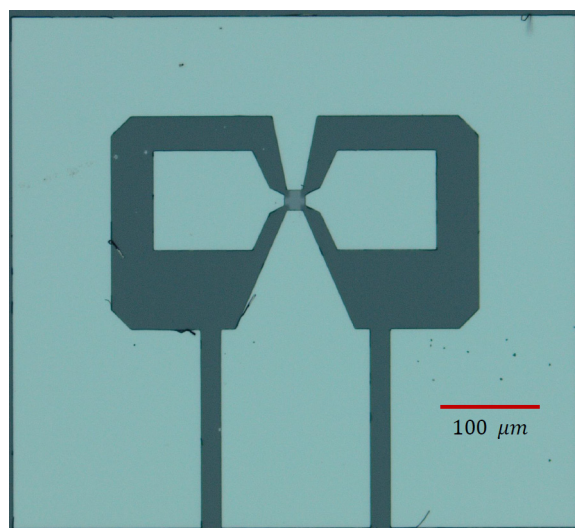


Figure 1: Spin torque ferromagnetic resonance device.

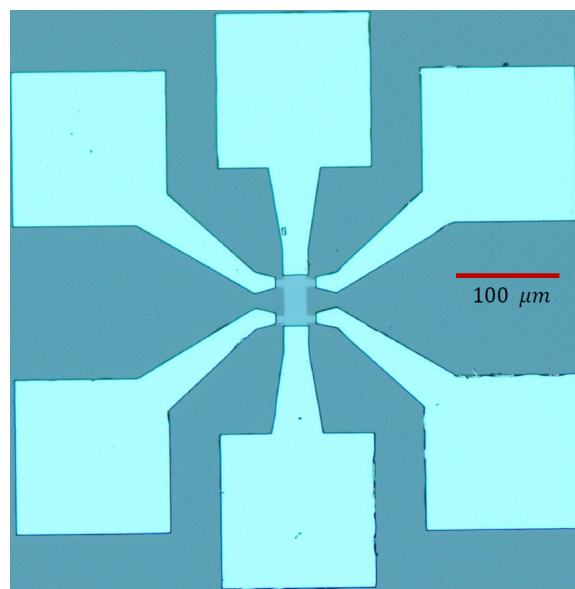


Figure 2: Hall device for second Harmonic Hall measurements.

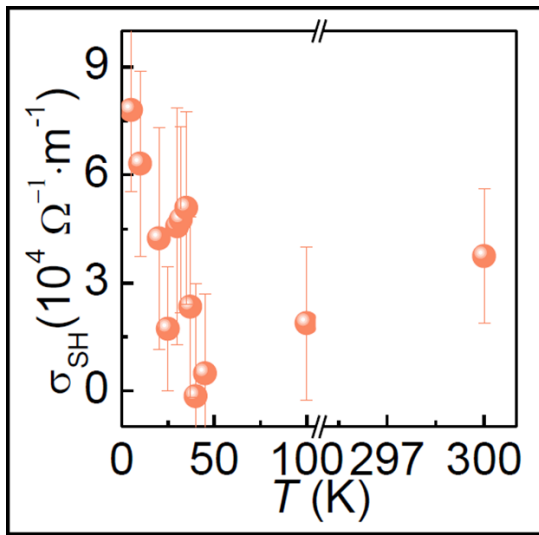


Figure 3: Spin Hall conductivity as a function of temperature for a 2 nm PdCrO₂ thin film.

10 × 40 μm and 20 × 70 μm are patterned with Heidelberg DWL 66fs laser direct writer. Then contacts made of Ti/Pt were deposited on the patterns in an AJA sputtering system. Spin current generation in PdCrO₂ were successfully detected with such devices; and the spin current generation efficiency as a function of temperature in PdCrO₂ is shown in Figure 3. A strong dependence of spin current generation on temperature is observed. Intriguingly, a strong upturn of spin current generation efficiency is seen at approximately the Neel temperature of PdCrO₂, implying the critical role that antiferromagnetic ordering plays in generating spin currents.

A manuscript on this work has been composed and is to be submitted soon. Another example on spin current generated with magnetic ordering is unconventional spin-orbit torque generation in SrRuO₃. SrRuO₃ thin films when grown on (001)-oriented SrTiO₃ substrates are shown to exhibit canted magnetization and ferromagnets with magnetic moment canted out of the plane are predicted to be able to produce tilted spin currents with tilted spin polarization [3]. The spin-orbit torque generation in SrRuO₃ is conducted on ST-FMR devices (Figure 1). When the rf current and oscillating magnetoresistance are mixed together, a dc mixing voltage is produced.

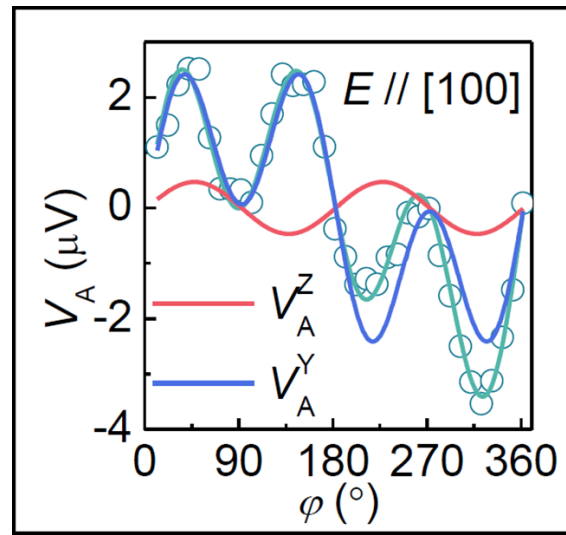


Figure 4: The anti-symmetric component of the mixing voltage for a 5 nm SrRuO₃ sample. The device is oriented parallel to [100] direction in the plane and the measurements were carried out at 110 K.

The anti-symmetric component of the mixing voltage is contributed by the out-of-plane torques. The fitting of the anti-symmetric voltage detected in SrRuO₃ thin films requires a $\sin 2\phi$ component (Figure 4), which is the signature of the out-of-plane damping like torque produced by the out-of-plane component of the spin polarization. This is the most exciting and important finding of our work so far and we are actively preparing a manuscript on this matter.

Conclusions and Future Steps:

Magnetic ordering plays a crucial role in either enhancing spin current generation or producing out-of-plane damping-like torques. We anticipate finishing characterizing the unconventional spin-orbit torque generation in these materials and start demonstrating magnetization switching PMA-magnetic nano-pillars.

References:

- [1] David MacNeill, et al., Nat. Phys. 13, 300 (2017).
- [2] Luqiao Liu, et al., Science 336, 555 (2012).
- [3] Tomohiro Taniguchi, et al., Phys. Rev. Lett. 3, 044001 (2015).

Van der Waals Magnetic Tunnel Junctions with Metallic Transition Metal Dichalcogenide Electrodes

CNF Project Number: 598-96

Principal Investigator(s): Daniel Ralph

User(s): Bozo Vareskic

Affiliation(s): Laboratory for Atomic and Solid State Physics, Cornell University

Primary Source(s) of Funding: Air Force Office of Scientific Research

Contact: dcr14@cornell.edu, bv227@cornell.edu

Primary CNF Tools Used: Heidelberg DWL-2000, GCA-AS200 i-line stepper, SC4500 Even/Odd-Hour Evaporator

Abstract:

Magnetic tunnel junctions (MTJs) are a useful platform for studying electrically insulating van der Waals magnets. The evolution of the tunneling current as a function of junction bias and applied external magnetic field has been shown to reveal information about the nature of interlayer exchange, spin-filtering, and two dimensional magnons [1-3]. These previous studies have employed few layer graphene for contact electrodes. Theoretical work [4], however, suggests that by replacing few layer graphene with a metallic transition metal dichalcogenide (TMD), the junction impedance can be lowered and the magnetoresistance increased, making the junctions more favorable for spintronic applications. Here, we fabricate MTJs where the barrier layer is antiferromagnetic CrCl_3 and the junction electrodes are TaSe_2 and measure the tunneling characteristics as a function of applied magnetic field.

Summary of Research:

CrCl_3 is a layered van der Waals magnet where each individual layer hosts ferromagnetic exchange interactions between neighboring spins while adjacent layers couple antiferromagnetically. The moments are pointed in the plane of the layers with no anisotropy within the plane. The weak interlayer coupling allows for the net magnetic moment to be manipulated by an external magnetic field. Previous studies with few layer graphene/ CrCl_3 /few layer graphene junctions have shown that the tunneling current is sensitive to the orientation of the layer magnetic moments relative to one another [1-3]. However, spintronics applications where the tunneling current can be used as a readout of the magnetic state will require lower impedance junctions.

First principles density functional theory calculations indicate that due to more favorable band alignment and higher density states that junctions with electrodes of metallic transitional metal dichalcogenides host larger junction conductivity and magnetoresistance compared to junctions with graphitic electrodes [4].

We fabricate $\text{TaSe}_2/\text{CrCl}_3/\text{TaSe}_2$ junctions by exfoliating all materials in an inert glove box environment to avoid exposure to ambient oxygen and water. The junction is encapsulated in hexagonal boron nitride from above and below and then transferred to prepatterned metallic electrodes that were prepared with the Heidelberg Mask Writer DWL-2000, GCA-AS200 i-line stepper, and SC4500 Even/Odd-Hour Evaporator. Figures 1 and 2 show a device schematic and micrograph, respectively.

Transport measurements are performed at $T = 2 \text{ K}$ by applying a DC bias voltage and measuring the resulting DC tunneling current. All external magnetic fields are applied in the plane of the device. Figure 3 shows the current voltage characteristic of the junction at $B = 0 \text{ T}$ and $B = 2 \text{ T}$. As the externally applied field is increased, the moments of the individual layers will reorient themselves and approach a parallel configuration to minimize energetic contributions from interlayer exchange and Zeeman effects. At $B = 2 \text{ T}$, due to spin filtering, this configuration will have a lower tunneling barrier and thus, a lower threshold voltage for the onset of Fowler-Nordheim tunneling than the antiparallel configuration at $B = 0 \text{ T}$.

We then apply a constant DC bias of $V = 1.25 \text{ V}$ and measure how the tunneling current evolves as a function of applied magnetic field. The tunneling current increases with an applied field as the moments evolve from antiparallel towards a parallel configuration. This

is consistent with the lowering of the tunneling barrier with increasing magnetic field via the spin filtering effect. The magnetoresistance is defined as

$$MR = 100 \times \frac{I(B) - I(B=0 \text{ T})}{I(B=0 \text{ T})},$$

and we measure a magnetoresistance of $\sim 150\%$. Future work will involve exploring different metals as electrode layers and fabricating devices suitable for four-point measurements to avoid contributions from contact resistance.

References:

- [1] Klein, D. R., et al. Probing magnetism in 2D van der Waals crystalline insulators via electron tunneling. *Science* 360, 1218 (2018).
- [2] Wang, Z., et al. Determining the phase diagram of atomically thin layered antiferromagnet CrCl_3 . *Nature Nano.* 14, 1116 (2019).
- [3] Cai, X., et al. Atomically thin CrCl_3 : An in-plane layered antiferromagnetic insulator. *Nano Letters* 19, 3993 (2019).
- [4] Heath, J. J., et al. Spin injection enhancements in van der Waals magnetic tunnel junctions through barrier engineering. *Phys. Rev. Applied* 16, L041001 (2021).

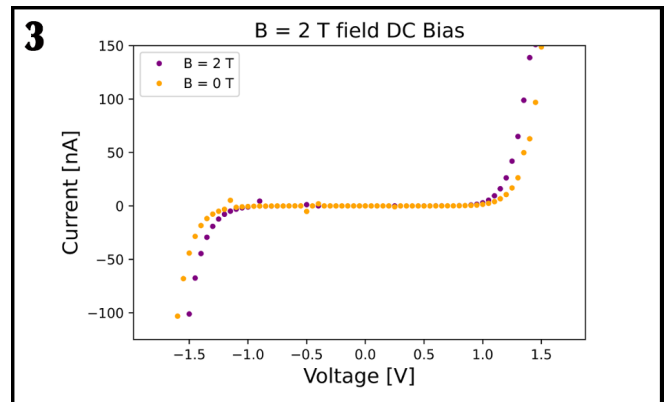
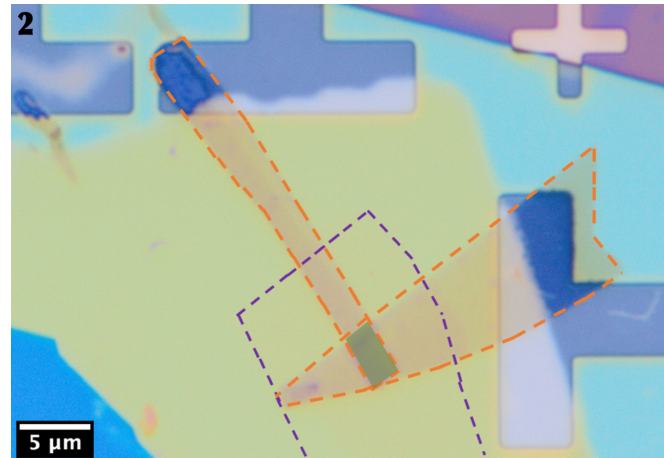
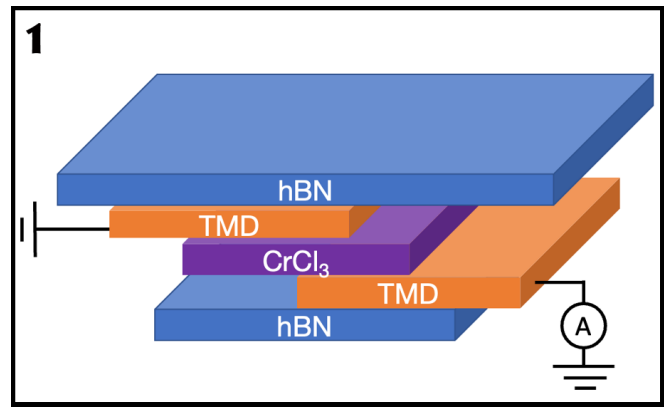
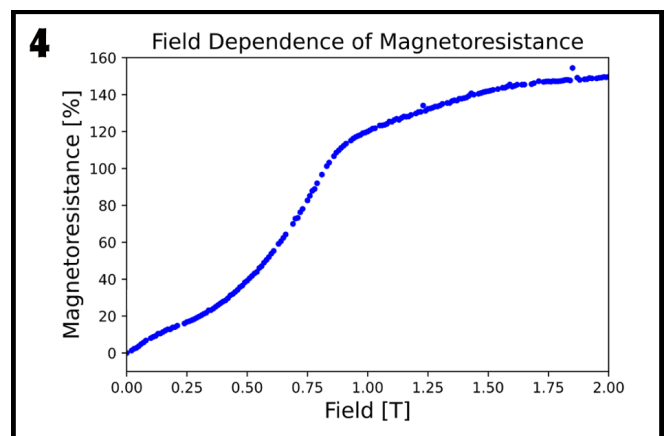


Figure 1: Device schematic of $\text{TaSe}_2/\text{CrCl}_3/\text{TaSe}_2$ magnetic tunnel junction. Hexagonal boron nitride is used to encapsulate the CrCl_3 to prevent degradation from ambient oxygen and water.

Figure 2: Micrograph of $\text{TaSe}_2/\text{CrCl}_3/\text{TaSe}_2$ magnetic tunnel junction. The TaSe_2 and CrCl_3 layers are outlined with the dashed orange and purple lines respectively. Scale bar: $5 \mu\text{m}$.

Figure 3: Tunneling current as a function of applied DC bias. The tunneling current at $B = 0 \text{ T}$ is orange and at $B = 2 \text{ T}$ is purple. Measurements are performed at $T = 2 \text{ K}$, and the magnetic field is applied in the plane.

Figure 4: Magnetoresistance as a function of in-plane magnetic field. A constant DC bias of $V = 1.25 \text{ V}$ is applied. The tunneling current increases as the moments of the individual layers approach a parallel configuration.



Nanofabricated Superconducting Devices for Vortex Dynamics and Qubits

CNF Project Number: 1314-05

Principal Investigator(s): Britton L.T. Plourde

User(s): Brad Cole, Kenneth Dodge, Clayton Larson, Eric Yelton

Affiliation(s): Department of Physics, Syracuse University

Primary Source(s) of Research Funding: Army Research Office

Contact: bplourde@syr.edu, bgcole@syr.edu, krdodgej@syr.edu, cllarson@syr.edu, epyelton@syr.edu

Primary CNF Tools Used: ASML Photostepper, JEOL 6300, Plasma-Therm 770

Abstract:

We fabricate superconducting microwave devices for studying the dynamics of vortices at low temperatures and for forming novel qubits. Vortices are quantized bundles of magnetic flux that thread many different superconductors over a particular range of applied magnetic field. By using disordered superconducting thin films to form high kinetic inductance wires combined with novel arrays of Josephson junctions, we are able to build structures that can lead to qubits that are topologically protected against decoherence. With charge-sensitive superconducting qubits, we are able to probe sources of correlated errors in quantum processors.

We can mitigate this quasiparticle poisoning through the use of electroplated Cu metallic reservoirs for downconversion of high energy phonons [5].

We fabricate our microwave resonators from various superconducting films, including aluminum and niobium, deposited onto silicon wafers in vacuum systems at Syracuse University. We define the patterns on the ASML stepper and transfer them into the films with a combination of reactive ion etching and liftoff processing. For defining Josephson junctions, we use the JEOL 6300 along with a dedicated deposition system at Syracuse University. We measure these circuits at temperatures of 100 mK and below in our lab at Syracuse University.

Summary of Research:

Superconducting microwave circuits play an important role in quantum information processing. Circuits composed of Josephson junctions and capacitors with superconducting electrodes can serve as qubits, the fundamental element of a quantum computing architecture. Various loss mechanisms limit the ultimate performance of these devices, including trapped magnetic flux vortices. Vortices can be trapped in the superconducting electrodes when background magnetic fields are present and contribute dissipation when driven with microwave currents [1]. Thus, techniques for controlling the trapping of vortices are critical to the development of large-scale quantum information processors with superconducting circuits.

By arranging nanoscale Al-AlO_x-Al Josephson tunnel junctions in novel arrays, it is possible to implement new qubit designs that are protected against decoherence [2-4]. We are also able to use such Al-AlO_x-Al tunnel junctions in superconducting qubits to probe poisoning effects from nonequilibrium quasiparticles, which are a source of correlated errors in quantum processors.

References:

- [1] Song, C., Heitmann, T.W., DeFeo, M.P., Yu, K., McDermott, R., Neeley, M., Martinis, John M., Plourde, B.L.T.; "Microwave response of vortices in superconducting thin films of Re and Al"; *Physical Review B* 79, 174512 (2009).
- [2] Doucot, B., Ioffe, L.; "Physical implementation of protected qubits"; *Reports on Progress in Physics* 75, 072001 (2012).
- [3] Cole, B., Dodge, K., Liu, Y., Shearrow, A., Snyder, M., Klots, A., Ioffe, L., McDermott, R., Plourde, B.; "Electronic capacitance in tunnel junctions for protected charge-parity qubits"; *Bull. Am. Phys. Soc.* 2024, <https://meetings.aps.org/Meeting/MAR24/Session/N48.3>
- [4] Dodge, K., Liu, Y., Klots, A., Cole, B., Shearrow, A., Senatore, M., Zhu, S., Ioffe, L., McDermott, R., Plourde, B.; "Hardware implementation of quantum stabilizers in superconducting circuits"; *Physical Review Letters* 131, 150602 (2023).
- [5] Iai, V., Ku, J., Ballard, A., Larson, C.P., Yelton, E., Liu, C.H., Patel, S., McDermott, R., Plourde, B.L.T.; "Phonon downconversion to suppress correlated errors in superconducting qubits"; *Nature Communications* 13, 6425 (2022).

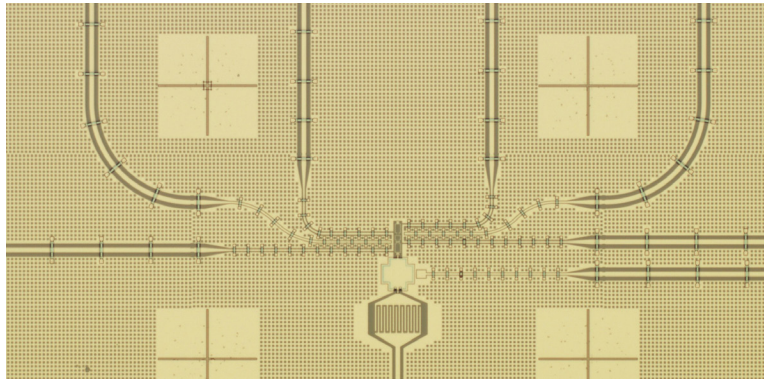


Figure 1: Optical micrograph of topologically protected superconducting quantum circuit.

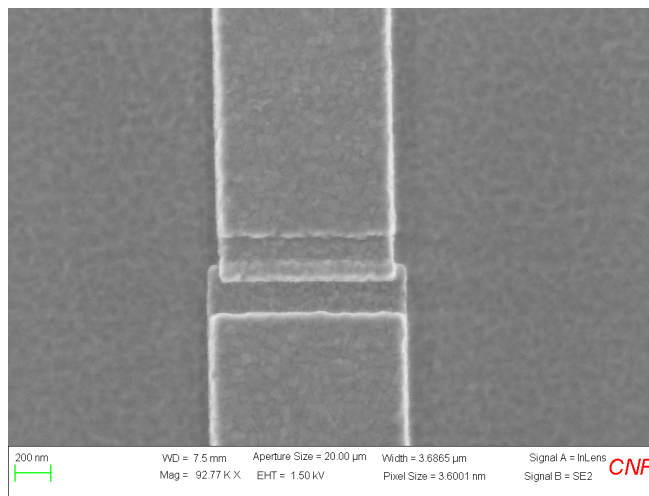


Figure 2: SEM image of Al-AlOx-Al Josephson tunnel junction for superconducting qubit.

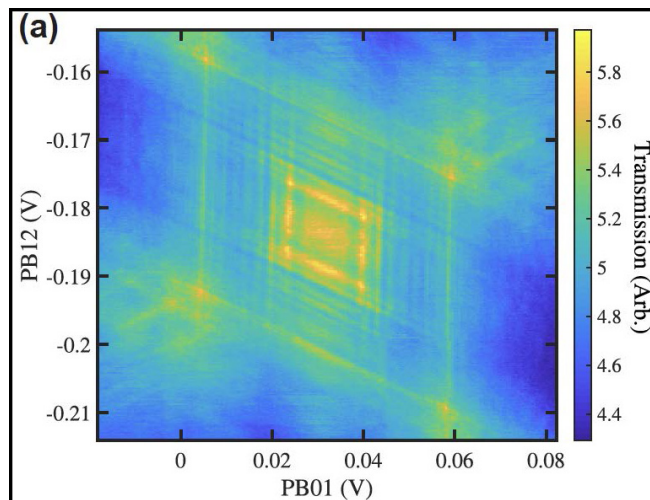


Figure 3: Measurement of microwave readout cavity modulation with magnetic flux using on-chip controllines coupled to topologically protected superconducting circuit.

Fabrication of Nanoscale Josephson Junctions for Quantum Coherent Superconducting Circuits

CNF Project Number: 1735-08

Principal Investigator(s): Britton L.T. Plourde

User(s): Brad Cole, Tianna McBroom, J.T. Paustian

Affiliation(s): Department of Physics, Syracuse University

Primary Source(s) of Research Funding: Air Force Research Lab, Air Force Office of Scientific Research

Contact: bplourde@syr.edu, bgcole@syr.edu, tamcbroo@syr.edu, jtpausti@syr.edu

Primary CNF Tools Used: ASML Photostepper, JEOL 6300, Plasma-Therm 770

Abstract:

We fabricate nanoscale superconductor tunnel junctions and other structures for experiments involving quantum coherent circuits. Such circuits have shown great promise in recent years for explorations of quantum mechanics at the scale of circuits on a chip and for forming qubits, the foundational elements of a quantum computer. The quantum state of these superconducting qubits can be manipulated with microwave radiation at low temperatures. We are currently developing superconducting metamaterial structures with novel microwave mode spectra for coupling to superconducting qubits.

are working on experiments to couple these left-handed lines and ring resonators to superconducting qubits for experiments involving the exchange of microwave photons [2-4].

In addition to multimode systems, we also fabricate and measure superconducting coplanar waveguide (CPW) microwave resonators to probe loss mechanisms that limit quality factors at low temperatures. Such resonator measurements serve as a proxy for characterizing decoherence sources in superconducting qubits. We also use CPW resonators to probe the microwave loss contributions from magnetic flux vortices in superconducting films [5].

We pattern these circuits at the CNF with nanoscale structures defined with electron-beam lithography on the JEOL 6300 integrated with photolithographically defined large-scale features. The junctions are fabricated using the standard double-angle shadow evaporation technique, in which a resist bilayer of copolymer and PMMA is used to produce a narrow PMMA airbridge suspended above the substrate. Evaporation of aluminum from two different angles with an oxidation step in between forms a small Al-AlO_x-Al tunnel junction from the deposition shadow of the airbridge. We have developed a process for defining these junctions with electron-beam lithography and we perform the aluminum evaporations in a dedicated chamber at Syracuse. We pattern large-scale features using the ASML stepper, with electron-beam evaporation of Al and sputter-deposition of Nb. Measurements of these circuits are performed in cryogenic systems at Syracuse University, including dilution refrigerators for achieving temperatures below 30 mK.

Summary of Research:

The unique properties of nanoscale Josephson junctions enable a wide range of novel superconducting circuits for investigations in many diverse areas. In recent years, circuits composed of such junctions have emerged as promising candidates for the element of a quantum computer, due to the low intrinsic dissipation from the superconducting electrodes and the possibility of scaling to many such qubits on a chip [1]. The quantum coherent properties of the circuits are measured at temperatures below 50 mK with manipulation of the qubit state through microwave excitation.

We are developing multimode microwave resonators using combinations of superconducting lumped-circuit elements to engineer metamaterial transmission lines, including metamaterial ring resonator devices. These structures exhibit novel mode structures characteristic of left-handed materials [2]. We are fabricating such metamaterial transmission lines from Al and Nb films on Si and characterizing these at low temperatures [2]. We

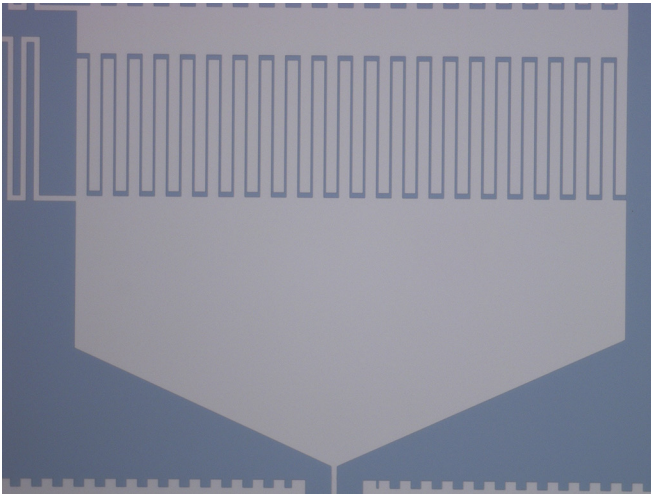


Figure 1: Optical micrograph of interdigitated capacitor in left-handed metamaterial ring resonator fabricated from Nb on Si.

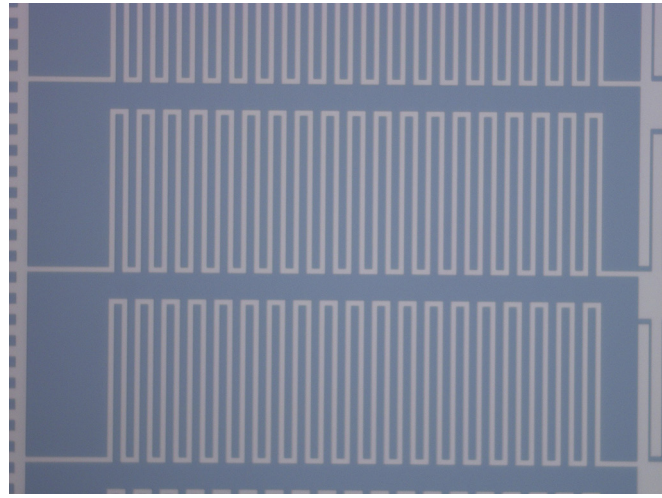


Figure 2: Optical micrograph of meander-line inductors in left-handed metamaterial ring resonator fabricated from Nb on Si.

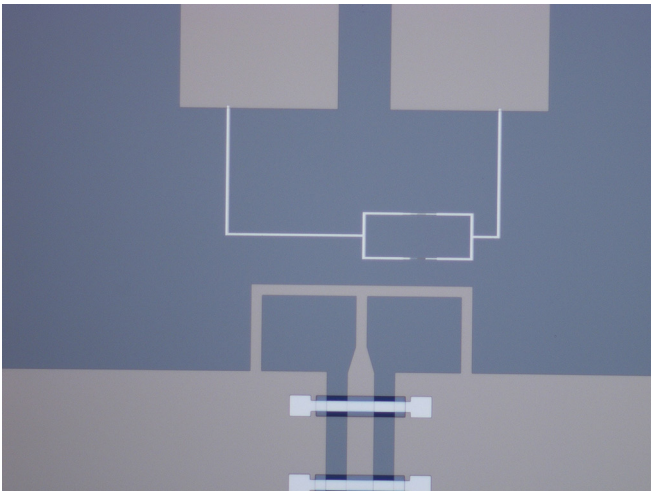


Figure 3: Zoomed-in optical micrograph of transmon qubit with Al-AlOx-Al junctions and Nb capacitor pads coupled to metamaterial transmission-line resonator with on-chip Nb flux-bias line.

References:

- [1] Clarke, J. and Wilhelm, F.K.; "Superconducting quantum bits"; Nature, 453, 1031 (2008).
- [2] Wang, H., Zhuravel, A., Indrajeet, S., Taketani, B., Hutchings, M., Hao, Y., Rouxinol, F., Wilhelm, F., LaHaye, M.D., Ustinov, A., Plourde, B.; "Mode Structure in Superconducting Metamaterial Transmission Line Resonators"; Physical Review Applied 11, 054062 (2019).
- [3] Indrajeet, S., Wang, H., Hutchings, M.D., Taketani, B.G., Wilhelm, F.K., LaHaye, M.D., Plourde, B.L.T.; "Coupling a Superconducting Qubit to a Left-Handed Metamaterial Resonator"; Physical Review Applied 14, 064033 (2020).
- [4] McBroom, T.A., Schlages, A., Xu, X., Ku, J., Cole, B.G., Indrajeet, S., LaHaye, M., Ansari, M., Plourde, B.; "Entangling Interactions Between Artificial Atoms Mediated by a Multimode Left-Handed Superconducting Ring Resonator"; Physical Review X Quantum 5, 020325 (2024).
- [5] Paustian, JT, Larson, C., Dodge, K., Plourde, B.; "Vortex viscosity in superconducting granular aluminum resonators"; Bull. Am. Phys. Soc. 2024, <https://meetings.aps.org/Meeting/MAR24/Session/N47.13>.

Realization of the Haldane Chern Insulator in a Moiré Lattice

CNF Project Number: 2633-18

Principal Investigator(s): Jie Shan, Kin Fai Mak

**User(s): Wenjin Zhao, Kaifei Kang, Yichi Zhang,
Zui Tao, Lizhong Li, Charles Tschirhart**

*Affiliation(s): Kavli Institute at Cornell for Nanoscale Science, Laboratory of Atomic and Solid State Physics,
School of Applied and Engineering Physics; Cornell University*

Primary Source(s) of Research Funding: DOE, NSF, AFOSR

Contact: jie.shan@cornell.edu, kinfai.mak@cornell.edu, wz435@cornell.edu,

kk726@cornell.edu, yz2662@cornell.edu, zt227@cornell.edu, ll646@cornell.edu, ct638@cornell.edu

*Primary CNF Tools Used: Zeiss Supra SEM, Nabity Nanometer Pattern Generator System (NPGS),
SC4500 Odd/Even-Hour Evaporator, Autostep i-line Stepper, Hamatech Wafer Processor Develop,
Heidelberg Mask Writer - DWL2000, Photolithography Spinners, Dicing Saw - DISCO*

Abstract:

The Chern insulator displays a quantized Hall effect without Landau levels. Theoretically, this state can be realized by engineering complex next-nearest-neighbor hopping in a honeycomb lattice — the so-called Haldane model [1]. We realize a Haldane Chern insulator in AB-stacked $\text{MoTe}_2/\text{WSe}_2$ moiré bilayers, which form a honeycomb moiré lattice with two sublattices residing in different layers [2]. We show that the moiré bilayer filled with two holes per unit cell is a quantum spin Hall insulator with a tunable charge gap. Under a small out-of-plane magnetic field, it becomes a Chern insulator with a finite Chern number because the Zeeman field splits the quantum spin Hall insulator into two halves of opposite valley — one with a positive and the other a negative moiré band gap. We also demonstrate experimental evidence of the Haldane model at zero external magnetic field by proximity coupling the moiré bilayer to a ferromagnetic insulator.

Summary of Research:

When a two-dimensional electron gas is exposed to high magnetic fields, it forms Landau levels, and quantized Hall conductance is observed [3]. Researchers aim to achieve a quantum Hall state without external magnetic fields, known as a Chern insulator [1]. These insulators have been realized in a few materials, such as magnetic topological insulators and moiré materials. A proposed method involves transforming a quantum spin Hall (QSH) insulator into a Chern insulator through magnetic interactions [4].

In this study, we use AB-stacked $\text{MoTe}_2/\text{WSe}_2$ moiré bilayer, which is a new QSH insulator with a tunable charge gap and unique spin-valley-layer locking. By

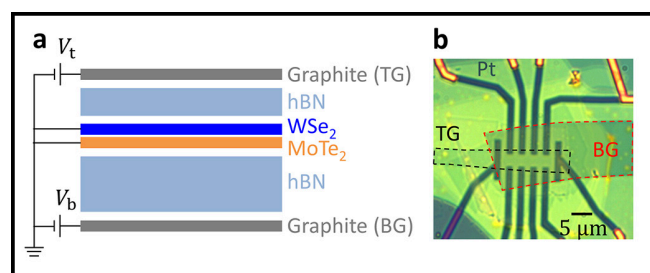


Figure 1: a, Device schematics. b, Optical microscope image of a dual-gated device. The scale bar is 5 μm .

applying an out-of-plane magnetic field or proximity coupling to a ferromagnetic insulator, the material transitions into a Chern insulator. This transformation is facilitated by valley-dependent magnetic interactions and Zeeman energies. We demonstrated that an out-of-plane magnetic field of about 1 Tesla or proximity coupling can induce this transition. We investigated the transport properties of these bilayers, showing the emergence of a nearly quantized Hall resistance for the Chern insulator state at specific electric and magnetic field conditions. The results support the realization of a Haldane Chern insulator and suggest a new method for creating Chern insulators through tunable band inversion and magnetic proximity effects.

Figure 1 shows the schematic and optical image of a device. We fabricated dual-gated $\text{MoTe}_2/\text{WSe}_2$ devices using a layer-by-layer dry-transfer technique. We deposited 5-nm Pt contacts on hBN by standard electron-beam lithography and evaporation, followed by another step of electron-beam lithography and metallization to form a bilayer of 5-nm Ti and 40-nm Au to connect the thin Pt contacts on hBN to pre-patterned electrodes.

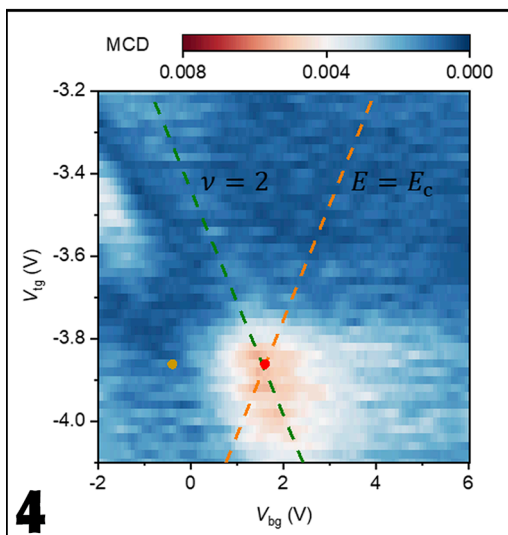
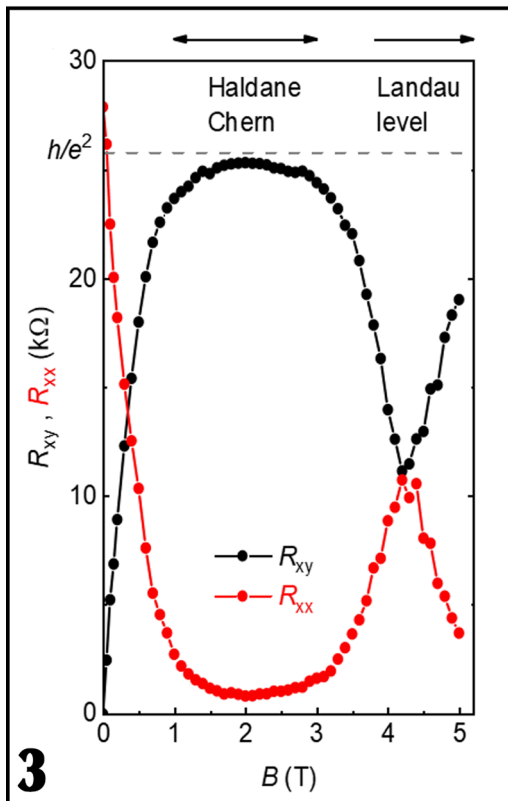
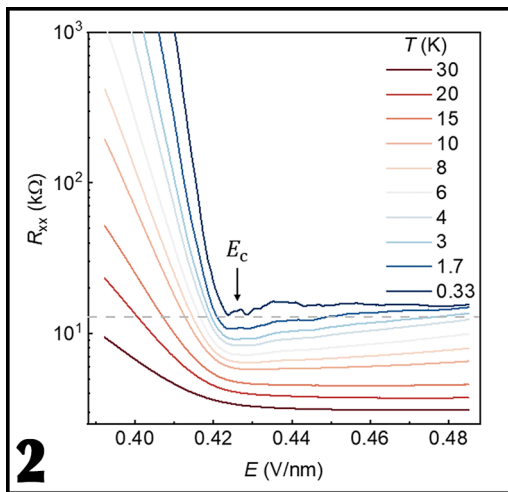


Figure 2 shows the electric-field dependence of R_{xx} at $\nu = 2$ and temperature $T = 0.33\text{--}30$ K. The resistance shows a minimum near E_c and distinct behaviors on two sides of E_c . Below E_c , R_{xx} decreases as E approaches E_c ; and at a fixed field, R_{xx} diverges as T decreases. This is a typical response of an insulator with a diminishing band gap towards E_c . Above E_c , R_{xx} plateaus, and the value saturates around $15\text{ k}\Omega \approx 1.16 h/2e^2$ at 0.33 K. The nearly quantized R_{xx} plateau suggests the emergence of a QSH insulator for $E > E_c$, where E_c corresponds to the quantum critical point for band inversion.

Figure 3 is the magnetic-field dependence of R_{xy} and R_{xx} to show this transition from the QSH insulator to the Haldane Chern insulator. The Hall resistance increases sharply from 0 at $B = 0$ T, plateaus between 1 T and 3 T, and displays non-monotonic field dependence for $B > 3$ T. The plateau value ($\approx 25.4\text{ k}\Omega$) is within 2% of the quantized Hall resistance, h/e^2 . Concurrently, R_{xx} drops sharply with increasing field and remains small ($< 1\text{ k}\Omega$) between 1 T and 3 T. Hence, when we set E near the band inversion critical point, a moderate magnetic field between 1 T and 3 T is sufficient to induce the Chern state.

Figure 4 shows the gate voltage dependence of the spontaneous magnetic circular dichroism (MCD) of a $\text{CrBr}_3\text{-MoTe}_2/\text{WSe}_2$ device, where the CrBr_3 is a ferromagnetic insulator. The observed MCD hot spot demonstrates spontaneous time reversal symmetry breaking near the band inversion critical point. This is consistent with the emergence of an exchange field from the magnetic proximity effect at the $\text{CrBr}_3\text{-MoTe}_2/\text{WSe}_2$ interface. Similar to the external magnetic field, the proximity exchange field splits the QSH insulator near band inversion to the Haldane model.

Conclusion and Future Steps:

We have realized a Haldane Chern insulator in AB-stacked $\text{MoTe}_2/\text{WSe}_2$ moiré bilayers. Our study presents a generic route to realizing Chern insulators through tunable band inversion and magnetic proximity coupling. The demonstrated large exchange field has the potential to stabilize a large-gap Chern insulator. Future transport studies with improved electrical contacts are required to further establish the Haldane physics under zero magnetic field.

References:

- [1] Haldane, F. D. M. Phys. Rev. Lett. 61, 2015-2018 (1988).
- [2] Li, T., et al. Nature 600, 641-646 (2021).
- [3] Klitzing, K. V., Dorda, G., and Pepper, M. Phys. Rev. Lett. 45, 494-497 (1980).
- [4] Liu, C., et al. Quantum Wells. 101, 146802 (2008).

Figure 2, top: Electric-field dependence of R_{xx} at $\nu = 2$ at different temperatures. Figure 3, middle: Magnetic-field dependence of R_{xx} and R_{xy} at $\nu = 2$ and $E = E_c$. The lines are guides to the eye. The Hall resistance is nearly quantized at h/e^2 (dashed line) between 1 T and 3 T. It is divided into the low-field (Haldane Chern) and high-field (Landau level) regimes. Figure 4, bottom: Spontaneous MCD of the $\text{CrBr}_3\text{-MoTe}_2/\text{WSe}_2$ device as a function of the top and bottom gate voltages. The dashed lines denote constant filling factor $\nu = 2$ (green lines) and constant electric field $E = E_c$ (orange lines).

Giant Spin Hall Effect in AB-Stacked $\text{MoTe}_2/\text{WSe}_2$ Bilayers

CNF Project Number: 2633-18

Principal Investigator(s): Jie Shan, Kin Fai Mak

User(s): Zui Tao, Bowen Shen, Wenjin Zhao, Tingxin Li, Shengwei Jiang, Lizhong Li

Affiliation(s): Laboratory of Atomic and Solid State Physics, School of Applied and Engineering Physics, Kavli Institute at Cornell for Nanoscale Science; Cornell University

Primary Source(s) of Research Funding: DOE, NSF, AFOSR

Contact: jie.shan@cornell.edu, kinfai.mak@cornell.edu, zt227@cornell.edu, bs792@cornell.edu, wz435@cornell.edu, tl684@cornell.edu, sj538@cornell.edu, ll646@cornell.edu

Primary CNF Tools Used: Zeiss Supra SEM, Nability Nanometer Pattern Generator System (NPGS), SC4500 Odd/Even-Hour Evaporator, Autostep i-line Stepper, Hamatech Wafer Processor Develop, Heidelberg Mask Writer - DWL2000, Photolithography Spinners, Dicing Saw - DISCO

Abstract:

The spin Hall effect (SHE) [1,2], in which an electrical current generates a transverse spin current, plays an important role in spintronics for the generation and manipulation of spin-polarized electrons. The phenomenon originates from spin-orbit coupling. In general, stronger spin-orbit coupling favors larger SHEs but shorter spin relaxation times and diffusion lengths. Achieving large SHEs and long-range spin transport simultaneously in a single material has remained a challenge [3]. Here we demonstrate a giant intrinsic SHE that coexists with ferromagnetism in TMD moiré bilayers by direct magneto optical imaging. We also observe long-range spin Hall transport and efficient non-local spin accumulation limited only by the device size (about $10 \mu\text{m}$). Our results demonstrate moiré engineering of Berry curvature and electronic correlations for potential spintronics applications.

Summary of Research:

In this study, we explore the intrinsic SHE in AB-stacked $\text{MoTe}_2/\text{WSe}_2$ bilayers (where the two monolayer crystals are twisted by about 180° and a moiré pattern with a period of about 5 nm due to the lattice mismatch is formed) [4]. The SHE, critical for spintronics, is typically enhanced by strong spin-orbit coupling, but the strong spin-orbit coupling also tends to shorten the spin relaxation times and diffusion lengths. It is therefore challenging to achieve large SHEs and long-range spin transport in a single material. We demonstrate that by using moiré engineering, these properties can be achieved simultaneously. We observe spin accumulation on transverse sample edges that nearly saturates the spin density under moderate electrical currents with density $< 1 \text{ A/m}$. We also observe long-range spin Hall transport, as demonstrated by the extended spin current distribution

profile. The giant SHE is observed near the interaction-driven Chern insulating state (with one hole per moiré unit cell) and emerges after the quantum anomalous Hall (QAH) breakdown and at low temperatures. Our results highlight the potential of moiré engineering for creating Berry curvature hotspots and controlling electronic correlations. The demonstration of giant SHEs in the same material platform as many reported exotic quantum many-body phenomena opens exciting opportunities for gate-defined lateral heterostructure quantum devices.

Figure 1 is the typical setup for spin Hall effect measurements. A bias current along the x-axis induces a spin Hall current along the y-axis. We fabricated dual-gated AB-stack $\text{MoTe}_2/\text{WSe}_2$ devices using the reported layer-by-layer dry-transfer technique [5]. Few-layer graphite and hexagonal boron nitride (hBN) are used as the gate electrode and gate dielectric, respectively, in both the top and bottom gates. We first deposited 5 nm Pt contacts on the bottom gate hBN by standard electron-beam lithography and evaporation. We then performed another step of electron-beam lithography and metallization to deposit 5 nm Ti/40-nm Au which connects the thin Pt contacts on hBN to pre-patterned electrodes on the Si substrate.

We transferred the $\text{MoTe}_2/\text{WSe}_2$ moiré bilayers on top of the hBN layer such that the Pt electrodes are in direct contact with the $\text{MoTe}_2/\text{WSe}_2$ moiré. Figure 1b shows an optical microscope image of a multi-terminal Hall bar device. The scale bar represents $5 \mu\text{m}$.

Figure 2 shows the giant spin accumulation and QAH breakdown. Bias current-dependent MCD images at 6 K (Figure 2a) and 1.6 K (Figure 2b) were taken at the center of the QAH region in the filling-displacement phase diagram. The black dashed lines mark the sample

boundaries, and the arrows show the bias current direction. Zero-bias spontaneous MCD is observed only at 1.6 K. The high-bias MCD images, which consist of two domains, are nearly identical for 1.6 K and 6 K. To analyze the interplay between the SHE and the Chern insulator state, we plot the current dependence of edge MCD from two points (P1 and P2) at 1.6 K and 6 K (top) and R_{xx} and R_{xy} at 1.6 K (bottom) in Figure 2c. QAH breakdown is observed near $0.5 \mu\text{A}$ at 1.6 K (the horizontal dashed line marks the resistance quantum). Concurrently, the MCD at P1 switches sign at the QAH breakdown whereas that at P2 increases gradually and saturates. These results suggest that the SHE dominates after the QAH breakdown with increasing bias current.

Figure 3 shows doping dependent non-local spin Hall transport. In this case, we bias the current between two Hall probes to allow for a longer spin propagation channel. The system supports long range spin transport, as evidenced by the MCD images (Figure 3a), MCD line profile (Figure 3b) and the corresponding spin Hall current density (Figure 3c) at varying filling factors (taken at the grey line in Figure 3a). Spin current J_s is normalized to the value at the current path centerline at $3 \mu\text{m}$ (vertical dashed line). Non-local spin Hall transport and spin accumulation far away from the current path centerline are most significant at lattice filling factor $\nu = 1$ for holes.

Conclusions and Future Steps:

We observe a giant SHE and long-range spin transport in AB-stacked $\text{MoTe}_2/\text{WSe}_2$ moiré bilayers via MCD imaging. The SHE-induced magnetization nearly saturates spin density under moderate biases. The effect is driven by intrinsic Berry curvature at the Chern insulating state. The effect is the strongest at $\nu = 1$ due to the Berry curvature hot spots and likely a long spin relaxation time, highlighting the potential for spintronics application and advanced quantum devices.

References:

- [1] Sinova, J., Valenzuela, S. O., Wunderlich, J., Back, C. H., and Jungwirth, T. Spin Hall effects. *Rev. Mod. Phys.* 87, 1213-1260 (2015).
- [2] Kato, Y. K., Myers, R. C., Gossard, A. C., and Awschalom, D. D. Observation of the Spin Hall Effect in Semiconductors. *Science* 306, 1910-1913 (2004).
- [3] Sarma, S. D. Spintronics: Fundamentals and applications. *Rev Mod Phys* 76, 88 (2004).
- [4] Li, T., et al. Quantum anomalous Hall effect from intertwined moiré bands. *Nature* 600, 641-646 (2021).
- [5] Tingxin Li, et al. Continuous Mott transition in semiconductor moiré superlattices. *Nature* 597, 350-354 (2021).

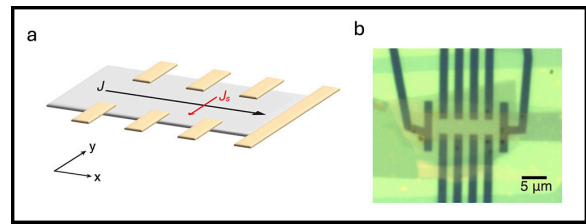


Figure 1: a, Schematic of the spin Hall effect measurements. b, Optical microscope image of a dual-gated device. The scale bar is $5 \mu\text{m}$.

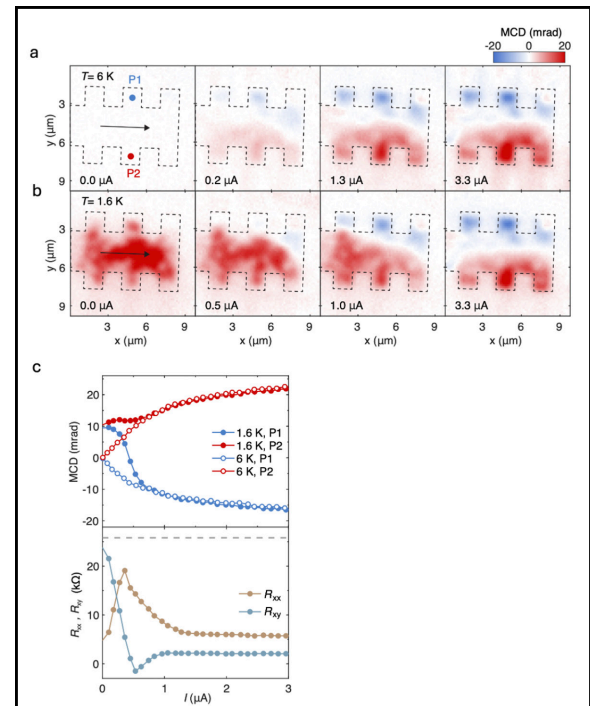


Figure 2: a, b MCD images at varying bias currents at 1.6 K (a) and 6 K (b). c, Bias current dependence of edge spin accumulation and interplay with quantum anomalous Hall breakdown.

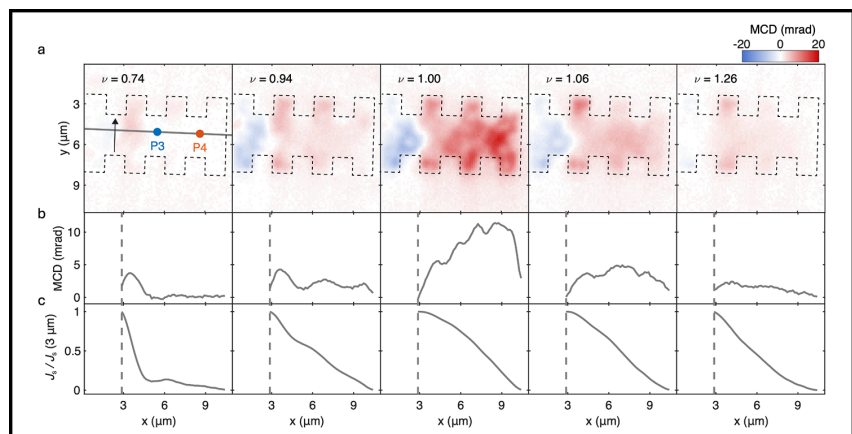


Figure 3: Filling dependence of non-local spin transport. MCD images (a) MCD line profile (b) and the corresponding spin Hall current density (c) at varying filling factors.

Thin-Film Deposition for Surface Characterization Studies for Superconducting Radio Frequency Cavity Application

CNF Project Number: 2779-19

Principal Investigator(s): Matthias Liepe

User(s): Nathan Sitaraman, Sadie Seddon-Stettler

Affiliation(s): Cornell Laboratory for Accelerator-based Sciences and Education, Cornell University

Primary Source(s) of Research Funding: The U.S. National Science Foundation under Award PHY-1549132, the Center for Bright Beams

Contact: mul2@cornell.edu, nss87@cornell.edu, sgs238@cornell.edu

Research Group Website: <https://physics.cornell.edu/matthias-liepe>

Primary CNF Tools Used: CVC SC4500, AJA Sputter Deposition 1 & 2

Abstract:

Superconducting radio-frequency (SRF) cavities are a key component of particle accelerators (with applications ranging from fundamental physics research to synchrotron X-ray sources, to e-beam microscopy and lithography) and are also being developed for applications in dark matter detection and quantum computing. We are developing next-generation surface treatments to enhance the performance of niobium superconducting surfaces. By using facilities at the CNF, we investigate the effect of metallic doping on the niobium surface. We highlight our recent success in altering the niobium native oxide by zirconium doping and by gold doping.

holder for clean transport to and from CNF for zirconium deposition. The sample then received an additional high pressure rinse and was delivered to the furnace in the clean-transport holder. This sample will undergo RF testing shortly.

We also used CNF's CVC SC4500 evaporation deposition system to deposit 5-10 nm gold layers on small niobium coupon samples. These samples received short 800°C vacuum bakes, and XPS analysis showed that the resulting surface had greatly reduced niobium oxide concentrations.

Summary of Research:

We used CNF's AJA sputter deposition tools to deposit zirconium on niobium sample plates for RF testing. This builds on our earlier development of a zirconium oxide capping layer recipe using the same CNF tool on small coupon samples. Prior to deposition, sample plates received a 60-micron electropolish followed by a 5-hour 800°C vacuum bake and a baseline RF performance test.

The first sample then received an acid wash and high pressure rinsing prior to zirconium deposition at CNF, followed by another 5-hour 800°C vacuum bake. The RF performance of this sample was poor, which post-analysis linked to contamination during transport between CNF and the vacuum furnace.

The second sample similarly received an acid wash and high pressure rinsing, then used a specialized sample

Conclusions and Future Steps:

We have now developed two methods to eliminate the niobium pentoxide from a niobium superconducting surface. We expect that this method may be applicable to niobium superconducting devices and niobium-zirconium alloy surfaces, as well as possibly other niobium-based superconducting surfaces which typically form a niobium-rich oxide. We plan to do further RF testing on zirconium-oxide-capped and gold-passivated niobium surfaces in the near future. We will also attempt to apply this method to the Nb₃Sn surface, and we will investigate other passive oxide layers such as hafnium, aluminum, and silicon oxide for SRF applications. We are also using the AJA sputter deposition tool to conduct preliminary investigations of Nb₃Al growth and oxide properties; coupon samples have received aluminum deposition and vacuum baking recipes are currently being finalized for testing.

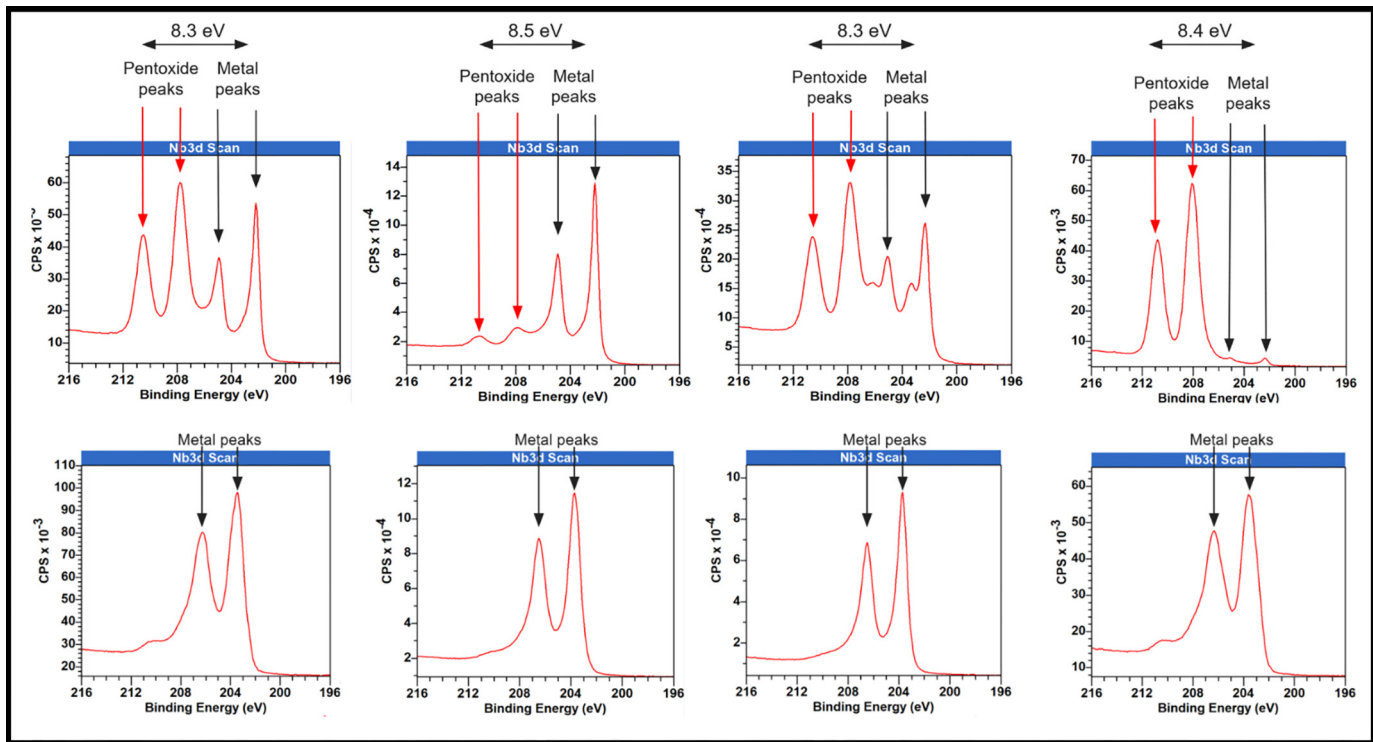


Figure 1: Top row, XPS data from niobium samples of various preparations without gold passivation. Niobium pentoxide peaks are consistently detected at a constant energy shift relative to the niobium metals peaks. Bottom row, XPS data from niobium samples after receiving different gold passivation recipes, none of which have peaks at the expected position for the pentoxide.

References:

- [1] Sitaraman, N.S., Sun, Z., Francis, B.L., Hire, A.C., Oseroff, T., Baraissov, Z., Arias, T.A., Hennig, R.G., Liepe, M.U., Muller, D.A. and Transtrum, M.K., 2023. Enhanced Surface Superconductivity of Niobium by Zirconium Doping. *Physical Review Applied*, 20(1), p.014064.
- [2] Seddon-Stettler, S., Liepe, M., Oseroff, T., and Sitaraman, N. Novel materials for beam acceleration. *Proc. IPAC'24*, 2680-2682.

Imaging Pulse-Induced Charge Density Wave Switching in 1T-TaS₂

CNF Project Number: 2967-21

Principal Investigator(s): Judy J. Cha

User(s): Saif Siddique, Stephen D. Funni, Yu-Mi Wu

Affiliation(s): Department of Materials Science and Engineering, Cornell University

Primary Source(s) of Research Funding: Gordon and Betty Moore foundation (EPiQS Synthesis Award #9062.01), Department of Energy, Basic Energy Sciences DE-SC0023905

Contact: jc476@cornell.edu, ms2895@cornell.edu, sdf68@cornell.edu, yw2658@cornell.edu

Research Group Website: <https://cha.mse.cornell.edu>

Primary CNF Tools Used: Zeiss Supra SEM, Nabity System for Supra SEM, CHA Evaporator, Harrick Plasma Generator

Abstract:

Charge density wave (CDW) is a macroscopic quantum state observed in low-dimensional materials, such as the two-dimensional (2D) layered material tantalum disulfide (TaS₂). In the 1T polytype of TaS₂, voltage pulses can induce CDW phase transitions, which are accompanied by a sharp insulator-to-metal transition. This makes 1T-TaS₂ promising for next-generation devices. We fabricated nanodevices of 1T-TaS₂ flakes and operated them within a scanning transmission electron microscope (STEM), allowing us to directly visualize the CDW structure and phase transitions during device operation with nanoscale spatial resolution and microsecond temporal resolution at cryogenic temperatures. Our study reveals that Joule heating drives the pulse-induced CDW transitions and the CDW transitions are directly correlated with the real-space structure and electronic properties of the material, which is crucial for developing reliable and scalable TaS₂-based electronics.

Summary of Research:

Charge density waves (CDWs) are periodic modulations of the electronic charge density within a material, which are accompanied by periodic distortions in the material's crystal lattice [1]. 1T-TaS₂ is a 2D quantum material that hosts several distinct CDW phases [2]. These include an insulating commensurate (C) CDW phase with long-range order, a metallic nearly-commensurate (NC) phase characterized by domains of commensurate CDW separated by phase slips (discommensurations), and a metallic incommensurate (IC) CDW phase lacking long-range order [3]. Below 200 K, 1T-TaS₂ is in the insulating C-CDW phase, but voltage pulses can switch it to the metallic NC-CDW phase [4]. This switching is fast, reversible and energy efficient, and results in a large change in electrical resistance, making 1T-TaS₂ promising for use in memristive and

neuromorphic devices [5]. However, the mechanism of pulse-induced switching is not fully understood. To use TaS₂ in nanoscale devices, it is crucial to have a detailed understanding of how the CDW phase transitions occur at nanoscale dimensions, and what factors affect the transition.

We fabricated 2-terminal devices by exfoliating ~ 55 nm thick flakes of 1T-TaS₂ from bulk crystals onto *in-situ* TEM chips. Electrical connections to the platinum electrodes on the *in-situ* TEM chips were made by placing graphite electrodes on the TaS₂ flakes (Figure 1a,b). We operated this device within a TEM using a Keithley 2400 source meter to measure the resistance of the flake as a function of temperature. Simultaneously, electron diffraction was acquired to measure the domain size (D_{NC}), the order parameter for the C to NC transition in 1T-TaS₂, hence characterizing its CDW state (Figure 1c) [6]. In the C-CDW phase, D_{NC} is > 100 nm while in the NC-CDW phase, D_{NC} is ~ 10 nm (Figure 1).

By applying a constant DC bias and heating the flake from the C to NC phase, we monitored the device resistance and D_{NC} (Figure 1c,d). We found that the domain size changes first, followed by the resistance change, showing that the structural CDW transition precedes the resistive transition by about 10 K, as indicated by changes in resistance and domain size during the C to NC transition (inset Figure 1d). This is unexpected, as the structural and electronic changes due to CDW transitions are assumed simultaneous.

To investigate this further, we applied a series of short square pulses with increasing voltage amplitudes (2 V to 9.6 V, 3 μ s pulse duration; Figure 2) to the TaS₂ flake in its C-CDW phase, using a Keysight 33600A waveform generator. For voltage pulses > 3.2 V, the flake transitions to the NC phase (Figure 2). Consistent with our earlier findings the structural CDW transition

preceded the electronic resistance transition. Additionally, larger voltage pulses produced smaller CDW domains and lower device resistance in the NC phase, suggesting that the applied voltage increases the temperature of the device through Joule heating.

To demonstrate that Joule heating drives the switching, we applied triangular voltage ramps (with maximum voltage between 0.1 V to 1.2 V) while collecting diffraction patterns at every 10 ms interval. We observed that voltages above 0.8 V caused a sudden decrease in DNC, indicating a transition from the C to NC and IC phases (Figure 3a). We extracted the in-plane flake strain from the diffraction data and converted it to corresponding temperature using thermal expansion coefficient.

At the 0.8 V threshold, we measure the flake temperature to be ~ 200 K, which corresponds to the C to NC transition temperature (Figure 3b). Thus, Joule heating from the applied voltage is sufficient to raise the temperature of 1T-TaS₂ devices above the CDW transition temperature.

Conclusions and Future Steps:

Our study conclusively demonstrates that bias-induced switching in 1T-TaS₂ is driven by Joule heating, causing a rapid thermal transition from the C to NC and IC phases. This mechanism applies for both steady-state biasing and microsecond voltage pulses. Further work is needed to study the claims of picosecond switching with energies below the Joule heating threshold, to determine if purely field-induced switching is possible. Our findings provide a microscopic understanding of CDW behavior in TaS₂ devices and provide a foundation for future studies to enhance the performance and reliability of TaS₂-based electronic devices.

References:

- [1] Grüner, Rev. Mod. Phys. 60, 1129 (1988).
- [2] Ishiguro and Sato, Phys. Rev. B 44, 2049 (1991).
- [3] Lee, et al., Phys. Rev. Lett., 122, 106404 (2019).
- [4] Hollander, et al., Nano Lett. 15, 1861-1866 (2015).
- [5] Mihailovic, et al., Appl. Phys. Lett. 119, 013106 (2021).
- [6] Hart, et al., Nat. Commun. 14, 8202 (2023).

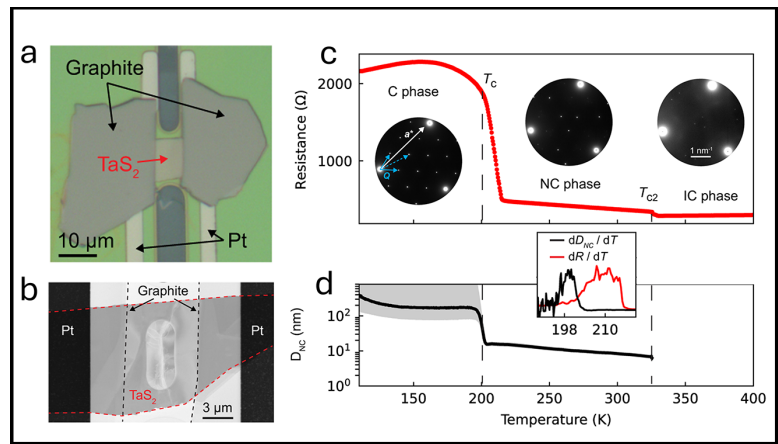


Figure 1: a. Optical microscope image of the studied device. b. STEM image of the same device. c. Resistance vs. temperature of the TaS₂ device measured in-situ inside the TEM. Insets show associated electron diffraction pattern for each phase. d. Domain size (D_{NC}) as a function of temperature. The inset shows the temperature derivatives of the resistance and D_{NC} .

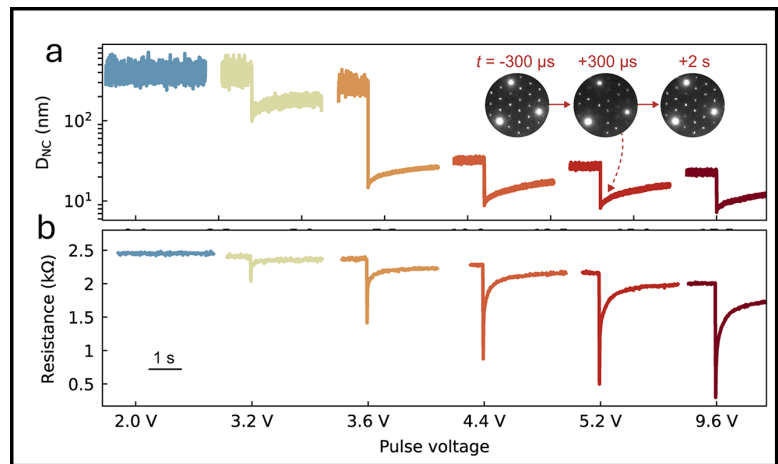


Figure 2: a. Time-resolved CDW domain size D_{NC} and b. device resistance during pulsing.

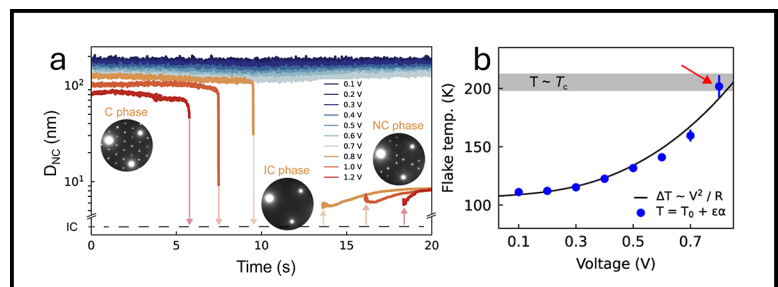


Figure 3: a. Measured D_{NC} during voltage ramps, with maximum voltage ranging from 0.1 V to 1.2 V. Insets show the diffraction pattern snapshots acquired during the 0.8 V ramp. b. Maximum flake temperature for voltage ramps from 0.1 V to 0.8 V.

Manufacturing SiN Bullseye Cavities and SOI Photonic Crystal Nanobeam Cavities

CNF Project Number: 3008-22

Principal Investigator(s): Professor Pablo A. Postigo

User(s): Christopher (Christer) Everly, Martin Sanchez

Affiliation(s): Institute of Optics, University of Rochester

Primary Source(s) of Research Funding: UoR Startup URA Award 2023-2024 from University of Rochester

Contact: ppostigo@ur.rochester.edu, ceverly@ur.rochester.edu, msanch23@ur.rochester.edu

Research Group Website: <https://www.postigolab.com>

Primary CNF Tools Used: JEOL 6300 & 9500, E-beam Spin Coaters, Olympus MX-50 Microscopes, Oxford 82, Oxford 100, PT770 RIE, Oxford Cobra ICP, Plasma-Therm Tikachi HDP-CVD, Oxford PECVD, Primaxx Vapor HF Etcher, Yes EcoClean Asher, Yes Asher, Filmetrics systems, Zeiss Ultra SEM, Zeiss SEM Supra, Veeco AFM, DISCO Dicer Saw

Abstract:

Our group is interested in quantum research on photonic platforms. Some topics we are currently exploring include: on-chip lasing and single-photon emission enhancement with circular Bragg gratings, and room temperature single phonon quantum sensing using phononic crystal enhanced optomechanical cavities. There have been recent reports of Purcell enhancement from circular Bragg cavities, as well as mechanical ground states being achieved at room temperature through use of well-designed phononic crystals.

been attempted in the lab to create anisotropic silicon etches during pattern transfer with great successes being achieved with a hydrobromic acid (HBr) inductively coupled plasma (ICP) etch, instead of the sulfur hexafluoride and oxygen (SF_6/O_2) chemistry frequently seen in literature for silicon etches. Finally, experimentation was completed with vapor hydrogen fluoride (HF) etching to successfully create suspended structures without any stiction. This was successful for suspended features in the tested range of tens of microns.

Summary of Research:

Users have done diligent work to refine the fabrication process for the circular Bragg grating (CBG) cavity, colloquially referred to as a bullseye cavity. A deposition recipe was developed on the Oxford PECVD that achieves repeatable SiO_2 followed by SiN deposition thicknesses. Experimentation was completed on different gas pressures during inductively coupled plasma (ICP) etching of silicon nitride in order to achieve the high aspect ratio, anisotropic etches required for the silicon nitride (SiN) bullseye cavities.

Additionally, the group has created our first fabrication procedure for creating suspended structures like nanobeams and phononic crystals. Due to the fine transverse structures required to make photonic crystal cavities, experimentation has been done with e-beam resist type, thickness, and dosage applied in lithography machines to match designed requirements. Experimentation was also completed on applying a varied bias to different regions in pattern files in order to account for reactive ion etch lag (RIE lag) affecting the transverse dimensions of nanostructures differently than larger structures. Different chemistries have

Conclusions and Future Steps:

Correcting the critical dimension blur is the last step to successful bullseye fabrication. After that is verified the next steps for the bullseye cavities will be to optically characterize the cavity resonance in lab.

As the nanobeam and phononic crystal fabrication is still in its incipiency, many next steps need to be taken both in the lab at University of Rochester and in the lab at Cornell. The fabricated nanobeams also need to be optically characterized. Many nanobeams were created with varying biases and cavity lengths with the hopes of pin-pointing an optical resonance in a new optical setup at the University of Rochester. Experiments need to be done with the HF vapor etch of much larger suspended structures. Simulations indicate that more phononic crystal layers increase mechanical Q -factor, so experiments need to be completed to make sure large, suspended structures in the range of hundreds of microns can be fabricated successfully using the same HF vapor etch without issues of stiction. Great success was achieved with the anisotropic HBr pattern transfer etch. More experiments need to be completed on the replicability of these results.

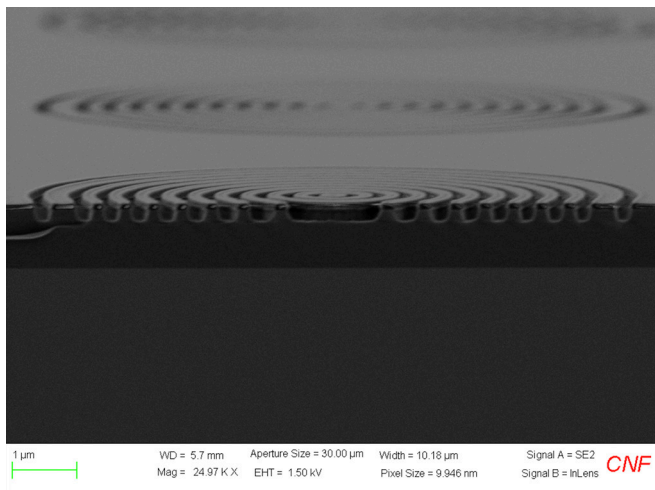


Figure 1: Cross-section of a bullseye cavity.

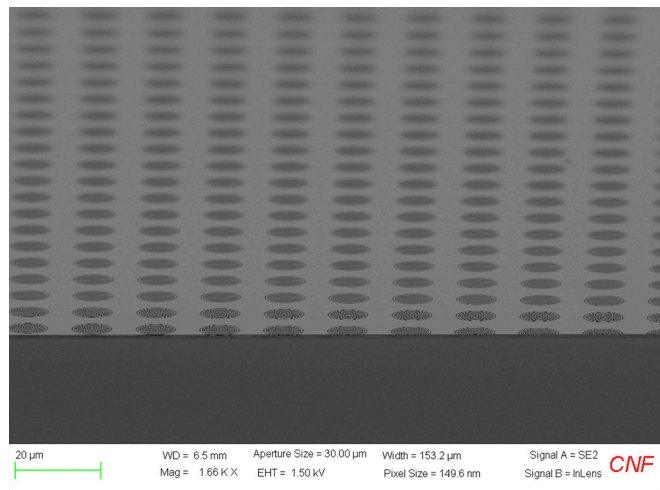


Figure 2: Array of bullseye cavities.

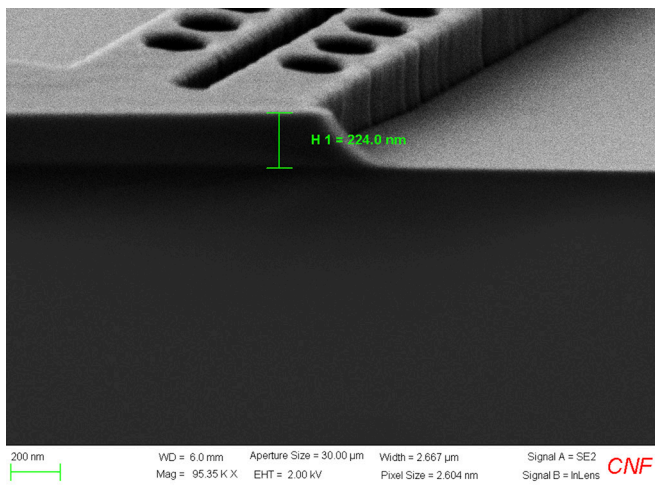


Figure 3: Cross section of nanobeams before release showing the device layer and pattern still with resist taken with the Zeiss SEM Ultra.

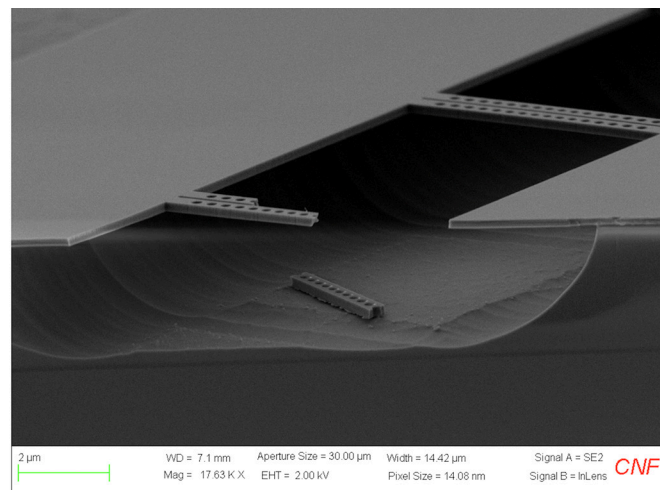


Figure 4: Nanobeam intentionally broken to show fully etched photonic crystal holes with intact suspended nanobeams in the background, taken with the Zeiss SEM Ultra.

References:

- [1] "Room-Temperature Lasing in Colloidal Nanoplatelets via Mie-Resonant Bound States in the Continuum"; Mengfei Wu, Son Tung Ha, Sushant Shendre, Emek G. Durmusoglu, Weon-Kyu Koh, Diego R. Abujetas, José A. Sánchez-Gil, Ramón Paniagua-Domínguez, Hilmi Volkan Demir, and Arseniy I. Kuznetsov, *Nano Letters* 2020 20 (8), 6005-6011, DOI: 10.1021/acs.nanolett.0c01975.
- [2] "Enhanced Emission from WSe₂ Monolayers Coupled to Circular Bragg Gratings"; Ngoc My Hanh Duong, Zai-Quan Xu, Mehran Kianinia, Rongbin Su, Zhuojun Liu, Sejeong Kim, Carlo Bradac, Toan Trong Tran, Yi Wan, Lain-Jong Li, Alexander Solntsev, Jin Liu, and Igor Aharonovich *ACS Photonics* 2018, 3950-3955 DOI: 10.1021/acsphotonics.8b00865.
- [3] "Exploring Regenerative Coupling in Phononic Crystals for Room Temperature Quantum Optomechanics"; Lukas M. Weituschat, Irene Castro, Irene Colomar, Christer Everly, Pablo A. Postigo, and Daniel Ramos, *Scientific Reports* 14, Article number: 12330 (2024), DOI: <https://doi.org/10.1038/s41598-024-63199-1>.
- [4] "Resolved-sideband cooling of a micromechanical oscillator"; A. Schliesser, R. Rivière, G. Anetsberger, O. Arcizet, and T.J. Kippenberg *Nature Physics* 4, 415-419 (2008), DOI: 10.1038/nphys939.

Weak Link Superconducting Quantum Interference Devices for High-Resolution Scanning Magnetometry

CNF Project Number: 3017-22

Principal Investigator(s): Katja Nowack

User(s): Alex Striff

Affiliation(s): Laboratory of Atomic and Solid State Physics, Cornell University

Primary Source(s) of Research Funding: Air Force Office of Scientific Research

(MURI FY21 Tunneling Phenomena in Interface Superconductors)

Contact: kcn34@cornell.edu, abs299@cornell.edu

Research Group Website: <https://nowack.lasp.cornell.edu>

Primary CNF Tools Used: AJA Sputter Deposition Tool (I), JEOL JBX-6300FS 100 kV Electron Beam Lithography System, CVC SC4500 Combination Thermal/E-gun Evaporation System (Odd-hour), Angstrom Load Lock E-beam Evaporator, DWL2000 Laser Pattern Generator and Direct Write System, Oxford PlasmaLab 80+ RIE System (Oxford 81), Zeiss Ultra 55 Scanning Electron Microscope

Abstract:

Magnetic imaging is a powerful tool for studying quantum materials. To make a sensitive magnetometer for use in a scanning probe microscope, a small super-conducting loop is interrupted by two Josephson junctions to create a super-conducting quantum interference device, or SQUID, which converts the magnetic flux coupled into the loop into a measurable signal. This research explores one way to increase the spatial resolution and maximum operating field of a SQUID, which is to replace the often-used superconductor-insulator-superconductor (SIS) Josephson junctions with narrow constrictions (weak links) in the super-conducting loop, which allow the size of the loop to be less than $1\ \mu\text{m}$ [1]. Initial measurements have demonstrated the sensitivity of test SQUIDs to magnetic flux, with improvements in progress.

Summary of Research:

Figure 1 depicts a weak link SQUID, made of a 50 nm niobium film with a 20 nm aluminum shunting layer on a silicon substrate. For the weak links to behave like Josephson junctions, they must have dimensions comparable to the super-conductor's coherence length [2], which necessitates the use of electron beam lithography to pattern a mask for the SQUID loop. A bilayer lift-off process patterns the SQUID loop in 20 nm of aluminum. Since the electron beam write time for bond pads would be excessive, instead a separate 20 nm layer of aluminum that overlaps with the SQUID loop is patterned by direct-write photolithography and lifted off. The two aluminum layers mask the niobium during a dry etch step, leaving a bilayer SQUID pattern with the layer stack depicted in Figure 2.

A SQUID with slightly different dimensions to those depicted in Figure 1 was measured in a liquid helium dipping probe setup at 4.6 K. As is the case for conventional SIS junction SQUIDs, a series SQUID array amplifier was used to voltage bias and read out the weak link SQUID, which avoids issues encountered when using noisy, high-impedance room temperature amplifier electronics [3]. Figure 3 depicts the voltage output from the array as a function of the magnet current applying a magnetic flux to the SQUID. The array output voltage modulates with flux, demonstrating that the niobium constrictions are behaving like weak links, as intended.

Conclusions and Future Steps:

While these weak link SQUIDs operate as magnetic flux sensors, some aspects of their behavior and use in a readout circuit are not fully understood. Future work will continue to explore the design parameter space for these devices. We will also develop an etching process to place the SQUID loop at the corner of a chip so that it may scan across a sample surface [4].

References:

- [1] Vasyukov, D., et al. *Nature Nanotech* 8, 639-644 (2013).
- [2] Likharev, K. K. *Rev. Mod. Phys.* 51, 101-159 (1979).
- [3] Huber, M. E., et al. *Review of Scientific Instruments* 79, 053704 (2008).
- [4] Pan, Y. P., et al. *Supercond. Sci. Technol.* 34, 115011 (2021).

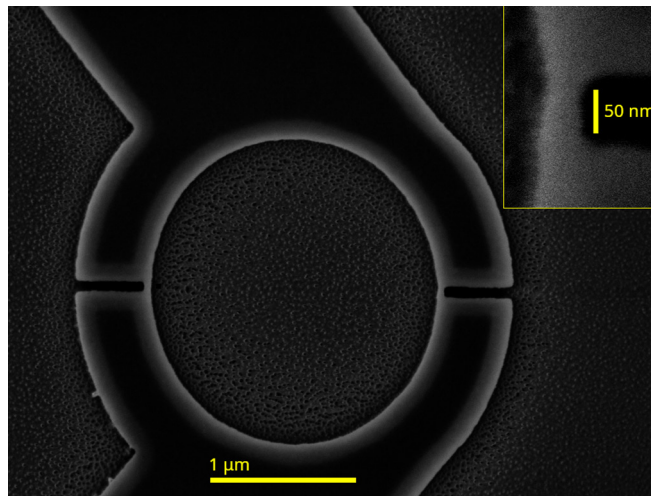


Figure 1: Scanning electron microscope image of the SQUID loop. Inset: Right constriction at higher magnification.

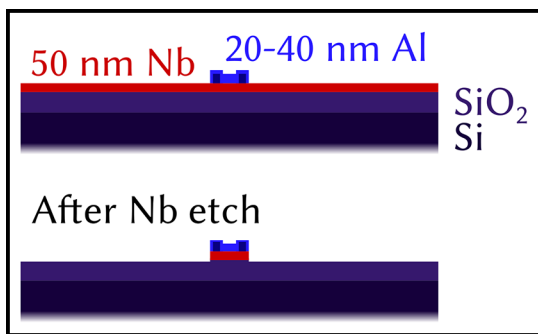


Figure 2: The SQUID fabrication process patterns a niobium film on a silicon substrate by using an aluminum hard mask (made of two overlapping aluminum layers to reduce the write time for electron beam lithography). A dry etch process transfers the aluminum pattern into the niobium.

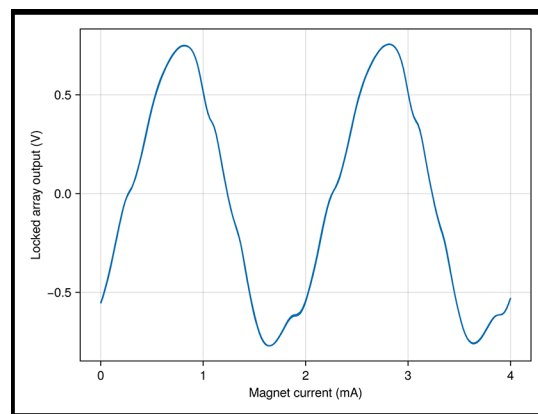


Figure 3: The voltage output of a series SQUID array amplifier (operated in a flux feedback locked loop) oscillates in response to a magnet coupling magnetic flux into a SQUID loop similar to the loop in Figure 1. Refinements to this readout scheme are in progress.

Fabrication of Fluxonium-Like Qubits

CNF Project Number: 3067-23

Principal Investigator(s): Ivan Pechenezhskiy

User(s): Benjamin Byrd, Kesavan Manivannan

Affiliation(s): Department of Physics, Syracuse University

Primary Source(s) of Research Funding: Syracuse University, Army Research Office

Contact: ivpechen@syr.edu, babyrd@syr.edu, kmanivan@syr.edu

Primary CNF Tools Used: ASML DUV Stepper, JEOL 6300, PT770 Plasma Etcher, Oxford81 Etcher, Heidelberg DWL2000 Mask Writer

Abstract:

We fabricate fluxonium and fluxonium-like qubits to study their potential for quantum computations, with our most recent study being focused on the behavior of broken Cooper pairs (quasiparticles) in superconducting coherent quantum devices. Quasiparticles are injected directly into our samples by driving a current through a Josephson junction larger than its critical current. Fluxonium qubits are intrinsically protected against charge noise and also against flux noise at the two flux sweet spots, making it easier to produce longer-lived devices. Some of these qubits have lifetimes exceeding a millisecond [1].

This project's fluxonium-like qubits are fabricated following a previously reported recipe [2].

Summary of Research:

A fluxonium qubit (Figure 1) is composed of a capacitor, with a Josephson junction shunting the capacitive element. The key difference between a fluxonium and the more commonly studied transmon qubit is the inclusion of an inductor made of a chain of Josephson junctions, which shunts the two capacitor pads (Figure 2). This forms a closed loop through which we can apply a magnetic field. At certain values of flux threading through this loop, the qubit is protected from some crucial loss channels. The qubit is capacitively coupled to a resonator, whose frequency is shifted based on the state of the fluxonium qubit, allowing us to determine the state of the qubit by measuring the shift in the resonator frequency.

Our devices are fabricated on Si wafers, first by sputtering a ~ 70 nm layer of niobium to act as a superconducting ground plane from which we pattern microwave resonators, capacitors and co-planar waveguides. After patterning large features using the ASML DUV stepper for photolithography, the pattern is etched into the

niobium using the PT770. After this, the devices are cleaned in the CNF hot strip bath, the Glen1000, then in a bath of 10:1 DI:HF. To form Josephson junctions, which are of the order of ~ 100 nm \times 100 nm, e-beam lithography using the JEOL 6300 is required. After the junction is patterned in the JEOL 6300, the junctions are formed via e-beam evaporation using the Dolan bridge technique at Syracuse University.

By fabricating samples with a wide range of different geometries, we have been able to tune our fabrication process to improve coherence times in our devices by an order of magnitude. Additionally, adjusting the geometry of our Al/AlOx/Al Josephson junctions in the array enables us to tune the phase-slip rate across each junction, improving dephasing times for these devices as well [3]. In the near future we expect that these changes will improve our qubit dephasing times by an order of magnitude as well.

Extending our fabrication repertoire further, we have also begun to work on the Xactix XeF₂ etcher. With this, we will be able to suspend all Josephson junctions similar to the junctions in the blochonium qubit [4], giving us a wider range of accessible qubit parameters and new avenues to probe qubit dynamics.

References:

- [1] A. Somoroff, et al. Millisecond Coherence in a Superconducting Qubit. *Phys. Rev. Lett.* 130, 267001 (2023). <https://doi.org/10.1103/PhysRevLett.130.267001>.
- [2] V. Iaia, et al. Phonon downconversion to suppress correlated errors in superconducting qubits. *Nature Communications* 13, 6425 (2022). <https://doi.org/10.1038/s41467-022-33997-0>.
- [3] M. Randeria, et al. Dephasing in Fluxonium qubits from Coherent Quantum Phase Slips. *arXiv:2404.02989*.
- [4] I. V. Pechenezhskiy, et al. The superconducting quasicharge qubit. *Nature* 585, 368 (2020). <https://doi.org/10.1038/s41586-020-2687-9>.

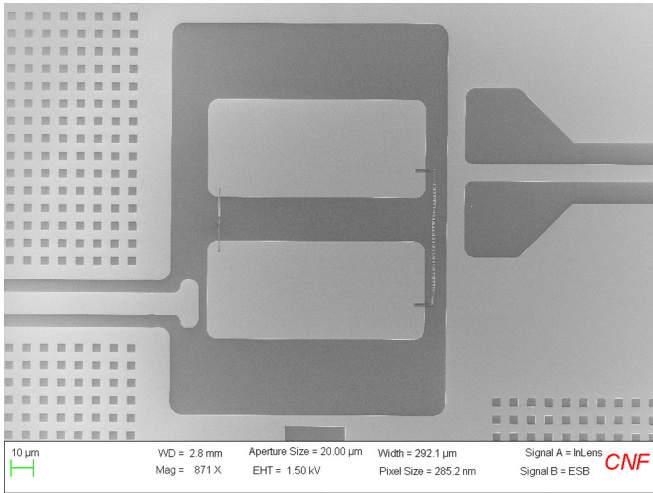


Figure 1: Scanning electron microscopy (SEM) image of one of the fluxonium qubits taken at CNF.

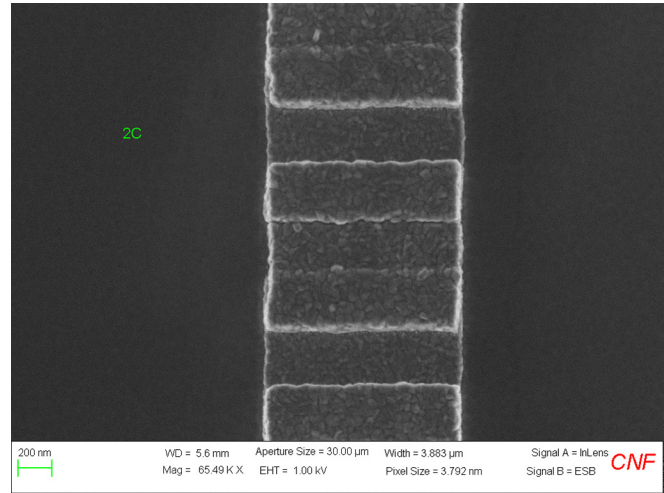


Figure 2: SEM image of a Josephson junction chain, taken at CNF.

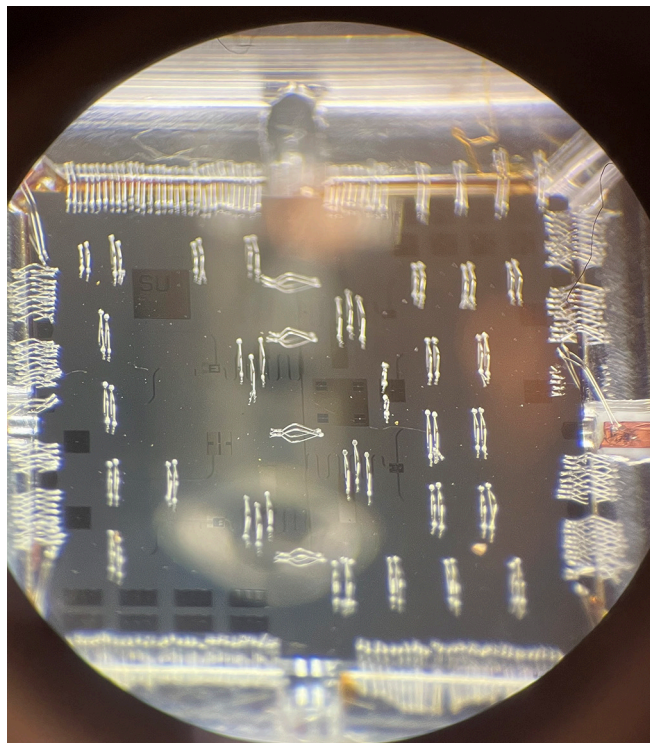


Figure 3: Photograph of a sample set into the holder wire-bonded for low-temperature measurements.

Characterization of Fluxonium Qubits

CNF Project Number: 3067-23

Principal Investigator(s): Ivan Pechenezhskiy

User(s): Benjamin Byrd, Kesavan Manivannan

Affiliation(s): Physics Department, Syracuse University

Primary Source(s) of Research Funding: Army Research Office

Contact: ivpechen@syr.edu, babyrd@syr.edu, kmanivan@syr.edu

Primary CNF Tools Used: ASML DUV Stepper, JEOL 6300, PT770 Plasma Etcher, Heidelberg DWL2000 Mask Writer

Abstract:

We fabricate and characterize superconducting fluxonium qubits, which are among the leading qubit candidates for scalable quantum computing processors. They possess very high (millisecond-long) characteristic times and large anharmonicity [1]. A comprehensive characterization of the different noise channels that affect fluxonia is required to devise appropriate mitigation strategies to enhance qubit performance for fault-tolerant operation. We aim to study the different extrinsic and intrinsic decoherence mechanisms that affect this qubit. In particular, we perform experiments to understand the quasiparticle effects in fluxonia.

Summary of Research:

Superconducting quantum systems have emerged as one of the leading platforms for quantum computing. Josephson tunnel junctions are the backbone of these superconducting qubits, providing the required anharmonicity. A fluxonium qubit consists of a small Josephson junction connected to two large capacitor pads and a chain of Josephson junctions acting as a large inductor [2].

An external magnetic flux is applied to tune the properties of this qubit. At the sweet spot, when a half-integer superconducting flux quantum threads the loop, the qubit exhibits a very high coherence, large anharmonicity, and is protected from flux noise decoherence.

The SEM image of our fluxonium qubit fabricated at CNF is shown in Figure 1a. The two niobium capacitor pads ($40 \mu\text{m} \times 80 \mu\text{m}$ each) set the capacitive energy scale $E_C/h \sim 1.31$ GHz. The Al/AIOx/Al small Josephson junction ($90 \text{ nm} \times 100 \text{ nm}$) between the pads determines the Josephson energy $E_J/h \sim 1.29$ GHz. The array of 130 Josephson junctions ($1.3 \mu\text{m} \times 0.1 \mu\text{m}$ each) to the immediate right of the pads is associated with the inductive energy $E_L/h \sim 0.21$ GHz. In the multistep

fabrication process, we utilized photolithography and electron-beam lithography tools at CNF, and an electron-beam evaporator and sputtering system at Syracuse University. The flux bias line can be seen in the right part of Figure 1a. Each qubit is capacitively coupled to a coplanar waveguide resonator, shown in the left part of Figure 1a, for dispersive readout of the qubit state. Figure 1b displays the injector Josephson junction, which can be brought to its resistive state to inject pair-breaking phonons and create quasiparticles at the qubit junctions [3].

The fabricated qubit is housed inside a sample box that sits on the 10 mK plate of a dilution refrigerator. Using the injector junction, we control the quasiparticle environment of the qubit to distinguish quasiparticle-induced effects from other decoherence channels. Figure 2 shows the exponential decay curves of the qubit T_1 measurement with (orange) and without (blue) a quasiparticle injection pulse. Compared to the baseline, we observe degradation in qubit energy relaxation time when the quasiparticle density at the qubit is elevated. Figure 3 shows the qubit T_1 as a function of external flux in three different situations: without injection, $2 \mu\text{s}$ injection, and $4 \mu\text{s}$ injection, illustrating a reduction in T_1 with injection. In the near future, we plan to study the effect of design variations in device geometry on inferred quasiparticle densities in the small and array junctions of fluxonia.

References:

- [1] A. Somoroff, et al. Phys. Rev. Lett. 130, 267001 (2023). <https://doi.org/10.1103/PhysRevLett.130.267001>.
- [2] L. Nguyen, et al. Phys. Rev. X 9, 041041 (2019). <https://doi.org/10.1103/PhysRevX.9.041041>.
- [3] V. Iaia, et al. Nature Communications, 13, 6425 (2022). <https://doi.org/10.1038/s41467-022-33997-0>.

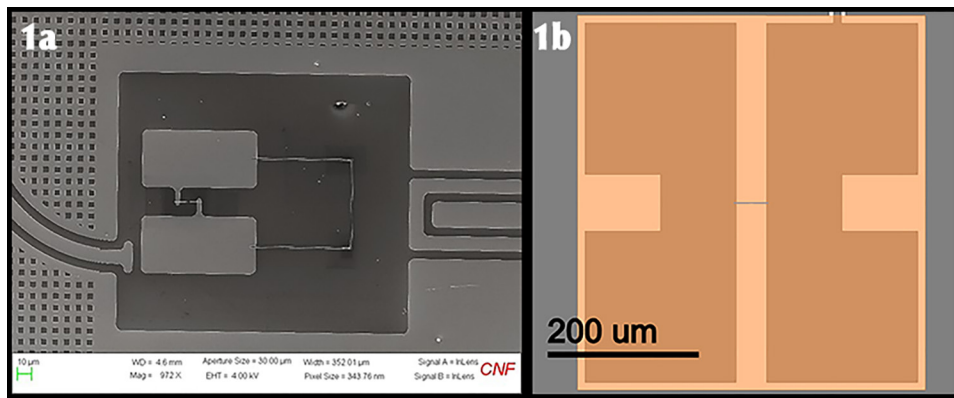


Figure 1: (a) SEM image of the fluxonium qubit showing the capacitor pads, single Josephson junction, and the chain of Josephson junctions. (b) Injector Josephson junction.

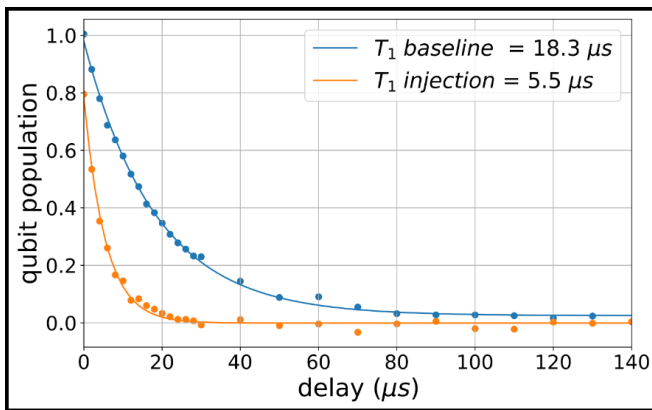


Figure 2: T_1 traces measured at $\Phi_{ext} = 0.0 \Phi_0$ for the baseline and injection cases.

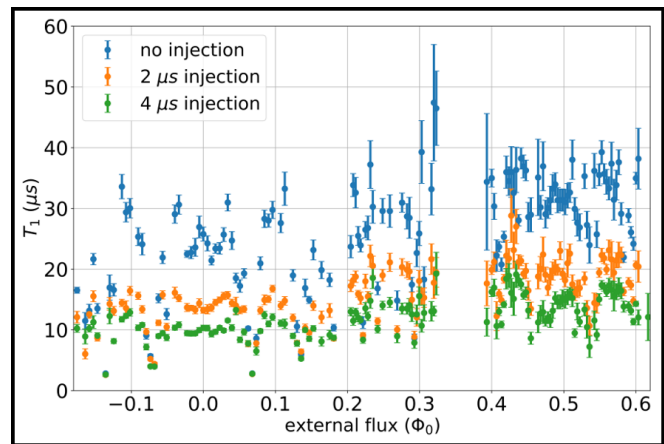


Figure 3: T_1 versus external flux for a fluxonium qubit measured in three cases: baseline, with 2 μ s injection pulse length, and with 4 μ s injection pulse length.

Probing Two-Dimensional Van der Waal Heterostructure and Height Characterization

CNF Project Number: 3098-23

Principal Investigator(s): Pankaj K. Jha

User(s): Jagi Rout

Affiliation(s): Department of Electrical Engineering and Computer Science (EECS), Syracuse University

Primary Source(s) of Research Funding: Syracuse University EECS Startup Funds

Contact: pkjha@syr.edu, jarout@syr.edu

Research Group Website: <https://qutechlab.syr.edu/>

Primary CNF Tools Used: Heidelberg Mask Writer - DWL2000, AFM Veeco Icon, DWL2000, Angstrom Evaporator, Odd and Even Hour Evaporator

Abstract:

This study describes a method for creating metal probes on Si/SiO₂ substrates. These probes are important for making measurements on superconducting 2D flakes in order to understand the transport properties of our superconductor and determine the critical current specific to our material. The fabrication process involves depositing metal layers precisely using techniques such as photolithography and electron beam evaporation. We optimized key parameters including substrate preparation, metal deposition rates, and patterning resolution to produce high-quality metal probes with excellent electrical and mechanical properties. The resulting metal probes show superior conductivity, durability, and adhesion to the Si/SiO₂ substrates. This work shows that the proposed fabrication method is feasible and scalable, offering potential for developing high-performance devices in microelectronics and nanotechnology.

Summary of Research:

Atomic Force Microscopy (AFM) is a widely used technique for measuring the thickness of two-dimensional (2D) materials down to a monolayer. Materials like graphene, molybdenum disulfide (MoS₂), and hexagonal boron nitride (hBN) have unique electronic, optical, and mechanical properties that depend largely on their thickness. Accurate determination of material thickness is essential for understanding and utilizing these properties in various applications, including electronics, photonics, and sensing. In AFM, a sharp tip attached to a cantilever scan over the sample surface. As the tip interacts with the sample, forces between the tip and the sample cause the cantilever to deflect. These deflections are measured by a laser beam reflected off the cantilever

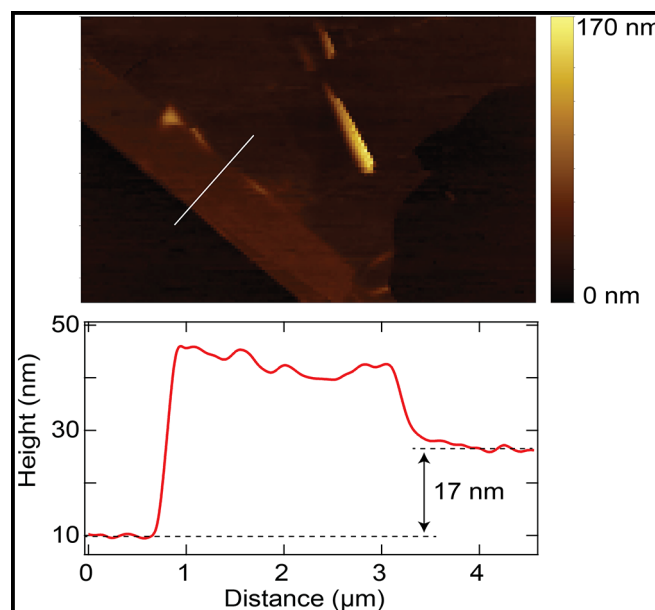


Figure 1: AFM study gives a thickness of 17.0 nm which corresponds to .28 layers [4].

onto a photodetector. By maintaining a constant force (contact mode) or distance (tapping mode) between the tip and the sample, AFM can generate high-resolution topographic images of the sample surface.

The sample needs to be meticulously prepared in order to measure the thickness of 2D material flakes using AFM. This process usually entails separating the 2D material from a larger crystal onto a substrate, commonly silicon with a silicon dioxide (Si/SiO₂) layer. The flatness and cleanliness of the substrate are crucial for precise measurements.

After preparing the sample, we use AFM to scan the surface and generate a topographic image. We can then

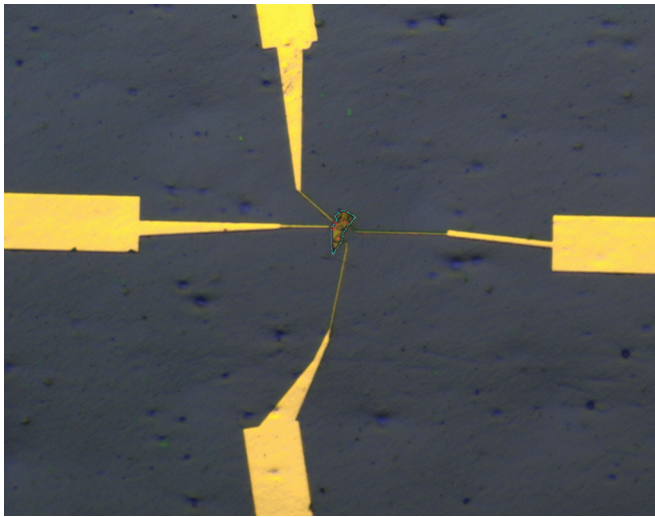


Figure 2: Ti/ Au contacts fabricated to probe superconducting flake Fe(Te,Se).

analyze the height profile of the image to determine the thickness of the 2D material flakes. The thickness is measured by comparing the height difference between the flake and the surrounding substrate. To ensure accurate measurements, it's important to select an area of the substrate adjacent to the flake as a reference point.

The critical current defines the operational limits of superconducting devices [4]. For applications in quantum computing and nanoelectronics, it is crucial to know the maximum current that the superconductor can handle without becoming resistive. Higher critical currents enable the development of more powerful and efficient superconducting circuits and devices.

Superconductors with higher transition temperatures can operate at more practical and potentially higher temperatures. This reduces the need for expensive cooling systems, which is especially important for developing superconducting electronics that can function at or near room temperature. This greatly enhances their practicality and cost-effectiveness.

By probing the critical current, researchers can identify the factors that limit superconducting performance. This

knowledge can be used to engineer materials with higher critical currents through strain engineering, doping, or creating heterostructures [3]. We used DWL66FS to write directly on Si/SiO₂ substrates, followed by metal deposition in the Angstrom evaporator. Ti/Au – 5/95 nm was deposited on the developed substrates exposed in DWL2000. Different feature sizes were experimented with while doing the direct writing, and a dose test was performed to optimize the energy required in the exposure. The bilayer photoresist spin coating option was preferred for the direct writing to minimize the undercut for the metal lift-off with acetone. Optimizing I_c can lead to the development of superior superconducting materials with tailored properties for specific applications [1,2].

Understanding the factors that influence the critical temperature (T_c) in 2D superconductors is important, as this understanding can help in the synthesis of new materials with higher transition temperatures. This may involve exploring new material systems, such as transition metal dichalcogenides (TMDs) or other layered compounds and manipulating their structure at the atomic level to enhance their superconducting properties [4].

We will work on etching our material to create nanostrips and study its electrical and optical properties.

References:

- [1] Qiu, G., Yang, HY., Hu, L., et al. Emergent ferromagnetism with superconductivity in Fe(Te,Se) van der Waals Josephson junctions. *Nat Commun* 14, 6691 (2023).
- [2] Qiu, Gang, et al. "Concurrent Ferromagnetism and Superconductivity in Fe(Te,Se) van der Waals Josephson Junctions." arXiv preprint arXiv:2303.00966 (2023).
- [3] Lee J, Lee W, Kim GY, Choi YB, Park J, Jang S, Gu G, Choi SY, Cho GY, Lee GH, Lee HJ. Twisted van der Waals Josephson Junction Based on a High-Tc Superconductor. *Nano Lett.* 2021 Dec 22;21(24):10469-10477.
- [4] A. K. Pattanayak, et al. Temperature-Dependent Optical Constants of Nanometer-thin Flakes of Fe(Te,Se) Superconductor in the Visible and Near-Infrared Regime (Manuscript under communication).

Observation of Exciton Polariton Band Structure

CNF Project Number: 3114-23

Principal Investigator(s): Bo Zhen

User(s): Zhi Wang

Affiliation(s): Department of Physics and Astronomy, University of Pennsylvania

Primary Source(s) of Research Funding: DARPA, ONR, Sloan foundation

Contact: bozhen@sas.upenn.edu, zhiw@sas.upenn.edu

Research Group Website: <https://web.sas.upenn.edu/bozhen/>

Primary CNF Tools Used: Plasma Enhanced Chemical Vapor Deposition (PECVD), Chemical Mechanical Polishing

Abstract:

Exciton polaritons are hybrid light-matter quasi-particles formed by the strong coupling between excitons (electron-hole pairs) in semiconductor materials and photons in photonic structures, such as cavity or photonic crystal (PhC) slabs. In our project, we want to observe polaritonic bands using molybdenum diselenide (MoSe_2) monolayer and PhC slab.

The PhC slabs we used are square lattices in silicon nitride layer. The square lattice consisted of air cylinder holes that were fabricated by etching the silicon nitride layer and later filled by plasma enhanced chemical vapor deposition (PECVD) TEOS oxide left a unflatten surface. To avoid the influence to monolayer caused by unflatten surface of PhC slab, chemical mechanical polishing (CMP) is needed.

Summary of Research:

To realize strong coupling, the coupling strength should be far greater than the linewidth of excitonic resonance and the linewidth of photonic resonance. Narrow linewidth of photonic resonance is easier to achieve compared to excitonic resonance. Therefore, a narrower linewidth of excitonic resonance is preferred in our experiment. The linewidth of excitons in MoSe_2 monolayer is easily affected by surrounding dielectric environment. People usually encapsulate the monolayer with hBN flakes, which have atomically flat surface to reduce the inhomogeneous broadening [1.] However, it's not doable for us now because the lateral size of PhC slabs is at least larger than $100 \mu\text{m}$ for observing a good band in experiment, and it is difficult to get very large and high quality hBN thin flakes by mechanical exfoliation. Also, large size MoSe_2 monolayers cannot be obtained by mechanical exfoliation. Good thing is that recently people can use gold exfoliation to get millimeter scale monolayers [2]. And dodecanal encapsulation method is used to make the gold exfoliated monolayer more intrinsic [3]. We are using these dodecanal encapsulated and gold exfoliated MoSe_2 monolayers in our devices.

Conclusions and Future Steps:

We already used PECVD TEOS to fill the air cylinder holes very well without voids. However, CMP process needs some improvements to get flat surface. And we already made some devices (Figure 1) but haven't observe polaritonic bands due to the unsuccessful CMP process which left unflatten surface and influenced the linewidth of excitonic resonance.

We will continue to improve CMP process and hopefully we will get some good data soon.

References:

- [1] F. Cadiz, et al., Excitonic Linewidth Approaching the Homogeneous Limit in MoS_2 -Based van der Waals Heterostructures. *Phys. Rev. X* 7, 021026 (2017).
- [2] Li, Q., et al. Macroscopic transition metal dichalcogenides monolayers with uniformly high optical quality. *Nat Commun* 14, 1837 (2023).
- [3] Liu, F., et al. Disassembling 2D van der Waals crystals into macroscopic monolayers and reassembling into artificial lattices. *Science* 367, 903-906 (2020).

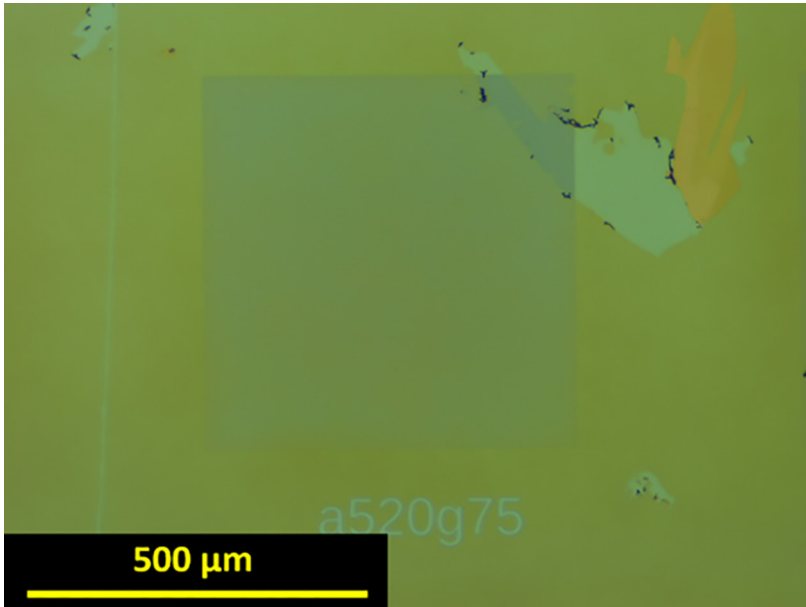


Figure 1: Dodecanal encapsulated MoSe_2 monolayer on a square lattice PhC slab.

Using Photolithography to Mass- Produce Rings of Controlled Size

CNF Project Number: 3123-23

Principal Investigator(s): Sarah Hormozi

User(s): Jonathan Lalieu

Affiliation(s): Smith School of Chemical and Biomolecular Engineering, Cornell University

Primary Source(s) of Research Funding: National Science Foundation

Contact: hormozi@cornell.edu, jkl227@cornell.edu

Research Group Website: <https://hormozi.cbe.cornell.edu/>

Primary CNF Tools Used: Heidelberg DWL2000, GCA AS200 i-line Stepper

Abstract:

The CNF user of the project trained on photolithography tools. We established that photolithography of SU-8 was an acceptable process to achieve our end goal of mass-producing rings of controlled size and aspect ratio, above ten micrometers, to use in rheology experiments of dense suspensions. We refined a recipe for the proper spinning, exposure and collection of said rings. We started the mass-production of one size of rings, that we have been able to use in rheology experiments. These experiments showed that, as we expected, the high aspect-ratio of these shapes induced a large additional stress in the rheology of the suspension, in the form of a rolling resistance in the contact between particles.

Summary of Research:

Our research focuses on the rheology of dense suspension, and more specifically on the role of rolling friction between particles. This rolling friction is purely geometrical [1], so we decided to focus on square cross-section ring-shaped particles because of their high symmetry. The rolling friction is then controlled by the aspect ratio between the thickness of the ring and its outer diameter. With rings, a large rolling friction coefficient can be achieved, which in turn will induce a large change in the jamming solid volume fraction for a contact-driven flow of a suspension [2,3].

We first prepared a photolithography mask with the Heidelberg DWL2000 mask writer that had rings of multiple sizes and aspect ratios to test the range of shape we could achieve. We spun SU-8 10 on 100 mm silicon wafers and refined the spinning speed to achieve a reproducible thickness of $20\ \mu\text{m}$, homogeneous on the wafer with a relative variation under 2%. We then exposed the wafers using the GCA AS200 i-line Stepper. We adjusted the exposure procedure to obtain polymerized devices of a good quality, both in

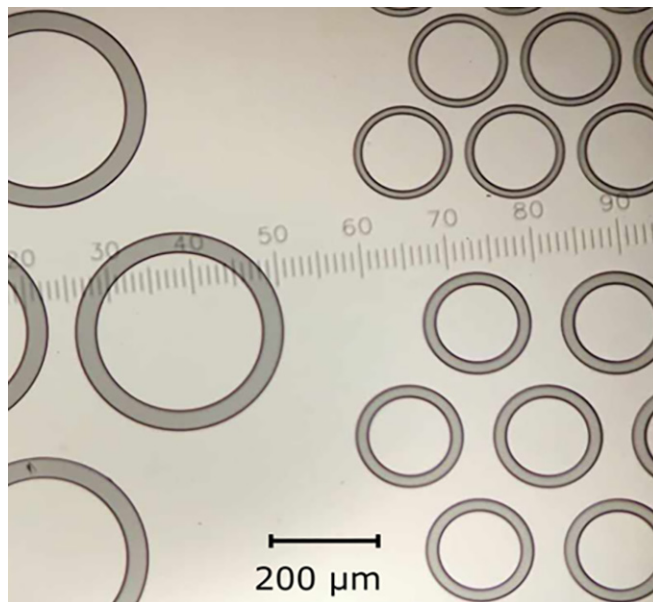


Figure 1: View of SU-8 rings on a wafer through a microscope, with two different diameters and aspect ratios.

adequation with their size on the mask and with large enough stiffness, as shown on Figure 1.

We then moved on to one specific size of rings for the mass-producing: rings of an outer diameter of $200\ \mu\text{m}$ and a thickness of $20\ \mu\text{m}$. This aspect ratio of 10 is directly proportional to the rolling friction coefficient and translates to a rolling friction coefficient of 5, much higher than the sliding friction coefficient. With this, we expect the rolling friction to be dominant in the rheology of dense suspensions with a large contribution from the contacts between particles. Our objective was to produce a few millions of these rings, and we managed to produce 50.000 per wafer. The main difficulty has been the ability to collect the rings and lift them off the wafers. We found that adding a layer of Omni-Coat before spinning SU-8, then hard baking the rings at 190°C after developing, and shaving the wafers with a sharp razor blade in a

water bath allowed us to collect most of them without undermining their structural integrity (Figure 2).

We just started doing rheology experiments using this batch of rings in a somewhat dense regime. The preliminary results show that for high shear-rates almost no contacts between particles are established, and we retrieve usual rheological behavior for suspension in the divergence of the viscosity with respect to the solid volume fraction. However, at low shear-rates the flow is mostly contact-driven, and we see the appearance of yield stresses at volume fraction much lower than what is usually seen for suspensions of spheres (Figure 3), as we expected when we settled on the ring-shape for the particles. Figure 2 also shows that the rings tend to align with each other, while having their main axis perpendicular to the flow direction.

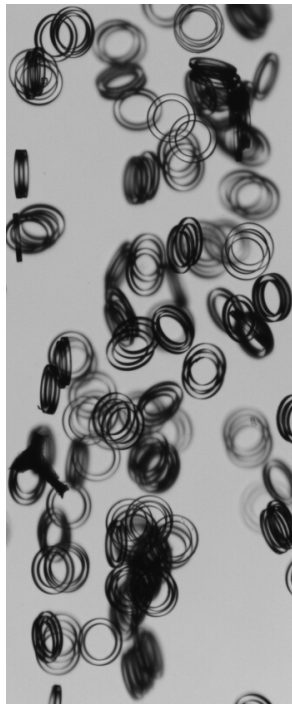


Figure 2: Photo captured of a flowing suspension made using SU-8 rings. The flow is in the downwards direction.

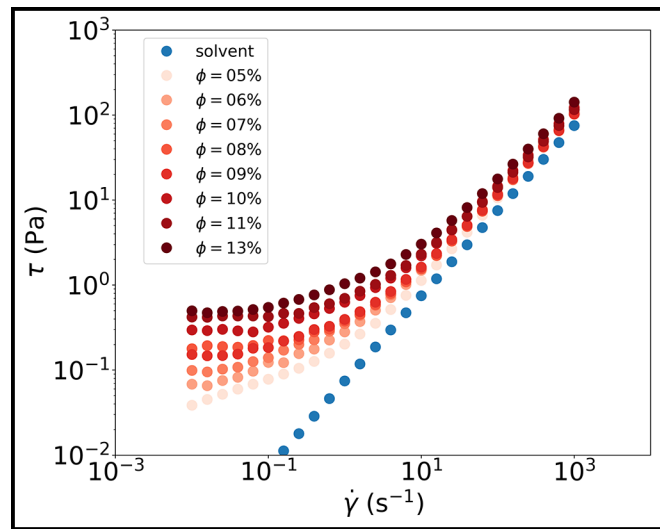


Figure 3: Shear stress as a function of shear-rate for different volume fraction, compared to the solvent alone.

References:

- [1] Agarwal, et al. (2021). Rolling friction measurement of slightly non-spherical particles using direct experiments and image analysis. *Granular Matter*, 23(3), 60.
- [2] Singh, et al. (2020). Shear thickening and jamming of dense suspensions: the “roll” of friction. *Physical Review Letters*, 124(24), 248005.
- [3] d’Ambrosio, et al. (2023). The role of rolling resistance in the rheology of wizarding quidditch ball suspensions. *Journal of Fluid Mechanics*, 974, A36.

Fabrication of Superconducting Resonators on hBN Thin Films

CNF Summer Student: River Chen

**Student Affiliation: Materials Science and Engineering,
University of Illinois Urbana-Champaign**

Summer Program(s): 2024 Cornell NanoScale Facility Research Experience for Undergraduates (CNF REU) Program

Principal Investigator(s): Professor Zhiting Tian, Sibley School of Mechanical and Aerospace Engineering, Cornell

Mentor(s): Joyce Christiansen-Salameh, Sibley School of Mechanical and Aerospace Engineering, Cornell University

Primary Source(s) of Research Funding: National Science Foundation under Grant No. NNCI-2025233;

AFOSR Award Number FA9550-22-1-0177

Contact: riveryc2@illinois.edu, zt223@cornell.edu, jc3496@cornell.edu

Summer Program Website(s): <https://cnf.cornell.edu/education/reu/2024>, <https://ztgroup.org/>

Primary CNF Tools Used: AJA Sputter 1 and 2, ABM Contact Aligner, Plasma-Therm 770 Etcher

Abstract:

Studying loss in superconducting devices is essential for high coherence quantum devices. Dielectric loss at the metal-substrate interface is a significant contributor to overall loss [1], which is why methods to study this important factor have been developed [2,3]. Hexagonal boron nitride (hBN) is a 2D material with several applicable properties, including low dielectric loss, chemical stability, and atomically flat surfaces free of dangling bonds, properties that make it an attractive material for integration into superconducting circuits [4]. In this research we employed a coplanar waveguide resonator design that is sensitive to dielectric loss at the metal substrate interface, comparing a “control” niobium (Nb)-on-sapphire resonator and an Nb-on-hBN-on-sapphire resonator.

Summary of Research:

Superconducting resonators are used to characterize materials loss in superconducting quantum computers [5]. The chip design used in this research implements eight multiplexed quarter wave resonators inductively coupled to a feedline with tapered bond pads as shown in Figure 1a. Areas where metal is removed are shown in orange, and metallized areas are shown in white. This design allows for 1:1 comparisons of dielectric losses at the metal substrate interface [2].

Any given resonator, as visible in Figure 1c, exhibited a gap width g of $3\ \mu\text{m}$ and conductor width s of $6\ \mu\text{m}$. This was also true for the feedline, and we qualified the resolution of our device features throughout our process development based on these metrics.

The original design, shown in Figure 1a, supports a 7.5×7.5 mm device size, and we were fabricating on 10

$\times 10$ mm sapphire substrates. Upon completion of our devices, they would be brought to a controlled facility which supports a 6×6 mm chip testing platform. We shrunk the design and added a guideline box around the device for improved mask alignment, better centering the new 6×6 mm device design (Figure 1b).

All 10×10 mm chips were cleaned via sonication for 10 minutes each in acetone, IPA, and water.

Molecular Beam Epitaxy (MBE). The first step in our device fabrication process was the growth of high-quality BN thin films via MBE on our $\sim 500\ \mu\text{m}$ thick sapphire substrate. Figure 2(a) shows resonant high-energy electron diffraction pattern indicating epitaxial quality of hBN film, Figure 2(b) is a Raman spectra showing the sharp characteristic hBN peak, and Figure 2(c) displays an AFM map of the film surface.

Sputter Deposition. After verifying the quality of our 5 nm thick hBN film, $600\ \text{\AA}$ of Nb were sputtered at the default 400 Watts on an AJA Sputter Deposition tool. In Figure 3, on the left side column, TEM of the hBN -Nb interface is shown to be damaged by the high-power metal ion bombardment.

We found, as shown in Figure 3 on the right-side column, that a lower sputter power of 50 watts maintained a pristine hBN film surface. Using a P7 profilometer, we determined that a sputter time of 10 minutes at this lower power yielded a $161\ \text{\AA}$ thick layer of Nb. Therefore, a sputter time of 37.27 minutes or 2236.03 seconds would yield our desired $600\ \text{\AA}$ of metal.

We were also interested in later comparing aluminum (Al) on sapphire and Al on hBN on sapphire resonators, so we also sputtered Al at 50 W for 10 minutes. Again, we used profilometry to determine an experimental

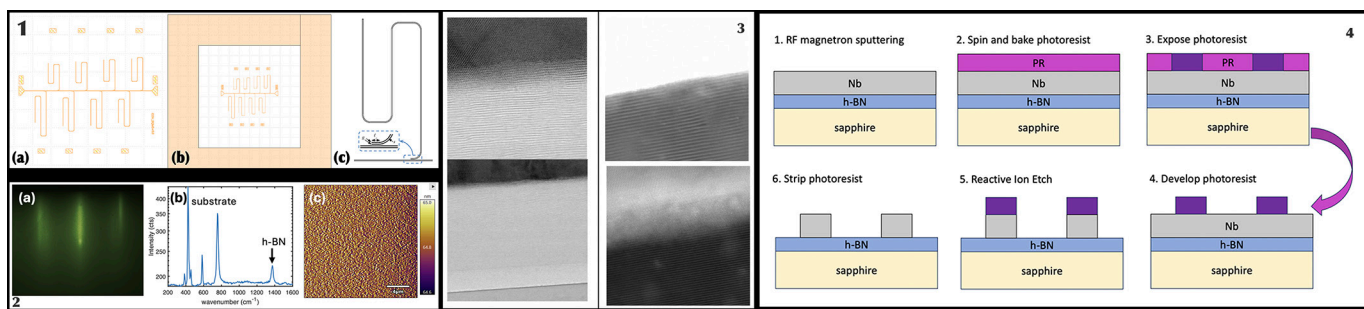


Figure 1: Device mask design. (a) Original 7.5 x 7.5 mm design. (b) Modified 6 x 6 mm design with border for alignment. (c) A single superconducting resonator with gap width g and conductor width s . Diagram from Kopas, et al. [2]. Figure 2: (a) Electron diffraction pattern, (b) Raman spectra, and (c) AFM map of hBN thin film. Figure 3: TEM of Nb sputter at 400W (left) and 50W (right) on hBN thin film. Figure 4: Complete fabrication process.

average of 265Å of sputtered Al through the 10-minute period.

Photolithography. We sputtered 60 nm Nb onto several 10 x 10 mm sapphire substrates in order to test and establish our photolithography process.

S1805 photoresist spun at 4000 rpm for 60 seconds yielded an average thickness of 500 nm. Our several resist-coated substrates were subsequently exposed at varying doses on the ABM Contact Aligner to determine the exposure time for optimal feature definition. The best exposure time was found to be 1.6 seconds.

Reactive Ion Etch (RIE). It was predicted that the RIE Cl₂ etch chemistry on the Plasma-Therm 770 etcher could also affect the hBN thin film upon etching through the Nb. Thus, the first step to mitigate this issue was to accurately determine the Nb etch rate. After 36.7 seconds of etching our device pattern, we found that 36.8 nm of Niobium was etched and 36.57 nm of resist was etched. These measurements establish a 1:1 etch selectivity and 1nm/second etch rate.

A similar process was performed on the hBN where a pattern was etched for 15 seconds. We determined that the hBN thin film experienced an etch rate of ~ 1 nm/3 seconds after performing atomic force microscopy on a sample.

Conclusions and Future Steps:

After establishing our etch process parameters, we would similarly verify the niobium was etched through by using a probe station to measure resistance between the gaps and the conductor, determining whether there is Nb in the gaps.

It has been shown that the superconducting transition temperature T_c of a metal can be affected by the substrate material [6]. We will observe this change using a Physical Property Measurement System, examining the change in resistance with varying extremely low temperatures.

As the pieces are required to conform to a 6 x 6 mm testing platform, they will be sent to DISCO laser dicing services.

Finally, the completed devices will be wirebonded and tested in a facility equipped with a He dilution fridge.

Acknowledgements:

I would like to thank Cornell University, NNCI, and the NSF for funding this research via grant NNCI-2025233. Thank you to Joyce, Professor Zhiting Tian, and the staff at the Cornell NanoScale Facility for all the guidance and support throughout this project.

References:

- [1] C. R. H. McRae, H. Wang, J. Gao, M. R. Vissers, T. Brecht, A. Dunsworth, D. P. Pappas, J. Mutus, *Rev. Sci. Instrum.* 1 September 2020; 91 (9): 091101. <https://doi.org/10.1063/5.0017378>.
- [2] Kopas, et al. arXiv 14 Apr 2022. <https://arxiv.org/abs/2204.07202>.
- [3] Woods, W., Calusine, G., Melville, A., Sevi, A., Golden, E., Kim, D. K. Oliver, W. D. (2019). *Phys. Rev. Appl.*, 12, 014012. doi:10.1103/PhysRevApplied.12.014012.
- [4] Wang, J.J., Yamoah, M.A., Li, Q., et al. *Nat. Mater.* 21, 398–403 (2022). <https://doi.org/10.1038/s41563-021-01187-w>.
- [5] C. McRae, H. Wang, J. Gao, M. R. Vissers, T. Brecht, A. Dunsworth, D. P. Pappas, and J. Mutus. *Review of Scientific Instruments* 91, 091101 (2020).
- [6] J. Liu, J. Li, T. Li, T. Li, W. Wu and W. Chen. *IEEE Transactions on Applied Superconductivity*, vol. 19, no. 3, pp. 245-248, June 2009, doi: 10.1109/TASC.2009.2019233.

Fabrication and Characterization of High-Resistivity Silicon Interposers

CNF Summer Student: Gannon Lemaster

Student Affiliation: Electrical Engineering, Brown University

Summer Program(s): 2024 Cornell NanoScale Facility Research Experience for Undergraduates (CNF REU) Program

Principal Investigator(s): James Hwang, School of Electrical and Computer Engineering, Department of Materials Science and Engineering; Cornell University

Mentor(s): Xiaopeng Wang, Yunjiang Ding, School of Electrical and Computer Engineering, Department of Materials Science and Engineering; Cornell University

Primary Source(s) of Research Funding: National Science Foundation under Grant No. NNCI-2025233

Contact: gannon_lemaster@brown.edu, jch263@cornell.edu, xw569@cornell.edu, yd439@cornell.edu

Summer Program Website: <https://cnf.cornell.edu/education/reu/2024>

Primary CNF Tools Used: ABM Contact Aligner, SÜSS Contact Aligner, AJA Sputter 1 and 2, AJA Ion Mill, Unaxis 770 Deep Si Etcher, Zeiss Ultra SEM, Zygo Optical Profilometer, Glen 1000 Resist Strip, Veeco Savannah ALD, DC Probe Station, Microwave Small-Signal Probe Station

Abstract:

A recent focus of advancement in semiconductor technology involves the heterogeneous integration of chiplets on an interposer. Typically, the interposer is made of polymers, glass, or doped silicon. This work explores high-resistivity (HR, $\rho > 1 \text{ k}\Omega\cdot\text{cm}$) silicon interposers fabricated at the Cornell NanoScale Facility for millimeter-wave applications. The most critical process is the etching and metallization of through-silicon vias (TSVs). The cross-sectional geometry of a TSV is shown in Figure 1. Using aluminum oxide (Al_2O_3) as a backside hard mask and a frontside layer of titanium as an etch stop layer, $155 \mu\text{m}$ deep silicon etching was successfully carried out with the Unaxis 770 Deep Silicon Etcher using the SF₆/C₄F₈ Bosch Process. Subsequently, using an argon beam operating at 600 V and 295 mA with a vacuum of 10-8 torr, the frontside titanium layer was ion milled with a removal rate of 27 nm/s for $50 \mu\text{m}$ diameter TSVs. The TSVs were then metallized with a layer of platinum deposited using atomic layer deposition and sputtered titanium and aluminum, resulting in a series resistance of 2.5Ω . The TSVs were also patterned for RF characterization to form grounded coplanar waveguides (GCPWs). The GCPWs were probed up to 40 GHz, resulting in an insertion loss of 2 dB/mm and a return loss of 26 dB at 40 GHz.

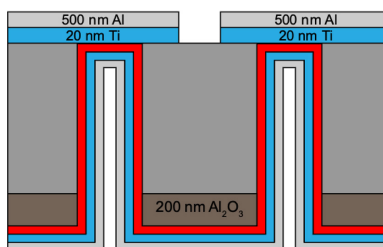


Figure 1: Cross-sectional geometry of through-silicon vias.

waveguides (SIWs) on silicon carbide and applying it to a doped silicon substrate. This process flow involved distinct frontside and backside processes: the frontside process produced structures necessary for interconnects, such as microstrip and coplanar transmission lines, while the backside process formed the geometry of the TSVs.

The electrical testing results obtained from this initial set of samples were quite poor, with TSVs exhibiting non-ohmic characteristics. It was hypothesized that this issue stemmed from inadequate etching through the frontside aluminum oxide or inadequate metallization of the TSVs. For future samples, the fabrication process was adjusted by varying the incident angle and duration of the ion milling process, as well as the thickness of the platinum seeding layer for TSV metallization by atomic layer deposition (ALD). These adjustments resulted in an ohmic IV curve but with a significantly high TSV resistance of 14 ohms. Etching through the frontside aluminum oxide hard mask layer proved time-consuming and inconsistent, leading to the decision to remove the layer entirely with future samples. Testing on these subsequent samples showed that Bosch etching through the silicon substrate and ion milling through the frontside titanium layer yielded better TSV resistance and uniformity. These samples were analyzed using the Microwave Small-Signal Probe Station at frequencies up to 40 GHz. A 10 dB/mm insertion loss was observed with a $2146 \mu\text{m}$ grounded coplanar waveguide (GCPW), with consistent results across various samples and GCPW lengths. After the electrical characterization,

Summary of Research:

The fabrication process began by adapting a previously verified method for creating substrate integrated

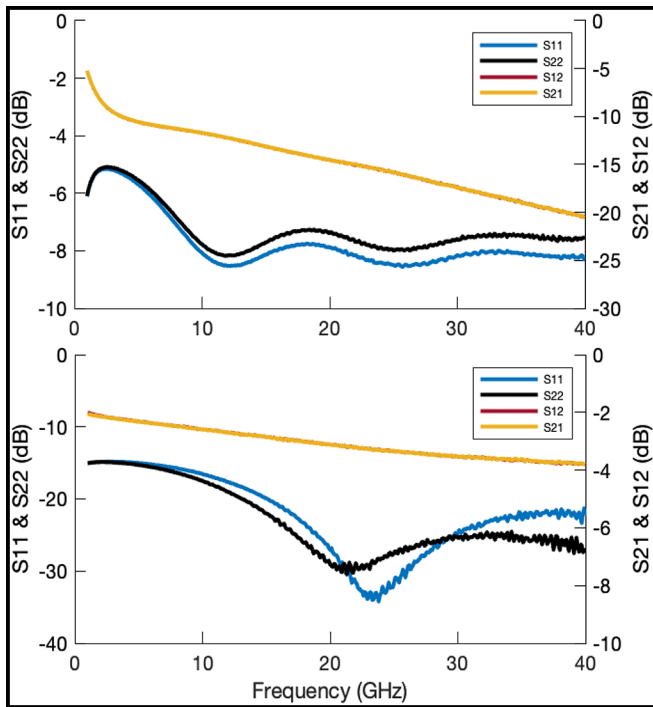


Figure 2: S-Parameters of 2146 μm GCPW test structures for doped silicon (above) and high-resistivity Si (below) up to 40 GHz.

the samples were cleaved to capture cross-sectional scanning electron microscope (SEM) images. The TSV dimensions observed in the SEM images were consistent with optical profilometer images taken earlier in the fabrication process and confirmed the successful sputtering of aluminum. This finalized procedure was then transferred from a doped silicon substrate to a high-resistivity silicon substrate. Electrical characterization of this sample yielded a TSV resistance of 2.5 ohms, with subsequent measurements using a 2146 μm GCPW indicating an insertion loss of 2 dB/mm and a return loss of 26 dB.

Conclusions and Future Steps:

A complete process flow for the fabrication of high-quality TSVs for use on doped silicon and high-resistivity silicon interposers has been developed and verified. However, a TSV resistance of less than 1 ohm remains to be achieved for a high-resistivity silicon sample. Moreover, the insertion loss of the fabricated high-resistivity silicon GCPWs is too high, making them unsuitable for effective use within their intended frequency range, the

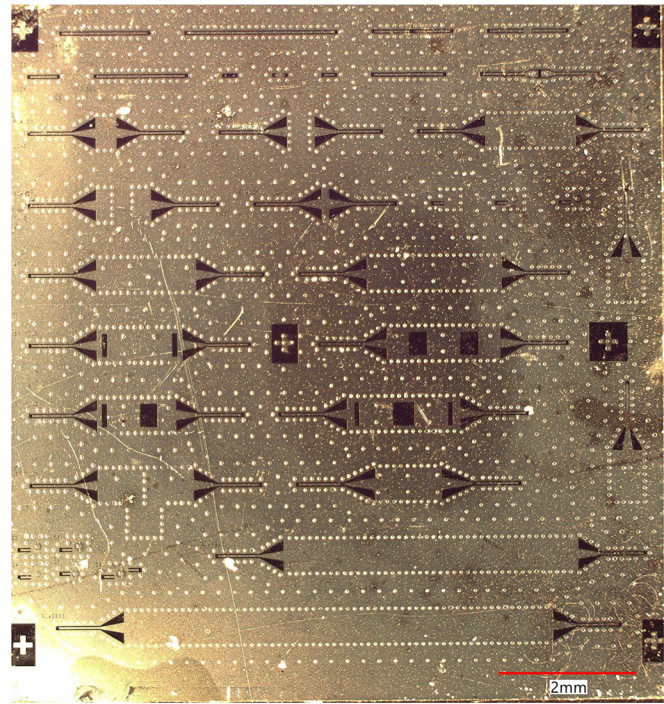


Figure 3: High-resistivity silicon sample, displaying frontside interconnect structures and backside TSVs.

D-band (110-170 GHz). It is theorized that this is due to an insufficient amount of frontside aluminum, which was sputtered at a thinner thickness than anticipated.

Acknowledgments:

I would like to acknowledge the National Science Foundation (NSF) grant no. NNCI-2025233, the National Nanotechnology Coordinated Infrastructure (NNCI), and the Cornell NanoScale Facility for funding and curating the Research Experiences for Undergraduates (CNF REU) opportunity. Additionally, I would like to acknowledge and thank Yunjiang Ding, Xiaopeng Wang, and James Hwang for their invaluable guidance and support.

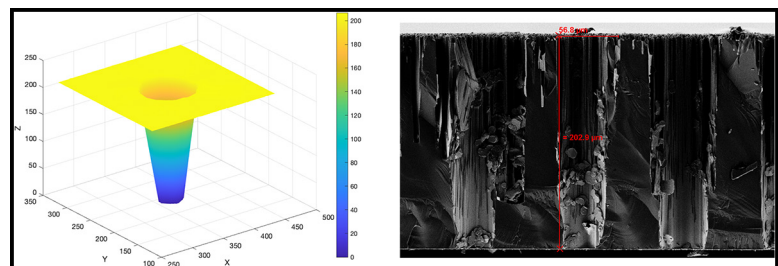


Figure 4: Optical profilometry image of TSV after through-substrate etching (left) and cross-sectional SEM image of TSV (right).

Atomic Layer Deposition of High-K Dielectrics

CNF Summer Student: Sarah Levine

Student Affiliation: Civil Engineering, Worcester Polytechnic Institute

Summer Program(s): 2024 Xing Army Educational Outreach Program (AEOP),

2024 Cornell NanoScale Facility Research Experience for Undergraduates (CNF REU) Program

Principal Investigator(s): Professor Grace (Huili) Xing, Electrical and Computer Engineering, Cornell University

Mentor(s): Jeremy Clark, Cornell NanoScale Science and Technology Facility, Cornell University

Primary Source(s) of Research Funding: 2024 Xing Army Educational Outreach Program (AEOP),

National Science Foundation under Grant No. NNCI-2025233

Contact: sjlevine@wpi.edu, grace.xing@cornell.edu, clark@cnf.conrell.edu

Summer Program Website: <https://cnf.cornell.edu/education/reu/2024>

Primary CNF Tools Used: Arradiance ALD Gemstar-6, AJA Sputter -2, SC4500 Odd-Hour Evaporator,

Woollam RC2 Spectroscopic Ellipsometer, Hamatech Hot Piranha, Oxford 81/82 Etcher,

Everbeing EB-6 Probe Station with Keithley SMU, Rapid Thermal Anneal -AG Associates Model 610

Abstract:

To keep making the world's most powerful central processing units faster and more energy-efficient dielectrics are used to increase the capacitance of these devices. Conventional HfO₂-based high K dielectrics gate stacks cannot produce such a small effective oxide thickness and the consequent high capacitance without removing the interfacial SiO₂, which negatively impacts electron transport and gate leakage current. The superlattice gate stacks offer much-reduced leakage current and zero mobility deterioration as they lack the need for this kind of scavenging. The gate stacks are used in GaN transistors for power and communication, the existing dielectric in these transistors causes significant leakage and damages the underlying material. Ultrathin ferroic HfO₂-ZrO₂ multilayers, stabilized with competing ferroelectric–antiferroelectric order, offer a new method for advanced gate oxide stacks in electronic devices beyond traditional HfO₂-based high-dielectric-constant materials. The project aims to develop a process to deposit the high-K HfO₂/ZrO₂superlattices whose new layers will help lower charge leakage. Atomic Layer Deposition (ALD) is used to build up the superlattice, we use ALD because it provides uniform and precisely tuned thickness, then through various depositing methods such as sputtering and e-beam evaporation aluminum was deposited through a capacitor shadow mask and then annealed through rapid thermal processing. The fabricated devices were characterized on a DC probe station and graphed for Capacitance -Voltage (C-V), to solve for the dielectric constant, also known as K, and also examine other material parameters such as defect density. The project works towards the smallest leakage at the smallest equivalent oxide thickness.

Summary of Research:

In capacitors, a tried and tested industry dielectric is SiO₂, which has a dielectric constant of 3.9. HfO₂ has become a forefront dielectric in the past few years with a dielectric constant between 18 and 25. The issue with this is that the smaller you make these capacitors, the higher the chance for electron leakage. The proposed HfO₂/ZrO₂ superlattice has new added layers that should help prevent such leakage and allow for a higher dielectric constant to be obtained. The goal is to be able to achieve smaller equivalent oxide thicknesses and keep leakage down.

The main part of this research has been to develop a process flow to deposit these high K dielectric HfO₂/ZrO₂superlattice devices. The first step in this process was to perform a hot piranha etch to get rid of any lingering organic material on the N-type silicon substrate. Next was to deposit the superlattice on the silicon substrate through Atomic Layer Deposition, which allowed for layer-by-layer deposition with increased control over thickness and composition at a relatively low growth temperature, which for this superlattice was 200°C. To determine the amount of loops used for each precursor ellipsometry was done to determine how much deposition was laid down with 300 loops. It was determined that 11 loops of ZrO₂ would be about equivalent to 1.2 nm whereas 3 loops of HfO₂ is about equivalent to 0.4 nm.

The next step in the process was to deposit aluminum and metalize the capacitor. This was done either through sputtering or e-beam evaporation. The sputtering while giving an incredibly uniform coating emits x-rays as a consequence of using plasma which can damage the sample. The evaporator was unable to provide that

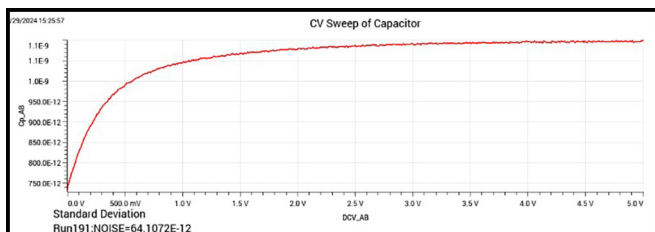


Figure 1: A CV sweep of a HfO₂ capacitor of voltage over capacitance in farads.

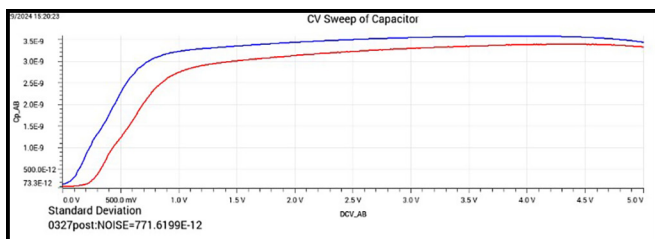


Figure 2: A CV Sweep of the capacitor of voltage over capacitance in farads. These graphs were used to determine the *K* dielectric of the capacitor. This particular sweep is of the Period x4 made on the evaporator, the red line is the pre-annealed data and the blue is the post-annealed.

same guaranteed uniformity, but aluminum has such a relatively low evaporation rate that the silicon substrate isn't as harmed by any x-rays emitted from e-beam evaporation. When depositing the superlattice residual deposition also ends up on the back side of the wafer, to remove this reactive ion etching, specifically a CF₄ etch, is used. To protect the capacitors, a clean silicon wafer was placed over the capacitors to not allow any CF₄ to etch off the needed dielectric. Aluminum is then deposited onto the back to improve overall contact resistance and thermal conduction.

The final step in the fabrication process is to perform rapid thermal annealing (RTA) using N₂ at 200°C for one minute. Characterization of these capacitors was done on a DC probe station and a Capacitance-Voltage (C-V) test was conducted. To test the C-V sweep and confirm our equation,

$$C = \frac{k\epsilon_0 A}{d}$$

solving for *k*, a sweep with HfO₂ as the dielectric was done resulting in pre-annealed data of 17.7. The graph for this data is shown in Figure 1, which is on the lower end of the expected dielectric constant range which confirmed the test being done.

Conclusions and Future Steps:

The data collected from the Capacitance-Voltage graphs, shown in Figure 3, showed the expected decrease in the dielectric constant as film thickness also decreased.

Period, Aluminum Deposition Method	Pre-Annealing Dielectric Constant	Post Annealing Dielectric Constant
x 1, Sputter	1.65	2.63
x 1, Evaporator	1.34	2.25
x 2, Sputter	1.13	2.83
x 2, Evaporator	3.37	3.25
x 4, Sputter	7.03	8.61
x 4, Evaporator	7.16	7.56
x 8, Sputter	11.30	11.12
x 8, Evaporator	11.27	9.66
x 12, Sputter	15.08	14.74
x 12, Evaporator	12.19	12.57

Figure 3, above: A chart of the different periods of pre-annealed and post-annealed dielectric constants. Figure 4, below: A picture of one of the wafers Levine fabricated through sputtering.

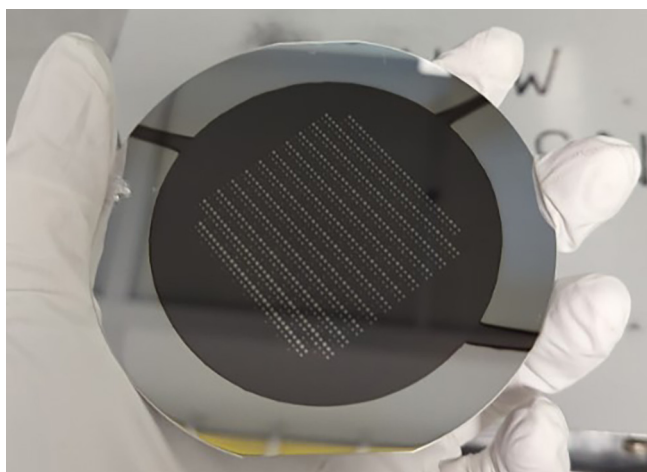


Figure 2 shows what a graph of pre and post-annealed data would look like for this C-V sweep. In the post-anneal data, it showed an increase in the dielectric constant for the thinner films after being annealed.

Future work on this project will be to take the superlattice and confirm the thicknesses through X-ray reflectivity (XRR) measurements and that will also ensure the ALD recipe is producing the film growth at the expected rate. Another step that could be taken to ensure the best dielectric constant is to etch the native oxide layer. Looking at higher annealing temperatures would be another variable that could increase the dielectric constant. Measuring the capacitors on different graphs such as doing a SMU-Sweep to characterize current versus voltage for leakage measurements.

Acknowledgements:

I would like to express my appreciation to my Principal Investigator Professor Grace (Huili) Xing, the Jena-Xing Group, and my mentor Jeremy Clark. This project would have been unsuccessful without their guidance. This work was performed at the CNF, an NNCI member supported by NSF Grant NNCI-2025233.

Investigating the Lateral Spreading of Vanadium-Based Ohmic Contacts

CNF Summer Student: Fabiana P. Mayol López

Student Affiliation: Natural Sciences. Ana G. Méndez University, Gurabo Campus

Summer Program(s): 2024 Cornell NanoScale Facility Research Experience for Undergraduates (CNF REU) Program

2024 CNF REU Principal Investigator(s): Prof. Huili “Grace” Xing, Department of MSE & ECE, Cornell University

2024 CNF REU Mentor(s): Joseph Dill, Department of AEP, Cornell University; Shivali Agrawal, Department of CBE, Cornell University; Xianzhi Wei, Department of MSE, Cornell University

Primary Source(s) of Research Funding: National Science Foundation under Grant No. NNCI-2025233

Contact: anapao73@outlook.com, grace.xing@cornell.edu, jed296@cornell.edu, sa2368@cornell.edu, xw694@cornell.edu

Summer Program Website: <https://cnf.cornell.edu/education/reu/2024>

Primary CNF Tools Used: SC4500 Odd-Hour Evaporator, Zeiss Supra Scanning Electron Microscope (SEM), Bruker Quantax 200 Energy Dispersive X-Ray Spectroscopy (EDS), GCA AS200 i-line Stepper, Glen 1000 Resist Strip, RTA-AG610b

Abstract:

Aluminum Gallium Nitride (AlGa_N) is a material of interest for the development of UV-emitting photonic devices. Vanadium-based metal stacks are a popular means of forming ohmic contacts to n-type AlGa_N. However, these metal stacks must be annealed to temperatures above 600°C [6] for VN to form during which the metals in the ohmic contact stack can spread laterally and short patterned devices. The aim of this study is to determine the annealing conditions that minimize the lateral spreading of V/Al/Ni/Au stacks and investigate the behavior of these stacks under annealing. Metal stacks were patterned on 8 x 8 mm silicon (Si) pieces and annealed for different temperatures and times. A “safe zone” of annealing conditions that didn’t short the devices was determined. The amount of spreading was determined from Scanning Electron Microscope (SEM) images of C-TLM structures. We also observed a “balling up” of the Ni under annealing, likely due to its high surface energy. This observation motivates switching Ni to a metal with a lower surface energy in future studies.

Summary of Research:

Background. Since the first realization of the GaN blue LED in 1993 [1], research attention has been devoted to AlGa_N-based light-emitting devices that would emit invisible UV light. Such devices would enable many novel technologies, including chemical-free sterilization of medical equipment and water purification [2]. One key challenge to this end is the formation of ohmic contacts to n-type AlGa_N. Several studies have achieved low resistance contacts using annealed V/Al/X/Au metal stacks [6,7]. When annealed in N₂, V

alloys with N to form VN on the surface, which has a work function of 3.55 [5]. The Al helps form donor-like N vacancies in the AlGa_N, and Au prevents oxidation and provides a soft surface for electrical probing. X is the “diffusion barrier” metal, usually V or Ni. However, annealing these metal stacks often leads to strange and undesirable metallurgical effects, such as the formation of Ni domains [7].

Methods. Annealed metal pads were fabricated on 8 x 8 mm Si pieces as follows:

1. Si pieces were cleaned in acetone, isopropyl alcohol (IPA), and deionized water for 5 minutes each with sonication to remove any organic contamination from the surface.
2. Pieces were spin-coated with AZ nLOF 2020 negative photoresist and baked.
3. Circular transmission line method (C-TLM) patterns were exposed using the GCA AS200 i-line Stepper, followed by a post-exposure bake.
4. The pattern was developed in 726 MIF developer for 30 sec.
5. An ozone descum was performed to remove all residual undeveloped photoresist.
6. A metal stack of 20nm of V, 80nm of Al, 40nm of Ni, and 100nm of Au was deposited by electron beam evaporation (see Figure 1).
7. Liftoff was performed by immersing the pieces in Microposit Remover 1165 and IPA with sonication.
8. Each sample was annealed in N₂ ambient. The anneal times and temperatures for each sample are shown in Figure 2a.

Results. Figures 2b and 2c show SEM images of a C-TLM structure with 0.8.μm spacing on samples 1 and

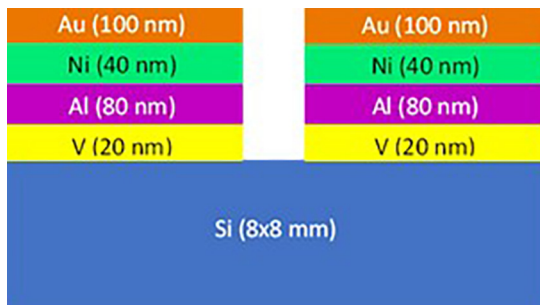


Figure 1: Cross-sectional view of sample.

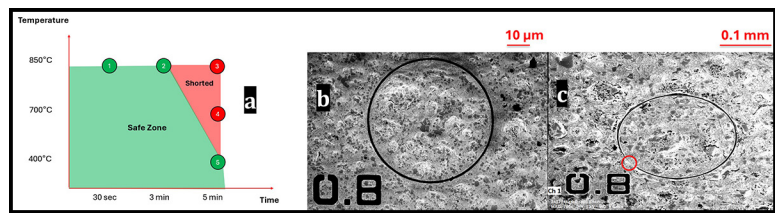


Figure 2: Plot of each annealed sample with temperature vs time annealed in (a). Post-anneal SEM images in (b) sample 1: 850°C, 30 seconds and (c) sample 3: 850°C, 5 minutes. Red circle indicates shorting in the C-TLM pattern.

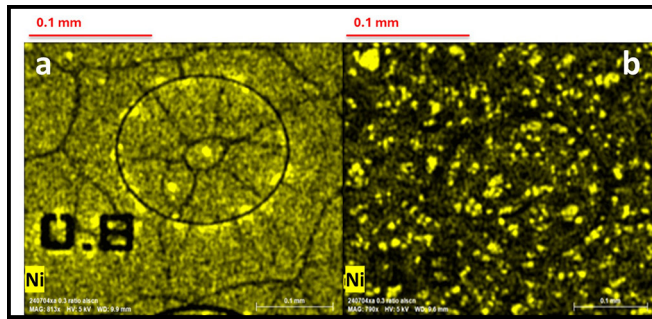


Figure 3: EDS map of Ni in (a) sample 5: 400°C, 5 minutes and (b) sample 3: 850°C, 5 minutes.

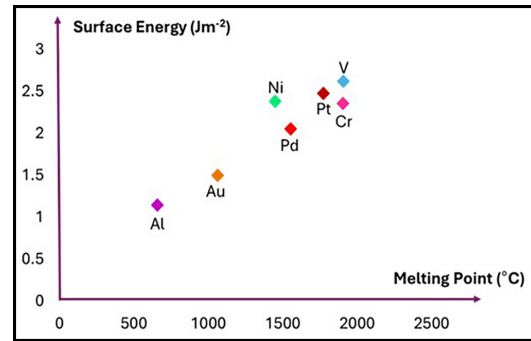


Figure 4: Plot of surface energy vs melting point. Values obtained from [4].

3, annealed at 850°C for 30 sec and 5 min, respectively. The red circle in 2c indicates a point where the C-TLM pad was shorted due to lateral spreading of the metal during annealing. The annealing conditions that did and didn't result in shorting of the 0.8.m pattern are summarized in Figure 2a. The annealing conditions for samples 1, 2, and 5 establish a “safe zone” in which annealing didn't cause shorting.

The annealed samples were imaged with Electron Dispersive X-Ray Spectroscopy (EDS) to investigate the motion of the constituent metals in the stack during annealing. As seen in Figure 3, Ni was observed to coalesce, forming domains that decreased in size with increasing anneal temperature. In sample 5, annealed at 400°C for 5 minutes, $\sim 40 \mu\text{m}$ -wide domains formed (see Figure 3a), and in sample 3, annealed at 850°C for 5 minutes, $\sim 5 \mu\text{m}$ -wide domains formed (see Figure 3b). This is likely a result of nickel's high surface energy.

Conclusions and Future Steps:

During annealing, a metal can minimize its surface energy by forming a spherical shape rather than remaining flat. These spheres will be tighter at higher temperatures to minimize the additional thermal free energy. We observe the initial stages of this in Figure 3a wherein the Ni begins forming wide domains, presenting a “cracked” appearance. Ni's tendency to ball up during annealing is used by Shi et al. to form Ni nanoparticles annealing sputtered Ni thin films [3].

Considering these findings, future ohmic contact stacks should utilize a diffusion barrier with a lower surface energy than Ni. The surface energies and melting points of V, Al, Ni, Au, and alternate diffusion barrier metals (Pd, Pt, Cr) are benchmarked in Figure 4. Of the candidate metals, Pd has the lowest surface energy. Future studies should also be conducted on AlGaN, rather than Si, such that the electrical performance of the ohmic contacts can be investigated in parallel with the metallurgical behavior under annealing.

Acknowledgements:

Special thanks to the Cornell NanoScale Science & Technology Facility Research Experience for Undergraduates (CNF REU) Program for hosting this internship. I would like to express my appreciation for the Jena-Xing Group, my PI Prof. Grace Xing, my mentors Joseph Dill, Xianzhi Wei, and Shivali Agrawal for their support and guidance.

References:

- [1] S. Nakamura, APL (1994).
- [2] H. Amano, Jour. of Phys D (2020).
- [3] Shi, Coatings, (2022).
- [4] Vitos, Surface Science (1998).
- [5] V. S. Fomenko, Handbook of Thermionic Properties (1966).
- [6] R. France, APL 90(6) (2007).
- [7] X. Guo, APL 124(23) (2024).

Effect of Temperature on Particle Morphology Polymerized via Initiated Chemical Vapor Deposition in Liquid Crystal

CNF Summer Student: Imrie Ross

Student Affiliation: Biochemical Engineering, University of Georgia

Summer Program(s): 2024 Cornell Robert Frederick Smith School of Chemical and Biomolecular Engineering FMRG: Cyber (CBE FMRG: Cyber) Summer Program, 2024 Cornell NanoScale Science & Technology Facility Research Experience for Undergraduates (CNF REU) Program

Principal Investigator(s): Dr. Nicholas Abbott, Dr. Rong Yang; Smith School of Chemical and Biomolecular Engineering, Cornell University

Mentor(s): Soumyamouli Pal, Shiqi Li; Smith School of Chemical and Biomolecular Engineering, Cornell University

Primary Source(s) of Research Funding: 2024 CBE FMRG: Cyber Summer Program, 2024 CNF REU Program via the National Science Foundation under Grant No. NNCI-2025233

Contact: icr32942@uga.edu, nla34@cornell.edu, ryang@cornell.edu, sp2476@cornell.edu, sl2869@cornell.edu

Summer Program Website: <https://cnf.cornell.edu/education/reu/2024>

Primary CNF Tool Used: Zeiss Supra Scanning Electron Microscope

Abstract:

The ability to create designed polymer particle shapes would greatly benefit many applications, including timed drug delivery and reconfigurable metamaterials because the polymer's intrinsic properties largely depend on the shape. Prior works from our research group have leveraged the use of an anisotropic medium, namely liquid crystals (LCs), as templates to direct the growth of polymer structures by initiated chemical vapor deposition (iCVD) [1]. In this work, we have successfully obtained a range of glycidyl methacrylate (GMA) and divinyl benzene (DVB) polymer morphologies in a one-step, one-pot polymerization process by iCVD in a nematic LC called E7 (a eutectic mixture of cyanobiphenyls). We established multiple substrate temperatures in a single polymerization run by leveraging a thermal gradient placed directly on a cooled reactor stage. A filament array above the stage radially heats the gradient, providing lower temperatures as the distance from the gradient to the filament increases. E7 has a nematic to isotropic phase transition temperature of $\sim 60^\circ\text{C}$, above which the orientational order of the LC mesogens no longer exists. We have investigated the effect of temperature on the rate of evaporation and phase change of the LC by utilizing a brightfield and cross-polarized optical microscope placed directly over the reactor for in-situ monitoring. Using a set of controls and experiments, we have mapped a set of reactor conditions where temperature solely influences the progression of particle morphology, allowing us to study how the morphology varies with temperature. These conditions limit the amount of evaporation and prevent isotropic phase change of the LC. Structural characterization using the Cornell NanoScale Facility Zeiss scanning electron microscope reveals the formation of different particle morphologies as a function of the various temperatures achieved.

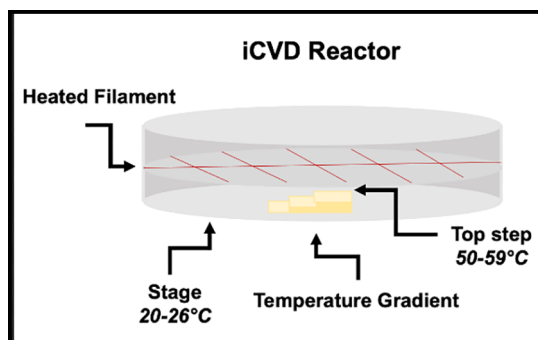


Figure 1: Schematic of the temperature gradient in the iCVD reactor.

Summary of Research:

Micro and nanoparticles are promising for future imaging, medical, and energy applications. The ability to synthesize and control the size and morphologies is crucial for utilizing these particles at an industrial scale. Initiated chemical vapor deposition (iCVD) is a promising technique for synthesizing nanoparticles since it allows for high control of continuous polymerization and provides multiple particle morphologies without external manipulation. We utilized liquid crystals (LCs) as an anisotropic medium to provide a template for the iCVD polymerization and to optically monitor the polymerization in-situ using a long-distance focal lens. Our work focused on determining the effect of temperature on the morphology of glycidyl methacrylate (GMA) and divinyl benzene (DVB) polymeric particles polymerized using the iCVD-in-LC system.

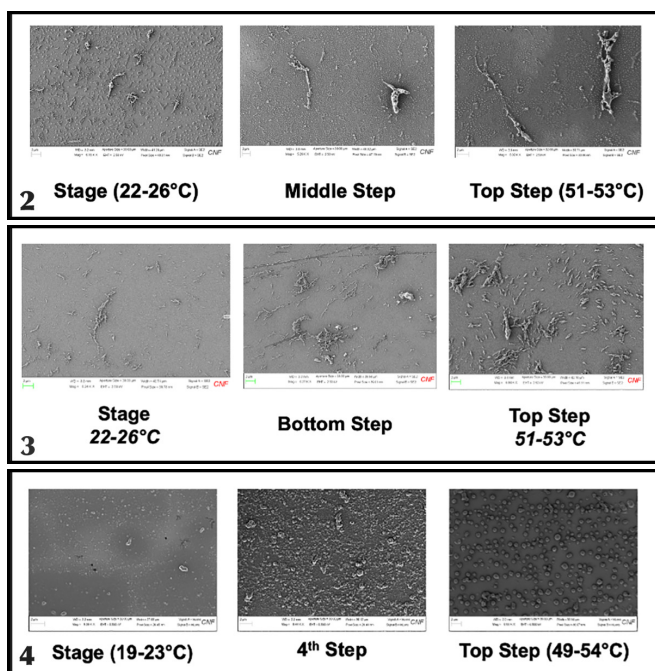


Figure 2: Morphologies of GMA particles polymerized on OTS. Figure 3: Morphologies of GMA particles polymerized on glass. Figure 4: Morphologies of DVB particles polymerized on OTS.

Utilizing a temperature gradient placed in the iCVD reactor, we achieved multiple temperatures within one polymerization run, as shown in Figure 1. The gradient was created by stacking glass slides in a staircase fashion. The reactor stage was cooled using a chiller set at 5°C, and a heated filament array was set above the reactor stage, reaching ~ 260°C. Our custom-built staircase sample holder experiences higher temperatures at the top step and lower temperatures at the bottom. We mapped the top step and reactor stage temperatures and consistently achieved a temperature difference of 20-25°C between the two extremes. We achieved multiple temperatures during each reactor run by placing samples on different steps of the staircase sample holder. This allowed us to compare the morphologies of the GMA particles polymerized in LC at different temperatures while minimizing the variables that could contribute to morphological differences. LCs are sensitive to temperature and change phase as temperature increases. The LC nematic phase provides mesogen orientational order and is the iCVD polymerization target phase. As temperature increases, the LC mesogens will transition to the isotropic phase; at this point, the LC loses its order and does not provide a templating effect. E7 LC was used for this project and has a nematic to the isotropic phase transition of ~ 60°C. To ensure the E7 remained in the nematic phase, we monitored multiple steps on the staircase and found no phase change of LC in the samples placed on any step during 30-minute and 60-minute polymerizations.

We also utilized two surfaces for the iCVD reactions: nochromix-treated glass and octadecyltrichlorosilane (OTS) substrates. Cross-polarized optical images of the LC samples were taken before and after the polymerization. We found

negligible evaporation and no phase change of the LC during the 60-minute polymerizations for both glass and OTS samples using the optical images and the long-distance lens placed directly above the reactor. However, an anchoring change was observed at the mid-range temperatures for OTS from homeotropic to planar/tilted LC anchoring. We are currently investigating the cause of the anchoring change. After the polymerization, we characterized the morphologies of the GMA particles using a Zeiss Supra scanning electron microscope. We found that the particle morphology for GMA particles on OTS and glass does not drastically change their morphology but instead becomes larger and more elongated, as shown in Figures 2 and 3.

Utilizing the temperature gradient, we also polymerized DVB particles on OTS. We found that DVB particle morphologies differ more significantly than GMA polymerized at similar temperatures, as shown in Figure 4. The lower temperatures provide 300-400 nm diameter DVB nanoparticles. As temperature increases, DVB particles become larger and less symmetrical; at higher temperatures, they become symmetrical microspheres 1 μm in diameter. We hypothesize that DVB can achieve more morphologies because of crosslinking, while GMA is linear, achieving fewer morphologies.

Conclusion and Future Steps:

Using a temperature gradient, we achieved multiple temperatures during a single LC-templated iCVD reactor run, allowing the comparison of GMA morphologies at different temperatures. We found that the GMA morphologies do not differ significantly with increasing temperature but increase in size and elongation. DVB particles were also polymerized using the temperature gradient, and the obtained morphologies changed more significantly. Reproducible reactor runs must be done to ensure the GMA particles are fully characterized at the different polymerization temperatures. The temperature gradient created for this project can also be used in future polymerizations to achieve multiple temperatures within a single polymerization.

Acknowledgments:

Thank you to CBE FMRG: Cyber and the CNF REU for all the funding and support I received during the 2024 summer. I also want to thank my mentors, Soumyamouli Pal and Shiqi Li, for their support and mentorship. Finally, thank you to my PIs, Dr. Abbott and Dr. Yang, for hosting me this summer and allowing me to work in their fantastic labs.

References:

- [1] Jain, A., Pal, S., Abbott, N. L., and Yang, R. (2023, March 10). Single-step synthesis of shape-controlled polymeric particles using initiated chemical vapor deposition in liquid crystals.

Stoichiometric Dependence of Physical and Electrical Properties of Silicon Nitride

CNF Summer Student: Daniel Teleshevsky

Student Affiliation: Electrical and Computer Engineering, Cornell University

*Summer Program(s): 2024 Xing Army Educational Outreach Program (AEOP),
2024 Cornell NanoScale Facility Research Experience for Undergraduates (CNF REU) Program*

Principal Investigator(s): Grace (Huili) Xing, Electrical and Computer Engineering, Cornell University

Mentor(s): Phil Infante, Cornell NanoScale Facility, Cornell University

*Primary Source(s) of Research Funding: Xing Army Educational Outreach Program (AEOP),
National Science Foundation under Grant No. NNCI-2025233*

Contact: dt532@cornell.edu, grace.xing@cornell.edu, infante@cnf.cornell.edu

Summer Program Website: <https://cnf.cornell.edu/education/reu/2024>

*Primary CNF Tools Used: LPCVD Furnace, CVC SC4500 Thermal Evaporation System,
Flexus, Woollam Spectroscopic Ellipsometer*

Abstract:

In recent years, nitride transistors have received much attention in the semiconductor device research community due to their wide bandgap, high thermal conductivity, and polarization properties. Two important performance metrics of these devices are the suppression of leakage current through the gate dielectric and its resilience under repeated use. Previous studies [1] have shown that these properties can be improved in SiN_x (a common gate dielectric for nitride transistors) by changing the stoichiometry of the dielectric deposition.

This investigation entails the physical and electrical characterization of silicon nitride (SiN_x) thin films deposited on silicon substrates by low-pressure chemical vapor deposition (LPCVD). Films were deposited at temperatures of 775°C, 750°C, and 725°C, and dichlorosilane to ammonia gas flow ratios of 5:1, 5:2, and 1:4, yielding a total of nine samples. Physical characterization measurements, including stress and index of refraction, were conducted on each film. The films with the lowest Si content showed the most stress and lowest index of refraction. Aluminum contacts were deposited on the silicon nitride using CNF's CVC SC4500 Thermal Evaporation System and patterned by contact lithography in a metal-first process to form MOS capacitors.

Capacitance-voltage behavior of the fabricated capacitors was measured at a DC probe station to determine the dielectric properties of the SiN_x. The leakage current through the capacitors under applied bias was also measured as a function of time to determine the time-dependent dielectric breakdown of each film.

Summary of Research:

The goal of this research was to check the impact of low pressure chemical vapor deposition conditions on the characteristics of physical and electrical properties of silicon nitride. This was done using a parallel plate capacitor that consisted of silicon and aluminum as its plates, and silicon nitride as the dielectric. The physical properties tested included the stress imposed by the dielectric and the index of refraction of the dielectric. The electrical properties consisted of the dielectric breakdown of the dielectric, and capacitance measurements of some of the capacitors that included the dielectric.

The process began with a plain 100 mm n-type silicon wafer, on which silicon nitride was deposited using low pressure chemical vapor deposition (LPCVD). This deposition was done at three different ammonia to dichlorosilane ratios and at three different temperatures. The goal of these varying conditions being to vary the concentration of silicon in the dielectric. The three dichlorosilane to ammonia ratios were regulated using the LPCVD furnace, and these three ratios were 5:1, 5:2, and 1:4. The three different temperatures chosen were 775°C, 750°C, and 725°C. This process resulted in nine wafers that had distinct deposition conditions. The physical properties, such as stress and index of refraction, were measured using the Flexus and the Woollam Spectroscopic Ellipsometer respectively. The silicon nitride index of refraction increased with the concentration of silicon during deposition. The stress imposed by the silicon nitride decreased with an increasing silicon concentration, as well as with higher temperatures during deposition (Figure 2).

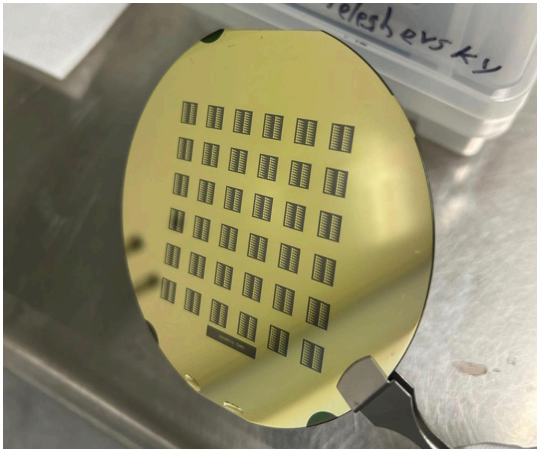


Figure 1: Photograph of the wafer with the individual capacitors visible on the black squares.

Then, the wafer was coated with aluminum using thermal evaporation, which was patterned by liftoff using photolithography. This resulted in six clear square capacitors whose width was 50 μm , 100 μm , 200 μm , 300 μm , 400 μm , and 500 μm (Figure 1).

As part of the electrical characterization, the dielectric breakdown of these capacitors, as well as the capacitances of the 500 μm capacitors were measured using the Everbeing EB-6 DC Probe Station. This study included two variables, which were the flow rate of dichlorosilane to ammonia ratios, and the deposition temperature. The dielectric breakdown of silicon nitride was tested in all nine different wafers. It was found that films with a higher concentration of silicon broke down at lower voltages (Figure 3). Different deposition temperatures also showed to impact dielectric breakdown, with higher deposition temperatures causing a dielectric breakdown at lower voltages (Figure 4).

Conclusions and Future Steps:

Both deposition temperatures and silicon content had an effect on the physical and electrical properties of the dielectric. Higher silicon content resulted in lower stress and a higher index of refraction, as well as a faster dielectric breakdown. Additionally, a higher deposition temperature resulted in lower stress and a faster dielectric breakdown. While both conditions did impact the properties of the film, silicon content had a greater effect than deposition temperature.

In the future, time-dependent measurements should be taken of the dielectric breakdown at each of the conditions, and this data should be collected in much larger quantities in order to

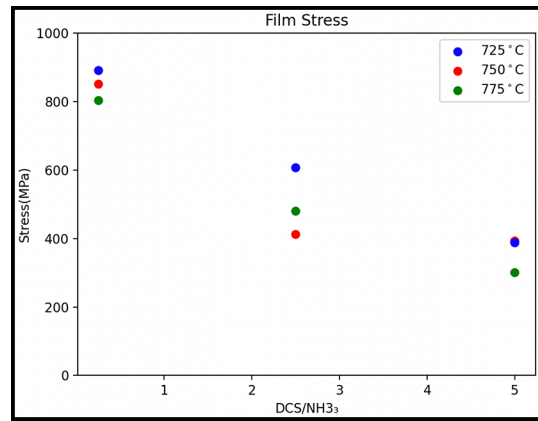


Figure 2: Graph of the stress of the wafer, which is one of the physical properties measured. A potential downward trend of increased stress with decreased silicon concentration is depicted.

conduct statistical analysis and determine the statistical significance of the data.

Acknowledgements:

I would like to thank: the Army Educational Outreach Program and the Cornell NanoScale Facility Research Experiences for Undergraduates program; Professor Grace (Huili) Xing, my principal investigator, and Joseph Dill of the Jena-Xing group who provided me with scientific guidance throughout this project; as well as Phil Infante, my mentor, and Ben Infante, without whom this project would have been impossible.

References:

[1] W. M. Waller, et al., in Proc. CS-MANTECH, Indian Wells, CA, USA, May 2017.

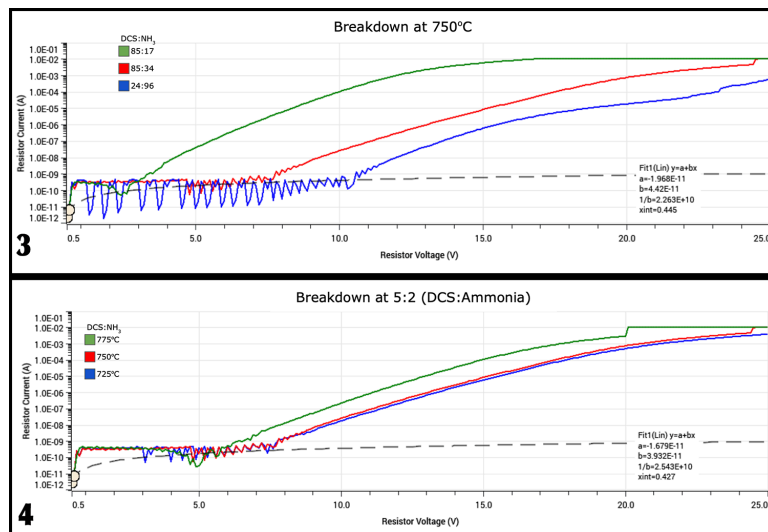


Figure 3, above: Graph of the dielectric breakdown of the silicon nitride at 750°C. A trend of a faster breakdown at higher concentrations of silicon is demonstrated. Figure 4, below: Graph of the dielectric breakdown of the silicon nitride at a 5:2 dichlorosilane to ammonia deposition ratio. A trend of faster breakdown at higher deposition temperatures is demonstrated.

Atomic Layer Etching of III-Nitride Semiconductors

CNF Summer Student: Hajo Johann Wise

Student Affiliation: Mechanical Engineering, Rochester Institute of Technology

*Summer Program(s): 2024 Xing Army Educational Outreach Program (AEOP),
2024 Cornell NanoScale Facility Research Experience for Undergraduates (CNF REU) Program*

*Principal Investigator(s): Professor Huili Grace Xing, Electrical and Computer Engineering,
Materials Science and Engineering, Cornell University*

Mentor(s): Dr. Xinwei Wu, Cornell NanoScale Science and Technology Facility, Cornell University

*Primary Source(s) of Research Funding: 2024 Xing Army Educational Outreach Program (AEOP),
National Science Foundation under Grant No. NNCI-2025233*

Contact: penguinhajo1@gmail.com, grace.xing@cornell.edu, xw77@cornell.edu

Summer Program Website: <https://cnf.cornell.edu/education/reu/2024>

Research Group Website: <https://jena-xing.engineering.cornell.edu/>

*Primary CNF Tools Used: Veeco Icon AFM, ABM Contact Aligner, Zeiss SEMS, Plasma-Therm Takachi ALE,
Oxford 81 RIE etcher, Oxford 100 PECVD, P-7 Profilometer, Woolam RC-2 Ellipsometer*

Abstract:

III-nitride semiconductors offer unique advantages in the manufacturing of high-voltage field effect transistors (FETS). However, production of nanoscale III-nitride FETs requires precise etching of III-nitride semiconductor films. We identified atomic layer etching (ALE) as an ideal technique for this application. ALE weakens the bond between a film and its surface layer via a chemical reaction with a reagent gas or plasma. The reagent is then purged, and the surface is bombarded with non-reactive ions. These ions impart enough energy to sputter away the reacted surface layer, but not enough to remove unreacted material underneath. These self-limiting characteristics allow for consistent removal of a few atomic layers at a time [1].

To adapt and characterize ALE for the processing of III-nitride films, samples with gallium nitride (GaN), aluminum nitride (AlN), and aluminum-gallium nitride (AlGaN) films were etched in the Cornell NanoScale Facility's (CNF) Plasma-Therm Takachi ALE tool. All ALE recipes tested used a Cl_2 and BCl_3 chemistry. However, key parameters such as gas flow rate, bias power, inductively coupled plasma (ICP) power, and step times were varied. Critical etch metrics such as surface roughness, film thickness, etch rate, and etch selectivity were recorded for each trial. By identifying recipe elements that yielded favorable etch results, this report gives preliminary guidance for the ALE of III-Nitride semiconductors.

Summary of Research:

The first round of ALE processing was performed with one of each sample type (GaN, AlN, AlGaN) and a photoresist mask process. Nlof-2020 negative photoresist was chosen due to its popularity in device fabrication. Test features were patterned onto the samples to provide convenient etch characterization sites. The recipe flowed 30 sccm each of Cl_2 and BCl_3 for surface modification and applied 10 W of bias power for ion

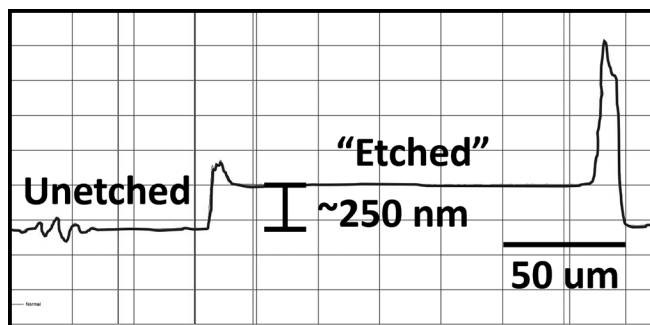


Figure 1: Profilometry reading of "etched" feature.

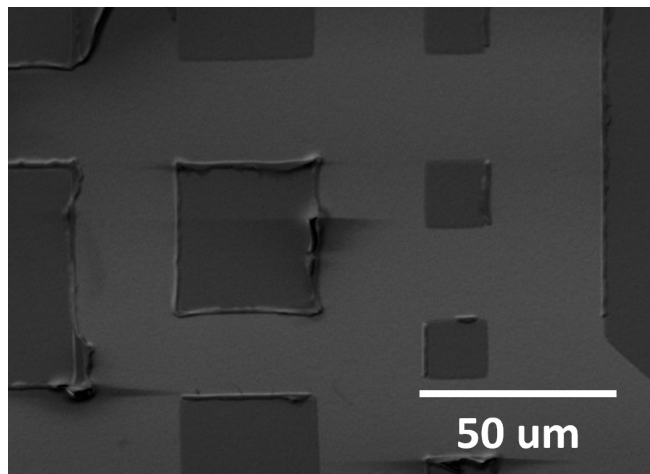


Figure 2: SEM image of "etched" squares.

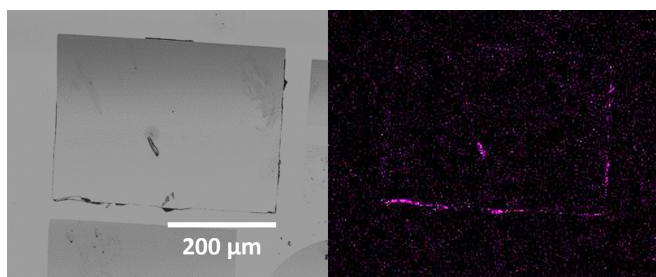


Figure 3: SEM and boron EDS imagery of photoresist-masked sample.

bombardment. All three samples were processed at the same time, for 20 ALE cycles.

Following ALE, profilometry was performed on the AlGaN sample, producing the reading shown in Figure 1. Notably, this reading indicated that the “etched” areas were ~ 250 nm higher than the unetched areas. This meant that something must have deposited during the etching process. This substance can be seen in SEM imagery of the sample (Figure 2), where the raised squares should be etched into the surface. Both the GaN and AlN samples exhibited deposition as well.

To identify the substance, energy-dispersive x-ray spectroscopy (EDS) was employed to map elements on the sample’s surface. Figure 3 shows an SEM image of the AlGaN sample with a corresponding boron EDS map. Boron correlates with deposits along the edge of the etch pad, suggesting that it played a role in deposition. However, EDS is not sensitive enough to lighter elements to positively identify the material.

While inconclusive, the EDS results hinted that photoresist might play a role in the deposition. Consequently, our process flow was adapted to use an SiO₂ hard mask for the next trial. Only AlN was tested, due to limited sample availability. The ALE recipe was altered to flow 30 sccm of Cl₂ and 3 sccm of BCl₃, while the bias power was reduced to 8 W. These changes limited boron concentration, reducing the likelihood of adverse reactions. The sample was processed for 100 total ALE cycles, with measurements taken after 50 cycles.

Initial results from the hard-mask sample were promising, with ellipsometry indicating an etch depth of 20 nm after 50 cycles. The etched surface was also significantly smoothed, with a pre-etch roughness of 2.66 nm RMS and a post-etch roughness of 1.70 nm RMS. Unfortunately, the sample also exhibited crystalline defects across all exposed AlN surfaces. These defects are visible in the SEM image of Figure 4, where they appear to have grown across the patterned surface.

EDS was once again used to analyze the defects, with the EDS image Figure 4 showing a Chlorine map of the sample. Chlorine hotspots strongly correlate with the defects, indicating that they contain Chlorine. However, no other elements demonstrated a similar correlation. This poses an issue, as pure chlorine is a gas at room temperature. Logically,

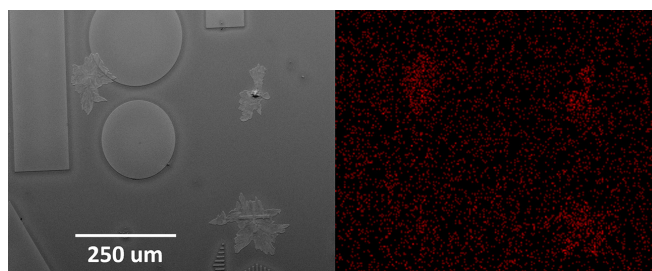


Figure 4: SEM and chlorine EDS image of hard-mask sample, including crystalline defects.

there must be other elements in the defects that we were unable to positively identify.

Conclusions and Future Steps:

While ALE processing was not wholly successful, these trials highlight “best practices” that will hopefully contribute to a mature process flow in the future. The use of a hard mask is the most apparent, as it likely contributed to the significantly cleaner result of the second trial. Hard masks, especially SiO₂, are known for their resistance to unwanted chemical interaction. This is especially valuable for a high precision process like ALE, where even minimal unexpected reactions can disrupt the etching cycle.

Looking to the future, there are several promising approaches to obtain more favorable results. First, it would be useful to analyze the deposits with wavelength-dispersive x-ray spectroscopy (WDS). This technique is similar to EDS, but it offers increased sensitivity to lighter elements. This may allow for positive identification of the deposited materials, and subsequent process alterations to prevent their formation. Aside from WDS, an ALE recipe without BCl₃ would entirely remove a potential source of unwanted chemical reactions. We believe that these techniques and alterations will bring us one step closer to the successful atomic layer etching of III-nitrides.

Acknowledgements:

This work was carried out at the Cornell NanoScale Science and Technology Facility, an NNCI member site supported by NSF grant no. NNCI-2025233. The opportunity to work at CNF was provided by the Army Educational Outreach Program. I’d like to give special thanks to Professor Grace Xing, Dr. Xinwei Wu, Wenwen Zhao, Jeremy Clark, Joseph Dill, Lynn Rathbun, and Melanie-Claire Mallison.

References:

- [1] K.J. Kanarik, S. Tan, and R.A. Gottscho. *Journal of PhyChemLetters* 2018 9 (16), 4814-4821 DOI: 10.1021/acs.jpcllett.8b00997 Copyright 2018 by American Chemical Society.

Fabricating Oxygen Managed and Thermally Robust Nb-Based Josephson Junction

CNF Project Number: 2126-12

Principal Investigator(s): Gregory David Fuchs

User(s): Jaehong Choi

Affiliation(s): Applied and Engineering Physics, Cornell University

Primary Source(s) of Research Funding: Air Force Office of Scientific Research

Contact: gdf9@cornell.edu, jc3452@cornell.edu

Primary CNF Tools Used: PT770 etcher, AJA sputter deposition, Oxford 81 etcher, Primaxx vapor HF etcher, SC4500 Even-hour evaporator, GCA 6300 DSW 5X g-line wafer stepper, DISCO dicing saw, Heidelberg mask writer - DWL2000, Zeiss SEM

Abstract:

Superconducting Josephson junctions (JJs) are important building blocks of a quantum qubit for next-generation quantum communication and technology. Fabrication of JJs has been heavily relied on aluminum due to its long coherence time and high-quality native oxide. However, aluminum has a low critical temperature (T_c), which makes Al-based JJs susceptible to quasiparticle poisoning and have a limited operation frequency [1-3]. Niobium, on the other hand, has higher T_c and provide a wide range of operation frequency. We fabricate niobium-based JJs that can withstand high temperature with minimized oxygen diffusion, leading to qubits with long coherence times. To achieve this, we create JJs from a trilayer where AlO_x is capped with an oxygen diffusion barrier and optimize the sidewall profile of JJs to mitigate loss.

Summary of Research:

AlO_x tunnel barrier suffers from chemical and thermal instability due to oxygen diffusion between the AlO_x and electrodes, which can cause qubit decoherence. To mitigate this diffusion, we are capping AlO_x with diffusion barrier. Materials with low heat of enthalpy such that it reduces the chemical gradient between AlO_x and electrodes are good candidates for diffusion barrier. We are still in process of finding an optimal material for this diffusion barrier in collaboration within Cornell, and among Syracuse University and NIST-Boulder.

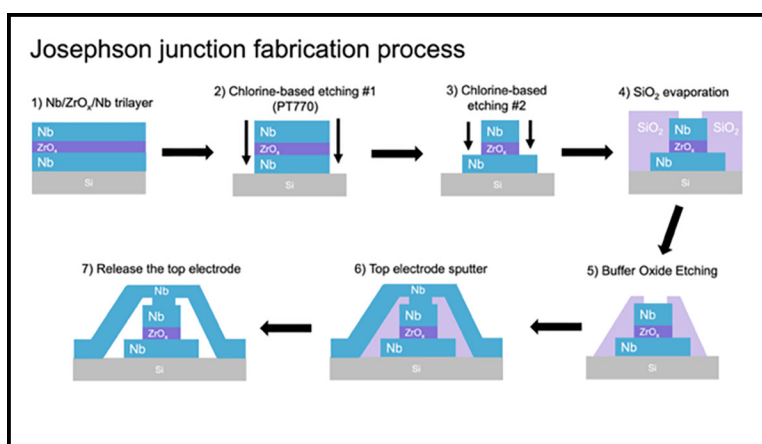


Figure 1: Fabrication process of a Nb/ZrO_x/Nb Josephson junction.

In the meantime, we start the fabrication process of the JJs to optimize etching process for sidewall characterization. We make JJs from a Nb/ZrO_x/Nb trilayer. ZrO_x is known to have good oxygen conservation [4], and we are going to compare its performance with that of a Nb/ AlO_x /Nb junction. We make junction geometry circular to allow sidewall access from any angles. Figure 1 summarizes the fabrication process. We use the GCA 6300 DSW 5X g-line wafer stepper to make a pattern of the junction. The junction diameter ranges from 2 μm to 9 μm within a device. Then, we use the PT 770 etcher for chlorine-based inductively coupled plasma (ICP) etching of the electrode and tunneling barrier. We evaporate the SiO_2 spacer layer after defining the mesa feature of the tunneling barrier. Subsequently, we sputter the top electrodes, which is followed by HF vapor etching of SiO_2 to release the top electrodes.

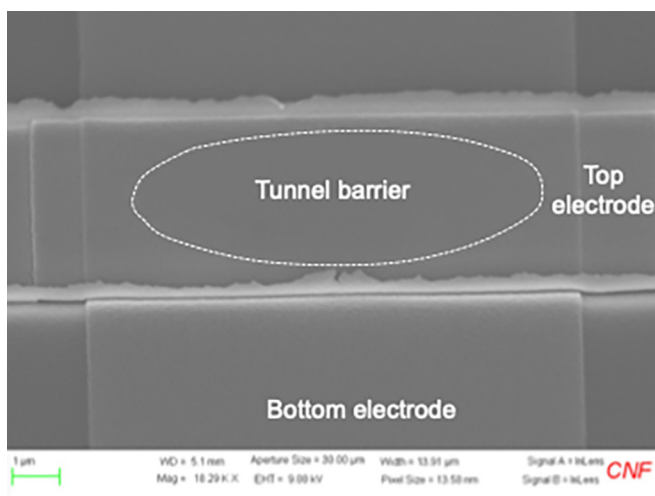


Figure 2: SEM image of the Josephson junction after releasing the top electrode.

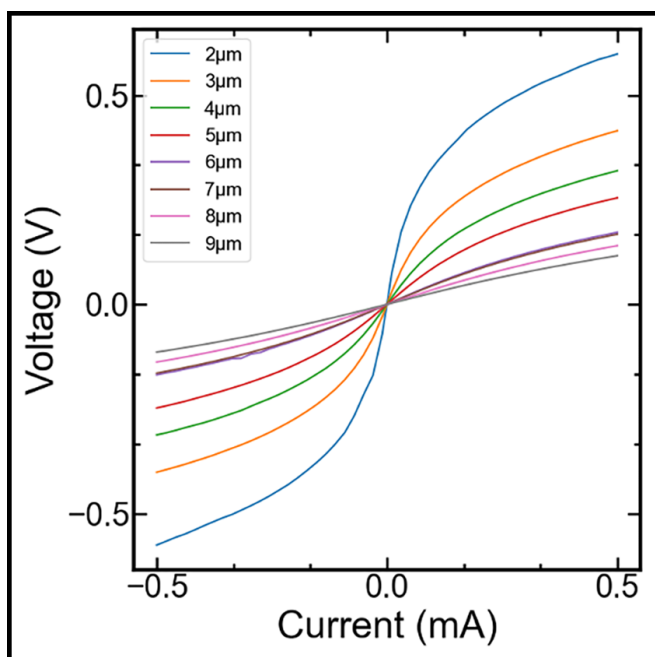


Figure 3: Current-voltage (I-V) curve from Josephson junctions of various diameter, ranging from 2 μm to 9 μm .

Figure 2 is an SEM image of the resultant Josephson junction. As shown in the image, lift-off residue persists despite multiple cycles of sonication. This is because sputtering is somewhat isotropic and not optimal for thick films. We can also see a gap between the top and bottom electrodes, indicating that the airbridge structure does not collapse after its release. We conduct four-wire voltage measurements by sourcing a current. Figure 3 is current-voltage (I-V) curves from the Nb/ZrOx/Nb JJs at room temperature. The I-V curves exhibit non-linear behavior, characteristic of tunnel junctions.

Conclusions and Future Steps:

We successfully fabricated a Nb/ZrOx/Nb JJ with non-linear I-V characteristics. Next, we will fabricate a Nb/AlOx/Nb JJ and compare its performance with that of the Nb/ZrOx/Nb JJs. Also, once the optimal material for diffusion barrier is determined, we will cap AlOx with that material and test its performance.

References:

- [1] Paik, H., et al, Phys. Rev. Lett. 107, 240501 (2011).
- [2] Reagor, M., et al, Phys Rev. B 94, 014506 (2016).
- [3] Connolly, T., et al, Phys. Rev. Lett. 132, 217001 (2024).
- [4] Nevirkovets, I.P., et al, Appl. Phys. Lett. 88, 212504 (2006).

Measuring Thickness of Extracellular Vesicle Mucin Coatings Using Nanoparticle Tracking Analysis

CNF Project Number: 2272-14

Principal Investigator(s): Dr. Matthew Paszek

User(s): Erik Chow

Affiliation(s): Department of Biomedical Engineering, Cornell University

Primary Source(s) of Research Funding: National Science Foundation Graduate Research Fellowship

Contact: paszek@cornell.edu, ec829@cornell.edu

Primary CNF Tools Used: Malvern NS300 Nanosight

Abstract:

Extracellular vesicles (EVs) transport DNA, RNA, and proteins between cells and therefore have great potential as tools for disease diagnosis and therapeutics. The significance of the glycocalyx in EV biogenesis and function is largely unexplored, and the capacity to effect EV production and properties through rational manipulation of the glycocalyx remains poorly understood. We have previously demonstrated that overexpressing the mucin glycoprotein MUC1 in the glycocalyx leads to a dramatic increase in the production of EVs. Here, we characterize the innate MUC1 surface coatings on these “mucin-induced” EVs and demonstrate the ability to bioengineer mucin biopolymer coatings through genetically encoded coating thickness.

Summary of Research:

Extracellular vesicles (EVs) have gained attention in numerous areas of biomedical engineering research — including disease pathogenesis and drug delivery, among others — for their ability to transport DNA, RNA, and proteins. The glycocalyx is a polymer meshwork of proteins, nucleic acids, and glycans which dictates numerous intercellular interactions, but its role in regulating EV biogenesis and function remains poorly understood. It has been previously shown that engineering the glycocalyx via the overexpression of mucin can result in membrane morphologies which are favorable for the formation of EVs [1]. This report summarizes research from the last year characterizing EV mucin coating thickness using nanoparticle tracking analysis (NTA).

MCF10A cells were genetically engineered to overexpress variable length, tetracycline-inducible MUC1 constructs with 0, 21, or 42 tandem repeats

(TRs). Separately, cells expressing inducible MUC1 were genetically engineered for differential expression of glycosyltransferase or sialyltransferase enzymes to achieve variable MUC1 glycosylation. Specifically, GCNT1 overexpressing cells express MUC1 with more core II glycans; C1GALT1 KO cells express MUC1 with truncated glycans; or GNE KO cells express MUC1 with no glycans terminated by sialic acid. To induce MUC1 overexpression, cells were treated with 1 $\mu\text{g}/\text{mL}$ doxycycline (Dox) for 24 h. Subsequently, cells were switched to serum-free media and cultured at 37 °C, 5% CO₂ for 15 h to 18 h. EV-containing media was harvested, and the EVs were isolated by PEG-enrichment according to an existing protocol [2]. EV mucin coatings were optionally removed by treatment with stcE mucinase [3], and EV sizes and concentrations were measured by nanoparticle tracking analysis (NTA) using the Malvern NS300 Nanosight.

Mucinase treatment of mucin-induced EVs resulted in a significant decrease in EV hydrodynamic radius (Figure 1). NTA of EVs from cells expressing variable-length MUC1 showed gradual increase in EV size correlated with mucin length, and significant increase in EV size was observed between EVs coated with MUC1 42xTR and those coated with MUC1 0xTR (Figure 2). Finally, mucin glycosylation had a measurable effect on EV coating thickness, with changes in EV size consistent with changes in parent cell glycocalyx thickness previously measured by scanning angle super-resolution microscopy [4] (Figure 3).

Conclusions and Future Steps:

These studies demonstrate that EV properties can be dramatically impacted by the glycocalyx. Overexpression

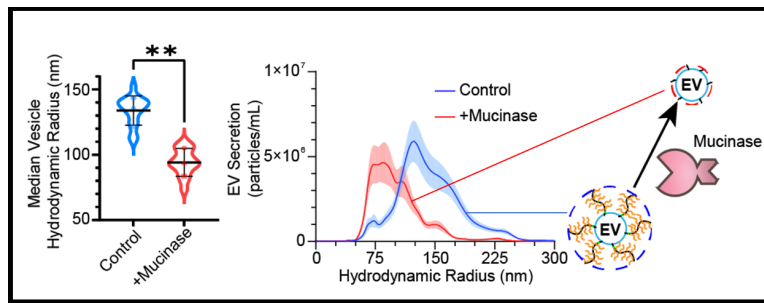


Figure 1: Mucin-induced EVs have MUC1 surface coatings. Comparison of hydrodynamic diameter of EVs before and after treatment with StcE mucinase, (** = $p < 0.01$, Left). Size distributions of EVs from 1E7 cells before and after 100 nM StcE mucinase treatment measured by NTA. Plotted are the average particle concentrations \pm SEM from three independent experiments (Right).

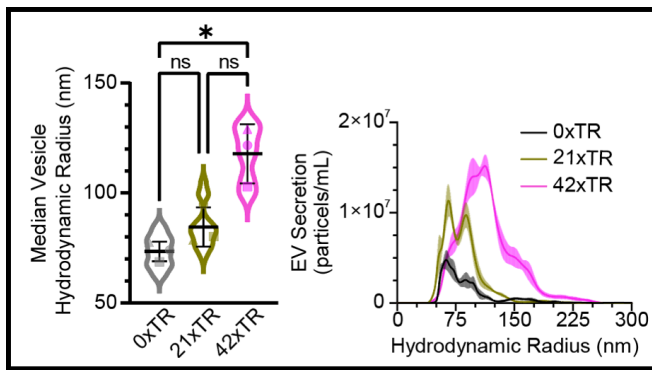


Figure 2: Expression of variable length mucins has a correlated effect on EV coating thickness. Comparison of median hydrodynamic radius of EVs from cells expressing MUC1 with 0-, 21-, or 42xTR (Left). Data were collected from three independent experiments (* = $p < 0.05$). Size distributions of EVs. Plotted are average particle concentrations \pm SEM from three independent experiments (Right).

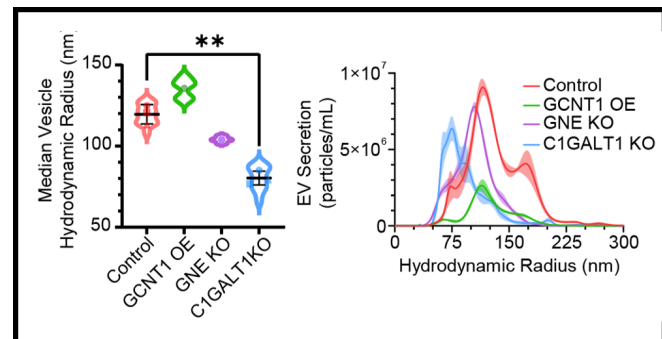


Figure 3: Differential MUC1 glycosylation changes EV coating thickness consistent with changes in parent cell glycocalyx thickness. Comparison of median hydrodynamic radius of EVs from GCNT1 overexpressing, GNE KO, or C1GALT1 KO cells across three independent experiments (* = $p < 0.05$). Size distributions of EVs. Plotted are average particle concentrations \pm SEM from three independent experiments (Right).

of MUC1 acts as a driver of EV release, and these EVs carry innate mucin surface coatings. Altogether, these data illustrate a synthetic biology approach to vesicle bioengineering by way of genetically encoded biopolymer coatings, which can be achieved either by direct manipulation of MUC1 biopolymer constructs or by genetic engineering of the EV parent cells to express mucins with varying glycosylation profiles. Future studies will assess the functional capabilities of mucin-coated EVs.

References:

- [1] Shurer, C. R., et al. Physical Principles of Membrane Shape Regulation by the Glycocalyx. *Cell*, 177(7), 1757-1770, <https://doi.org/10.1016/j.cell.2019.04.017> (2019).
- [2] Rider, M., et al. ExtraPEG: A Polyethylene Glycol-Based Method for Enrichment of Extracellular Vesicles. *Sci Rep* 6, 23978, <https://doi.org/10.1038/srep23978> (2016).
- [3] Malaker, S.A., et al. The mucin-selective protease StcE enables molecular and functional analysis of human cancer-associated mucins. *PNAS*, 116(15), 7278-7287, <https://doi.org/10.1073/pnas.1813020116> (2019).
- [4] Park, S., Colville, M.J., Paek, J.H. et al. Immunoengineering can overcome the glycocalyx armour of cancer cells. *Nat. Mater.* 23, 429-438, <https://doi.org/10.1038/s41563-024-01808-0> (2024).

Polymer Film Microstructures via Surface-Directed Condensed Droplet Polymerization

CNF Project Number: 2784-19

Principal Investigator(s): Dr. Rong Yang

User(s): Dr. Kwang-Won Park

Affiliation(s): Smith School of Chemical and Biomolecular Engineering, Cornell University

Primary Source(s) of Research Funding: National Science Foundation (CMMI-2144171)

Contact: ryang@cornell.edu, kp526@cornell.edu

Research Group Website: <https://theyanglab.com>

Primary CNF Tools Used: ABM contact aligner

Abstract:

Non-spherical polymer particles exhibit unique flow dynamics that enhance drug delivery by improving permeation through blood vessels walls. However, traditional synthetic methods are complex and inefficient. We developed a facile and scalable method called condensed droplet polymerization to address these challenges. In a chemical vapor deposition reactor, vaporized monomers condense onto a cold substrate, forming droplets that polymerize upon introduction of an initiator. Using a photoresist template with circular holes, we achieved monodisperse, hexagonally arranged polymer droplets. Removing the photoresist revealed concave-shaped polymers with potential nanoscale lens or drug delivery applications. This method offers precise control over particle size and morphology, paving the way for large-scale production and diverse biomedical applications.

Summary of Research:

Non-spherical polymer particles have shown great potential as drug delivery vehicles, exhibiting unique flow dynamics in blood vessels that enhance permeation through the vessel walls. However, the synthesis of non-spherical particles has been challenging due to complicated, time-consuming, and inefficient multi-step processes. Recently, our group demonstrated a facile and scalable synthetic strategy in the vapor phase, called condensed droplet polymerization [1].

In brief, within a conventional chemical vapor deposition vacuum reactor, vaporized monomer is introduced and subsequently condensed dropwise onto a cold substrate. These monomer droplets grow through continuous condensation and coalescence.

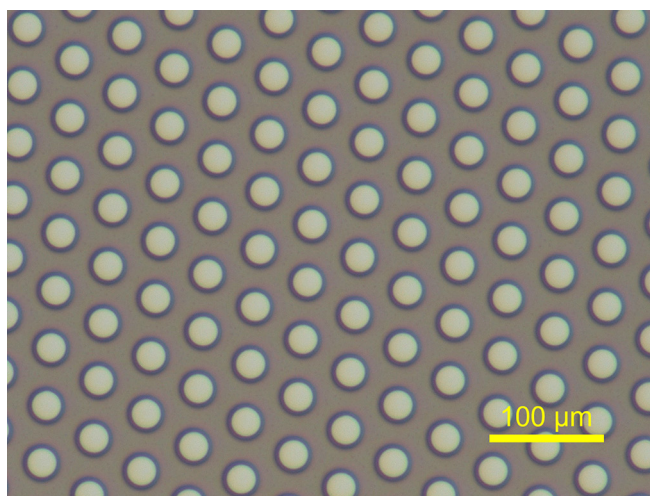


Figure 1: Optical microscopy image of SPR220-4.5 photoresist with a hexagonal array of circular holes with 30 μm diameter.

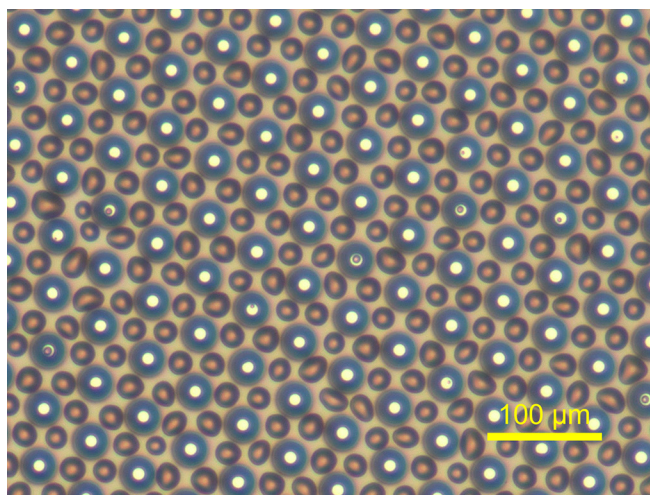


Figure 2: Optical microscopy image of benzyl methacrylate monomer droplets condensed on the photoresist template shown in Figure 1.

Once the droplet reaches the desired size, an initiator is introduced and decomposed into reactive radicals by heated filament arrays, initiating polymerization of the droplets. After a few minutes of polymerization (typically less than 2 minutes), the reaction is terminated by turning off the filament array and evacuating the reactor, resulting in polymer dome arrays. This CDP process has demonstrated that polymer particle size and morphology can be controlled and is suitable for large-scale production due to its rapid vacuum process. However, the random nature of condensation leads to a broad distribution of polymer particle sizes, which needs to be addressed. For drug delivery applications, the production of monodisperse polymer particles is critical to ensuring predictable and controlled drug release.

To address this issue, we created a template with an array of circular holes in the photoresist (Figure 1) and conducted the experiment using this template. The condensed droplet polymerization experiments confirmed that monomer droplets condensed simultaneously inside the holes and on the surface of the photoresist, regardless of the thickness of the photoresist (1 to 10 μm). As shown in Figure 2, when a densely packed hole array was used, we observed that monodisperse monomer droplets arranged themselves in a hexagonal pattern. This was an important result, demonstrating the potential to produce polymer domes of uniform size.

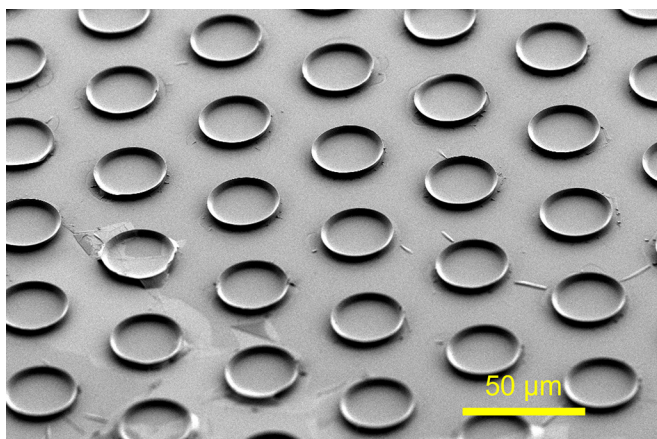


Figure 3: Scanning electron microscopy image of poly(benzyl methacrylate) patterns on Si substrate.

Interestingly, after completely removing the photoresist, the polymer formed inside the holes initially exhibited a concave shape due to the meniscus of the monomers (Figure 3). These polymer particles with such shapes are being closely monitored because they may exhibit nanoscale lens properties or unique drug delivery characteristics.

Conclusions and Future Steps:

In conclusion, our study demonstrated the effectiveness of the condensed droplet polymerization method in producing non-spherical polymer particles with controlled size and morphology. By utilizing a photoresist template with an array of circular holes, we achieved monodisperse monomer droplet condensation and observed hexagonal arrangement patterns. These results highlight the potential of the process for large-scale production of uniform polymer domes, which are critical for drug delivery applications due to their unique flow dynamics and enhanced permeation properties. To build these findings, we are currently looking at further refinement of the patterned substrate design to enhance the uniformity of monomer droplet condensation, aiming for even more precise control over particle size, shape, and distribution.

References:

- [1] Franklin, Trevor, Danielle L. Streever, and Rong Yang. "Versatile and rapid synthesis of polymer nanodomains via template- and solvent-free condensed droplet polymerization." *Chemistry of Materials* 34.13 (2022): 5960-5970.

Tuning the Surface Wettability of Alumina Membrane for Carbonate Crystallization

CNF Project Number: 2983-21

Principal Investigator(s): Dr. Greeshma Gadikota

User(s): Akanksh Mamidala

Affiliation(s): Civil and Environmental Engineering, Cornell University

Primary Source(s) of Research Funding: National Science Foundation Faculty

Early Career Development Program (NSF CAREER)

Contact: gg464@cornell.edu, am2489@cornell.edu

Research Group Website: <https://gadikota.cee.cornell.edu/>

Primary CNF Tools Used: Ramé-Hart Contact Angle Goniometer 500

Abstract:

Uncovering the nucleation and crystallization of calcium- and magnesium-carbonate in confined nanochannels is pivotal in interpreting the polymorph formation and stabilization in various physicochemical conditions having applications ranging from carbon sequestration to construction, plastics, and pharmaceuticals [1-3]. These carbonates exhibit anomalous physical and chemical phenomena due to finite size effects, and ionic effects altering their energies and kinetics of phase formation [4]. Accounting for these effects, the current research focuses on precipitating calcium- and magnesium-carbonate in confined alumina membranes and siliceous nanochannels having discrete pore sizes. Specifically, to account for the influence of surface wettability on carbonate growth, the alumina and siliceous nanochannels are transformed from hydrophilic to hydrophobic. This variation in surface wettability provides insights into

the role of interfacial water on the growth/dissolution of carbonates. To probe and corroborate the synthesis of hydrophilic nanochannels into hydrophobic, a contact angle measurer was utilized and the mean contact angle of the hydrophilic and hydrophobic nanochannels was measured as 23.9° and 93.9°.

Summary of the Research:

Understanding the influence of variation in surface wettability on carbonate growth and phase evolution is crucial and to alter the surface wettability the purchased anodic alumina membrane is first rinsed with ethanol and water and dried at 85°C for 30 minutes. Thereafter, the membranes were immersed in a solution of lauric acid in ethanol (20 g/L) for 15 minutes at 50°C and stirred at 120 rpm. The surface-modified membranes were again rinsed with ethanol and DI water and dried at 85°C for 30 minutes. This surface-altering process replaces the hydroxide moieties attached to the aluminum ion with lauric acid.

Contact angle measurement was performed using Ramé-Hart Contact Angle Goniometer 500 having a volume step of 10 .L and delay time of 4000 milliseconds to determine the surface wettability of the hydrophilic and hydrophobic surface. The contact angles measured were 23.6°, and 24.3° for the left side (.) and right side (.) of the droplet respectively

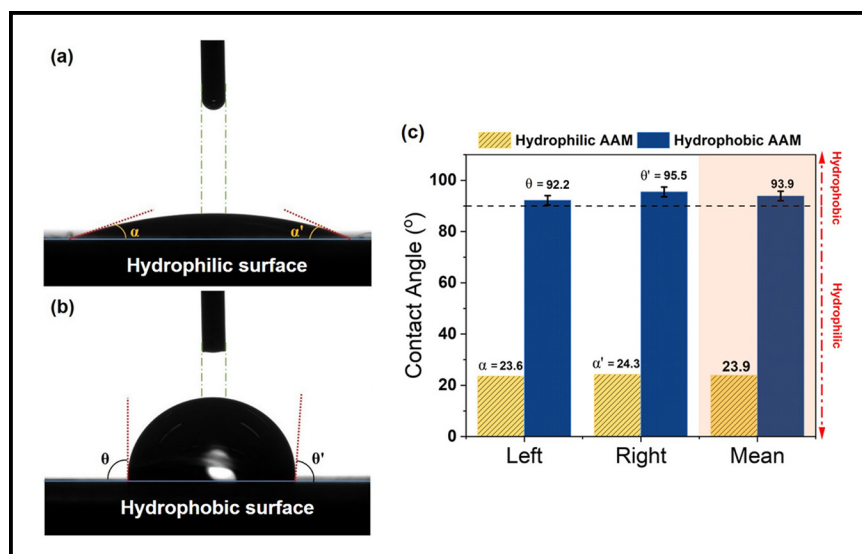


Figure 1: Contact droplet angles.

for the hydrophilic membrane and 92.2° , and 95.5° for the left side (.), and right side (.) of the droplet respectively for the hydrophobic membrane as shown in Figure 1. The mean contact angles were 23.9° and 93.9° for hydrophilic and hydrophobic anodic alumina membrane respectively. Based on the analysis, synthesis of the membrane from hydrophilic to hydrophobic was accomplished.

Conclusion and Future Steps:

The behavior of fluids in nanoconfinement is an intricate mechanism characterized by anomalous phase behavior, spatial density profiles, and unique ion transport dynamics [4,5]. In this research, a similar mechanism is studied by analyzing the evolution of calcium- and magnesium-carbonate in nanoconfinement in different surface wettability environments. Before analyzing the phase evolution, synthesizing hydrophilic membranes into hydrophobic was performed using lauric acid, and to corroborate the hydrophobicity, a contact angle measurement was performed. The mean contact angle for the hydrophobic membrane attained was 93.9° validating the synthesis approach.

The future steps involve the transformation of anodic alumina membranes using lauric acid of different pore sizes and investigating the intricate relation between pore size and surface contact angle. Furthermore, the surface of silica nanochannels will be modified into hydrophobic using agents like sodium dodecyl sulfate

(SDS), ethanol, methanol, etc. [6,7], and the contact angle for these membranes will be measured.

References:

- [1] Mei, X., et al. Phase Transition of Ca- and Mg-Bearing Minerals of Steel Slag in Acidic Solution for CO₂ Sequestration. *Journal of Sustainable Metallurgy* 7, (2021).
- [2] De Vito, C., Medeghini, L., Mignardi, S., and Leccese, F. Synthesis of amorphous Mg-Carbonates for the application in the production of advanced materials. in 5th IEEE International Workshop on Metrology for AeroSpace, MetroAeroSpace 2018 - Proceedings (2018). doi:10.1109/MetroAeroSpace.2018.8453526.
- [3] Hong, S., Moon, S., Cho, J., Park, A. H. A., and Park, Y. Effects of Mg ions on the structural transformation of calcium carbonate and their implication for the tailor-synthesized carbon mineralization process. *Journal of CO₂ Utilization* 60, (2022).
- [4] Singh, N., Simeski, F., and Ihme, M. Computing Thermodynamic Properties of Fluids Augmented by Nanoconfinement: Application to Pressurized Methane. *Journal of Physical Chemistry B* 126, (2022).
- [5] Leoni, F., Calero, C., and Franzese, G. Nanoconfined Fluids: Uniqueness of Water Compared to Other Liquids. *ACS Nano* 15, (2021).
- [6] Qiao, B., Liang, Y., Wang, T. J., and Jiang, Y. Surface modification to produce hydrophobic nano-silica particles using sodium dodecyl sulfate as a modifier. *Appl Surf Sci* 364, (2016).
- [7] Luo, T., et al. Hydrophobic Modification of Silica Surfaces via Grafting Alkoxy Groups. *ACS Appl Electron Matter* 3, (2021).

Lithography for Topological Nanowires

CNF Project Number: 3032-22

Principal Investigator(s): Judy Cha

User(s): Han Wang

Affiliation(s): Department of Materials Science and Engineering, Cornell University

Primary Source(s) of Research Funding: Semiconductor Research Corporation (SRC) JUMP 2.0 SUPREME

Contact: jc476@cornell.edu, hw578@cornell.edu

Primary CNF Tools Used: JEOL 6300, PT 720 etcher, CVC SC4500 Combination Thermal/ E-gun Evap System, Zeiss Supra SEM, Naby Nanometer PGS, YES Asher, Woollam RC2 Spectroscopic Ellipsometer

Abstract:

The resistivity scaling of copper interconnects with decreasing dimensions remains a major challenge in the continued downscaling of integrated circuits, which causes increased signal delay and power consumption in the circuits [1]. Therefore, new materials are needed for the next generation of interconnects beyond the 7 nm technology node. Topological semimetals like molybdenum phosphide (MoP), owing to their topologically protected surface states and suppressed electron backscattering, show promising resistivity values compared to copper interconnects at nanometer scale [2]. Here, with the assist of electron beam lithography and reaction ion etching, we successfully synthesized 1D topological MoP nanowires with tunable line width and thickness to investigate its resistivity scaling effect at nanometer scale.

Summary of Research:

The fabrication flow chart of single crystalline topological MoP is shown in Figure 1. We start from commercially available single crystalline molybdenum disulfide (MoS_2) bulk crystals. Single crystalline MoS_2 flakes exfoliated from bulk crystals were placed on dry thermal oxide silicon wafer. These wafers were pre-patterned with alignment grids designed by our lab to locate flakes of interest (Figure 2a). First round of e-beam exposure was performed using JEOL 6300 to produce the dumbbell-shaped pattern as the mask of etching. Then, reactive ion etching was performed using PT720 etcher with SF_6 etchant to etch away MoS_2 in the exposed area, leaving the dumbbell-shaped MoS_2 with 1D wire in the middle (Figure 2b). SF_6 fluorinates top layers of PMMA, making them hard to remove by acetone. Therefore, O_2 plasma etching using the same tool was subsequently performed to remove the top layer of fluorinated PMMA. Then, using template-assisted chemical vapor deposition (CVD), the MoS_2 nanowire

was converted to 1D MoP nanowire by reacting with PH_3 gas (Figure 2c). To deposit electrodes and measure the resistance, second round of e-beam lithography was done using Naby-NPGS system to produce the electrode pattern. After descum in YES Asher, 10 nm chromium and 100 nm gold was deposited on the wafer as electrodes using SC4500 evaporator. After lift-off, the device was done and ready for measurement.

Figure 3 (a) shows the scanning electron microscope (SEM) images of the 1D topological MoP nanowire synthesized via the method described above with a line width of 80 nm (left) and 30 nm (right), separately. Figure 3 (b) shows the Raman spectra of the wires before and after conversion. Before conversion, the E_{12g} and A_{1g} peaks of MoS_2 can be clearly seen at 384 and 409 cm^{-1} , respectively. After conversion, the two Raman modes of MoS_2 disappeared and one peak at about 402 cm^{-1} shows up, which is an indication of MoP according to the literature [3]. Wires with any other designated line width can be fabricated by changing the pattern arrangement, e-beam dose, or the etching time. Wires with different thickness can also be fabricated through choosing exfoliated MoS_2 flakes of different thicknesses. This method thus provides an excellent approach for fabricating 1D topological nanowires to investigate the unconventional resistivity scaling effect expected for them.

References:

- [1] Gall, D., Cha, J. J., Chen, Z., Han, H. J., Hinkle, C., Robinson, J. A., Sundaraman, R., and Torsi, R. (2021). Materials for interconnects. *MRS Bulletin*, 1-8.
- [2] Han, H., Kumar, S., Jin, G., Ji, X., Hart, J., Hynek, D., Sam, Q., Hasse, V., Felser, C., Cahill, D., Sundaraman, R., and Cha, J. (2023). *Advanced Materials*, 35(13), 2208965.
- [3] Kwon, K., Choi, S., Lee, J., Hong, K., Sohn, W., Andoshe, D., Choi, K., Kim, Y., Han, S., Kim, S., and Jang, H. W. (2017). *J of Materials Chemistry A*, 5(30), 15534-15542.

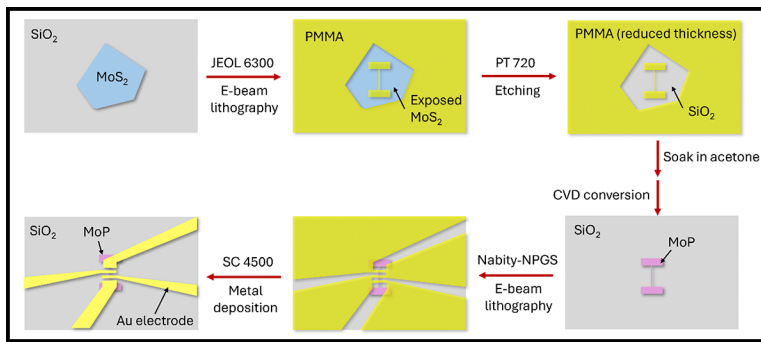


Figure 1: Process flow of 1D MoP nanowires as well as the 4-point transport measurement devices.

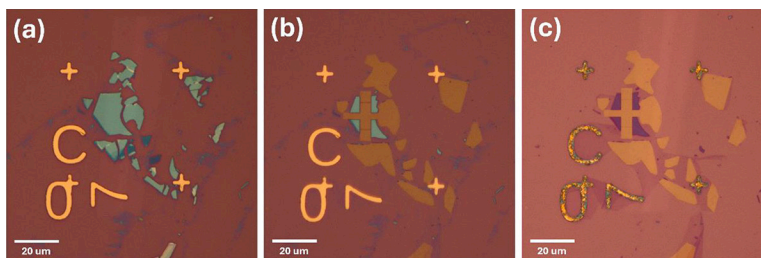


Figure 2: (a) Exfoliated MoS_2 on the pre-patterned dry thermal oxide wafer. (b) Dumbbell shaped MoS_2 with 1D nanowires in the middle after e-beam lithography and etching. (c) 1D MoP nanowires after template-assisted CVD conversion from MoS_2 .

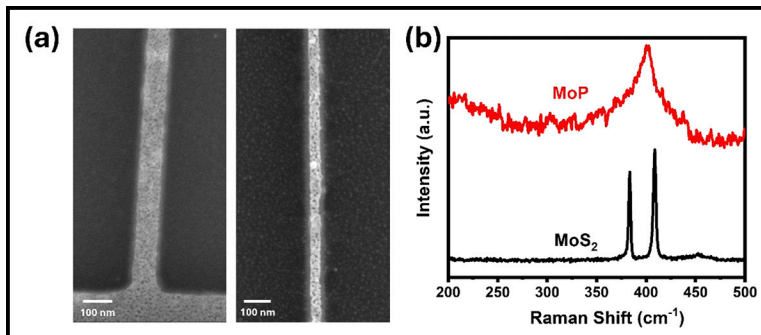


Figure 3: (a) SEM images of 1D topological MoP wires with line width of 30 nm (left) and 80 nm (right). (b) Raman spectra of MoS_2 and converted MoP wires.

Through-Silicon Vias for Substrate-Integrated Waveguides

CNF Project Number: 3078-23

Principal Investigator(s): James C. M. Hwang

User(s): Jin Hong Joo, Xiaopeng Wang, Yunjiang Ding

*Affiliation(s): Department of Materials Science and Engineering,
School of Electrical and Computer Engineering; Cornell University*

Primary Source(s) of Research Funding: SUPREME Center funded by SRC/DARPA

Contact: jch263@cornell.edu, jj593@cornell.edu, xw569@cornell.edu, yd439@cornell.edu

*Primary CNF Tools Used: ABM Contact Aligner, SUSS MA6-BA6 Contact Aligner, AJA Sputter Deposition – 1 & 3,
UNAXIS 770 Deep Silicon Etcher, AJA Ion Mill, Zygo Optical Profilometer*

Abstract:

As the demand for heterogeneous-integrated RF chips emerges, substrate-integrated waveguides (SIWs) based on through-silicon vias (TSVs) have become increasingly important due to their low loss and high power capacity across a wide frequency range. In particular, above 110 GHz, SIWs are small enough to be integrated in Si interposers for high-power interconnects. They can also be used to form high-quality passive devices such as filters and antennas, which have been difficult to integrate on chip. This enables system on chip. In this study, we investigate the fabrication of SIWs in Si interposers with a thickness on the order of 100 μm . The thin Si wafers were patterned and etched using the Bosch deep reactive ion etching (DRIE) process to create TSVs. Preliminary results indicate an etch rate of approximately 27 nm/s, which is too slow to etch through the Si interposer. Work is in progress to improve the etch rate.

Summary of Research:

Silicon (Si) is most extensively used material in semiconductor devices due to its exceptional electrical and mechanical properties, including a high dielectric constant, electrical resistivity, breakdown strength and low loss tangent. These characteristics make it an attractive candidate for SIWs. However, its relatively low mechanical toughness and high thermal conductivity compared to materials like silicon carbide (SiC) pose challenges during processing, particularly in etching processes. Our group has successfully demonstrated SiC as a viable substrate material for SIW processing. The methodology developed for SiC SIW fabrication is adapted as a proof of principle for Si SIW fabrication.

To demonstrate the feasibility and develop a processing recipe for Si SIWs, we obtained a thinned high-resistivity

Si wafer with a thickness of approximately 150 μm and resistivity of $> 1000 \text{ ohm-cm}$. Drawing from a similar approach used for SiC SIWs, our methodology began with depositing a 50 nm layer of aluminum oxide (Al_2O_3) on the frontside of the Si wafer as an etch stop layer. This deposition was carried out using AJA Sputter Deposition – 1, achieving a deposition rate of approximately 2.8 \AA/s .

Following this, the frontside was patterned using an ABM Contact Aligner, after which a titanium/aluminum (Ti/Al) layer was deposited using AJA Sputter Deposition – 2 to metalize the frontside. Concurrently, the backside of the wafer was patterned, and Al_2O_3 was deposited to define the etching pattern for TSVs. Al_2O_3 is chosen for its excellent masking properties in the Bosch DRIE process for Si, offering a selectivity as high as 1:1000.

For the DRIE, UNAXIS 770 Deep Silicon Etcher was used. To facilitate effective cooling during the reactive etching, the Si wafer was bonded to a sapphire carrier wafer using cool grease. The etching chemistry used was $\text{C}_4\text{F}_8/\text{SF}_6$, which reacts with and removes Si to create the vias anisotropically.

Using a Zygo Optical Profilometer, we repeatedly measured the depth of the TSVs and observed an etch rate of 3.3 \AA/loop or approximately 27.3 nm/s throughout the process as shown in Figure 1.

Due to the fragility of the thinned Si wafer, precautions were taken during post-etching processes when removing cool grease and carrier wafer. Dicing streets were drawn on the Si wafer as shown in Figure 2, to facilitate simultaneous etching for easier detachment and dicing into smaller chips. Finally, the etch stop layer was physically removed using an AJA Ion Mill, and the backside was metallized with Ti/Al using AJA Sputter Deposition – 2 to fill the TSVs and establish connections to the frontside. The Si wafer after etching is shown

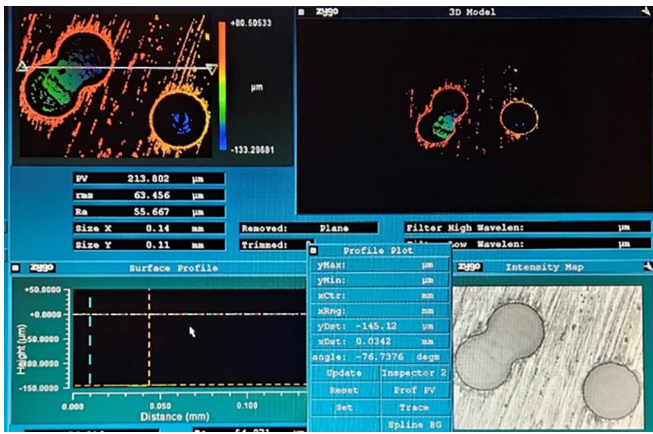


Figure 1: Zygo Optical Profilometer image for TSV depth measurement.

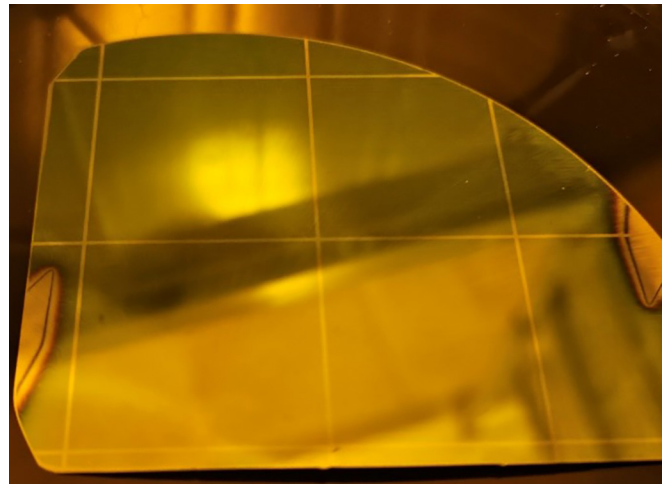


Figure 2: Dicing street pattern on Si wafer.

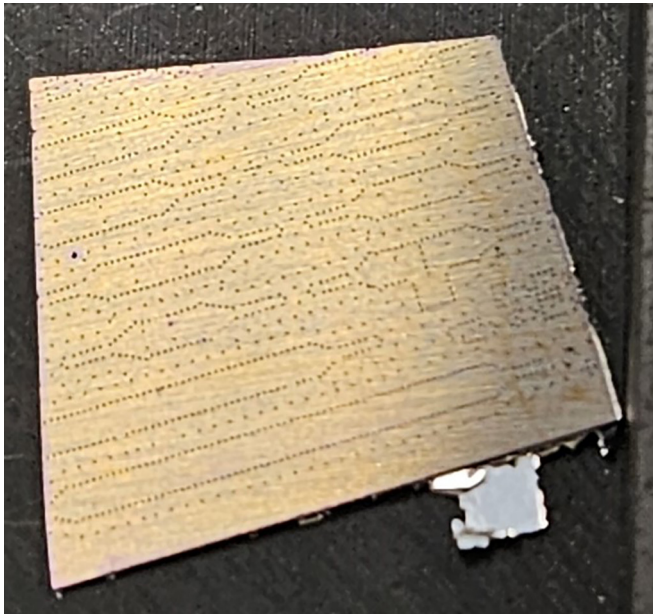


Figure 3: Si SIW chip after the Bosch DRIE process.

in Figure 3 and the structural details and final product configurations are illustrated in Figure 4, showcasing the possibility of processing SIWs with thinned high resistivity Si wafers.

Conclusion and Future Steps:

The fabrication of Si SIWs focused on studying the Bosch DRIE of thinned Si wafers, achieving an etch rate of 27 nm/s with uniform anisotropic etching across the wafer. With the etching process proven feasible, the next phase involves investigating the most effective methods and materials for metallizing the SIWs, particularly to fill the TSVs. Initially, atomic layer deposition (ALD) of platinum (Pt) is planned to coat the chip. Pt is chosen for its superior properties in enhancing interconnect reliability compared to Ti, which is prone to oxidation,

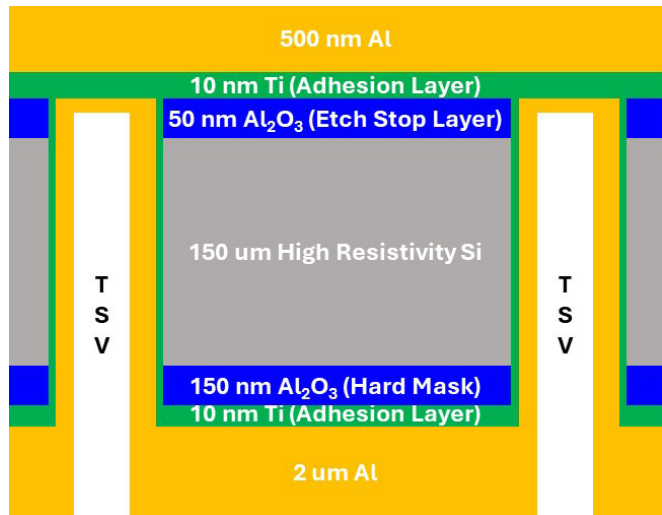


Figure 4: Structure of Si SIW.

potentially compromising device quality. Following the completion of processing steps, measurements will be conducted at the High Frequency Test Lab (HFTL) using the 220 GHz single-sweep probe station located at Cornell University. This comprehensive testing environment will provide critical insights into the performance and functionality of the fabricated SIWs at high frequencies.

References:

- [1] M. J. Asadi, L. Li, K. Nomoto, Y. Tang, W. Zhao, P. Fay, D. Jena, H. G. Xing, and J. C. M. Hwang. 2021 IEEE MTT-S Int. Microw. Symp. (IMS), Atlanta, GA, USA, 2021, pp. 669-672.
- [2] D. Malta, E. Vick, S. Goodwin, C. Gregory, M. Lueck, A. Huffman, and D. Temple. 2010 IEEE International 3D Systems Integration Conference (3DIC), Munich, Germany, 2010, pp. 1-6.

CNF NORDTECH Internship: Characterization of Oxynitride Films

CNF Project Number: CNF Summer Internship
Principal Investigator(s): Ron Olson, Lynn Rathbun
User(s): Ben Infante

Affiliation(s): Cornell NanoScale Science & Technology Facility (CNF), Cornell University

Primary Source(s) of Research Funding: Cornell NanoScale Facility (CNF), a member of the National Nanotechnology Coordinated Infrastructure (NNCI), which is supported by the National Science Foundation (Grant NNCI-2025233)

Contact: olson@cnf.cornell.edu, rathbun@cnf.cornell.edu

Research Group Website: <https://www.cnf.cornell.edu/>

Primary CNF Tools Used: MRL Industries E4 Furnace

Abstract:

As part of the CNF NORDTECH internship program, various projects were worked upon this summer. One of the projects was the characterization of an oxynitride process using the MRL Industries LPCVD furnaces. The oxynitride film is heavily used in photonics, and specifically done to gather information for a remote request for the film. The characterization of the thin film involved varying the gas ratios in order to determine the effect of adding oxygen to the recipe. Other factors such as pressure, and temperature were kept constant. The time variable was flexible since the sample needed to be thick enough to gather the data. The main objective of the characterization was to determine the deposition rate, the index of refraction and the stress of the film. From the data gathered, a few conclusions were drawn. As the concentration of oxygen in the film increased, the index of refraction, the deposition rate, and the stress all decreased.

TABLE 1: MFC GASSES	
Mass Flow Controller	
NH3	200 sccm
N2O	200 sccm
DCS	150 sccm

TABLE 2: CONSTANT PARAMETERS	
Constants	
Pressure	200 mTorr
DCS %	40%
DCS	60 sccm

Experimental Procedure:

The oxynitride film was deposited using the Low-Pressure Chemical Vapor Deposition (LPCVD). In order to properly determine the effects of different gas ratios, many of the determining variables were kept constant throughout the experiment. These included the chamber pressure, and the dichlorosilane set percentage. For the gas flow settings, the mass flow controller (MFC) has a set amount of gas flow it can allow measured in standard cubic centimeters per minute (sccm). The gas ratios are a percentage of that flow. For the oxynitride run, there are 3 different gasses used to deposit the film. The gasses given are Ammonia (NH₃), Nitrous Oxide (N₂O) and Dichlorosilane (DCS). Using the gasses we can determine the constant parameters for the experiment. These gasses can be viewed in Table 1 and the constant parameters in Table 2.

TABLE 3: GAS FLOW PARAMETERS					
Wafer ID	Time	NH3 %	NH3 Sccm	N2O %	N2O Sccm
ON-1	30	90	180	0	0
ON-2	30	90	180	0	0
ON-9	30	80	160	10	20
ON-10	30	80	160	10	20
ON-11	30	70	140	20	40
ON-12	30	70	140	20	40
ON-13	30	60	120	30	60
ON-14	30	60	120	30	60
ON-15	30	50	100	40	80
ON-16	30	50	100	40	80
ON-17	60	40	80	50	100
ON-18	60	40	80	50	100
ON-19	60	30	60	60	120
ON-20	60	30	60	60	120
ON-21	60	20	40	70	140
ON-22	60	20	40	70	140
ON-23	90	10	20	80	160
ON-24	90	10	20	80	160

From these initial parameters, a formulated experiment can be developed. Starting out by scribing our wafers, the gas ratios can be compiled. Silicon Nitride is formed using NH₃ and DCS. So that will become the start point. After the initial run the NH₃ percentage will decrease while the N₂O percentage will increase. This pattern will be repeated until there is no NH₃ flow left, and the only gasses in the chamber are N₂O and DCS. The specific gas flows used can be viewed in Table 3.

From this table, one of the most noticeable columns is the time column. Initially time was supposed to be held as a constant. But as the N₂O percentage increased, the deposition rate decreased dramatically which will be showcased later in the results section. If the time was not increased, the thickness of the film would have been way too thin to gather any usable data.

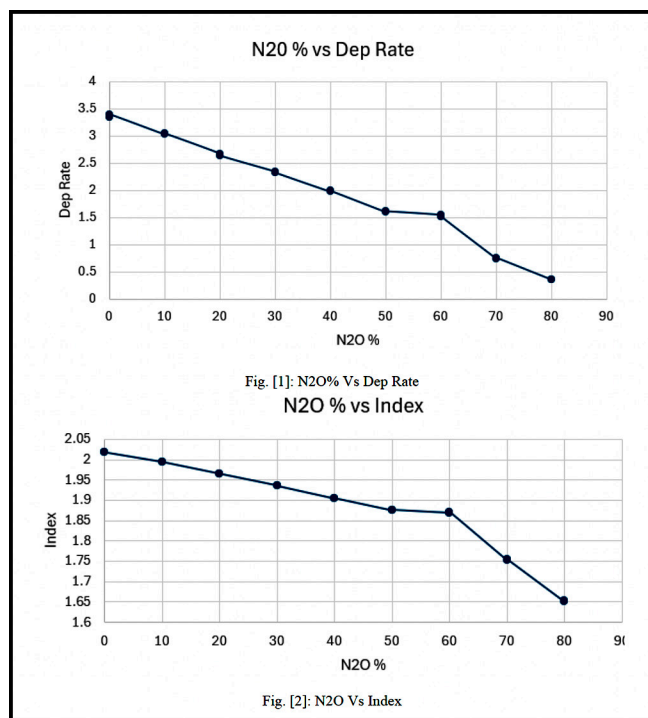
Results:

After each run was performed, the films were tested using the J. A. Woollam RC2 Ellipsometer. This was used to determine the thickness of the film, which would allow the deposition rate to be calculated. The ellipsometer also provided the index of refraction of the film. After the initial film properties were gathered, the film on the back side of the wafer was etched, to make a stress measurement using the FleXus. This allowed for the film to generate stress on only the top side of the wafer, so the stress of the film can be measured. Before the furnace process, each wafer was tested to determine an initial stress value. This can then be used to determine the stress of the film by taking the difference. The overall results can be viewed in Table 4.

TABLE 4: RESULTS									
Wafer ID	Time	NH3 %	NH3 Sccm	N2O %	N2O Sccm	Thickness	Dep Rate	Index	Stress
ON-1	30	90	180	0	0	100.37	3.345667	2.0174	
ON-2	30	90	180	0	0	101.89	3.396333	2.0176	
ON-9	30	80	160	10	20	90.73	3.024333	1.994	
ON-10	30	80	160	10	20	91.35	3.045	1.994	
ON-11	30	70	140	20	40	80.2	2.673333	1.965	
ON-12	30	70	140	20	40	79.04	2.634667	1.965	
ON-13	30	60	120	30	60	70.19	2.339667	1.936	856.915
ON-14	30	60	120	30	60	69.65	2.321667	1.935	
ON-15	30	50	100	40	80	59.06	1.968667	1.90369	848.105
ON-16	30	50	100	40	80	59.58	1.986	1.90474	
ON-17	60	40	80	50	100	95.66	1.594333	1.87467	
ON-18	60	40	80	50	100	96.59	1.609833	1.87606	677.133
ON-19	60	30	60	60	120	92.59	1.543167	1.8689	732.999
ON-20	60	30	60	60	120	90.93	1.5155	1.87191	
ON-21	60	20	40	70	140	44.28	0.738	1.75273	619.534
ON-22	60	20	40	70	140	45.33	0.7555	1.75518	
ON-23	90	10	20	80	160	31.59	0.351	1.65041	321.178
ON-24	90	10	20	80	160	32.2	0.357778	1.65213	

From the results we can observe the decrease in deposition rate, index of refraction and stress as a factor of the gas ratio. For the stress data, only one wafer was etched, to leave a complete wafer still intact for more possible further exploration such as etch tests etc. The first few wafers there were no stress data for, due to some errors with the furnace, that led to the tool needing maintenance. With the other data, a better visualization is provided in Figures 1 and 2.

The figures tend to show a very linear trend for the deposition rate, with one outlier at the 60 percent mark. A similar trend appears with the index. At this range the film possibly has a larger concentration of oxygen than nitrogen. The same point also shows an inverse exponential regression of the index of refraction. As the original few points are very linear, at 60 percent N₂O, the index decreases rapidly. Overall the characterization will allow users to better produce certain films to their specifications. Consistent characterization of tools allows for more accurate results based on the tool information sheets. With tools going down, and requiring maintenance, the results of a process may change over time. This experiment should allow users to produce an accurate oxynitride film to their specifications.



Nanotechnology Workforce and Curriculum Development

CNF Project Number: CNF Summer Internship

Principal Investigator(s): Ron Olson¹, Lynn Rathbun¹

User(s): David M. Syracuse²

Affiliation(s): 1. Cornell NanoScale Science and Technology Facility (CNF), Cornell University;

2. Tompkins-Seneca-Tioga Board of Cooperative Educational Services (TST BOCES)

Primary Source(s) of Research Funding: Cornell NanoScale Facility (CNF), a member of the National Nanotechnology Coordinated Infrastructure (NNCI), which is supported by the National Science Foundation (Grant NNCI-2025233)

Contact: ro246@cornell.edu, lcr2@cornell.edu, dms435@cornell.edu

Research Group Website(s): <https://www.cnf.cornell.edu/>, www.mistersyracuse.com

Primary CNF Tools Used: Unaxis 770 Deep Silicon Etcher, ABM Contact Aligner, Hammatech Wafer Developer, Anatech Plasma Asher

Abstract:

Nanotechnology, and all of the promises and penitential that it holds, is becoming increasingly important from an economic, workforce. Microprocessors, computer memory, and other technologies that make modern life possible all depend on research and development at the nanoscale. It is therefore critical that more people are exposed to possible careers and ideas surrounding this concept. While it is important to ensure that current employment needs in this field are met, it's critical that we look toward the future of the industry. This requires students in K-12 educational programs to be well-versed in these concepts and ideas. I worked to make sure that teachers, students, and industry partners are working together to achieve these goals.

engineering design, none of them are specifically relevant to solving problems at the nanoscale. There are also expectations at all grade levels for students to build devices that transform one type of energy into another, but again, nothing is mentioned about the scale. This presents an opportunity to include nanoscale examples where older, macroscale examples might have been previously used.

Dr. Tamer Uyar in the fiber science department studies a process called electrospinning, whereby a polymer is extruded from a needle via an electric field. Varying the voltage, humidity, or a number of other factors can change the size of the nanofibers that are produced. I worked with Dr. Uyar this summer to develop ways that this technology can be demonstrated in the classroom, and will continue to do so over the course of this academic year.

Because nanotechnology is inherently cross-curricular, it's also the ideal vehicle to deliver instruction that highlights the crosscutting concepts that the NYSSLS emphasize at every level. Most practicing scientists realize that a working knowledge of chemistry, physics, math, and myriad other subjects is necessary to grow our collective understanding and make progress in any field. To that end, I worked with and presented to in-service teachers through the United Federation of Teachers and the American Federation of Teachers to show them how nanoscale concepts can fit into their curricula.

I also presented at the Northeast Regional Defense Technology meeting at Rensselaer Polytechnic Institute on the value of creating and maintaining industry-education partnerships.

Summary of Research:

Curriculum Development:

The New York State Science Learning Standards (NYSSLS) are being rolled out progressively, with 2026 as the target date for a complete transition away from the previous standards, which have been in place since 1996.¹ In the intervening thirty years, there have been new discoveries from animals to elements that have reshaped how humans interact with their world. Chief among these is an explosion in the possibilities that nanotechnology can offer.

The new standards, while commendable, do not explicitly call out nanoscale concepts. For example, while there are performance expectations at all grade levels around

Education and Outreach:

The goals of developing a competent and dynamic workforce for the burgeoning US semiconductor industry depend on students being knowledgeable of and interested in the field. To that end, I worked with students at several outreach events, including a Micron chip camp and two visits from students from New York City. These students came away with an appreciation for the complexity of the devices that are around them every day, as well as the possibilities for future education and employment in the field. I also gave tours to incoming first-year Cornell undergraduate students and to first-year graduate students. These tours gave a comprehensive perspective on what the CNF can offer in terms of research possibilities.

Because not all students or workers have access to a facility like CNF or the programs that it offers, I worked to help develop virtual reality (VR) modules that teach about important concepts in nanoscale manufacturing.

Workforce Development:

A shifting economy requires a nimble workforce in order to be sustainable. The United States has invested in this ideal through initiatives like the CHIPS act, which, among other things, aims to bring more semiconductor manufacturing and job force training back to the country. In service of this, workforce development needs to happen on two main fronts: retraining of people already in the workforce, and preparation of students who will be entering it in the future.

I worked with the New York State Department of Labor to show them the mismatch between current educational programs and the needs of the semiconductor workforce, and will continue to work with them as one of many options to disseminate our virtual reality content.

Microfluidic Device Fabrication:

While students can understand commercial microprocessors and the tools and methods used to produce them, their small size, immense complexity, and sensitivity to contaminants makes them difficult to work with in the K-12 setting. Microfluidic devices are fabricated with identical techniques on identical substrates, but are much more forgiving. It's also possible to interact with them outside a cleanroom and on a scale that is smaller, but familiar, to most students. They therefore provide an ideal method to engage students with nanofabrication techniques in a way that allows for easy measurement and interaction with equipment already present in most science labs.

I have prepared several microfluidic devices that students can use to explore concepts related to the NYSSLS, and also use as jumping-off points for other concepts in a wide variety of STEM courses.

References:

- [1] <https://www.nysed.gov/curriculum-instruction/science-implementation-roadmap-and-timeline>.

Cornell NanoScale Facility High School Summer Internship

CNF Project Number: CNF Summer Internship
Principal Investigator(s): Ron Olson, Lynn Rathbun
User(s): Elyas Talda, Julius Won

Affiliation(s): Cornell NanoScale Facility, Cornell University

Primary Source(s) of Research Funding: Cornell NanoScale Facility (CNF), a member of the National Nanotechnology Coordinated Infrastructure (NNCI), which is supported by the National Science Foundation (Grant NNCI-2025233)

Contact: olson@cnf.cornell.edu, rathbun@cnf.cornell.edu, ehtalda@gmail.com, nowsuiuluj@gmail.com

Primary CNF Tools Used: Oxford 81, Oxford 82, ASML DUV Stepper, P7 Profilometer, Zeiss Supra SEM, Unaxis 770 Deep Silicon Etcher, Plasma-Therm Versaline Deep Silicon Etcher, Oxford Cobra ICP Etcher, Gamma Automatic Coat-Develop Tool

Abstract:

Our internship was mainly spent between two projects: characterization of multiple different tools and cleanroom upkeep, maintenance, and development. We helped to install new gas lines for compressed air and house nitrogen in an upstairs lab space. We also assisted in orbital welding a new exhaust pipe to a cleanroom etcher. Our other main project was working towards characterizing many different etch recipes on multiple Reactive Ion Etching (RIE) tools. We ran various etches, measuring the feature step-heights after pre-etch, etch, and cleaning processes. Late in our data-collection, we realized our measurements were incorrect when we calculated negative process selectivity rates. We attribute this error to noise in our larger measurements registering as larger than the change in photoresist height, potentially caused by multiple issues in our process. While we are disappointed by this, we have learned much about the levels of exactitude required in the cleanroom as well as how to consider acceptable margins of error and stay within them.

Summary of Research:

Our characterization project focused on running etch recipes on multiple tools throughout the lab and measuring pre-, during-, and post-process step-heights. We could then take that data, calculate etch rates and selectivity, and compare it to previously collected data to determine how each tool functioned now versus in the past. This could illuminate tool issues or determine needed recipe adjustments as tools age.

Our characterization happened in several waves. In the first, we grew silicon nitride, silicon oxide, and polysilicon layers on silicon wafers before spinning photoresist and exposing and developing our pattern.

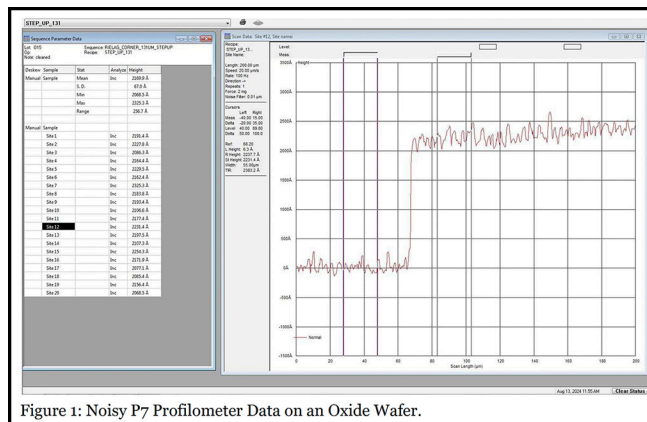


Figure 1: Noisy P7 Profilometer Data on an Oxide Wafer.



Figure 2: Compressed Air (left) and House Nitrogen Gas Lines Ran in Lab 238. We installed six of these valves and their pipework under Paul's supervision.

We then performed an anti-reflective coating (ARC) etch on each wafer before using the P7 Profilometer to measure the step-height of our pattern's features. We utilized a measurement sequence that took step-height measurements at 20 different locations across the wafer's surface to characterize the selectivity of each tool. Afterwards, we ran various etch recipes on the wafers using both the Oxford 81 and 82 (Table 1). After using the P7 to measure the post-etch height, we conducted a photoresist clean on the wafers before performing a final post-process measurement on each wafer.

In the second wave, we performed a similar process with bare silicon wafers using the Unaxis 770 Deep Silicon Etcher, the Oxford Cobra ICP Etcher, and the Plasma-Therm Versaline Deep Silicon Etcher (Table 2). Our process was identical to the first wave, beginning with an ARC etch, moving to the characterization etch, and ending with a photoresist clean, though this wave, we ran recipe duplicates. We used the same sequence on the P7 to measure each wafer after ARC etch, characterization etch, and clean. Unfortunately, we eventually determined that much of our data was unusable towards characterization due to noise in our measurements appearing larger than the change in photoresist height (Figure 1). This resulted in a negative selectivity rate.

We also decided to duplicate the processes done on the Oxford 81 and 82 in a third wave of wafers. This would not only fill in some data gaps from the first wave, but also provide us with a second set of data points to verify our findings. This third wave data, however, also proved to be critically mismeasured, again containing measurement noise that obscured the change in photoresist height. Many small issues with our measurements could have caused the overlarge noise, including problems in our sample loading, unseen profilometer needle slant, and

a lack of clear parameters for acceptable data results, causing overlarge margins of error. We are disappointed by these nonresults; yet we have learned much through our mistakes. We have gained key knowledge on how to avoid small inaccuracies and mismeasurements that can sum into critical issues by clearly defining acceptable error margins and catching errors as they appear.

Additionally, we assisted Paul Pelletier, Senior Process Engineer, in many different tasks around the cleanroom, its service chassis, and other CNF lab spaces. We began working with him as he introduced us to the basics of high-purity gas line welding and cutting. We helped him weld and install a new exhaust line with a removable section for the Oxford 100 ICP Dielectric Etcher. Upcoming research in the CNF cleanroom will involve analyzing chemical compounds found in etching tool exhausts, making a removable exhaust necessary. Paul also gave us an introduction in working with copper and stainless-steel piping when we installed compressed air and house nitrogen lines above the ceiling in a second-floor lab space (Figure 2). We learned to fit, bend, and cut these pipes as well as how to analyze a space and think creatively around problems.

Conclusions and Future Steps:

Our time as interns at CNF has been a great learning experience and engaging job for both of us. Working at a well-established facility with such experienced and knowledgeable staff is an opportunity that most don't get, much less directly after high school. Though the summer was short, we learned many different skills, from tool-operation and handling to report-writing and professional interaction. We also learned much about handling mistakes and unexpected outcomes, developing our response and correction skills. On a broader scale, CNF was both our first in-depth introductions to microelectronics and nanoscale work. We walk away from this internship with increased knowledge of what it means to work in the nanoscale field and the many opportunities it holds, information that may impact our futures as we head into our first year of college and beyond.

Acknowledgements:

Special thanks to; Ron Olson, Ben Infante, Phil Infante, Jeremy Clark, Tom Pennell, Stacy Clementson, Paul Pelltier, and Sam Wright, for all their work in supporting us throughout our internship.

Recipe Name	RF Power (Watts)	CF4 Flow Rate (sccm)	CHF3 Flow Rate (sccm)	SF6 Flow Rate (sccm)	Ar Flow Rate (sccm)	O2 Flow Rate (sccm)	Oxide Wafers Run	Nitride Wafers Run	Polyoxide Wafers Run
CF4	150	30					1	1	1
CHF3+Ar	200		45		15		1		
CHF3+O2 Oxide	150/200		50			2	1		
CHF3+O2 Nitride	150		50			5		1	
Si anISO 100 mm	100		26	26		17			1

Table 1: Oxford 81 and 82 Recipes and Wafers Ran. Note that the CHF3+O2 Oxide recipe ran at 150 watts on the Oxford 82, while the 81 ran at 200.

Tool	Unaxis	Unaxis	Versaline	Cobra
Process	otrench	Photonics	IAT	HBr+Ar PR 2
Time/Loops	80 loops	5 mins	100 loops	10 mins

Table 2: Etch Recipes Ran on Each Deep Silicon Etcher.

The Effects of Nitrogen Annealing on Etch Rates of HDPECVD and PECVD Silicon Dioxide Films

CNF Project Number: Cornell NanoScale Facility Staff Research
User(s): Aaron Windsor

Affiliation(s): Cornell NanoScale Facility, Cornell University

Primary Source(s) of Research Funding: National Science Foundation under Grant No. NNCI-2025233

Contact: windsor@cnf.cornell.edu

Research Group Website: <https://www.cnf.cornell.edu/>

Primary CNF Tools Used: Plasma-Therm Takachi HDP-CVD System, Oxford Plasmalab System 100 PECVD, Woollam RC2 Spectroscopic Ellipsometer, Anneal LPCVD Furnace Tube, Verteq 1800.6 Spin Rinse Dryer

Abstract:

Plasma-enhanced chemical vapor deposition (PECVD) is a reliable technique for depositing silicon dioxide (SiO_2), but these films are notably less dense than thermal oxidation. It has been proposed that as-deposited PECVD films are composed of 5% by volume of micropores [1]. Over time, this porosity becomes susceptible to humidity, affecting stress and device performance. To collapse these micropores and improve film quality, PECVD SiO_2 films are often thermally annealed after deposition. While there is an abundance of information on annealing PECVD films, little has been published about films deposited/annealed by high density plasma enhanced chemical vapor deposition (HDPECVD). Unlike the weak ionization produced by PECVD capacitive plasma systems, HDPECVD generates high density plasma with an inductively coupled plasma (ICP) source coiled around the deposition chamber. This denser plasma increases free electron/precursor interactions which gives HDPECVD the advantage of operating with lower gas flows and at lower pressures than PECVD. The ICP power combined with wafer biasing gives HDPECVD the unique capability of depositing SiO_2 at 100°C. This work will compare the effects nitrogen annealing on HDPECVD and PECVD SiO_2 films by examining changes in film thickness and wet etch rates.

The SiO_2 etch reaction in pure hydrofluoric acid (HF) is the combination of the following two reactions:

- $\text{SiO}_2 + 6\text{HF} \rightarrow \text{H}_2\text{SiF}_{6(\text{aq})} + 2\text{H}_2\text{O}$
- $\text{SiO}_2 + 3\text{HF}_2 + \text{H}^+ \rightarrow \text{SiF}_6^{2-} + 2\text{H}_2\text{O}$

With concentrations of pure HF lower than 10M, the fluoride (F^-) and bifluoride (HF_2^-) ions are the dominant etch species with the bifluoride etching silicon dioxide 4.5 times faster than HF [2]. Etching silicon dioxide in pure HF is rapid and is used for completely removing the oxide or the native oxide without damaging the silicon

wafer. For a more controllable silicon dioxide etch used in semiconductor processing, buffer oxide etch (BOE) is preferred. The addition of ammonium fluoride (NH_4F) with HF suppresses the difluoride resulting in the HF complex becoming the dominant etch species [3].

Summary of Research:

For this work, approximately 1000 nm of SiO_2 was deposited on single side polished N-type, 100 mm diameter, 525 μm thick, prime, <100> silicon wafers. For HDPECVD, all ten depositions were completed on a Plasma-Therm Takachi HDP-CVD System at the as-deposited temperature of 100°C with silane (SiH_4) and oxygen (O_2) precursor gases. For PECVD, an Oxford Plasmalab System 100 PECVD tool was used to deposit SiO_2 on nine wafers at an as-deposited temperature of 350°C with SiH_4 and nitrous oxide (N_2O). All wafers were MOS cleaned and nitrogen annealed from 300-1100°C for one hour. The anneal temperatures were calibrated from the combination of three separate heating elements in a low temperature chemical vapor deposition (LPCVD) furnace tube. A Woollam RC2 Spectroscopic Ellipsometer was used for all thickness measurements. The percent change in film thicknesses was calculated by the difference in as-deposited/annealed thicknesses divided by the as-deposited thickness and expressed as a percentage.

Wafers were submerged into room temperature (approximately 20°C in the temperature-controlled CNF cleanroom) 6:1 BOE at thirty-seconds intervals. After thirty seconds, the wafers were immediately submerged in deionized wafer and rinsed again using a Verteq 1800.6 spin rinse dryer. Three wafers were etched at a time and a new BOE solution was used after each three-wafer etching cycle. Wafers were etched process side up

to prevent any bubbles from effecting the etch results and the position of the wafers (top, middle and bottom) was rotated in the Teflon® wafer holder after each etch. Etching measurements were done after each thirty-second etch and ended after the oxide was etched below 150 nm. Etch rates were determined by averaging the differences in thicknesses after each thirty second etch. For comparison, the etch rate for LPCVD thermally wet oxide grown at 1100°C was calculated using this same method.

All the oxide films decreased in thickness when annealed, but the percentage change in thickness after annealing was significantly higher for HDPECVD films (Figure 1). As annealing temperatures increase above 400°C for PECVD oxide, remaining hydrogen from the silane precursor breaks down leaving extra micropores. Higher temperatures will collapse free hydrogen and as-deposited micropores and above 600°C, Si-O bonds will relax and become more ordered [4]. The relaxation of the PECVD oxide is apparent above 700°C, but the HDPECVD densification curve is different due to the lower temperature, gas flows and operating pressure required for the deposition. Denser films and reduced porosity resulted in lower 6:1 BOE etch rates as annealing temperatures increase (Figure 2). When annealed at 1100°C, both films had comparable etch rates to thermal oxide grown at 1100°C (Table 1). From both graphs, trends in annealing temperature densifications correlate with etch rate non-linearities. Future work should examine changes in the absorbance spectra of annealed Si-O networks from both deposition methods.

References:

- [1] J. S. Herman and F. L. Terry, "A Two-temperature Technique for PECVD Deposition of Silicon Dioxide," in *IEEE Electron Device Letters*, vol. 12, no. 5, pp. 236-237, May 1991, doi: 10.1109/55.79568.
- [2] K. R. Williams and R. S. Muller, "Etch Rates for Micromachining Processing," in *Journal of Microelectromechanical Systems*, vol. 5, no. 4, pp. 256-269, Dec. 1996, doi: 10.1109/84.546406.
- [3] H. Proksche and G. Noagorsen, "The Influence of NH₄F on etch rates of Undoped SiO₂ in Buffered Oxide Etch," in *J. Electrochem. Soc.*, Vol. 139, 521-524, February 1992, doi: 10.1149/1.2069249.
- [4] Fu, J., Shang, H., Li, Z., et al. "Thermal annealing effects on the stress stability in silicon dioxide films grown by plasma-enhanced chemical vapor deposition," *Microsyst Technol* Vol. 23, 2753–2757 (2017), doi: 10.1007/s00542-016-3005-1.

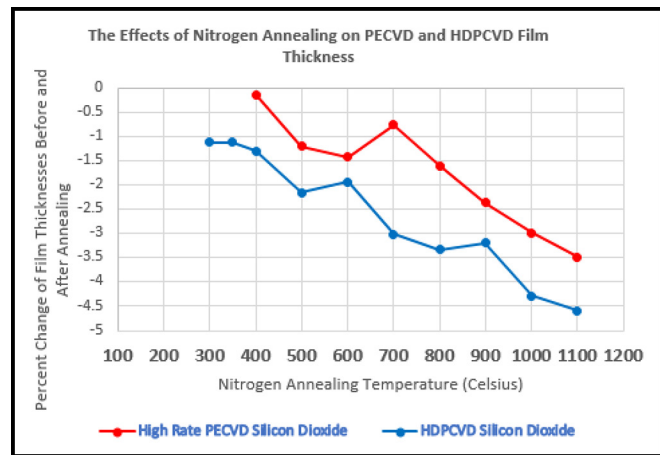


Figure 1: Changes in SiO₂ thicknesses as nitrogen annealing temperatures increase for PECVD and HDPECVD films.

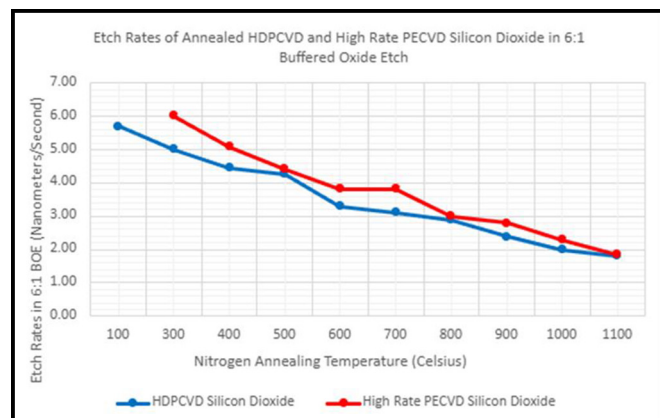


Figure 2: Changes in SiO₂ etch rates as nitrogen annealing temperatures increase for PECVD and HDPECVD films.

SiO ₂ Films	Etch Rate (nm/min)
High Rate PECVD Annealed @ 1100°C	1.86
HDPCVD Annealed @ 1100°C	1.85
Wet Thermal Oxidation @ 1100°C	1.76

Table 1: Etch rates for SiO₂ deposited or grown films @ 1100°C.

The Effects of Nitrogen Annealing on Stress of HDPECVD and PECVD Silicon Dioxide Films

CNF Project Number: Cornell NanoScale Facility Staff Research
User(s): Aaron Windsor

Affiliation(s): Cornell NanoScale Facility, Cornell University

Primary Source(s) of Research Funding: National Science Foundation under Grant No. NNCI-2025233

Contact: windsor@cnf.cornell.edu

Research Group Website: <https://www.cnf.cornell.edu/>

Primary CNF Tools Used: Plasma-Therm Takachi HDP-CVD System, Oxford Plasmalab System 100 PECVD, Woollam RC2 Spectroscopic Ellipsometer, Flexus 2320-S Stress Measurement System, Anneal LPCVD Furnace Tube

Abstract:

While thermal oxidation is the most common method for batch processing silicon dioxide (SiO_2), the high thermal energy required (800°C -1200°C) and low deposition rates limits its use in modern semiconductor fabrication. In the late 1960's, the emergence of plasma enhanced chemical vapor deposition (PECVD) revolutionized the semiconductor industry. An inert plasma can dissociate precursor gases and provide the activation energy necessary to deposit thin films at temperatures between 200°C -450°C. Along with higher deposition rates, PECVD became a reliable method for depositing many dielectrics, but this process does not produce the same SiO_2 film quality as thermal oxidation. Typically, SiO_2 films have a moderate compressive stress which is beneficial for integrated circuit processing [1], but over time, humidity and ambient moisture will cause the stress to drift and become more compressive [2]. Controlling film stress and wafer flatness directly impacts the long-term quality of devices and excessive stress can lead to buckling or delamination. To stabilize stress, PECVD SiO_2 films are often thermally annealed after deposition to collapse micropores and breaks down bonded hydrogen (H) and hydroxyl groups (OH) [3].

Optimizing PECVD deposition parameters seems to be an alternative path for improving film quality, so in early 2022, the CNF installed a Plasma-Therm Takachi High Density Plasma Chemical Vapor Deposition (HDPECVD) system for depositing silicon oxide. This HDPECVD system uses an inductively coupled plasma (ICP) source to create a denser plasma than other conventional parallel plate PECVD systems such as our Oxford Plasmalab System 100. The higher density plasma translates into more free electrons to interact with reactive gas species, eliminating the need for high process gas flows. Combined with the capability of biasing the wafer, HDPECVD can deposit high quality

films at significantly lower temperatures. While there is an abundance of information on PECVD films, little has been published about films deposited/annealed by HDPECVD. This work will compare the effects nitrogen annealing has on HDPECVD and PECVD SiO_2 film stress and wafer flatness.

Summary of Research:

For this work, approximately 1.0 μm of SiO_2 was deposited on single side polished (SSP) N-type, 100 mm diameter, 525 μm thick, prime, <100> silicon wafers. For HDPECVD, all ten depositions were completed on a Plasma-Therm Takachi HDP-CVD System at the as-deposited temperature of 100°C with silane (SiH_4) and oxygen (O_2) precursor gases. For PECVD, an Oxford Plasmalab System 100 PECVD tool was used to deposit SiO_2 on nine wafers at an as-deposited temperature of 350°C with SiH_4 and nitrous oxide (N_2O). All wafers were MOS cleaned and nitrogen annealed from 300-1100°C for one hour. The anneal temperatures were calibrated from the combination of three separate heating elements in a low temperature chemical vapor deposition (LPCVD) furnace tube. A Woollam RC2 Spectroscopic Ellipsometer was used for all thickness measurements before and after annealing. Stress measurement calculations were based on these thicknesses. All the oxide films decreased in thickness when annealed, but the percentage change in thickness after annealing was significantly higher for HDPECVD films. Film stress and wafer bow were measured on a Flexus 2320-S Stress Measurement System. Measurements were at room temperature using a 670 nm laser light source and at the zero- and ninety-degree (0° and 90°) orientation.

Results:

The average as-deposited compressive stress at both orientations for HDPECVD SiO₂ was -235 MPa which is almost one-hundred MPa higher than the as-deposited PECVD oxide (-136 MPa). Both oxide films became less compressive (more tensile) as annealing temperatures were increased to 600° C, and more compressive at higher annealing temperatures (Figure 1). While the PECVD stress curve peaked at -32 MPa before becoming more compressive, the HDPECVD oxide annealed at 350° C had almost zero stress (-0.74 MPa) and films became tensile when annealed between 400°C - 700°C. At 1100°C, both films had a similar compressive stress (HDPECVD @ -244MPa and PECVD @ -246 MPa).

Wafer bow is an indicator of the flatness of a wafer in semiconductor processing. A compressive film will have a positive wafer bow and a tensile film will have a negative. New SSP wafers had an average wafer bow of -1.3 μm at the 0° orientation and -1.76 at 90° orientation. The average as-deposited wafer bow was higher for the HDPECVD films (+21.3 μm at 0° and +20.9 μm at 90°) which correlates with the higher compressive stress than the PECVD oxide (+12.3 μm at 0° and +12.1 μm at 90°). As with the stress, wafer bow changed significantly more negative (tensile) for the HDPECVD SiO₂ than the PECVD (Figure 2). Wafer bow was between +/- 3μm for SiO₂ annealed at 300°C, 350°C and 800°C for the HPCVD and from 500°C -700°C for PECVD SiO₂.

References:

- [1] M. S. Haque, et al. "Characterization of High Rate Deposited PECVD Silicon Dioxide Films for MCM Applications" J. Electrochem. Soc. Vol.142, 3864-3869 (1995), doi: 10.1149/1.2048425.
- [2] M.S Haque, H.A Naseem, W.D Brown. "Post-deposition processing of low temperature PECVD silicon dioxide films for enhanced stress stability," Thin Solid Films, Volumes 308-309, 68-73 (1997), [https://doi.org/10.1016/S0040-6090\(97\)00542-7](https://doi.org/10.1016/S0040-6090(97)00542-7).
- [3] Fu, J., Shang, H., Li, Z., et al. "Thermal annealing effects on the stress stability in silicon dioxide films grown by plasma-enhanced chemical vapor deposition," Microsyst Technol Vol. 23, 2753-2757 (2017), doi: 10.1007/s00542-016-3005-1.

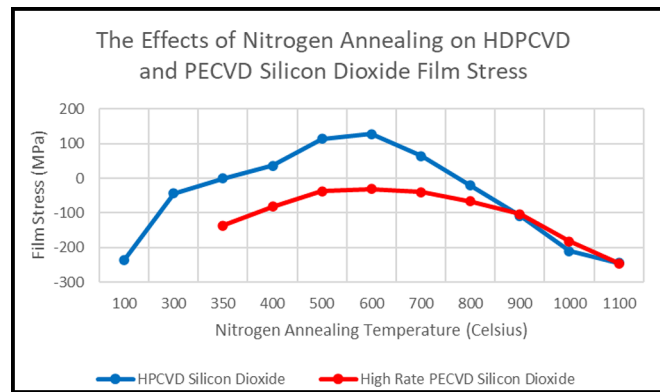


Figure 1: Changes in SiO₂ stress as nitrogen annealing temperatures increase for PECVD and HDPECVD films.

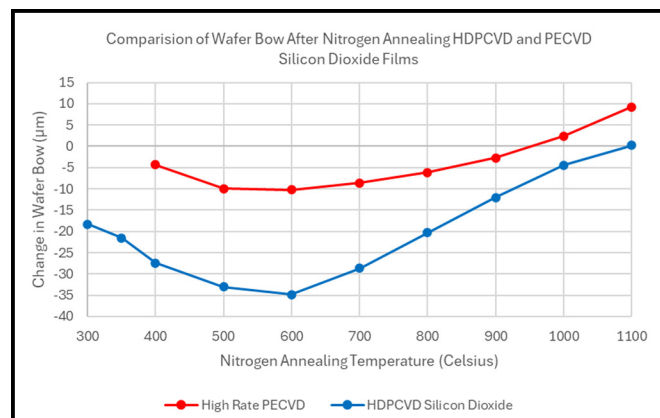


Figure 2: Changes in SiO₂ wafer bow as nitrogen annealing temperatures increase for PECVD and HDPECVD films.

The Viability of 1,3,3,3-Tetrafluoropropene as a Low Global Warming Potential Silicon Dioxide Etch Gas at the Cornell NanoScale Facility

CNF Project Number: Cornell NanoScale Facility Staff Research

User(s): George McMurdy, Jeremy Clark, Robert G. Syvret, Aaron Windsor, Ron Olson

Affiliation(s): Cornell NanoScale Facility, Cornell University; EFC Gases & Advanced Materials

Contact: windsor@cnf.cornell.edu

Research Group Website: <https://www.cnf.cornell.edu/>

Primary CNF Tools Used: Oxford Plasmalab System 100 ICP RIE system,

FilMetrics F50-EXR Optical Measurement System, B2 Thermal Oxide LPCVD Furnace Tube

Abstract:

Silicon dioxide (SiO_2) is one of the most common dielectric materials in the semiconductor industry. Not only is SiO_2 an excellent insulator for integrated circuits and transistors, but it is also an effective hard mask and can be easily patterned at the microscale. While the ability to reactively ion etch (RIE) precise anisotropic features is vital for the future of the industry, many of the etch gases used are reactive hydrofluorocarbons (HFCs) which are considered greenhouse gases (GHGs). These gases hinder the earth's ability to cool down by absorbing/redirecting shortwave radiation from the sun and reflecting longwave radiation admitted from the earth's surface. For the past fifty years, climate scientists have been concerned that GHGs may have varying effects on the warming of the planet. In 1987, the Montreal Protocol was finalized to phase out the use and consumption of ozone depleting gases (OFCs) such as chlorofluorocarbons (CFCs) and bromofluorocarbons (halons) [1]. HFCs were once developed as replacements for OFCs but were later found to be warming the atmosphere at a faster rate than carbon dioxide [2] which is why in 2016, the Kigali Amendment was adopted to the Montreal Protocol to include limits on their use worldwide. Most recently, the United States Congress has taken further steps to reduce HFCs by enacting the American Innovation and Manufacturing (AIM) Act. This grants the U.S. Environmental Protection Agency (EPA) the authority to phase down eighteen HFC gases they consider having high Global-Warming Potentials or GWP.

The Aim Act wants the production and consumption of HFCs to be reduced by 40% between 2024–2028 and 85% by 2036 [1,3].

To reduce their consumption of HFCs while expanding chip manufacturing throughout the United States,

the semiconductor industry is seriously exploring the next generation of lower GWP gases for etching semiconductors and dielectrics such as SiO_2 .

The hydrofluoroolefin (HFO) 1,3,3,3-Tetrafluoropropene ($\text{C}_3\text{H}_2\text{F}_4$) has been recommended as a substitute gas for etching SiO_2 . HFOs are considered a promising environmentally friendly replacement for CFCs, halons, hydrochlorofluorocarbons (HCFCs) and HFCs as refrigerants and for other industrial processes [4]. These gases have high gas phase reactivity along with exchange values (numerically equivalent of 100-year GWP) much lower than legacy etch gases such as trifluoromethane (HFC-23, CHF_3) and difluoromethane (HFC-32, CH_2F_2) [5].

This work will investigate the viability of the unsaturated fluorocarbon $\text{C}_3\text{H}_2\text{F}_4$ for etching SiO_2 when directly exchanged for difluoromethane, a known saturated fluorocarbon etch gas (both gases supplied by Electronic Fluorocarbons). Repeated blanket SiO_2 films were etched with both gases as a direct comparison of etch rates and uniformity on 100 mm wafers. Difluoromethane etches were done before and after repeated $\text{C}_3\text{H}_2\text{F}_4$ etches to examine possible unwanted side effects this HFO may have on the etch chamber and/or future etches.

Experimental:

Approximately 500 nm of wet thermal oxide were grown on 100 mm diameter, 550 μm thick, single side polished, P-type prime silicon wafers. All dielectric etches were done on an Oxford PlasmaLab 100 inductively coupled plasma (ICP) RIE system that has dependably etched SiO_2 at the Cornell NanoScale Facility for over fifteen years. The etch parameter for both gases are illustrated

$C_3H_2F_4$ or CH_2F_2	20 sccm
Helium	80 sccm
ICP	3000 W
RIE	60 W
Chamber Pressure	4 mTorr
Electrode Temperature	10 °C

in Table 1. Both $C_3H_2F_4$ and difluoromethane were individually introduced through a gas ring just above the wafer on the electrode. Helium is applied for backside wafer cooling.

Blanket silicon dioxide thicknesses were mapped on twenty-four wafers and divided into three, eight wafer groups. The first group of eight wafers were etched consecutively with difluoromethane for ninety seconds and mapped again for thickness. The second group of eight wafers were etched for ninety seconds with $C_3H_2F_4$ and the third group of eight wafers were etched again with difluoromethane. Before all three etch groups, a ten-minute oxygen plasma chamber clean and seasoned for two-minute with either difluoromethane or $C_3H_2F_4$. Full wafer mapping and mean etch rates were calculated by measuring film thicknesses before and after etching using a FilMetrics F50-EXR Optical Measurement System. Each wafer map was measured at twenty-five points with 10 mm edge exclusion and aligned to the wafer's flat. The final average etch rates were calculated by the average of the mean etch rates for all eight wafers in a group.

Results:

The full wafer etch test demonstrated that $C_3H_2F_4$ is an equivalent etch gas for SiO_2 . The average mean etch rate is higher than difluoromethane (Table 2). The standard deviation was higher for $C_3H_2F_4$ than both difluoromethane runs. Further, the average etch rate was slightly lower and the standard deviation slightly higher for the last difluoromethane etch group than the first etch group. This demonstrates that a ten-minute oxygen clean is effective for cleaning the chamber after

Etch Gas Groups	Average SiO_2 Etch Rate (nm/min)	Standard Deviation (nm/min)
First CH_2F_2	135.26	0.5
$C_3H_2F_4$	160.85	1.1
Last CH_2F_2	133.46	0.65

720 seconds of $C_3H_2F_4$ etching and the unsaturated fluorocarbon does not display any obvious detrimental effects to the etch chamber or later etch processes. This first test was promising, but more work needs to be done in the future.

References:

- [1] U.S. Department of State. (n.d.). The Montreal Protocol on Substances That Deplete the Ozone Layer. U.S. Department of State. <https://www.state.gov/key-topics-office-of-environmental-quality-and-transboundary-issues/the-montreal-protocol-on-substances-that-deplete-the-ozone-layer/>.
- [2] Scott Denning, (2024, May 22). Cooling conundrum: HFCs were the "safer" replacement for another damaging chemical in refrigerators and air conditioners – with a treaty now phasing them out, what's next? The Conversation. <https://theconversation.com/cooling-conundrum-hfcs-were-the-safer-replacement-for-another-damaging-chemical-in-refrigerators-and-air-conditioners-with-a-treaty-now-phasing-them-out-whats-next-191172>.
- [3] Environmental Protection Agency. (2024, January). Final Rule – Phasedown of Hydrofluorocarbons: Establishing the Allowance Allocation and Trading Program under the American Innovation and Manufacturing (AIM) Act. EPA. <https://www.epa.gov/system/files/documents/2021-09/hfc-allocation-rule-nprm-fact-sheet-finalrule.pdf>.
- [4] Cynthia B. Rivela, Carmen M. Tovar, Mariano A. Teruel, Ian Barnes, Peter Wiesen, María B. Blanco, CFCs replacements: Reactivity and atmospheric lifetimes of a series of Hydrofluoroolefins towards OH radicals and Cl atoms, Chemical Physics Letters, Volume 714, 2019, Pages 190-196, ISSN 0009-2614, <https://doi.org/10.1016/j.cplett.2018.10.078>.
- [5] Fouad, W.A. and Vega, L.F. (2018), Next generation of low global warming potential refrigerants: Thermodynamic properties molecular modeling. AIChE J., 64: 250-262. <https://doi.org/10.1002/aic.15859>.

An Evaluation of 1,3,3,3-Tetrafluoropropene as a Low Global Warming Potential Silicon Dioxide Etch Gas at the Cornell NanoScale Facility

CNF Project Number: Cornell NanoScale Facility Staff Research

User(s): Aaron Windsor, Robert G. Syvret, Jeremy Clark, and Ron Olson

Affiliation(s): Cornell NanoScale Facility, Cornell University; EFC Gases & Advanced Materials

Primary Source(s) of Research Funding: National Science Foundation under Grant No. NNCI-2025233

Contact: windsor@cnf.cornell.edu

Research Group Website: <https://www.cnf.cornell.edu/>

Primary CNF Tools Used: Oxford Plasmalab System100 ICP RIE system, SUSS MicroTec Gamma cluster tool, ASML PAS 5500/300C DUV Wafer Stepper, Oxford PlasmaLab 80+ RIE System, SCE-110-RF Anatech Plasma Etcher, FilMetrics F50-EXR Optical Measurement System, Zeiss Ultra Scanning Electron Microscope, B2 Thermal Oxide LPCVD Furnace Tube

Abstract:

Currently, fluorocarbon (FC) and hydrofluorocarbon (HFC) gases are the primary choice for high aspect ratio etching of dielectric materials. The reason for this is that among the known and commonly used gases, one has access to a wide range of F:C ratios, e.g. from 4:1 in CF_4 to 1:1 in CHF_3 , as well as great structural diversity including straight-chain and cyclic saturated alkanes (e.g., CH_2F_2 and C_4F_8), unsaturated alkenes (e.g., C_3F_6 and C_5F_8) and dienes (e.g., C_4F_6). These diverse characteristics provide a wealth of tunable options related to the aggressiveness of radical species generated in a plasma environment as well as, in some cases, important protective deposition properties of the resulting plasma fragments. Furthermore, each of the FC and HFC gases are readily available in high purity. However, despite all the positive attributes of FC and HFC gases, most have in common a serious downside, and that is related to their chemical and thermal stability. Most of the FC and HFC gases have a high global warming potential (GWP) and are damaging to the environment, and as a result, they are targeted for phase down and possibly eventual elimination through regulatory vehicles such as the U.S. AIM Act of 2021 [1].

One potential alternative to the use of FC and HFC gases is the use of low-GWP hydrofluoroolefins (HFOs). These HFOs have been developed by the fluorochemical industry and commercialized over the last decade or longer to replace high-GWP environmentally damaging refrigerants such as HFC-134a and foam expansion agents such as HFC-245fa. Amongst the known low-GWP HFOs one can find a range of F:C and H:C ratios. Thus, this group presents a potentially viable and environmentally friendly alternative to the use of legacy FCs and HFCs [2]. After promising initial tests etching blanket SiO_2 with the HFO 1,3,3,3-Tetrafluoropropene

($\text{C}_3\text{H}_2\text{F}_4$), the logical next step was to attempt real-world etches of patterned micron and submicron lines. This work will compare SiO_2 etches using the environmentally friendly alternative $\text{C}_3\text{H}_2\text{F}_4$ with saturated alkane legacy gases trifluoromethane (HFC-23, CHF_3) and difluoromethane (HFC-32, CH_2F_2).

Experimental:

Approximately 500 nm and 1000 nm of wet thermal oxide were grown on 100 mm diameter, 550 μm thick, single side polished, P-type prime silicon wafers. All dielectric etches were done on an Oxford PlasmaLab 100 inductively coupled plasma (ICP) reactive ion etch (RIE) system. Both $\text{C}_3\text{H}_2\text{F}_4$ and CH_2F_2 were individually introduced through the gas ring just above the wafer on the electrode.

An automated SUSS MicroTec Gamma cluster tool and an ASML PAS 5500/300C DUV Wafer Stepper were used for all photolithography processing. Wafers were coated with approximately 62 nm of DUV 42P antireflective coating (ARC) followed by approximately 600 nm of DUV 210 positive photoresist, baked at 135°C for ninety-seconds and developed with AZ MIF 726 developer for sixty-seconds. Patterned etched features consisted of eight 5000 μm lines with widths between 5 μm and 300 nm. 40 μm x 400 μm “L” shaped corners were added to the CAD for the profilometer measurements. After development, each wafer was etched with an Oxford PlasmaLab 80+ RIE System to remove the ARC. A ten-minute oxygen plasma chamber clean and two-minute etch on a bare silicon wafer was done to season the chamber before etching with the process gas. For comparison, all three

Etch Time (seconds)	Average SiO ₂ Etch Rate (nm/min)	Average Resist Etch Rate (Angstrom/second)	Average Selectivity
45	208.9	6.5	5.37
120	206.3	5.7	6.04
150	212.6	6.2	5.79
240	210.8	5.2	6.84

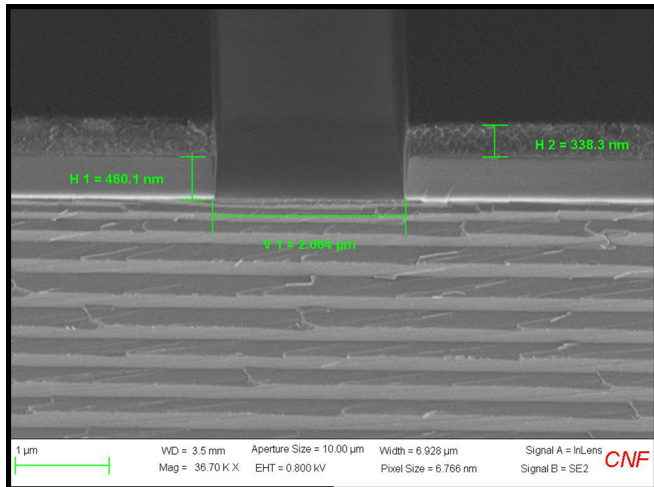


Figure 1: 2000 nm silicon dioxide line etched with C₃H₂F₄ for 160 seconds. SEM image was taken at a 70-degree angle. The actual calculated thicknesses are approximately Height #1 (SiO₂) = 487nm and Height #2 (Photoresist)= 359 nm.

gases etched patterned wafers for two and four minutes. Feature etch rates/selectivity were determined using a KLA Tencor P-7 Stylus Profilometer by measuring an automated programed sequence of twenty step heights across the wafer. The three step heights measured were the height of the DUV 210 resist after the ARC etch, the step height after the dielectric etch, and the step height of the etch after the resist was stripped in an oxygen plasma using a SCE-110-RF Anatech Plasma Etcher. The selectivity was determined by the ratio between the SiO₂ and photoresist etched. Cross-sectional etch profiles were observed using a Zeiss Ultra scanning electron microscope (SEM).

Results:

Four separate C₃H₂F₄ patterned etches between forty-five and two hundred forty seconds established consistent etch rates and etch selectivity for DUV 210 resist (Table 1). When compared to the two legacy gases (Table 2), C₃H₂F₄ had the highest etch rate for SiO₂. The desired selectivity between the oxide and the resist was

Two-Minutes		
Etch Gas Groups	Average SiO ₂ Etch Rate (nm/min)	Selectivity
C ₃ H ₂ F ₄	206.3	6.04
CHF ₃ /O ₂	182.5	1.51
CH ₃ F ₃	158.7	2.24
Four-Minutes		
Etch Gas Groups	Average SiO ₂ Etch Rate (nm/min)	Selectivity
C ₃ H ₂ F ₄	210.8	6.84
CHF ₃ /O ₂	181.3	1.55
CH ₃ F ₃	158.4	2.63

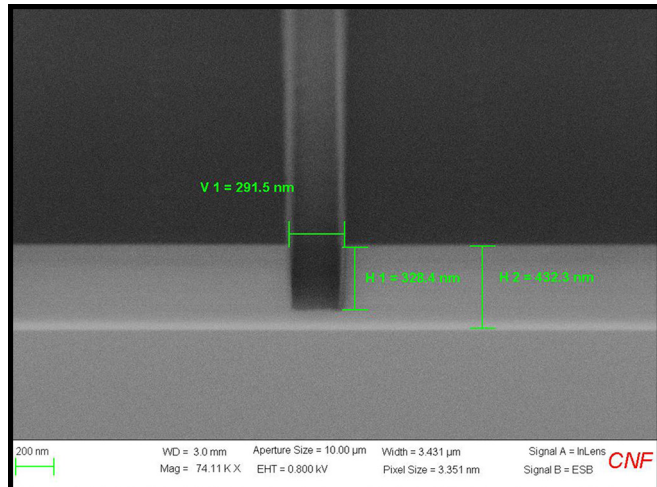


Figure 2: 300 nm silicon dioxide line etched with C₃H₂F₄ for 120 seconds. The photoresist was stripped. SEM image was taken at a 70-degree angle. The actual SiO₂ calculated thicknesses are approximately Height #1 = 348 nm and Height #2 = 458 nm.

much higher than etches using trifluoromethane and difluoromethane. Cross-sections of all C₃H₂F₄ patterned SiO₂ etches appear to have smooth, vertical sidewalls, without signs of resist undercutting (Figure 1). There was evidence of RIE lag for the narrower features (Figure 2). Overall, these etch tests demonstrated that C₃H₂F₄ is a viable alternative for reactive ion etching SiO₂.

References:

- [1] Environmental Protection Agency. (2024, January). Final Rule – Phasedown of Hydrofluorocarbons: Establishing the Allowance Allocation and Trading Program under the American Innovation and Manufacturing (AIM) Act. EPA. <https://www.epa.gov/system/files/documents/2021-09/hfc-allocation-rule-nprm-fact-sheet-finalrule.pdf>.
- [2] Cynthia B. Rivela, Carmen M. Tovar, Mariano A. Teruel, Ian Barnes, Peter Wiesen, María B. Blanco, CFCs replacements: Reactivity and atmospheric lifetimes of a series of Hydrofluoroolefins towards OH radicals and Cl atoms, Chemical Physics Letters, Volume 714, 2019, Pages 190-196, ISSN 0009-2614, <https://doi.org/10.1016/j.cplett.2018.10.078>.

Reports by CNF Principal Investigators & Users

A

Abbaspourrad, Alireza	18
Abbott, Nicholas L.	60, 144
Aggarwal, Kushagra	46
Agrawal, Richa	8
Alfonso, Felix	6
Alzgoor, Mohammad	82
Ash, Benjamin	90
Azhar, Bilal	70

B

Beam, Alex	100
Beeghly, Garrett	22
Best, Eleanor	2
Biradar, Madan Rajendra	32
Brown, Nicholas	50
Butcher, Jonathan T.	14
Byrd, Benjamin	126, 128

C

Cardenas, Jaime	88
Cestarollo, Ludovico	80
Cha, Judy J.	72, 120, 158
Chao, Zhongmou	2
Chen, Peng	6
Chen, River	136
Chen, Siyi (Cathy)	34
Chiarot, Paul	52
Chivukula, Kaushik	76
Choi, Jaehong	150
Chow, Eric	152
Clark, Jeremy	140, 172, 174
Cleland, Andrew	86
Cohen, Itai	84
Cole, Brad	110, 112
Crowley, Jack	22

D

D'Orazio, Giancarlo	54, 104
Daniel, Susan	2
Dhar, Akshey	40
Dill, Joseph	142
Ding, Yunjiang	138, 160
Dodge, Kenneth	110
DuLaney, George	38
Dunbar, Tom	96
Duong, Khoan	102

E

El-Ghazaly, Amal	44, 80
Ellis, Sherri	78
Elpers, Maggie	8
Everly, Christopher (Christer)	122

F

Fang, Qiyi	76
Fatemi, Valla	46
Favakeh, Amirhossein	18
Fernandez-Ruiz, Antonio	26
Finsterer, Azriel	38
Fischbach, Claudia	22
Fitzgerald, Jordan	2
Fors, Brett	30
Fuchs, Gregory D.	58, 150
Funni, Stephen D.	120

G

Gadikota, Greeshma	156
Garudapalli, Ashutosh	76
Ghajari, Shahab	16
Gingerich, Marcus	48

H

Henretta, Sarah	8
Hester, Emma	62
Hong, Yifeng	4
Hormozi, Sarah	134
Housser, Graeme	48
Huang, Steven He.	10
Huang, Xiaoxi.	106
Hwang, James C. M.	138, 160

I

Infante, Ben	162
Infante, Phil	146

J

Jaramillo, Oscar	92
Jena, Debdeep	40, 42
Jentis, Eitan	8
Jha, Pankaj K.	130
Jiang, Shengwei	116
Joo, Jin Hong	160

K

Kang, Kaifei	114
Karaba, Lindsay	26
Khilwani, Devesh	16
Kiliclar, Huseyin Cem	32
Kingsley, Bryce	52
Kumar, Sushant.	88

L

Lalieu, Jonathan	134
Lammerding, Jan	8
Larson, Clayton	110
Lee, Esak (Isaac)	20
Lee, Sihun	72
Lee, Sunwoo	16

Lemaster, Gannon	138
Lepak, Lori	94
Levine, Sarah	140
Li, Lizhong	114, 116
Li, Shiqi	144
Li, Sixuan	50
Li, Weiyi	84
Liang, Zexi	80, 84
Liepe, Matthias	118
Lim, Melody Xuan	84
Lu, Haoran	46
Lu, Renhao	20

M

Ma, Warrick	64
Mahalanabish, Aditya	12
Mak, Kin Fai	114, 116
Mamidala, Akanksh	156
Manivannan, Kesavan	126, 128
Marohn, John A.	38
Marui, Rika	28
Mayol López, Fabiana P.	142
McBroom, Tianna	112
McEuen, Paul L.	84
McMahon, Peter	90
McMahon, Shane	48
McMurdy, George	172
Mehta, Karan K.	92
Mokhtare, Amir	18
Molnar, Alyosha C	16
Moore, Chad	48

N

Nair, Hair P.	70
Nowack, Katja	124

O

- Ober, Christopher K.28, 32, 62, 68
 Oliva Gonzalez, Azahara26
 Olson, Ron78, 162, 164, 166, 172, 174
 Ostwalt, Alexis2

P

- Pal, Soumyamouli144
 Pal, Srishti58
 Park, Jaehyo26
 Park, Kwang-Won154
 Paszek, Matthew152
 Paustian, J.T.112
 Pechenezhskiy, Ivan126, 128
 Peng, Yansong20
 Plourde, Britton L.T.110, 112
 Poon, Mong Lung Steve14
 Postigo, Pablo A.122
 Poulsen, Chris.100

Q

- Quansah, Elizabeth54

R

- Ralph, Daniel C.106, 108
 Rathbun, Lynn78, 162, 164, 166
 Remias, Richard A.102
 Richmond, Dylan48
 Ringuette, Anna30
 Ross, Imrie144
 Rout, Jagi130
 Roy, Saswata46

S

- Sadeghi, Sanaz16
 Sam, Quynh102
 Sanchez, Martin122
 Saylor, Hunter104
 Schrlau, Michael24
 Seddon-Stettler, Sadie118
 Sempertegui, Nicole22
 Shah, Rahul98
 Shan, Jie114, 116
 Shao, Yu68
 Shen, Bowen116
 Shen, Po-Ting10
 Shvets, Gennady10, 12
 Siddique, Saif120
 Siddiqui, Mujtaba Y.K.24
 Silberstein, Meredith74
 Sitaraman, Nathan118
 Smart, Conrad80, 84
 Smith, Kathleen42
 Sobhani, Sadaf54, 104
 Striff, Alex124
 Syracuse, David M.164
 Syvret, Robert G.172, 174

T

- Talda, Elyas166
 Tang, Danni56
 Tao, Zui114, 116
 Tate, Mark50
 Teleshevsky, Daniel146
 Tepermeister, Max74
 Thom-Levy, Julia50
 Towfighian, Shahrzad82
 Tschirhart, Charles114
 Tulegenov, Dias12

V

Valentine, Jason G...	..98
Van Herck, Simon66
van Wijngaarden, Ellen74
Vareskic, Bozo	108

W

Walsh, Timothy36
Wang, Han	158
Wang, Michelle D.	4
Wang, Xiaopeng138, 160
Wang, Yadong64, 66
Wang, Zhi	132
Wei, Xianzhi	142
Wiesner, Ulrich56
Williams, Natalie72
Windsor, Aaron	168, 170, 172, 174
Wise, Hajo Johann	148
Won, Julius	166
Wu, Xinwei	148
Wu, Yu-Mi.	120

X

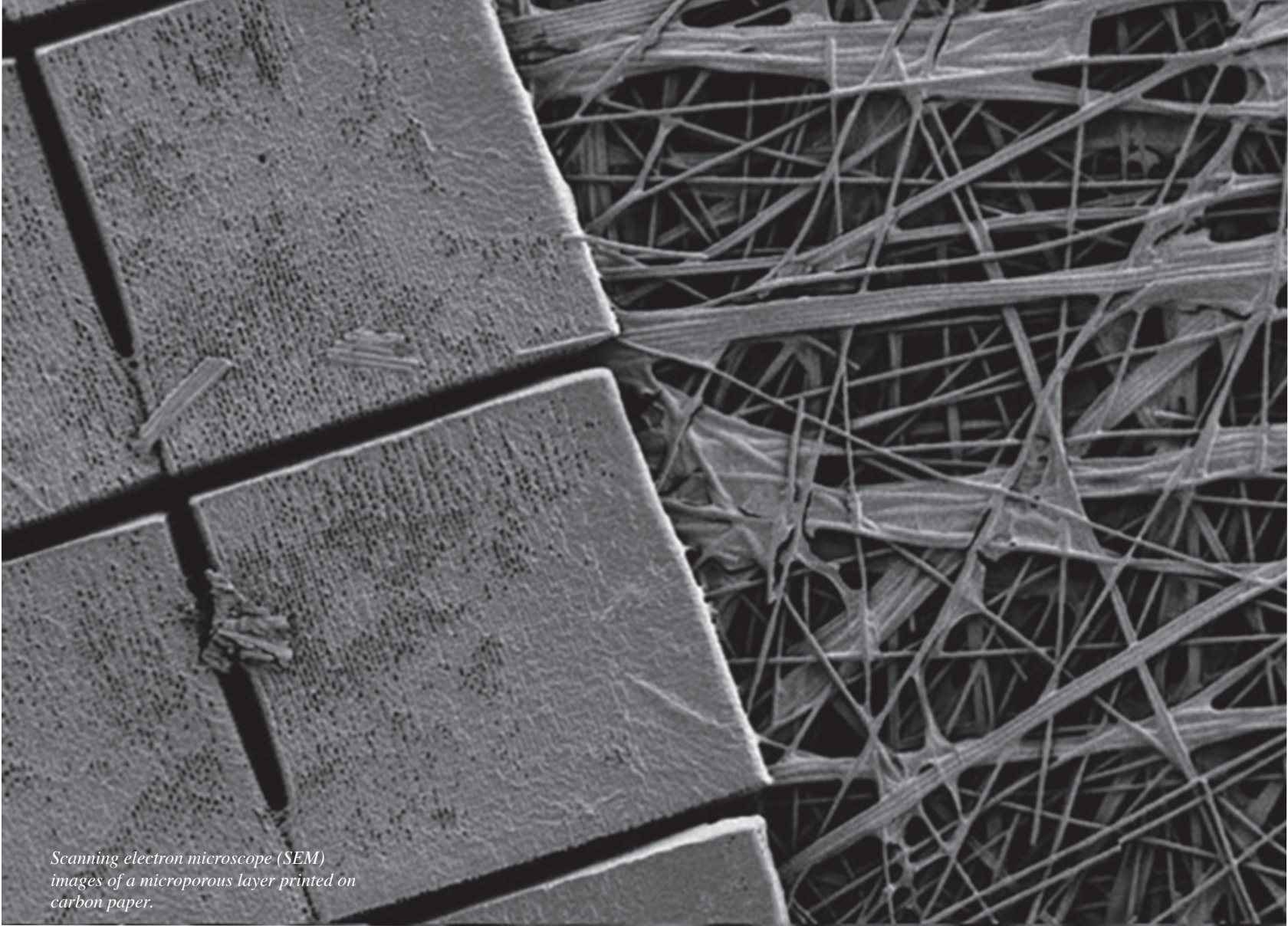
Xing, Huili Grace ..	36, 42, 140, 142, 146, 148
Xu, Qin58

Y

Yahya, Rabia44
Yanagimoto, Ryotatsu90
Yang, Rong144, 154
Yeh, Chia-Wei66
Yelton, Eric	110
Yin, Haosen44
Yin, Shufan20
Yoshida, Erina28
Yuan, Chenyun28

Z

Zhang, Hanyu Alice60
Zhang, LuoJia46
Zhang, Yichi114, 116
Zhao, Wenjin114, 116
Zhao, Zifang26
Zhen, Bo	132
Zhong, Yu34, 76
Zhou, Haolei76



*Scanning electron microscope (SEM)
images of a microporous layer printed on
carbon paper.*

CNF is a member of the
National Nanotechnology Coordinated Infrastructure (www.nnci.net)
and is supported by the National Science Foundation
under Grant No. NNCI-2025233,
New York State Empire State Development, Cornell University, Industry,
and our Users.

The 2023-2024 CNF Research Accomplishments are also available on the web in
full color:

http://cnf.cornell.edu/publications/research_accomplishments



**Empire State
Development**

**Cornell
Research
& Innovation**